



UHASSELT

KNOWLEDGE IN ACTION

Doctoral dissertation submitted to obtain the degree of
Doctor of Sciences: Mathematics, to be defended by

Stephan Benjamin Lunowa

DOCTORAL DISSERTATION

Dynamic Capillarity and
Hysteretic Effects in Two-Phase
Flow in Porous Media:
Modeling, Upscaling and
Simulation

DSI
DATA SCIENCE
INSTITUTE

 **UHASSELT**

Promoter: Prof. Dr Iuliu Sorin Pop | UHasselt

Co-promoters: Prof. Dr Carina Bringedal | University of Stuttgart
Prof. Dr Veerle Cnudde
Ghent University | Utrecht University

D/2022/2451/65

*To my wife and to my parents,
for their patience and support through all the years.*

Stephan B. Lunowa, Dynamic Capillarity and Hysteretic Effects in Two-Phase Flow in Porous Media: Modeling, Upscaling and Simulation, PhD thesis, Hasselt University, Belgium, 2022.

Belgian Royal Library depot number D/2022/2451/65.

Copyright © 2022 Stephan Benjamin Lunowa. All rights reserved.

This work was funded by the Special Research Fund (BOF) at UHasselt (project BOF17NI01) and the Research Foundation Flanders (FWO, project G051418N).

Abstract

Flow and transport processes in porous media are relevant for a huge variety of applications covering all areas of modern society. To describe and predict the relevant processes, it is crucial to understand the complicated underlying phenomena. The mathematical models are based on fundamental balance equations, which are complemented by constitutive equations describing the specific material behavior. These relations must be expressed using effective parameters, which should combine all pore-scale effects.

However, these parameters are simply postulated in many state-of-the-art models and not derived from a pore-scale model. In particular, the interface dynamics between the fluids are typically neglected or incorporated on an empirical basis. In the first part of this work, we consider these effects for simple pore geometries and apply upscaling techniques to derive effective two-phase flow equations.

The upscaled models at the Darcy scale are coupled, nonlinear partial differential equations, which may even degenerate and can involve strong heterogeneities or even discontinuous physical properties. These issues raise analytical and numerical challenges. Besides appropriate discretization methods, linearization schemes must be applied. By domain decomposition methods, essentially different regions are decoupled to parallelize computations and reach a reasonable performance. These numerical aspects are considered in the second part of this work.

Two-phase flow in single pores

First, we consider the flow of two immiscible fluids in a single pore, which is idealized to a long, thin strip or tube. The fluids are separated by a moving interface, which is in contact with the pore wall. Its evolution is driven by the fluid flow and the surface tension. Assuming a scale separation induced by a small aspect ratio of the pore, we apply matched asymptotic expansions to derive effective models for the two-phase flow in the limit as this ratio approaches zero. The resulting averaged model combines Darcy-type equations for the flow with a capillary pressure - saturation relationship involving dynamic effects. Numerical examples illustrate the effects of a varying wall width, of the physical parameters, as well as of having a dynamic and hysteretic contact angle model.

Moreover, we apply the averaged model to the capillary rise of a fluid in cylindrical tubes. Here, the model extends the classical Lucas–Washburn model by incorporating a dynamic contact angle and slip. We further extend the model to account for inertial effects. To validate the different models, their solutions are compared to experimental data. In contrast to the Lucas–Washburn model, the results of the models with dynamic contact angle match the experimental data well, both the rise height and the contact angle, even at early times.

Numerical methods at the Darcy scale

First, we discuss linearized domain decomposition methods for models of two-phase flow in porous media incorporating non-equilibrium effects like dynamic capillarity and hysteresis. For the temporally discretized, nonlinear equations, we propose two schemes which combine the L-scheme and a non-overlapping domain decomposition method into one iteration. We prove the existence and convergence of the solutions for both iterative schemes. The convergence holds independently of the initial guess, and under mild constraints on the time step. Additionally, the schemes are independent of the spatial discretization, and avoid the computation of derivatives. Numerical examples confirm the theoretical results and demonstrate the robustness of the schemes.

Domain decomposition methods can have poor performance when applied to degenerate problems. We consider the linear stationary advection-diffusion equation in one dimension as a prototypical application for non-overlapping domain decomposition methods with Robin transmission conditions. We show that the continuous algorithm is asymptotic-preserving only if the parameter in the transmission condition tends to the advection speed for vanishing diffusion. After discretization by a cell-centered finite volume method, the discrete algorithm can inherit the properties of the continuous one. However, we prove that a proper, but asymmetric choice of the discrete Robin transmission conditions yields an asymptotic-preserving discrete algorithm without constraint on the transmission parameter. We illustrate our results with numerical experiments in one and two dimensions.

Finally, we propose a non-overlapping domain decomposition method with Robin transmission conditions for nonlinear advection-diffusion equations. We prove the existence and convergence of the iterative solutions, and present a discretization for the iterative problems using a forward Euler method in time and a finite volume method in space. The algorithm includes a local Newton iteration for solving the nonlinear transmission conditions. Using the results of the previous linear case, the discrete algorithm is asymptotic-preserving, i.e., robust in the vanishing diffusion limit. Numerical results confirm the theoretical findings. In particular, we show the successful application of this method for two-phase flow problems in porous media involving strongly nonlinear fluxes.

Acknowledgments

During the past four years, which have eventually lead to this dissertation, I have been fortunate to interact and work with many people who supported me in various ways. I would like to use these lines to thank all the people who have accompanied me on this journey.

First of all, I would like express my sincere gratitude to my main supervisor, Prof. Dr. Iuliu Sorin Pop, for the opportunity to join his research group and work in a fascinating and interdisciplinary environment. I am thankful to my co-supervisor, Jun.-Prof. Dr. Carina Bringedal, for the joint effort and support of my doctorate. Their patience and generosity enabled me to work freely on own ideas, while their invaluable knowledge, advice and guidance kept me on the straight and narrow whenever necessary. Sorin and Carina inspired and constantly encouraged me in my quest for knowledge.

Part of my research has been achieved within the FWO project “VisioFlow: Advanced macro-model generation based on micro-scale visualization experiments of two-phase flow through porous sedimentary rocks”. This project was a cooperation between the Computational Mathematics group at UHasselt and the PProgress group at Ghent University. I would like to thank my co-supervisor, Prof. Dr. Veerle Cnudde, for her active interest in my work. I am very thankful to her, Dr. Tom Bultreys and Arjen Mascini for the regular discussions and the fruitful collaboration, which significantly enriched my understanding of porous media beyond the mathematical theory.

Moreover, I would like to thank Prof. Dr. Jochen Schütz for the commitment in my doctoral committee and for the valuable experience as teaching assistant for his lectures on functional and Fourier analysis. Sharing his insights and opinions, as well as the appreciation and encouragement have been indispensable. Further sincere thanks are reserved for Prof. Dr. Béatrice Rivière and Prof. Dr. Barbara Wohlmuth, who kindly agreed to be jury members for this thesis. I would also like to thank Prof. Wohlmuth for the discussion at the Technical University of Munich and her hospitality.

In the course of my studies, I had the pleasure to also work together with Prof. Dr. Martin Gander, Prof. Dr. Barry Koren and Prof. Dr. Christian Rohde. I am grateful for their advice and the fruitful collaboration on linearization and domain decompo-

sition methods. In this regard, I would like to also thank Prof. Dr. Florin Radu, Dr. Koondanibha Mitra, Dr. Davide Illiano, and Dr. David Seus for the insightful discussions on these topics. Likewise, I gratefully acknowledge the discussions with Prof. Dr. Helge Dahle, Prof. Dr. Rainer Helmig and Dr. Martin Schneider about dynamic pore-network modeling, as well as those with Prof. Dr. Michael Celia, Dr. Markus Gahn and Lars von Wolff about upscaling techniques and the intricacy concerning boundary conditions. Special thanks go to Prof. Dr. Mohammad Heshmati and Prof. Dr. Mohammad Piri for providing the experimental data used in [Chapter 3](#).

Furthermore, I would like to express my warmest gratitude to all my colleagues at the Department of Mathematics and Statistics and especially in the Computational Mathematics group, who provided a pleasant working atmosphere. In particular, I would like to thank Dr. Manuela Bastidas Olivares, Sohely Sharmin and Arjun Thenery Manikantan for the good times and the diverse discussions at our shared office. I owe special thanks to Dr. Alexander Jaust for the IT support concerning the Flemish Supercomputer Center (VSC), and to Jeremy Chouchoulis for taking over my teaching obligations when I was indisposed. I would also like to thank the aforementioned and all other colleagues, Prof. Dr. Fred Vermolen, Dr. Jonas Zeifang, Maikel Bosschaert, Ansfried Janssens, Yiorgos Patsios, Roel Schrooten, Eleni Theodosiou, Hoang-An Tran, for always finding an open door for discussions of problems and having enjoyable breaks.

I take this opportunity to thank the Special Research Fund (BOF) at Hasselt University (project BOF17NI01) and the Research Foundation Flanders (FWO, project G051418N) for the financial support, which facilitated my PhD project and the scientific visits to various conferences. Likewise, I thank the German Research Foundation (DFG) for funding the Collaborative Research Centre "Interface-Driven Multi-Field Processes in Porous Media — Flow, Transport and Deformation" (SFB 1313, project 327154368). The workshops and the involvement in the Integrated Research Training Group have extended my understanding of porous media.

Finally, I would like to thank all my friends and family for the support and encouragement. In particular, I am deeply grateful to my parents and my brother, who have cared for me since the very beginning. Last but not least, I would like to thank my loving wife for her never-ending support during all these years. She kept me motivated and patiently endured my scientific curiosity.

Stephan Lunowa

Hasselt, September 2022

Contents

Abstract	v
Acknowledgments	vii
List of Publications	xiii
1. Introduction	1
1.1. Scales and modeling approaches	2
1.2. Modeling of two-phase flow at the pore scale	3
1.2.1. Flow of the fluid phases	5
1.2.2. Moving contact line	5
1.3. Modeling of two-phase flow at the Darcy scale	8
1.3.1. Non-equilibrium capillary pressure	9
1.3.2. Fractional flow formulation	10
1.4. Upscaling and multi-scale methods	10
1.5. Numerical methods	12
1.5.1. Temporal discretization	13
1.5.2. Spatial discretization	15
1.5.3. Linearization	16
1.5.4. Domain decomposition	18
1.6. Outline of this thesis	19
2. Averaged models for two-phase flow with surface tension and dynamic contact angle	25
2.1. Introduction	25
2.2. Mathematical model of two-phase flow in pores	27
2.3. Dimensionless formulation	31
2.4. Asymptotic expansions	33
2.4.1. Flow in the bulk domains	36
2.4.2. Interface with small deformations	39

2.4.3. Unsaturated flow limit	44
2.4.4. Hysteretic contact-angle model	45
2.5. Upscaling for a thin cylindrical tube	47
2.5.1. Non-dimensional model	47
2.5.2. Asymptotic expansion	49
2.6. Averaged models and effective quantities	53
2.6.1. Transversal average: Darcy's law	53
2.6.2. Effective quantities: Dynamic capillary pressure	55
2.7. Numerical experiments	58
2.7.1. Thin strip of constant width	58
2.7.2. Constricted "pore throat"	65
2.8. Conclusion	72
3. Dynamic effects during the capillary rise of fluids in cylindrical tubes	73
3.1. Introduction	73
3.2. Mathematical models	75
3.2.1. Upscaled model and analytic solution	75
3.2.2. Extended model including inertial effects	78
3.3. Comparison with experimental data	79
3.3.1. Glycerol	79
3.3.2. Soltrol 170	80
3.3.3. Water	82
3.4. Discussion	84
3.4.1. The dynamic parameter as physical property	84
3.4.2. The influence of the initial transient regime	85
3.4.3. The meniscus shape	85
3.4.4. Wetting films and slip	86
3.4.5. Uncertainty and limitations of the models and of the fitting	86
3.5. Conclusion	87
4. Linearized domain decomposition methods for non-equilibrium two-phase flow models	91
4.1. Introduction	91
4.2. Modeling of non-equilibrium two-phase flow in porous media	93
4.2.1. Notation	95
4.2.2. Assumptions on the coefficient functions	95
4.3. Temporal discretization and iterative schemes	97
4.3.1. Discretization in time	97
4.3.2. Linearization and domain decomposition schemes	98
4.4. Existence and convergence of the iterative solutions	102
4.4.1. LDD-scheme I	102

4.4.2. LDD-scheme II	108
4.5. Numerical experiments	112
4.5.1. Analytic test cases	113
4.5.2. Realistic test case	123
4.6. Conclusion	126
5. Asymptotic-preserving Robin transmission conditions for singularly perturbed elliptic equations	129
5.1. Introduction	129
5.2. The continuous problem and non-overlapping DDM	130
5.3. Cell-centered finite volume discretization	131
5.3.1. Consistency of the discrete domain decomposition method	133
5.3.2. Convergence of the discrete domain decomposition method	133
5.4. Numerical examples	135
5.5. Conclusion	136
6. Non-overlapping Schwarz waveform-relaxation for nonlinear advection-diffusion equations	139
6.1. Introduction	139
6.2. Problem formulation and the non-overlapping SWR algorithm	141
6.3. Existence of solutions and well-posedness of the SWR algorithm	143
6.4. Convergence of the non-overlapping SWR algorithm	149
6.5. Numerical discretization for two-dimensional domains	152
6.5.1. The general finite volume method	152
6.5.2. Discretization of the transmission condition	154
6.6. Numerical results	155
6.6.1. Error functionals and notations	156
6.6.2. A problem with known solution	157
6.6.3. Simplified two-phase flow with capillary pressure	159
6.6.4. Two-phase flow with strongly nonlinear capillary pressure	163
6.7. Conclusion	164
7. Conclusion and outlook	167
7.1. Two-Phase Flow in Single Pores	167
7.2. Numerical Methods at the Darcy Scale	169
7.3. Ongoing work on dynamic pore-network models	171
A. Combined effects for the averaged two-phase flow in a thin strip	177
B. Detailed results of the fitting for the capillary rise experiments	185
Bibliography	195
Curriculum vitae	229

List of Publications

This thesis is based on the following publications¹ and software:

Peer-reviewed journal articles

- S. B. Lunowa, I. S. Pop, B. Koren, *Linearized domain decomposition methods for two-phase porous media flow models involving dynamic capillarity and hysteresis*, Computer Methods in Applied Mechanics and Engineering, 372 (2020), 113364. doi.org/10.1016/j.cma.2020.113364
- S. B. Lunowa, C. Bringedal, I. S. Pop, *On an averaged model for immiscible two-phase flow with surface tension and dynamic contact angle in a thin strip*, Studies in Applied Mathematics 147 (2021), pp. 84–126. doi.org/10.1111/sapm.12376
- S. B. Lunowa, A. Mascini, C. Bringedal, T. Bultreys, V. Cnudde, I. S. Pop, *Dynamic effects during the capillary rise of fluids in cylindrical tubes*, Langmuir 38 (2022), pp. 1680–1688. doi.org/10.1021/acs.langmuir.1c02680

Peer-reviewed conference proceedings

- S. B. Lunowa, I. S. Pop, B. Koren, *A linear domain decomposition method for non-equilibrium two-phase flow models*, in: Numerical Mathematics and Advanced Applications ENUMATH 2019, Springer, Cham (2021), pp. 145–153. doi.org/10.1007/978-3-030-55874-1_13
- M. J. Gander, S. B. Lunowa, C. Rohde, *Consistent and Asymptotic-Preserving Finite-Volume Robin Transmission Conditions for Singularly Perturbed Elliptic Equations*, in: Domain Decomposition Methods in Science and Engineering XXVI, Springer (2022), pp. 419–426. In press. link.springer.com/book/9783030950248

¹Stephan B. Lunowa is the main and contributing author of all publications. Note that it is common for mathematical publications to state the authors in lexicographic order.

Submitted manuscripts

- M. J. Gander, S. B. Lunowa, C. Rohde, *Non-overlapping Schwarz waveform-relaxation for nonlinear advection-diffusion equations*, submitted in revised form to SIAM Journal of Scientific Computing (03/2022), UHasselt CMAT Preprint UP-21-03 (2021): www.uhasselt.be/media/mufgoyse/up2103.pdf

Software

- S. B. Lunowa, *Solver for the asymptotic model of immiscible two-phase flow with moving contact line in a thin strip*, GitHub repository (2020).
github.com/s-lunowa/AsymptoticThinStripMCLSolver
- S. B. Lunowa, *Software for Fitting the Upscaled and Extended Model of Capillary Rise to Experimental Data*, GitHub repository (2021).
github.com/s-lunowa/dynamic-capillary-rise

Introduction

Flow and transport processes in porous media are research fields of importance for a variety of applications covering all areas of modern society. Originating from the field of subsurface flow [30, 86, 156], these phenomena quickly attracted interest in related areas such as reservoir engineering for enhanced oil recovery [200], geological CO₂ storage [245], soil remediation [80] and microbial bio-film growth [202], etc. Beyond the geosciences, it is relevant in biological processes such as flow and transport in tissue [222, 309], in industrial processes such as reactive transport and catalysis [173], as well as in the design of thin structures from printing paper and hygiene products to buildings and pavement to fuel cells [92, 258, 300].

In all these applications, it is crucial to understand the complex underlying phenomena to describe and predict the relevant processes. Experimental observations lay the foundation for the development of theories and models. However, detailed experimental measurements are often extremely costly, e.g. in reservoirs several kilometers below the surface; if feasible at all, e.g. in bio-medical applications of drug delivery in living brain tissue. Instead, mathematical modeling, analysis and numerical simulations provide a broad set of tools to investigate such processes. This allows for various levels of abstraction depending on the desired accuracy in the application, while having minimal direct consequences on the subject of interest, and might even lead to a reduction of required experiments.

The mathematical models typically consist of partial differential equations, which describe the evolution of quantities of interest, such as velocities, concentrations, etc., based on fundamental balance equations for mass, momentum and energy [31]. These equations are then complemented by constitutive equations, which describe the specific material behavior, e.g. Darcy's law for the flow of a fluid through a porous medium [86]. The complex pore structure and the exact distribution of fluids are simplified into a representation by averaged quantities such as the porosity and saturation. The relations between these macroscopic quantities

must be expressed with the help of effective parameters, which should combine all pore-scale effects. However, these parameters are simply postulated in many state-of-the-art models and not derived from a model valid at the pore scale. In particular, effects due to interface dynamics between the fluids are typically neglected or incorporated on an empirical basis. In the first part of this work, we consider these effects for simple pore geometries and use upscaling techniques to derive effective equations for two-phase flow.

The resulting upscaled models, as well as the standard models, are coupled, non-linear partial differential equations, which may even degenerate and change type in an a-priori unknown manner, depending on the solution itself. Furthermore, these models can involve strong heterogeneities due to largely varying or even discontinuous physical properties and parameters. This tremendous complexity leads to significant analytical and numerical challenges for the simulation of these processes. Hence, the mathematical design and analysis of suitable and robust computational methods are required. Besides appropriate discretization methods in time and space, linearization schemes must be applied to resolve the nonlinear equations. In the situation of block-type heterogeneities, a typical approach is the additional application of domain decomposition methods to decouple the essentially different regions. This reduces the computational cost for the individual sub-domains at the cost of a further iteration to recover the correct interface conditions. The main advantage lies in the parallelization of the sub-domain computations to reach a reasonable performance for large-scale applications. These numerical aspects are considered in the second part of this work for nonlinear advection-diffusion equations in the context of two-phase flow in porous media.

In the remainder of this chapter, we discuss the fundamentals used within this work. We begin with the conceptual ideas of scales and modeling approaches in [Section 1.1](#). This is followed by the modeling applied at pore scale in [Section 1.2](#) and at Darcy scale in [Section 1.3](#). Furthermore, we introduce upscaling approaches in [Section 1.4](#) as tools to derive effective constitutive equations at Darcy scale based on an underlying pore-scale model. The numerical methods required to solve these models are discussed in [Section 1.5](#). Finally, [Section 1.6](#) outlines this work.

1.1. Scales and modeling approaches

Modeling of flow and transport phenomena is possible at various scales, depending on the desired application, see [Fig. 1.1](#). At the molecular scale, the movement and interactions of atoms and molecules are considered. Due to the enormous number of molecules, this approach is infeasible for domain lengths above few micrometers. However, physical properties used on larger scales, such as density, viscosity or interfacial tensions, can be derived at this scale based on molecular properties.

The continuum hypothesis is used at larger scales to model the behavior of mate-

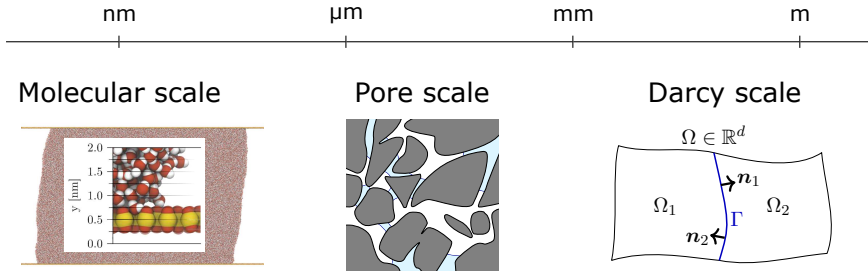


Figure 1.1.: Scales and modeling approaches. Leftmost sub-figure taken and rearranged from [221, Fig. 2] (CC-BY 4.0).

rials. Then, the physical properties of a phase are modeled by typically continuous functions in space and time, similar to the result of an averaging over a significant number of molecules around each point in space-time. Although a phase might consist of a mixture of substances, it has a unified set of constitutive equations, also known as equations of state. As a consequence, phases are typically immiscible and separated by sharp interfaces, across which the physical properties may be discontinuous.

At the pore scale, one can distinguish between the fluid and solid phases, so that the detailed geometry, including individual interfaces, grains, fractures, etc. are recognizable. Measurements at this scale are possible in the range of micrometers up to a few centimeters, see e.g. Fig. 1.2. The modeling of flow is typically based on the Navier–Stokes equations and includes interactions of the phases at interfaces, such as interfacial tension.

To represent larger domains of porous media, a further averaging is applied over a so-called representative elementary volume. This has to be chosen in such a way that the averaged quantities again satisfy the continuum hypothesis. As a consequence, the micro-structure is no longer identifiable, and all phases fill the continuum simultaneously. The modeling on this scale is typically based on conservation laws including the phase saturations, the capillary pressure between fluid phases, which results from interfacial tension, and the (extended) Darcy law for fluid flow. Thanks to the latter, this scale is often also called Darcy scale.

In the following two sections, we discuss in detail the mathematical modeling of two-phase flow in porous media based on the continuum hypothesis — first at the pore scale and subsequently at the Darcy scale.

1.2. Modeling of two-phase flow at the pore scale

At the pore scale, we assume a rigid solid matrix, such that its domain is not explicitly taken into account. The pore walls form a fixed boundary Γ_w for the void space, denoted as domain $\Omega \subset \mathbb{R}^d$ of dimension $d \in \{2, 3\}$, which is available for the

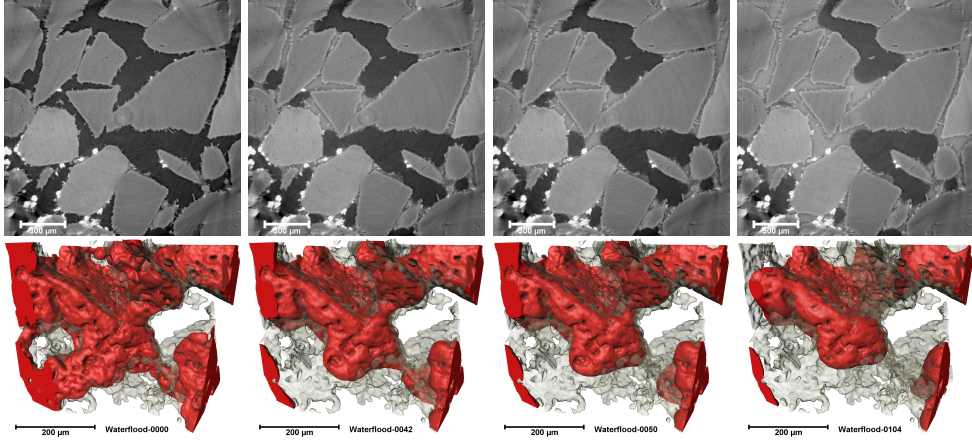
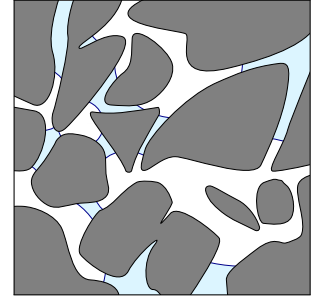


Figure 1.2.: Water-flooding experiment in a porous sandstone sample. *Top row*: Two-dimensional slices of dynamic μ -CT images at several times. *Bottom row*: Three-dimensional rendering of dynamic μ -CT images at several times. The black phase in the slices and the red phase in the rendering is oil. Images kindly provided by Arjen Mascini, Department of Geology, University of Ghent, Belgium.

Figure 1.3: General porous domain filled by two fluid phases (white and light blue). When the fluid-fluid interface Γ (dark blue) is in contact with the solid wall Γ_w (black), there is a contact line between all three phases.



flow of the fluid phases, see Fig. 1.3. Each fluid phase α occupies a sub-domain Ω_α of the domain Ω , such that the separate sub-domains add up to the whole domain

$$\overline{\Omega} = \bigcup_{\alpha} \overline{\Omega_\alpha}, \quad \Omega_\alpha \cap \Omega_\beta = \emptyset \quad \text{for } \alpha \neq \beta.$$

Due to the flow, the spatial distribution of the fluid phases in the pore space can change, so that the respective sub-domains $\Omega_\alpha = \Omega_\alpha(t)$ depend on time $t \geq 0$. The mathematical model consists of conservation laws for mass and momentum, valid in these time-dependent domains. Furthermore, the evolution of the fluid-fluid interfaces Γ depends on the flow and on the surface tension between the fluids. When an interface is in contact with the solid wall Γ_w , a contact point (in two dimensions) or contact line (in three dimensions) separates all three phases. Its motion must be taken into account, which also requires a model for the contact angle formed between the fluid-fluid interface and the pore wall.

In the subsequent subsections, the complete model is described in detail. In [Chapter 2](#), we use this model to derive an upscaled model of two-phase flow, which is furthermore validated in [Chapter 3](#) by comparison to experiments.

1.2.1. Flow of the fluid phases

The fluid phases are assumed to be incompressible Newtonian fluids. Then, the balance laws for the mass and the momentum, which model the flow of the phase α , are given by the (dimensional) Navier–Stokes equations

$$\rho_\alpha (\partial_t \mathbf{u}_\alpha + (\mathbf{u}_\alpha \cdot \nabla) \mathbf{u}_\alpha) = -\nabla p_\alpha + \mu_\alpha \Delta \mathbf{u}_\alpha + \rho_\alpha \mathbf{g} \quad \text{in } \Omega_\alpha(t), \quad (1.1)$$

$$\nabla \cdot \mathbf{u}_\alpha = 0 \quad \text{in } \Omega_\alpha(t), \quad (1.2)$$

where $\mathbf{u}_\alpha(t, \mathbf{x})$ and $p_\alpha(t, \mathbf{x})$ are the velocity and pressure of the fluid phase α . The parameters ρ_α and μ_α denote the density and the dynamic viscosity of the fluid, while \mathbf{g} is the gravitational acceleration. Note that, besides gravity, further external forces can be considered in (1.1), but are not relevant in this work.

The evolution of the interface $\Gamma(t)$ separating the sub-domains of the two fluid phases is not known a-priori, but its location and shape depend on the velocities of the fluids and on the surface tension between the fluids. Therefore, the interface appears as a free boundary in the mathematical model. Assuming no phase-transition effects, the mass conservation implies that the velocities of the fluids at this interface and the velocity \mathbf{v}_Γ of the interface coincide,

$$\mathbf{u}_I = \mathbf{u}_{II} = \mathbf{v}_\Gamma \quad \text{on } \Gamma(t). \quad (1.3)$$

Because of friction, the continuity of the tangential stress also holds. However, the surface tension between the fluids, which is caused by the curved interface, leads to a jump in the normal stress [308]

$$-(p_I - p_{II})\mathbf{n}_\Gamma + 2(\mu_I \mathbf{D}(\mathbf{u}_I) - \mu_{II} \mathbf{D}(\mathbf{u}_{II}))\mathbf{n}_\Gamma = \sigma \kappa \mathbf{n}_\Gamma \quad \text{on } \Gamma(t). \quad (1.4)$$

Here, $\mathbf{D}(\mathbf{u}) = \frac{1}{2}(\nabla \mathbf{u} + (\nabla \mathbf{u})^T)$ is the symmetric strain, σ denotes the constant interfacial tension between the two fluids, and $\kappa = \nabla \cdot \mathbf{n}_\Gamma$ is the local mean curvature of the interface with the normal vector \mathbf{n}_Γ .

1.2.2. Moving contact line

When the fluid-fluid interface is in contact with the solid wall, there is a contact line between all three phases. At this contact line, a contact angle θ is formed between the solid wall and the fluid-fluid interface, see [Fig. 1.4](#). Under equilibrium conditions, this angle is given by the minimization of the total surface energy. This

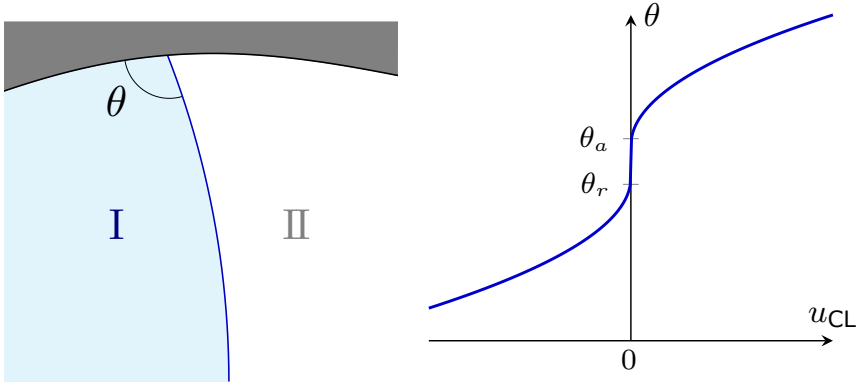


Figure 1.4.: The contact angle θ at the contact line formed between the fluid-fluid interface and the pore wall (left) has a dynamic and hysteretic dependence on the contact-line velocity u_{CL} (right). The advancing and receding contact angles are denoted θ_a and θ_r .

yields the well-known Young's relation for the static contact angle θ_s

$$\cos \theta_s = \frac{\sigma_I - \sigma_{II}}{\sigma},$$

where σ_I and σ_{II} denote the surface tension coefficients between the solid and the two fluids, respectively, while σ is the surface tension coefficient between the two fluids. For $\theta_s < \frac{\pi}{2}$, the fluid phase I is called the wetting phase, while the phase II is the non-wetting one, and vice versa for $\theta_s > \frac{\pi}{2}$.

Experiments performed under dynamic conditions for drops [78, 188, 203, 301] and for capillary tubes [108, 168, 189] show that the contact angle also has a dynamic behavior. This is expressed as an apparent contact angle θ , and has a major influence on the overall flow dynamics [42]. Observations made for an increasing contact-line velocity u_{CL} have revealed that advancing contact angles are increasing, while receding ones are decreasing [41, 97]. Therefore, the θ - u_{CL} relation is assumed to be essentially monotonic, as illustrated in Fig. 1.4.

There are mainly two theories to describe this phenomenon: the hydrodynamic theory and the molecular kinetic theory, for detailed reviews see [42, 46, 265]. The hydrodynamic theory emphasizes on dissipation due to viscous flow within the wedge of liquid near the moving contact line. This region is analyzed based on asymptotic expansions [83, 87, 97, 170, 321]. For two-phase flow, this yields the well-known Cox law for the dynamic contact angle

$$g(\theta) = g(\theta_s) + \frac{C\mu}{\sigma} u_{CL},$$

where μ denotes the viscosity, the constant C depends on the specific slip model, and g is an analytically derived function, which can be approximated by $g(\theta) \approx \theta^3$

for small angles [83]. The other approach is the molecular kinetic theory, in which the dissipation is described based on a dynamic friction associated with the moving contact line. This yields the relation

$$u_{\text{CL}} = C_1 \sinh(C_2 \sigma (\cos \theta_s - \cos \theta))$$

with the constants C_1 and C_2 depending on molecular properties [41, 43, 79]. Assuming small variations in the contact angles, after linearization one obtains

$$u_{\text{CL}} = \frac{\sigma}{\xi} (\cos \theta_s - \cos \theta) + \mathcal{O}((\cos \theta_s - \cos \theta)^2),$$

where ξ denotes the coefficient of wetting-line friction [42].

The contact angle is strongly affected by the surface wettability and roughness. In [42, 265], the resulting effects are made responsible for the contact angle hysteresis. This means that the static contact angle can actually lie in a whole range $\theta_r < \theta_s < \theta_a$, where θ_a and θ_r denote the advancing and receding contact angles, respectively. The static contact angle must then be understood as an element of the maximal monotone graph

$$\theta_s \in \begin{cases} \{\theta_r\} & \text{for } u_{\text{CL}} < 0, \\ [\theta_r, \theta_a] & \text{for } u_{\text{CL}} = 0, \\ \{\theta_a\} & \text{for } u_{\text{CL}} > 0. \end{cases}$$

Furthermore, the movement of the contact line requires a careful choice of the flow boundary conditions in its neighborhood. Traditionally, the no-slip condition $\mathbf{u} = \mathbf{0}$ on Γ_w is used under the assumption that the fluid adheres to the solid wall. However, the no-slip condition leads to a singularity in the pressure and in the shear stress at the contact line [97, 98, 172], which therefore would stay at a fixed position. To overcome this issue, several alternative boundary conditions have been proposed, to be used in particular in regions close to the contact line, see [46, 269, 298] and the references therein. In this work, we consider impermeable pore walls such that there is no fluid flow in normal direction, together with the Navier-slip condition

$$\mathbf{u} \cdot \mathbf{n}_w = 0, \quad \mathbf{t}_w \cdot (\mathbf{u} + 2\lambda \mathbf{D}(\mathbf{u}) \mathbf{n}_w) = 0 \quad \text{on } \Gamma_w. \quad (1.5)$$

Here, λ denotes the slip length and \mathbf{n}_w , \mathbf{t}_w are the normal and tangential unit vectors at the solid wall Γ_w . This condition has been proposed originally by Huh and Scriven [172] to resolve the contact-line problem, and has been frequently used since then [87, 148, 167, 171, 270, 288]. Note that in (1.5), the location of the contact point or line does not appear explicitly. Often, the Navier-slip condition is only applied close to the contact line. In this case, a variable slip length $\lambda(x)$ is adopted, decaying rapidly to zero away from the contact line, see e.g. [26, 83,

142, 148]. This can be justified by molecular dynamics simulations which show that the no-slip boundary condition is only violated in a small region (up to some nanometers) around the contact line [192, 193, 194, 305, 306]. Additionally, surface wettability and roughness strongly affect the slippage behavior, see e.g. [28, 131, 185, 226] for a mathematical analysis.

1.3. Modeling of two-phase flow at the Darcy scale

At the Darcy-scale, the mathematical modeling of two-phase flow in porous media is based on quantities defined by averaging over a representative elementary volume. In particular, these quantities involve the saturation S_α and the pressure p_α of the wetting and non-wetting phases $\alpha \in \{w, n\}$. The saturation $S_\alpha \in [0, 1]$ is defined as the fraction of the pore space occupied by the phase α . Since the two phases fill the entire pore space, there holds

$$S_w + S_n = 1. \quad (1.6)$$

Furthermore, let $\phi \in (0, 1)$ denote the porosity of the medium, defined as the fraction of the pore space in the total volume. Then, the mass balance equation for an incompressible phase α in a rigid porous medium reads

$$\phi \partial_t S_\alpha + \nabla \cdot \mathbf{u}_\alpha = q_\alpha, \quad (1.7)$$

where \mathbf{u}_α is the fluid velocity and q_α is the source rate of the phase α .

Based on column experiments for fully-saturated single-phase flow in a porous medium, Darcy [86] observed a proportionality between the velocity and the pressure gradient $\mathbf{u} = -\mu^{-1} \mathbf{K} \nabla p$. Here, μ is the dynamic viscosity of the fluid, and \mathbf{K} denotes the intrinsic permeability of the porous medium, which depends only on the porous medium, but not on the fluid. This characteristic property of the porous medium is a second rank tensor for general anisotropic media. Based on further experiments, see e.g. [238, 271, 318], the theory was extended to unsaturated single-phase flow and two-phase flow in porous media. Then, the fluid velocity \mathbf{u}_α is related to the phase pressure p_α by the extended Darcy law

$$\mathbf{u}_\alpha = -\lambda_\alpha(S_\alpha) \mathbf{K} (\nabla p_\alpha - \rho_\alpha \mathbf{g}), \quad (1.8)$$

which involves the gravitational acceleration \mathbf{g} , as well as the density ρ_α and the relative mobility λ_α of the phase α . The relative mobility λ_α is a scaling factor that depends on the dynamic viscosity μ_α of the fluid and includes the additional reduction of flow due to the interactions of both fluids at the pore scale. For a detailed introduction to Darcy-scale modeling, we refer to [31, 156, 245].

1.3.1. Non-equilibrium capillary pressure

To close the system of equations, a constitutive equation relating the pressures p_w and p_n is necessary. Typically, one assumes that the phase-pressure difference $p_n - p_w$ is a decreasing function of the wetting saturation. This difference is called equilibrium capillary pressure $p_c(S_w)$ and can be obtained by experiments under quasi-equilibrium conditions. Commonly used models are those proposed by van Genuchten [318] and by Brooks and Corey [59]. Such nonlinear, but monotonic equilibrium capillary pressure functions have been used for decades. However, it was already shown in [238] that the capillary pressure also depends on the process — imbibition or drainage. Besides this hysteresis, further dynamic effects were reported in many experiments [50, 91, 137, 290, 332, 333], leading to a variety of non-monotonic curves which cannot be reduced to a simple capillary pressure function depending on saturation only.

To overcome the mismatch between the experimental results and the mathematical models, several extensions of the capillary pressure - saturation relation have been proposed. Typically, dynamic effects and hysteresis are directly expressed in terms of spatial or temporal derivatives of the saturation leading to different capillary pressure models, e.g. [32, 33, 34, 154, 250], for an overview see [284]. Alternatively, the interfacial area was introduced as an additional state variable leading to a capillary pressure function depending on saturation and interfacial area, so that the dynamic and hysteretic effects are implicitly modeled via the change in interfacial area [154, 155, 243, 255]. Other hysteresis models are based on the concept of percolating/non-percolating phases [162, 163, 164].

In Chapter 4, we consider the play-type hysteresis model proposed in [32, 154],

$$p_n - p_w \in p_c(S_w) - \gamma \operatorname{sign}(\partial_t S_w) - \tau(S_w) \partial_t S_w, \quad (1.9)$$

where $\gamma \geq 0$ and the non-negative function τ model the effects due to hysteresis and dynamic capillarity, respectively. This type of model is able to reproduce non-monotonic phenomena such as saturation overshoots and fingering as shown by a traveling wave approach for dynamic capillarity in [296, 312, 315] and additionally including hysteresis in [166, 235, 237, 313], by qualitative analysis of an equivalent free boundary problem [282], and by numerical simulations for a percolation model in [95, 165], for Richards' equation in [201, 333] and for two-phase flow in [191, 275, 277].

For uniformly positive τ , the multi-valued equation (1.9) can be solved for $\partial_t S_w$, as done in [72, 191, 283]. This yields a single-valued function Ψ , such that one can rewrite the capillary pressure relation in the inverted formulation

$$\partial_t S_w = \Psi(S_w, p_n - p_w). \quad (1.10)$$

This has the major advantage that it imposes explicit values for the time derivative

of the saturation, and avoids a multi-valued relation like (1.9). Moreover, it is possible to only include hysteresis and no dynamic effects. Then, one can regularize Ψ by replacing its vertical elements through steeply increasing ones, which is similar to including a small dynamic effect, namely taking $\tau \equiv \varepsilon > 0$.

1.3.2. Fractional flow formulation

Often, a reformulation of the two-phase flow equations is used. Summation of the mass balance equation (1.7) for both phases using (1.6) yields for the total velocity $\mathbf{u} = \mathbf{u}_w + \mathbf{u}_n$

$$\nabla \cdot \mathbf{u} = q, \quad (1.11)$$

where $q = q_w + q_n$ is the total source rate. Note that this implies that the total velocity \mathbf{u} is divergence free when the total source rate q vanishes. Combination of (1.8) for the two phases using an equilibrium capillary pressure model $p_n - p_w = p_c(S_w)$ yields

$$\mathbf{u}_w = f_w(S_w)\mathbf{u} + \kappa(S_w)\mathbf{K}(\nabla p_c(S_w) + (\rho_w - \rho_n)\mathbf{g}), \quad (1.12)$$

where

$$f_w = \frac{\lambda_w}{\lambda_w + \lambda_n} \quad \text{and} \quad \kappa = \frac{\lambda_w \lambda_n}{\lambda_w + \lambda_n}$$

are the so-called fractional flow coefficients. Knowing the total velocity \mathbf{u} by solving (1.11), one can then solve for S_w using (1.12) in (1.7), which reads

$$\phi \partial_t S_w + \nabla \cdot (f_w(S_w)\mathbf{u} + \kappa(S_w)\mathbf{K}(\nabla p_c(S_w) + (\rho_w - \rho_n)\mathbf{g})) = q_w. \quad (1.13)$$

Note that this equation is a possibly degenerate, nonlinear advection-diffusion equation of parabolic type due to $p'_c(S_w) \leq 0$. This formulation is used for the numerical simulations in Section 6.6.

1.4. Upscaling and multi-scale methods

The computational representation of the complex geometry and the interactions of the fluids at the pore scale is only possible for relatively small domains, while the standard models at the Darcy scale require balance laws and constitutive equations based on pore-scale information. To bridge this gap, one can employ upscaling and asymptotic expansion methods to derive effective equations valid at larger scale based on detailed small-scale models. Additionally, one can obtain estimates of the errors that are introduced by the respective upscaling technique.

There exists a large variety of upscaling techniques like homogenization, volume

averaging, transversal averaging, etc., see [84] for an overview. Volume averaging methods are used to derive the balance equations for quantities at the Darcy scale, while the form of the constitutive equations can be restricted using the second law of thermodynamics. This technique was successfully applied to single-phase and two-phase flow in porous media in [153, 154, 155, 261, 323]. However, additional assumptions are necessary to obtain explicit expressions for the effective parameters in the constitutive equations via closure problems.

As an alternative, the homogenization technique uses an asymptotic expansion approach for systems which feature a clear scale separation. After non-dimensionalization, this scale separation leads to a small parameter $\varepsilon \ll 1$ in the problem formulation (e.g. the ratio of a typical pore diameter to a Darcy-scale length). The idea of homogenization is to approximate the solution by the limit problem and its solution as $\varepsilon \rightarrow 0$. This solution typically depends on the regime, i.e., the scaling of the dimensionless numbers with respect to ε . An introduction to this method is presented in [169] and the references therein. Rigorous results are often obtained using the concept of two-scale convergence [17, 241] or compactness arguments, see also [169, Appendix A by G. Allaire] and the references therein. Similarly, matched asymptotic expansions are used when the expansion is singular, e.g. at a boundary or interface. Then, a rescaling in this region allows to resolve the singularity. Finally, to obtain a solution on the whole domain, the solutions of the differently scaled regions must match in an intermediate scaling. For a detailed introduction to matched asymptotic expansion method we refer to [317]. We use this method in Chapter 2 to combine the bulk flow of single phases with the fluid-fluid interface region connecting them.

Homogenization is typically applied to periodic systems and leads then to so-called cell problems defining the effective properties. Note that the local periodicity assumption is similar to the closure condition for volume averaging. This assumption can be further weakened in stochastic homogenization using ergodicity. For single-phase flow in porous media, many results have been obtained. Darcy's law was derived in [13, 15, 228, 276, 302] based on the Stokes equations or the Navier-Stokes equations in perforated domains. In [14, 16], it was shown that the size of the solid inclusions determines whether the homogenized system obeys Darcy's law, the Brinkmann law, or even again the (Navier-)Stokes equations with effective parameters. While inertial effects are negligible in the aforementioned results, a non-local filtration law arises when inertial effects are significant [227, 229].

For two-phase flow, these results were extended under restrictive assumptions. An extended Darcy law was derived in [24, 25] based on quasi-static assumptions for the fluid-fluid interface, combined with Biot-type elasticity in case of a deformable porous medium. Homogenization of the Stokes equation in a domain with free surface yields in [279] a Darcy-type equation for unsaturated flow. The Buckley-Leverett equation was recovered in [233] starting from a thin domain

with two phases, when surface tension is negligible. Thin strip and thin tube models were used in [231,252,287] to derive variants of the extended Darcy law combined with capillary pressure relations depending on the underlying fluid distribution.

These thin-domain models use a simplified geometry, namely a single pore, as a representative for the porous medium. This has the advantage that the upscaling yields explicit, closed-form expressions for the upscaled quantities, while the resulting Darcy-scale models still possess the same structure as well-recognized Darcy-scale models in general porous media, see e.g. [231,233,252,287]. In these references, the fluid domains are assumed to be layered, so that the fluid-fluid interface does not come into contact with the solid wall. On the contrary, we consider a transversal interface that is in contact with the pore walls in Chapter 2. In particular, we incorporate a slowly varying pore wall and a dynamic or even hysteretic contact-angle model. Using a matched asymptotic expansion approach, we obtain an upscaled model that provides insight into sources of non-equilibrium behavior.

Further dynamic effects and trapping of phases occur due to heterogeneities of the porous medium. Effective interface conditions are analyzed in [39,67,310,311,314], applied numerically in [157,158], and upscaled equations are derived in [52,132,159,230,281,316]. Finally, note that the averaging and resulting definition of Darcy-scale quantities must be done carefully, since systematic dependencies of the intrinsic averages on heterogeneities, such as fluid fronts, within the representative elementary volume affect the resulting equations. In [246,247], this is shown to lead to inconsistencies with classical literature. However, these issues disappear when considering an appropriate averaging that takes such effects into account by incorporating the mass-center of the phases.

1.5. Numerical methods

The mathematical models of two-phase flow in porous media consist of coupled, nonlinear partial differential equations. As analytical (closed-form) solutions do only exist for few, very restricted applications (typically in one spatial dimension), numerical methods are necessary to solve the equations. First, we discuss appropriate temporal and spatial discretization methods in Sections 1.5.1 and 1.5.2. Furthermore, the nonlinearities must be resolved. To this end, linearization schemes are introduced in Section 1.5.3. Finally, we discuss domain decomposition methods in Section 1.5.4 as a tool to decouple essentially different regions or to improve the performance due to parallelization and better conditioned, smaller system of discrete equations.

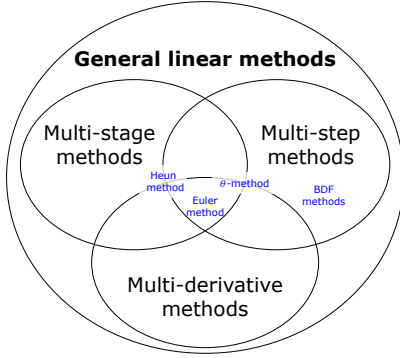


Figure 1.5: Venn-diagram of the main categories within the class of general linear methods including the methods used in this thesis.

1.5.1. Temporal discretization

We consider time-dependent problems in a Banach space \mathcal{W} of the form

$$\frac{du}{dt} = f(t, u), \quad t \in (0, T], \quad u(0) = u_0 \in \mathcal{W}, \quad (1.14)$$

where $T > 0$ is the final time, $f : [0, T] \times \mathcal{W} \rightarrow \mathcal{W}$ is a Lipschitz-continuous function and u_0 a given initial condition. The theorem of Picard–Lindelöf guarantees that (1.14) has a unique solution $u \in C^1([0, T]; \mathcal{W})$. Note that problems with higher order time derivatives can be rewritten in the form (1.14) by expansion into a system of ordinary differential equations using additional variables, e.g. by

$$\frac{d^2 u}{dt^2} = g\left(t, u, \frac{du}{dt}\right) \quad \Leftrightarrow \quad \frac{d}{dt} \begin{pmatrix} u \\ v \end{pmatrix} = \begin{pmatrix} v \\ g(t, u, v) \end{pmatrix}.$$

Furthermore, time-dependent partial differential equations lead to problem (1.14) after spatial discretization. Parabolic partial differential equations can also be understood in the sense of (1.14) when f denotes the application of the spatial operator. We omit the further details here.

To solve the problem (1.14) numerically, the time interval $[0, T]$ is discretized into $K \in \mathbb{N}$ time steps. For simplicity, we choose an equidistant mesh, such that $\Delta t = T/K$ is the uniform time-step size. At the time points $t^k := k\Delta t$, the solution is approximated by $u^k \approx u(t^k)$. For this, there exist many methods, of which most belong to the class of general linear methods. These methods can be further categorized into three main sub-classes: those using multiple previous time-steps, multiple interior stages (intermediate solutions), or multiple derivatives for the approximation, see Fig. 1.5. All these methods are additionally classified as explicit or implicit methods by their dependence on the solution at the current time-step. For a general introduction to the topic, we refer to [61, 146, 147]. Here, we focus on the methods used in this work. In particular, we mainly consider low-order methods for simplicity, and due to the low regularity of the solutions to the studied problems. Nevertheless, high-order methods would be beneficial outside the

low-regularity regions.

First, we discuss the θ -scheme, which is a single-step method of Runge–Kutta-type with two stages. It results from the approximation of the time derivative by a simple finite difference and weighting the righthand sides of the previous and the current time-step. Given $\theta \in [0, 1]$, its application to (1.14) reads

$$\frac{u^k - u^{k-1}}{\Delta t} = (1 - \theta)f(t^{k-1}, u^{k-1}) + \theta f(t^k, u^k) \quad (1.15)$$

for $1 \leq k \leq K$. For $\theta = 0$, this method is explicit and equals the forward Euler method, while for $\theta > 0$ this method is implicit. It coincides with the trapezoidal or Crank–Nicolson method for $\theta = \frac{1}{2}$, and with the backward Euler method for $\theta = 1$. The θ -scheme with $\theta < \frac{1}{2}$ is only conditionally stable requiring $L_f \Delta t < 2/(1 - 2\theta)$, where L_f denotes the Lipschitz constant of f [27, 146]. However, the method is A-stable for $\theta \geq \frac{1}{2}$. Furthermore, the θ -scheme is first-order convergent, and for $\theta = \frac{1}{2}$ even second-order convergent. In Chapter 4, we use this method as temporal discretization for the non-equilibrium two-phase flow model. In Chapter 6, the explicit Euler method is applied to nonlinear advection-diffusion equations.

A closely related method is the Heun method. Instead of using the implicit trapezoidal rule, the righthand side at time t^k is approximated explicitly by the forward Euler method. This leads to an explicit, second-order convergent, conditionally stable Runge–Kutta method with two stages, which is given by

$$\frac{u^k - u^{k-1}}{\Delta t} = \frac{1}{2}(f(t^{k-1}, u^{k-1}) + f(t^k, \tilde{u}^k)), \quad \frac{\tilde{u}^k - u^{k-1}}{\Delta t} = f(t^{k-1}, u^{k-1}) \quad (1.16)$$

for $1 \leq k \leq K$. This method is used in Chapter 2 for the implementation of the explicit solver for the pore-scale model with hysteretic contact angle in [215] to avoid numerical issues of implicit methods for hysteresis.

Backward differentiation formulas (BDF) are linear multi-step methods based on the Lagrange interpolation at the points t^{k-p} to t^k , for some $p \in \mathbb{N}$. Furthermore, the derivative of this interpolation polynomial in the point t^k is used as approximation for the left-hand side of (1.14). In fact, this is equivalent to the use of the p -th order backward difference approximation of the time derivative, leading to

$$\sum_{s=0}^p \alpha_s u^{k-s} = \Delta t f(t^k, u^k), \quad (1.17)$$

with some coefficients $\alpha_0, \dots, \alpha_p \in \mathbb{R}$ which can be computed from the Lagrange interpolation. For $p \leq 6$, this implicit method is zero-stable and p -th-order convergent [146, 147]. An adaptive, variable-order (1–5) version of this method is used in Chapter 2 for the implementation of the implicit solver for the pore-scale model with dynamic contact angle in [215] and in Chapter 3 for the implementation of the implicit solver for the extended model for capillary rise in [216] to obtain highly

accurate results.

1.5.2. Spatial discretization

For space-dependent problems, a discretization is required as well. However, partial differential equations only have weak solutions in general. Therefore, spatial discretizations of problems are typically different to the temporal ones. The spatial discretization is usually based on a triangulation or on a (Cartesian) mesh. On this mesh, one defines the discrete solutions using an approximation of the differential equation. To this end, four classical approaches exist: finite difference methods directly approximate the derivatives, while finite element methods, finite volume methods and discontinuous Galerkin methods are based on different approximations of the weak formulation.

For the finite difference method, one replaces the differential operators at the mesh points by suitable finite differences, see [57, 211, 251, 274] for applications to two-phase flow in porous media. While this approach is very easy for structured grids, the application to arbitrary, complicated geometries becomes challenging, so that we do not consider the finite difference method in this work.

Finite element methods are based on the weak formulation of the equations. The classical version, also known as continuous Galerkin method, uses a globally continuous approximation of the solution based on local basis functions defined on the triangulation, see e.g. [104, 274] for applications to miscible two-phase flow in porous media, and [134, 135, 182, 244] for degenerate, immiscible two-phase flow. This approach is used in Chapter 4 for non-equilibrium two-phase flow. Mixed and hybrid finite elements ensure the local conservation of mass by explicit discretization of the fluxes [55], and have been applied e.g. to Richards' equation [29], to two-phase flow in porous media [22, 327] and to the latter also including dynamic capillarity in [70].

This conservation requirement, together with the low regularity of the solutions, points to the common discretization by the finite volume method [105]. It is based on the integration of the balance equation over control volumes (mesh elements) using the Gauss theorem. The approximation of the solution uses piece-wise constant functions connected by numerical fluxes between the volumes. This also allows the treatment of hyperbolic equations, as well as problems where the diffusive second-order terms might vanish. For two-phase flow in porous media, this is used e.g. for heterogeneous media with discontinuous capillary pressure [53, 54, 66, 99] and additionally including dynamic capillarity [157, 158] or hysteresis [249]. For two-phase flow with dynamic capillarity, two- and multi-point flux approximations are discussed in [51, 71]. A nonlinear finite volume method for two-phase flow is proposed in [3]. A posteriori error estimates for the finite volume method applied to two-phase flow are derived in [69]. We use a cell-centered finite volume method in Chapters 5 and 6 for degenerate, nonlinear advection-diffusion equations.

A more general, locally conservative class of methods are discontinuous Galerkin methods [23, 90, 94, 161, 273]. These combine properties of classical finite elements and of finite volume methods. In particular, the representation is based on local basis functions on the mesh. However, these are not connected globally by continuity as for classical finite elements. Instead, one uses the Gauss theorem as in finite volume methods to approximate the interactions by numerical fluxes. In the context of porous-media flow, discontinuous Galerkin methods are used for Darcy flow [8, 56], for two-phase flow [100, 101], for heterogeneous media and discontinuous capillary pressure [102, 107, 183], and dynamic capillarity [186, 187].

1.5.3. Linearization

After discretization of the model equations, one obtains a large system of typically nonlinear equations. The most common method to solve nonlinear equations is the Newton method, also called Newton–Raphson method. For a continuously differentiable function $\mathbf{f} : \mathbb{R}^d \rightarrow \mathbb{R}^d$, the method finds approximate solutions of $\mathbf{f}(\mathbf{x}) = \mathbf{0}$ by iteratively solving the tangent plane equation. For an initial guess $\mathbf{x}_0 \in \mathbb{R}^d$, the iterates are given by

$$\mathbf{x}_{i+1} = \mathbf{x}_i - (\mathbf{f}'(\mathbf{x}_i))^{-1} \mathbf{f}(\mathbf{x}_i), \quad \text{for } i \geq 0,$$

where $\mathbf{f}' : \mathbb{R}^d \rightarrow \mathbb{R}^{d \times d}$ denotes the derivative (Jacobian) of \mathbf{f} . The Newton method is locally quadratic convergent if \mathbf{f} is twice continuously differentiable around its zero \mathbf{x}_* and $\mathbf{f}'(\mathbf{x}_*)$ is locally invertible [89]. We use this method in Chapter 6 for the discrete transmission conditions.

For large systems of equations ($d \gg 1$), the Newton method has the disadvantage of requiring the solution of a huge linear system ($d \times d$) involving the computation of the derivative. This may become very costly for discretizations using fine meshes or higher order approximations. This issue can be circumvented by using so-called quasi-Newton methods, which only approximate the derivative \mathbf{f}' or its inverse [89]. A further drawback of the Newton method is its local convergence, which requires a good initial guess. For time dependent problems, one can choose the solution at the previous time step. However, this does severely restrict the time-step size which is required to ensure convergence [264]. In practice, the bound may be milder, but one easily observes divergence. Furthermore, the Newton method does not work for degenerate cases, when the derivative \mathbf{f}' becomes (partially) zero or infinite and thus is not invertible. For such degenerate cases, the Jäger–Kačur method [175, 184] was proposed. It regularizes the Newton method and achieves linear convergence.

Alternatively, the Picard method can be used. Its idea is to fix all coefficients at the old iteration. In particular, for a function $\mathbf{f}(\mathbf{x}) = \mathbf{A}(\mathbf{x})\mathbf{x} + \mathbf{b}(\mathbf{x})$ with coefficients

$\mathbf{A} : \mathbb{R}^d \rightarrow \mathbb{R}^{d \times d}$ and $\mathbf{b} : \mathbb{R}^d \rightarrow \mathbb{R}^d$, the iteration with initial guess $\mathbf{x}_0 \in \mathbb{R}^d$ is given by

$$\mathbf{x}_{i+1} = \mathbf{x}_i - (\mathbf{A}(\mathbf{x}_i))^{-1} \mathbf{f}(\mathbf{x}_i), \quad \text{for } i \geq 0.$$

Based on the Banach fixed-point theorem, the iteration is locally linearly convergent if the function $\mathbf{x} \mapsto (\mathbf{A}(\mathbf{x}))^{-1} \mathbf{b}(\mathbf{x})$ is a contraction (i.e., has a Lipschitz constant below one) close to the zero \mathbf{x}_* of \mathbf{f} . Since most nonlinear problems do not satisfy this contraction property, the applicability of this method is very limited. Instead, in the context of two-phase flow in porous media, a modified Picard method was introduced in [76]. There, the idea is to linearize the temporal discretization as in the Newton method, whereas the nonlinearities in spatial coefficients are approximated using the previous iteration as in the Picard method. Hence, this method coincides with the Newton method when the spatial discretization is linear (due to constant coefficients or for Kirchhoff transformed problems). In general, the modified Picard method is only locally, linearly convergent, but more robust than the Newton method and the classical Picard method [76, 210, 264].

To improve the robustness, another simple, modified fixed-point iteration, the L-scheme, has been proposed [254, 293]. This method uses the monotonicity of the function \mathbf{f} to replace the derivative in the Newton scheme by a constant, diagonal matrix \mathbf{L} . Its iterates are given by

$$\mathbf{x}_{i+1} = \mathbf{x}_i - \mathbf{L}^{-1} \mathbf{f}(\mathbf{x}_i), \quad \text{for } i \geq 0.$$

Based on the monotonicity and fixed-point arguments, one can prove that this method is globally linearly convergent for sufficiently large \mathbf{L} if \mathbf{f} is monotone and Lipschitz-continuous. In particular, the convergence rate of the L-scheme is independent of the spatial discretization, in contrast to the modified Picard method and the Newton method. Furthermore, the L-scheme does not involve the computation of any derivatives. It has been used for various discretizations of two-phase flow models, see e.g. [71, 187, 254, 263, 285, 286]. Whereas the analysis is commonly accomplished assuming Lipschitz-continuous parameter functions, it was extended in [48, 262] to Richards' and two-phase equations, involving only Hölder-continuous coefficients, such as the often used van-Genuchten–Mualem parameterization. We use the L-scheme in Chapter 4 for the derivation of linearized domain decomposition methods for non-equilibrium two-phase flow models.

To improve the convergence rate of the L-scheme, one can adaptively choose \mathbf{L}_i , as proposed for modified L-schemes [12, 236]. Furthermore, the L-scheme and the (modified) Picard method can be used with Anderson acceleration [49, 174, 211] or as a preconditioner for the Newton method [210]. For completeness, we also mention the application of the semi-smooth Newton method [196] in the context of two-phase flow.

1.5.4. Domain decomposition

The idea of decomposing a domain was first used in 1870 to solve elliptic partial differential equations when the boundary is only piece-wise smooth [278]. About a hundred years later, domain decomposition methods became subject to intensive research as technique for numerical methods, see [93, 259, 294, 307, 324] and the references therein. Commonly, one uses domain decomposition methods for parallelization and to obtain better conditioned systems of equations — thereby reaching reasonable performance in practice, see e.g. [82, 181, 190]. These methods split the domain appropriately into sub-domains and then solve the problem on the decoupled sub-domains iteratively. The convergence is achieved by imposing suitable transmission conditions between the sub-domains for consecutive iterations.

A non-overlapping domain decomposition method with Robin transmission conditions was introduced in [209] and analyzed in [212, 239] for stationary advection-diffusion problems. Independently, a variant of this method was proposed in [88], which avoids the explicit use of normal derivatives in the Robin transmission conditions. Henceforth, the optimization of the transmission conditions and of the involved parameters was studied intensively, see the review [113] and the references therein. These methods can be applied to problems with heterogeneous and discontinuous coefficients, as typically found for flow in porous media. For simple settings, this was proposed in [37, 65]. Richards' equation and the two-phase flow equations were considered in [285, 286], where the domain decomposition is integrated in the linearization process after temporal discretization. In [5], this approach is used for single-phase flow in a fractured medium to solve the mixed-dimensional problem. We apply the combination of linearization and domain decomposition to non-equilibrium two-phase flow in Chapter 4.

For time-dependent partial differential equations, Schwarz waveform-relaxation methods were proposed. These are time-parallel time integration methods [115], that combine waveform-relaxation techniques invented in [204] with spatial domain decomposition methods for the parallelization. Over the past three decades, Schwarz waveform-relaxation were studied for various evolution problems. Starting with [40, 111, 128, 133] for linear parabolic problems with typical superlinear convergence, the approach was adopted for hyperbolic problems [118, 123], where these algorithms typically reach zero residual in a finite number of steps. Optimal and optimized transmission conditions were introduced based on [122]. Such transmission conditions are crucial to reach an adequate performance, as demonstrated e.g. for the linear advection-reaction-diffusion equation in [117, 225]. By the Fourier transform, asymptotic expressions for the optimal parameters in the transmission conditions were derived in [35, 36, 119] for linear equations.

For singularly-perturbed advection-diffusion equations, the question arises how to impose the transmission conditions so that they are robust in the limit of vanishing diffusion. For this, adaptive Dirichlet–Neumann and Robin–Neumann algo-

rithms were proposed in [75], accounting for transport along characteristics. The discretized, as well as damped versions were analyzed in [130] when using a modified quadrature rule to recover the hyperbolic limit. A non-overlapping Schwarz method for the stabilized finite element discretization of singularly perturbed problems was discussed in [212], see also [120, 121] for heterogeneous couplings. However, the behavior of these domain decomposition methods in the limit of vanishing diffusion has not been addressed. Therefore, we study in Chapter 5 the limit behavior of the Schwarz method with Robin transmission conditions, and show under which conditions the continuous and discrete methods are consistent and asymptotic-preserving.

In the case of nonlinear problems, only a few partial cases were studied. Superlinear convergence was proved for classical overlapping Schwarz waveform-relaxation for semi-linear reaction-diffusion equations in [112], and for advection-dominated nonlinear conservation laws in [127]. A non-overlapping Schwarz waveform-relaxation for semi-linear wave propagation was analyzed in [149]. For nonlinear reactive transport, optimized transmission conditions were discussed in [144, 145]. Application of the Schwarz waveform-relaxation to Richards' equation and to two-phase flow in porous media was proposed in [4, 6, 7]. In Chapter 6, we apply a non-overlapping Schwarz waveform-relaxation to fully nonlinear advection-diffusion equations and rigorously prove the convergence of the method.

1.6. Outline of this thesis

In this introductory chapter, an overview of the mathematical background of this work has been given. The scientific methodology and results are detailed in the following five chapters, as discussed below. These are separated in two parts. The first one covers the modeling, averaging, and validation on the pore scale. In the second part, we discuss the numerical simulation on the Darcy scale with respect to domain decomposition methods and linearization. Finally, conclusions and an outlook are given in Chapter 7.

PART I: Two-Phase Flow in Single Pores

In Chapter 2, we consider a model for the flow of two immiscible fluids in a single pore of a porous medium. The geometry is idealized to a long, thin strip or tube with slowly varying radius. The fluids are separated by a moving interface, which is in contact with the pore wall. Its evolution is driven by the fluid flow and the surface tension. The contact line model incorporates Navier-slip boundary conditions and a dynamic and possibly hysteretic contact angle law. Assuming a scale separation induced by a small aspect ratio of the typical radius to the length of the pore, we apply matched asymptotic expansions to derive effective models for

the two-phase flow in the limit as this ratio approaches zero. The resulting model forms a system of differential algebraic equations for the interface position and the flux. This model combines Darcy-type equations for the flow with a capillary pressure - saturation relationship involving dynamic effects. Finally, we provide several numerical examples to illustrate the effects of a varying wall width, of the viscosity ratio and of the slip length, as well as of having a dynamic and hysteretic contact-angle law.

In [Chapter 3](#), we apply the previously derived, averaged model to the capillary rise of a fluid in circular cylindrical tubes. Here, this model extends the classical Lucas–Washburn model by incorporating a dynamic contact angle and slippage. We extend the model further to account for inertial effects, which can be relevant at early times. To validate the different models, their solutions are compared to experimental data. In contrast to the Lucas–Washburn model, the numerical results of the models with dynamic contact angle match the experimental data well, both the rise height and the contact angle, even at early times. The models have a free parameter through the dynamic contact-angle law, which is fitted using the experimental data. The findings here suggest that this parameter depends only on the fluid properties, but is independent of geometrical features, such as the tube radius.

PART II: Numerical Methods at the Darcy Scale

In [Chapter 4](#), we discuss two linearization and domain decomposition methods for mathematical models of two-phase flow in porous media at the Darcy scale. The medium consists of two adjacent regions with possibly different parametrizations. The model accounts for non-equilibrium effects like dynamic capillarity and hysteresis. For the temporal discretization of the equations, the θ -scheme is adopted leading to nonlinear time-discrete equations. For these, we propose two iterative schemes, which combine the L-scheme and a non-overlapping domain decomposition method into one iteration. We prove the existence of unique solutions to the iterative problems and give the rigorous convergence proof for both iterative schemes towards the solution of the time-discrete equations. The convergence holds independently of the initial guess, and under mild constraints on the time step. The developed schemes are independent of the spatial discretization or the mesh, and avoid the use of derivatives as in Newton based iterations. Finally, the presented numerical examples confirm the theoretical results and demonstrate the robustness of the schemes. In particular, the second scheme is well suited for models incorporating hysteresis.

In [Chapter 5](#), we consider domain decomposition methods applied to singularly perturbed advection-diffusion problems. These methods can have poor performance for degenerate problems, when classical transmission conditions are used. We discuss here the linear stationary advection-diffusion equation in one dimension

as a prototypical application for non-overlapping domain decomposition methods with Robin transmission conditions. We first show that the continuous algorithm is asymptotic-preserving only if the transmission parameter in the Robin transmission condition tends to the advection speed when the diffusion tends to zero. We then discretize the problem with a cell-centered finite volume method with upwind fluxes and study the effect of different choices for the discretized Robin transmission conditions. We show that the discrete algorithm can inherit the properties of the continuous one, but one can do even better: with a proper, but asymmetric choice of centered and upwind discretizations in the Robin transmission conditions, one can obtain an asymptotic-preserving discrete algorithm without constraint on the parameter in the Robin transmission condition. We illustrate our results with numerical experiments in one and two spatial dimensions.

In [Chapter 6](#), we propose a non-overlapping domain decomposition method of Schwarz waveform-relaxation type for nonlinear advection-diffusion equations. This method relies on nonlinear Robin transmission conditions between the subdomains that ensure the continuity of the converged solution and of its normal flux across the interface. We prove the existence of unique iterative solutions and the convergence of the method. We then present a numerical discretization for solving the iterative problems using a forward Euler discretization in time and a cell-centered finite volume method in space, including a local Newton iteration for solving the nonlinear transmission conditions. Using the results of the previous chapter, the discrete algorithm is asymptotic-preserving, i.e., robust in the vanishing diffusion limit. Finally, we present numerical results that confirm the theoretical findings, in particular the convergence of the algorithm. Moreover, we show that this method can be successfully applied to two-phase flow problems in porous media as paradigms for evolution equations with strongly nonlinear advective and diffusive fluxes.

PART I

Two-Phase Flow in Single Pores

Averaged models for immiscible two-phase flow with surface tension and dynamic contact angle

This chapter is based on the following publication [217]:

- S. B. Lunowa, C. Bringedal, I. S. Pop, *On an averaged model for immiscible two-phase flow with surface tension and dynamic contact angle in a thin strip*, Studies in Applied Mathematics 147 (2021), pp. 84–126.
doi.org/10.1111/sapm.12376
Copyright © 2021, Wiley Periodicals LLC.

Here, [Section 2.5](#), discussing the three-dimensional case, was added and [Section 2.6](#) was adapted to take the two- and three-dimensional case into account. The numerical examples were obtained using the following software [215]:

- S. B. Lunowa, *Solver for the asymptotic model of immiscible two-phase flow with moving contact line in a thin strip*, GitHub repository (2020).
github.com/s-lunowa/AsymptoticThinStripMCLSolver

2.1. Introduction

At the Darcy scale, the two-phase flow is modeled by averaged quantities and relations between them, expressed with the help of effective parameters. The relations should combine all pore-scale effects, which occur due to the complicated pore structure and the exact distribution of the fluids. However, in many state-of-the-art models these parameters are postulated and not derived from a pore-scale model. In particular, we discussed in [Section 1.3.1](#) the necessity to include dynamic effects and hysteresis in the capillary pressure model to be able to describe experimental observations. However, all the extended models discussed here only

consider the Darcy-scale quantities. It is crucial to understand the dependence of the effective parameters on the underlying pore structure. At the pore scale, the mathematical model can incorporate the detailed physical processes, but it is posed in the entire pore space, which is extremely complex, and needs to account for all interfaces between phases. Resolving the whole complicated pore space of realistic scenarios in direct numerical simulations is infeasible, so that further simplifications are necessary to link the properties of the different scales.

To approach this task, there exists a large variety of analytical upscaling techniques, see [Section 1.4](#) and the references therein. The volume averaging method does only provide explicit expressions for the effective parameters in the constitutive equations via closure problems, when additional assumptions are made. Alternatively, the homogenization method is a (matched) asymptotic expansion approach for systems with clear scale separation. Many results for flow in porous media were obtained by homogenization, see e.g. [\[13, 16, 24, 228, 231, 233, 287\]](#), leading either to explicit expressions or to so-called cell problems for the effective parameters. In both cases, knowledge of the underlying pore structure allows for the explicit computation of the effective parameters. Therefore, we apply the homogenization method to explicitly derive effective relations.

Here we consider a simplified geometry, namely the flow through a single, long and thin pore as a representative for the porous medium. Despite the very simplistic representation, the upscaling of thin-strip and thin-tube models typically leads to Darcy-scale models with the same structure as well-recognized Darcy-scale models in general porous media, see e.g. [\[231, 233, 252, 287\]](#). Additionally, using a single pore allows for the explicit derivation of closed-form expressions for the upscaled quantities. We assume that the pore is filled by two incompressible and immiscible fluid phases. The interface separating the two fluids is traversal to the flow direction. The mathematical model consists of conservation laws for mass and momentum in time-dependent domains representing the fluids. Assuming a horizontal setting, we disregard gravity effects. The evolution of the interface separating the domains is not known a-priori, but depends on the velocities of the fluids and on the surface tension between the fluids. Hence, the development of the boundary of the domains must be accounted for, and we have a free boundary problem.

While the fluid domains are assumed to be layered in [\[231, 233, 252, 287\]](#), such that the fluid-fluid interface does not come into contact with the solid wall, we here consider the case when the interface is in contact with the pore walls. This requires a contact-angle model, which is allowed to be dynamic or even hysteretic. In particular, this also implies that each fluid is only present either at the inlet or at the outlet. Note that the plug flow scenario considered in [\[252\]](#) has a similar fluid distribution, but the authors assume a fixed interface shape and a residual thin-film, which yields dynamics that are very different from those generated by a variable

interface with moving contact line. Furthermore, we allow for a slowly varying solid wall instead of a constant-width strip or tube used in [231, 233, 252, 287].

Based on the discussed pore-scale model, we derive upscaled (Darcy-scale) models for two-phase or unsaturated single-phase flow in a porous medium under reasonable assumptions on the underlying physics. We follow the ideas in [231, 233, 287], where asymptotic expansions and transversal averaging is applied to obtain a macro-scale model based on the simple, layered pore. We complement this with volume averages to account for the different geometry and fluid distribution. A similar strategy has been used to show that the upscaled models significantly differ for different flow regimes assuming stationary fluid-fluid interface shapes in [252], and in [287] when assuming a layered, parallel flow regime. In general, the thin-strip or thin-tube approach allows the derivation of explicit relations between the averaged quantities, while various additional features and processes can be easily incorporated, see e.g. [58, 197, 287, 319].

This chapter is organized as follows. In Section 2.2 we formulate the mathematical model for two-phase flow with evolving interface in a thin strip, which is then rescaled to obtain a non-dimensional formulation. Next, we formally derive in Section 2.4 the effective models in the bulk domains and close to the interface when the ratio between the width and length of the thin strip approaches zero. These models form a system of differential algebraic equations for the interface position and the total flux. In Section 2.5, these results are extended to thin, cylindrical tubes including gravity. Based on the derived models, we discuss averaged and effective quantities and their relations in Section 2.6. In particular, there holds a Darcy-type equation for the flow and a capillary pressure - saturation relationship involving dynamic effects. Finally, Section 2.7 provides some numerical examples showing the behavior of the effective models for a constant as well as a varying wall width. The effect of the viscosity ratio, of the slip length and of having a dynamic contact-angle law are discussed in detail.

2.2. Mathematical model of two-phase flow in pores

We consider a two-dimensional thin strip of length $L > 0$, which is axisymmetric at $\hat{\Gamma}_{\text{sym}} := [0, L] \times \{0\}$. Let $\hat{w} : [0, L] \rightarrow (0, \infty)$ be a given smooth function (which is bounded away from zero), that describes the wall $\hat{\Gamma}_w := \{\hat{x} \in (0, L) \times (0, \infty) \mid \hat{x}_2 = \hat{w}(\hat{x}_1)\}$. Here and in the following, the subscripts \cdot_1 and \cdot_2 denote the components of a vector. Then the domain of interest is $\hat{\Omega} := \{\hat{x} \in (0, L) \times (0, \infty) \mid \hat{x}_2 < \hat{w}(\hat{x}_1)\}$. At each time $\hat{t} \in [0, \infty)$, the domain is partitioned into two sub-domains $\hat{\Omega}_I(\hat{t})$ and $\hat{\Omega}_{II}(\hat{t})$, which represent the parts occupied by the two fluids; one at the inlet boundary $\hat{\Gamma}_{\text{in}} := \{0\} \times [0, \hat{w}(0)]$ and the other at the outflow boundary $\hat{\Gamma}_{\text{out}} := \{L\} \times [0, \hat{w}(L)]$. For an illustration of the geometry, see Fig. 2.1.

We consider the particular case when the two fluids are separated by an axisym-

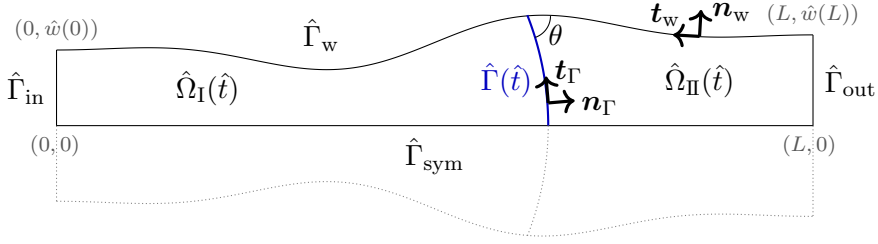


Figure 2.1.: Sketch of the half thin strip $\hat{\Omega}$ filled by two fluids with interface $\hat{\Gamma}(\hat{t})$ at time \hat{t} .

metric fluid-fluid interface $\hat{\Gamma}(\hat{t}) := \partial\hat{\Omega}_I(\hat{t}) \cap \partial\hat{\Omega}_{II}(\hat{t})$, which is in contact with the solid wall $\hat{\Gamma}_w$. This interface has an a-priori unknown location and shape, and therefore appears as a free boundary in the mathematical model. It is parametrized by $\hat{\gamma} : [0, \infty) \times [0, 1] \rightarrow \hat{\Omega}$, such that $\hat{\Gamma}(\hat{t}) = \{\hat{\gamma}(\hat{t}, s) \mid s \in [0, 1]\}$. The parametrization starts at the symmetry boundary and ends at the wall, i.e.,

$$\hat{\gamma}_2(\hat{t}, 0) = 0, \quad \hat{\gamma}_2(\hat{t}, 1) = \hat{w}(\hat{\gamma}_1(\hat{t}, 1)). \quad (2.1)$$

The point $\hat{x}^*(\hat{t}) := \hat{\gamma}(\hat{t}, 1)$ is the so-called contact point.

At all boundaries of $\hat{\Omega}$, the outward normal and tangential unit vectors are denoted \mathbf{n} and \mathbf{t} with an index specifying the part of the boundary, e.g. \mathbf{n}_{sym} for the normal vector at the symmetry boundary $\hat{\Gamma}_{\text{sym}}$. At the fluid-fluid interface $\hat{\Gamma}(\hat{t})$, the normal unit vector pointing from $\hat{\Omega}_I(\hat{t})$ into $\hat{\Omega}_{II}(\hat{t})$ is denoted by \mathbf{n}_Γ , while the tangential unit vector is \mathbf{t}_Γ . Therefore, these vectors are given by

$$\begin{aligned} \mathbf{t}_\Gamma &= \frac{\partial_s \hat{\gamma}}{|\partial_s \hat{\gamma}|} = \frac{1}{\sqrt{(\partial_s \hat{\gamma}_1)^2 + (\partial_s \hat{\gamma}_2)^2}} \partial_s \hat{\gamma}, & \mathbf{n}_\Gamma &= \frac{\partial_s \mathbf{t}_\Gamma}{|\partial_s \mathbf{t}_\Gamma|} = \frac{1}{\sqrt{(\partial_s \hat{\gamma}_1)^2 + (\partial_s \hat{\gamma}_2)^2}} \begin{pmatrix} \partial_s \hat{\gamma}_2 \\ -\partial_s \hat{\gamma}_1 \end{pmatrix}, \\ \mathbf{t}_w &= -\frac{1}{\sqrt{1 + (\partial_{\hat{x}_1} \hat{w})^2}} \begin{pmatrix} 1 \\ \partial_{\hat{x}_1} \hat{w} \end{pmatrix}, & \mathbf{n}_w &= \frac{1}{\sqrt{1 + (\partial_{\hat{x}_1} \hat{w})^2}} \begin{pmatrix} -\partial_{\hat{x}_1} \hat{w} \\ 1 \end{pmatrix}, \\ \mathbf{t}_{\text{sym}} &= \begin{pmatrix} 1 \\ 0 \end{pmatrix}, & \mathbf{n}_{\text{sym}} &= \begin{pmatrix} 0 \\ -1 \end{pmatrix}, \\ \mathbf{t}_{\text{in}} &= \begin{pmatrix} 0 \\ -1 \end{pmatrix}, & \mathbf{n}_{\text{in}} &= \begin{pmatrix} -1 \\ 0 \end{pmatrix}, \\ \mathbf{t}_{\text{out}} &= \begin{pmatrix} 0 \\ 1 \end{pmatrix}, & \mathbf{n}_{\text{out}} &= \begin{pmatrix} 1 \\ 0 \end{pmatrix}. \end{aligned}$$

In each sub-domain $\hat{\Omega}_\alpha(\hat{t})$, $\alpha \in \{I, II\}$, we assume that the flow is modeled by the incompressible Navier–Stokes equations, which are written in dimensional form

$$\rho_\alpha (\partial_{\hat{t}} \hat{\mathbf{u}}_\alpha + (\hat{\mathbf{u}}_\alpha \cdot \hat{\nabla}) \hat{\mathbf{u}}_\alpha) + \hat{\nabla} \hat{p}_\alpha = \mu_\alpha \hat{\Delta} \hat{\mathbf{u}}_\alpha \quad \text{in } \hat{\Omega}_\alpha(\hat{t}), \quad (2.2)$$

$$\hat{\nabla} \cdot \hat{\mathbf{u}}_\alpha = 0 \quad \text{in } \hat{\Omega}_\alpha(\hat{t}), \quad (2.3)$$

where $\hat{\mathbf{u}}_\alpha(\hat{t}, \hat{\mathbf{x}})$ and $\hat{p}_\alpha(\hat{t}, \hat{\mathbf{x}})$ are the velocity and pressure of fluid α . The parameters ρ_α and μ_α denote the density and the dynamic viscosity of the fluid, see Table 2.1 for an overview of all parameters and quantities. The symmetry condi-

Parameter	Symbol	Dim.-less number	Symbol	Value
Length of the thin strip	L	Scale ratio	ε	$\hat{w}(0)/L$
Characteristic velocity	U	Density ratio	R	$\rho_{\text{II}}/\rho_{\text{I}}$
Density of fluid phase α	ρ_{α}	Viscosity ratio	M	$\mu_{\text{II}}/\mu_{\text{I}}$
Viscosity of fluid phase α	μ_{α}	Reynolds number	Re	$\rho_{\text{I}}UL/\mu_{\text{I}}$
Surface tension coefficient	σ	Capillary number	Ca	$\mu_{\text{I}}U/\sigma$
Gravitational acceleration	g	Eff. capillary number	$\overline{\text{Ca}}$	Ca/ε
		Eff. gravity number	G	$\varepsilon^2\rho_{\text{I}}gL^2/(\mu_{\text{I}}U)$

Quantity	Dim.	Dim.-less [scaling]	Inner expansion [scaling]
Position	\hat{x}	\boldsymbol{x} $[L, \varepsilon L]$	\boldsymbol{X} $[\varepsilon L, \varepsilon L]$
Time	\hat{t}	t $[L/U]$	t $[L/U]$
Velocity of fluid phase α	$\hat{\boldsymbol{u}}_{\alpha}$	\boldsymbol{u}_{α} $[U]$	\boldsymbol{U}_{α} $[U]$
Pressure of fluid phase α	\hat{p}_{α}	p_{α} $[\mu_{\text{I}}U/(\varepsilon^2L)]$	P_{α} $[\mu_{\text{I}}U/(\varepsilon^2L)]$
Interface parametrization	$\hat{\gamma}$	γ $[L, \varepsilon L]$	\boldsymbol{Y} $[\varepsilon L, \varepsilon L]$
Interface curvature	$\hat{\kappa}$	κ $[1/L]$	K $[1/\varepsilon L]$
Slip length	$\hat{\lambda}$	λ $[\varepsilon L]$	λ $[\varepsilon L]$
Wall function (width)	\hat{w}	w $[\varepsilon L]$	w $[\varepsilon L]$
Contact angle	θ	θ $[1]$	θ $[1]$

Table 2.1.: Summary of parameters (*top left*), dimensionless numbers (*top right*), dimensional and dimensionless quantities and their scaling (*bottom*).

tions at $\hat{\Gamma}_{\text{sym},\alpha}(\hat{t}) := \hat{\Gamma}_{\text{sym}} \cap \partial\hat{\Omega}_\alpha(\hat{t})$ are

$$\hat{\mathbf{u}}_\alpha \cdot \mathbf{n}_{\text{sym}} = 0, \quad \mathbf{t}_{\text{sym}} \cdot \left(\hat{\nabla} \hat{\mathbf{u}}_\alpha \mathbf{n}_{\text{sym}} \right) = 0, \quad \hat{\nabla} \hat{p}_\alpha \cdot \mathbf{n}_{\text{sym}} = 0 \quad \text{on } \hat{\Gamma}_{\text{sym},\alpha}(\hat{t}), \quad (2.4)$$

$$\mathbf{n}_\Gamma \cdot \mathbf{n}_{\text{sym}} = 0 \quad \text{at } s = 0. \quad (2.5)$$

The walls $\hat{\Gamma}_{\text{w},\alpha}(\hat{t}) := \hat{\Gamma}_{\text{w}} \cap \partial\hat{\Omega}_\alpha(\hat{t})$ in contact with fluid $\alpha \in \{\text{I}, \text{II}\}$ are assumed impermeable. As discussed in [Section 1.2.2](#), we impose a Navier-slip condition to allow for the movement of the contact point. These conditions read

$$\mathbf{t}_{\text{w}} \cdot (\hat{\mathbf{u}}_\alpha + 2\hat{\lambda}\hat{\mathbf{D}}(\hat{\mathbf{u}}_\alpha)\mathbf{n}_{\text{w}}) = 0 \quad \hat{\mathbf{u}}_\alpha \cdot \mathbf{n}_{\text{w}} = 0 \quad \text{on } \hat{\Gamma}_{\text{w},\alpha}(\hat{t}), \quad (2.6)$$

where $\hat{\mathbf{D}}(\hat{\mathbf{u}}) := (\hat{\nabla}\hat{\mathbf{u}} + (\hat{\nabla}\hat{\mathbf{u}})^T)/2$ denotes the symmetric strain and $\hat{\lambda}$ is the slip length. Often, the Navier-slip condition is only applied close to the contact point. In this case, a variable slip length $\hat{\lambda}(\hat{t}, \hat{x}_1)$ is adopted, decaying rapidly to zero away from the contact point $\hat{\mathbf{x}}^*(\hat{t})$, see e.g. [\[26, 83, 142, 148\]](#).

Remark 2.1. To be general, we will consider two cases here: a constant slip length $\hat{\lambda}$ on the whole wall $\hat{\Gamma}_{\text{w}}$, or a varying slip length $\hat{\lambda}(\hat{t}, \hat{x}_1) = \hat{\lambda}_e \exp(-c|\hat{x}_1 - \hat{x}_1^*(\hat{t})|)$ which decreases exponentially away from the contact point $\hat{\mathbf{x}}^*(\hat{t})$. Note that the overall dynamics of the two-phase system will be independent of the latter, local slip condition, and especially of the exact form used; only the flow field close to the interface will be affected, see [Section 2.4](#). This is in accordance with the results in [\[97, 288\]](#). Furthermore, note that we consider for simplicity the same slip length $\hat{\lambda}$ for both fluids, although they could in principle differ. It is possible to extend the analysis below to incorporate fluid dependent slip lengths.

At the contact point $\hat{\mathbf{x}}^*(\hat{t})$, the contact angle θ between the wall $\hat{\Gamma}_{\text{w}}(\hat{t})$ and the fluid interface $\hat{\Gamma}(\hat{t})$ must be prescribed. As discussed in [Section 1.2.2](#), the contact angle is dynamic and possibly hysteretic. To represent this behavior, we assume the contact angle θ to depend on the velocity $-\partial_t \hat{\mathbf{x}}^*(\hat{t}) \cdot \mathbf{t}_{\text{w}}$ of the contact point parallel to the wall. Recall that $\hat{\mathbf{x}}^* = \hat{\gamma}|_{s=1}$, so this contact angle condition is expressed as

$$\cos(\theta(-\partial_t \hat{\gamma} \cdot \mathbf{t}_{\text{w}}|_{\hat{x}_1=\hat{\gamma}_1})) = \mathbf{t}_\Gamma \cdot \mathbf{t}_{\text{w}}|_{\hat{x}_1=\hat{\gamma}_1} \quad \text{at } s = 1, \quad (2.7)$$

where $\theta : \mathbb{R} \rightarrow (0, \pi)$ is a given dynamic contact-angle model. Note that any dynamic contact-angle model that satisfies assumption [\(A5\)](#) below can be used. Specific relations for hysteretic θ and their effect on the behavior will be discussed in [Section 2.4.4](#). Furthermore, to account for heterogeneities, the following analysis can be straightforwardly extended to the case when the contact angle also depends on the position $\hat{x}_1^*(\hat{t})$ of the contact point.

At the interface $\hat{\Gamma}(\hat{t})$, there holds continuity of the velocity and of the tangential

stress, while the jump in the normal stress is caused by the surface tension

$$\hat{\mathbf{u}}_{\text{I}} = \hat{\mathbf{u}}_{\text{II}} \quad \text{on } \hat{\Gamma}(\hat{t}), \quad (2.8)$$

$$-(\hat{p}_{\text{I}} - \hat{p}_{\text{II}})\mathbf{n}_{\Gamma} + 2(\mu_{\text{I}}\hat{\mathbf{D}}(\hat{\mathbf{u}}_{\text{I}}) - \mu_{\text{II}}\hat{\mathbf{D}}(\hat{\mathbf{u}}_{\text{II}}))\mathbf{n}_{\Gamma} = \sigma\hat{\kappa}\mathbf{n}_{\Gamma} \quad \text{on } \hat{\Gamma}(\hat{t}), \quad (2.9)$$

where $\hat{\kappa} = \det(\partial_s \gamma, \partial_s^2 \gamma) / |\partial_s \gamma|^3$ is the local mean curvature of the interface. Note that this curvature generalizes to $\hat{\nabla} \cdot \mathbf{n}_{\Gamma}$ for three-dimensional domains. The interface moves according to the normal velocity of the fluids,

$$\partial_{\hat{t}} \hat{\gamma} \cdot \mathbf{n}_{\Gamma} = \hat{\mathbf{u}}_{\text{I}} \cdot \mathbf{n}_{\Gamma} \quad \text{on } \hat{\Gamma}(\hat{t}). \quad (2.10)$$

At the inlet boundary $\hat{\Gamma}_{\text{in}}$, either the pressure \hat{p}_{in} or the velocity $\hat{\mathbf{u}}_{\text{in}}$ is given, namely either

$$\hat{p}_{\text{I}} = \hat{p}_{\text{in}}, \quad \hat{\mathbf{u}}_{\text{I}} \cdot \mathbf{t}_{\text{in}} = 0 \quad \text{or} \quad \hat{\mathbf{u}}_{\text{I}} = \hat{\mathbf{u}}_{\text{in}} \quad \text{on } \hat{\Gamma}_{\text{in}}, \quad (2.11)$$

while an outflow boundary condition is applied at $\hat{\Gamma}_{\text{out}}$ (corresponding to $\hat{p}_{\text{out}} = 0$)

$$\hat{p}_{\text{II}} = 0, \quad \hat{\mathbf{u}}_{\text{II}} \cdot \mathbf{t}_{\text{out}} = 0 \quad \text{on } \hat{\Gamma}_{\text{out}}. \quad (2.12)$$

The problem is closed by the initial conditions $\hat{\gamma}|_{\hat{t}=0} = \hat{\gamma}_0$ for the position of the interface $\hat{\Gamma}(0)$ and $\hat{\mathbf{u}}_{\alpha}|_{\hat{t}=0} = \hat{\mathbf{u}}_{\alpha,0}$ for the velocity in $\hat{\Omega}_{\alpha}(0)$. In the following, we will omit the initial conditions and implicitly require them to match the asymptotic solutions in [Section 2.4](#) to avoid possible initial layer solutions for small times.

2.3. Dimensionless formulation

To quantify the importance of the different terms of the model, we rewrite the equations in a dimensionless form. As we consider a single, thin pore, we introduce the small parameter $\varepsilon = \hat{w}(0)/L \ll 1$ which characterizes the ratio of the typical width to the length of the thin strip. Note that in a general porous medium, ε would reflect the ratio of the size of a pore to the length scale of a representative elementary volume. With this, we rescale the governing equations using the dimensionless quantities (see also [Table 2.1](#))

$$\begin{aligned} x_1 &:= \frac{\hat{x}_1}{L}, \quad x_2 := \frac{\hat{x}_2}{\hat{w}(0)} = \frac{\hat{x}_2}{\varepsilon L}, \quad t := \frac{\hat{t}U}{L}, \quad \lambda^\varepsilon := \frac{\hat{\lambda}}{\hat{w}(0)} = \frac{\hat{\lambda}}{\varepsilon L}, \\ \gamma_1^\varepsilon(t, s) &:= \frac{\hat{\gamma}_1(\hat{t}, s)}{L}, \quad \gamma_2^\varepsilon(t, s) := \frac{\hat{\gamma}_2(\hat{t}, s)}{\hat{w}(0)} = \frac{\hat{\gamma}_2(\hat{t}, s)}{\varepsilon L}, \quad w^\varepsilon(x_1) := \frac{\hat{w}(\hat{x}_1)}{\hat{w}(0)} = \frac{\hat{w}(\hat{x}_1)}{\varepsilon L}, \\ \theta^\varepsilon(u) &:= \theta(uU), \quad \mathbf{u}_\alpha^\varepsilon(t, \mathbf{x}) := \frac{\hat{\mathbf{u}}_\alpha(\hat{t}, \hat{\mathbf{x}})}{U}, \quad p_\alpha^\varepsilon(t, \mathbf{x}) := \frac{\hat{p}_\alpha(\hat{t}, \hat{\mathbf{x}})\varepsilon^2 L}{\mu_{\text{I}}U}, \end{aligned}$$

where $U > 0$ denotes a characteristic velocity. In particular, the pressure reference $\mu_{\text{I}}U/(\varepsilon^2 L)$ is chosen such that pressure and viscous stress terms in [\(2.2\)](#) are

balanced. For moderate Reynolds number, this choice ensures laminar flow driven by the pressure gradients, which is crucial for the validity of Darcy's law on the Darcy scale. Note that the coordinates x_1 and x_2 are scaled differently to obtain a domain of order 1, $\mathcal{O}(\varepsilon^0)$. Hence, the non-dimensional differential operators are

$$\nabla^\varepsilon = \begin{pmatrix} \partial_{x_1} \\ \varepsilon^{-1} \partial_{x_2} \end{pmatrix}, \quad \Delta^\varepsilon = \partial_{x_1}^2 + \varepsilon^{-2} \partial_{x_2}^2,$$

and the divergence changes accordingly. The non-dimensional domains and boundaries become

$$\begin{aligned} \Gamma^\varepsilon(t) &= \{\gamma^\varepsilon(t, s) \mid s \in [0, 1]\}, & \Omega^\varepsilon &= \{\mathbf{x} \in (0, 1) \times (0, \infty) \mid x_2 < w^\varepsilon(x_1)\}, \\ \Gamma_{\text{in}}^\varepsilon &= \{0\} \times [0, 1], & \mathcal{M} &:= \{O \subset \Omega^\varepsilon \setminus \Gamma^\varepsilon(t) \mid O \cup \Gamma_{\text{in}}^\varepsilon \text{ is connected}\}, \\ \Omega_{\text{I}}^\varepsilon(t) &= \bigcup_{O \in \mathcal{M}} O, & \Omega_{\text{II}}^\varepsilon(t) &= \Omega^\varepsilon \setminus (\Gamma^\varepsilon(t) \cup \Omega_{\text{I}}^\varepsilon(t)), & \Gamma_{\text{out}}^\varepsilon &= \{1\} \times [0, w^\varepsilon(1)], \\ \Gamma_{\text{sym}, \alpha}^\varepsilon(t) &= \{\mathbf{x} \in \partial\Omega_\alpha^\varepsilon(t) \mid x_2 = 0\}, & \Gamma_{\text{w}, \alpha}^\varepsilon(t) &= \{\mathbf{x} \in \partial\Omega_\alpha^\varepsilon(t) \mid x_2 = w^\varepsilon(x_1)\}. \end{aligned}$$

After the rescaling of (2.1)–(2.12), the dimensionless equations read

$$\varepsilon^2 \text{Re}(\partial_t \mathbf{u}_{\text{I}}^\varepsilon + (\mathbf{u}_{\text{I}}^\varepsilon \cdot \nabla^\varepsilon) \mathbf{u}_{\text{I}}^\varepsilon) + \nabla^\varepsilon p_{\text{I}}^\varepsilon = \varepsilon^2 \Delta^\varepsilon \mathbf{u}_{\text{I}}^\varepsilon \quad \text{in } \Omega_{\text{I}}^\varepsilon(t), \quad (2.13)$$

$$\varepsilon^2 \text{RRe}(\partial_t \mathbf{u}_{\text{II}}^\varepsilon + (\mathbf{u}_{\text{II}}^\varepsilon \cdot \nabla^\varepsilon) \mathbf{u}_{\text{II}}^\varepsilon) + \nabla^\varepsilon p_{\text{II}}^\varepsilon = \text{M} \varepsilon^2 \Delta^\varepsilon \mathbf{u}_{\text{II}}^\varepsilon \quad \text{in } \Omega_{\text{II}}^\varepsilon(t), \quad (2.14)$$

$$\nabla^\varepsilon \cdot \mathbf{u}_\alpha^\varepsilon = 0 \quad \text{in } \Omega_\alpha^\varepsilon(t), \quad (2.15)$$

$$\mathbf{u}_\alpha^\varepsilon \cdot \mathbf{n}_{\text{sym}} = 0, \quad \mathbf{t}_{\text{sym}} \cdot (\nabla^\varepsilon \mathbf{u}_\alpha^\varepsilon \mathbf{n}_{\text{sym}}) = 0 \quad \text{on } \Gamma_{\text{sym}, \alpha}^\varepsilon(t), \quad (2.16)$$

$$\nabla^\varepsilon p_\alpha^\varepsilon \cdot \mathbf{n}_{\text{sym}} = 0, \quad \text{on } \Gamma_{\text{sym}, \alpha}^\varepsilon(t), \quad (2.17)$$

$$\text{either } p_{\text{I}}^\varepsilon = p_{\text{in}}^\varepsilon, \quad \mathbf{u}_{\text{I}}^\varepsilon \cdot \mathbf{t}_{\text{in}} = 0, \quad \text{or } \mathbf{u}_{\text{I}}^\varepsilon = \mathbf{u}_{\text{in}}^\varepsilon \quad \text{on } \Gamma_{\text{in}}^\varepsilon, \quad (2.18)$$

$$p_{\text{II}}^\varepsilon = 0, \quad \mathbf{u}_{\text{II}}^\varepsilon \cdot \mathbf{t}_{\text{out}} = 0 \quad \text{on } \Gamma_{\text{out}}^\varepsilon, \quad (2.19)$$

$$\mathbf{t}_{\text{w}}^\varepsilon \cdot (\mathbf{u}_\alpha^\varepsilon + 2\varepsilon \lambda^\varepsilon \mathbf{D}^\varepsilon(\mathbf{u}_\alpha^\varepsilon) \mathbf{n}_{\text{w}}^\varepsilon) = 0, \quad \mathbf{u}_\alpha^\varepsilon \cdot \mathbf{n}_{\text{w}}^\varepsilon = 0 \quad \text{on } \Gamma_{\text{w}, \alpha}^\varepsilon(t), \quad (2.20)$$

$$\partial_t \left(\frac{\gamma_{\text{I}}^\varepsilon}{\varepsilon \gamma_{\text{II}}^\varepsilon} \right) \cdot \mathbf{n}_{\Gamma}^\varepsilon = \mathbf{u}_{\text{I}}^\varepsilon \cdot \mathbf{n}_{\Gamma}^\varepsilon, \quad \mathbf{u}_{\text{I}}^\varepsilon = \mathbf{u}_{\text{II}}^\varepsilon \quad \text{on } \Gamma^\varepsilon(t), \quad (2.21)$$

$$-(p_{\text{I}}^\varepsilon - p_{\text{II}}^\varepsilon) \mathbf{n}_{\Gamma}^\varepsilon + 2\varepsilon^2 (\mathbf{D}^\varepsilon(\mathbf{u}_{\text{I}}^\varepsilon) - \text{M} \mathbf{D}^\varepsilon(\mathbf{u}_{\text{II}}^\varepsilon)) \mathbf{n}_{\Gamma}^\varepsilon = \frac{\varepsilon^2}{\text{Ca}} \kappa^\varepsilon \mathbf{n}_{\Gamma}^\varepsilon \quad \text{on } \Gamma^\varepsilon(t), \quad (2.22)$$

$$\mathbf{n}_{\Gamma}^\varepsilon \cdot \mathbf{n}_{\text{sym}} = 0 \quad \text{at } s = 0, \quad (2.23)$$

$$\cos(\theta^\varepsilon(-\partial_t \gamma^\varepsilon \cdot \mathbf{t}_{\text{w}}^\varepsilon|_{x_1=\gamma_1^\varepsilon})) = \mathbf{t}_{\Gamma}^\varepsilon \cdot \mathbf{t}_{\text{w}}^\varepsilon|_{x_1=\gamma_1^\varepsilon} \quad \text{at } s = 1, \quad (2.24)$$

for $\alpha \in \{\text{I}, \text{II}\}$, where the dimensionless numbers R , M , Re and Ca are given in Table 2.1. The non-dimensional strain is given by $\mathbf{D}^\varepsilon(\mathbf{u}^\varepsilon) = \frac{1}{2}(\nabla^\varepsilon \mathbf{u}^\varepsilon + (\nabla^\varepsilon \mathbf{u}^\varepsilon)^T)$ and the transformed normal and tangential vectors are

$$\mathbf{t}_{\text{w}}^\varepsilon = -\frac{1}{\sqrt{1 + \varepsilon^2 (\partial_{x_1} w^\varepsilon)^2}} \begin{pmatrix} 1 \\ \varepsilon \partial_{x_1} w^\varepsilon \end{pmatrix}, \quad \mathbf{n}_{\text{w}}^\varepsilon = \frac{1}{\sqrt{1 + \varepsilon^2 (\partial_{x_1} w^\varepsilon)^2}} \begin{pmatrix} -\varepsilon \partial_{x_1} w^\varepsilon \\ 1 \end{pmatrix},$$

$$t_1^\varepsilon = \frac{1}{\sqrt{(\partial_s \gamma_1^\varepsilon)^2 + \varepsilon^2 (\partial_s \gamma_2^\varepsilon)^2}} \begin{pmatrix} \partial_s \gamma_1^\varepsilon \\ \varepsilon \partial_s \gamma_2^\varepsilon \end{pmatrix}, \quad n_1^\varepsilon = \frac{1}{\sqrt{(\partial_s \gamma_1^\varepsilon)^2 + \varepsilon^2 (\partial_s \gamma_2^\varepsilon)^2}} \begin{pmatrix} \varepsilon \partial_s \gamma_2^\varepsilon \\ -\partial_s \gamma_1^\varepsilon \end{pmatrix}.$$

Furthermore, the non-dimensional curvature is given by

$$\kappa^\varepsilon = \frac{\varepsilon \det(\partial_s \gamma^\varepsilon, \partial_s^2 \gamma^\varepsilon)}{((\partial_s \gamma_1^\varepsilon)^2 + \varepsilon^2 (\partial_s \gamma_2^\varepsilon)^2)^{3/2}} = \frac{\varepsilon (\partial_s \gamma_1^\varepsilon \partial_s^2 \gamma_2^\varepsilon - \partial_s \gamma_2^\varepsilon \partial_s^2 \gamma_1^\varepsilon)}{((\partial_s \gamma_1^\varepsilon)^2 + \varepsilon^2 (\partial_s \gamma_2^\varepsilon)^2)^{3/2}}.$$

Remark 2.2. Integrating (2.15) for $\alpha = \text{I}$ over $V_a = \{\mathbf{x} \in \Omega_1^\varepsilon(t) \mid x_1 < a\}$ for any $a < \min_{s \in [0,1]} \gamma_1^\varepsilon(t, s)$ yields by the Gauss theorem and the boundary conditions (2.16) and (2.20)

$$0 = \int_{V_a} \nabla^\varepsilon \cdot \mathbf{u}_1^\varepsilon d\mathbf{x} = \int_{\partial V_a} \mathbf{u}_1^\varepsilon \cdot \mathbf{n} ds = \int_0^{w^\varepsilon(a)} u_{1,1}^\varepsilon|_{x_1=a} dx_2 - \int_0^1 u_{1,1}^\varepsilon|_{x_1=0} dx_2.$$

Denoting the total flux into the half strip by $q^\varepsilon(t, 0) := \int_0^1 u_{1,1}^\varepsilon(t, \mathbf{x})|_{x_1=0} dx_2$, we obtain that for all $a < \min_{s \in [0,1]} \gamma_1^\varepsilon(t, s)$ the total flux $q^\varepsilon(t, a) := \int_0^{w^\varepsilon(a)} u_{1,1}^\varepsilon|_{x_1=a} dx_2 = q^\varepsilon(t, 0)$. Analogously, integrating (2.15) for $\alpha = \text{I}$ over $\Omega_1^\varepsilon(t)$ and for $\alpha = \text{II}$ over $V_a = \{\mathbf{x} \in \Omega_{\text{II}}^\varepsilon \mid x_1 < a\}$ for any $a > \max_{s \in [0,1]} \gamma_1^\varepsilon(t, s)$ yields by the Gauss theorem, the boundary conditions (2.16) and (2.20) and the continuity of velocity at the interface (2.21) that

$$0 = \int_{\Omega_1^\varepsilon} \nabla^\varepsilon \cdot \mathbf{u}_1^\varepsilon d\mathbf{x} + \int_{V_a} \nabla^\varepsilon \cdot \mathbf{u}_{\text{II}}^\varepsilon d\mathbf{x} = -q^\varepsilon(t, 0) + \int_0^{w^\varepsilon(a)} u_{\text{II},1}^\varepsilon|_{x_1=a} dx_2,$$

i.e., the total flux $q(t, a) := \int_0^{w^\varepsilon(a)} u_{\text{II},1}^\varepsilon|_{x_1=a} dx_2 = q^\varepsilon(t, 0)$ for all $a > \max_{s \in [0,1]} \gamma_1^\varepsilon(t, s)$. Within the interval $[\min_{s \in [0,1]} \gamma_1^\varepsilon(t, s), \max_{s \in [0,1]} \gamma_1^\varepsilon(t, s)]$, the same calculation shows that the sum of the two fluxes over the respective parts of the domain equals the total flux $q^\varepsilon(t, 0)$. This means that the total flux is independent of x_1 , so we will simply use $q^\varepsilon(t)$ in this result for the subsequent analysis.

2.4. Asymptotic expansions

In this section, we derive the formal solution for the two-phase flow system (2.13)–(2.24) in the asymptotic limit as $\varepsilon \rightarrow 0$, i.e., the behavior in the limit when the thin strip becomes infinitely thin. We start with the solution in the bulk domains $\Omega_\alpha^\varepsilon(t)$, $\alpha \in \{\text{I}, \text{II}\}$, away from the interface $\Gamma^\varepsilon(t)$, where either fluid I or II is present, respectively. In the subsequent section, we show that these bulk solutions are connected via a boundary layer solution in the vicinity of $\Gamma^\varepsilon(t)$. Altogether, the solution is of Hagen–Poiseuille type in the bulk coupled by a dynamic Young–Laplace law at the interface, such that the interface position and the total flux are given by differential algebraic equations. Furthermore, we show in Section 2.4.3 that the solution is regular in the viscosity ratio M , such that it matches the asymptotic limit for un-

saturated single-phase flow in the limit of vanishing viscosity ratio $M \rightarrow 0$. Finally, a reformulation for hysteretic contact angle models is discussed in [Section 2.4.4](#).

For the following analysis we use an asymptotic expansion technique with respect to ε to derive effective models. All variables are assumed to be smooth and to depend regularly on ε starting with the leading order $\mathcal{O}(\varepsilon^0)$. We apply the homogenization ansatz

$$\begin{aligned} \mathbf{u}_\alpha^\varepsilon(t, \mathbf{x}) &= \mathbf{u}_\alpha^0(t, \mathbf{x}) + \varepsilon \mathbf{u}_\alpha^1(t, \mathbf{x}) + \mathcal{O}(\varepsilon^2), \\ p_\alpha^\varepsilon(t, \mathbf{x}) &= p_\alpha^0(t, \mathbf{x}) + \varepsilon p_\alpha^1(t, \mathbf{x}) + \mathcal{O}(\varepsilon^2), \\ \gamma^\varepsilon(t, s) &= \gamma^0(t, s) + \varepsilon \gamma^1(t, s) + \mathcal{O}(\varepsilon^2), \end{aligned}$$

for $\alpha \in \{\text{I}, \text{II}\}$. Inserting the asymptotic expansions into the two-phase flow equations (2.13)–(2.24) and equating terms of the same order in ε , we will obtain the asymptotic equations and solutions in the limit as $\varepsilon \rightarrow 0$. To this end, we need some assumptions on the parameters of the model.

(A1) The Reynolds number Re and its product with the density ratio R are uniformly bounded for all $0 < \varepsilon \ll 1$, i.e., there exists $C \in (0, \infty)$ such that $\text{Re} \leq C$ and $R\text{Re} \leq C$ independent of ε . In other words $\text{Re} \leq \mathcal{O}(\varepsilon^0)$ and $R\text{Re} \leq \mathcal{O}(\varepsilon^0)$.

(A2) The viscosity ratio M of the fluids is of order 1, $M = \mathcal{O}(\varepsilon^0)$.

(A3) According to [Remark 2.1](#), the slip length λ^ε has the form

$$\lambda^\varepsilon(t, x_1) = \lambda^0 + \lambda_e \exp\left(-\frac{|x_1 - x_1^*(t)|}{\varepsilon}\right),$$

for given constants $\lambda^0, \lambda_e \geq 0$ that are independent of ε . Moreover, there holds either $\lambda_e = 0$, or $\lambda^0 = 0$. Note that the latter represents the case of rapidly decaying slip away from the interface, so that λ^ε has the expansion $\lambda^\varepsilon(t, x_1) = \mathcal{O}(\varepsilon^N)$ for arbitrary $N \in \mathbb{N}$ as long as $x_1 - x_1^*(t) \gg \varepsilon$.

(A4) The wall function w^ε has a uniform expansion

$$w^\varepsilon(x_1) = w^0(x_1) + \varepsilon w^1(x_1) + \mathcal{O}(\varepsilon^2),$$

where $w^\varepsilon, w^0 : [0, 1] \rightarrow (0, \infty)$ are continuously differentiable, and thus bounded away from zero. Moreover, there holds $w^0(0) = 1$ and $\partial_{x_1} w^0(0) = \partial_{x_1} w^0(1) = 0$.

(A5) The contact angle relation θ^ε has a uniform expansion

$$\theta^\varepsilon(u) = \theta^0(u) + \varepsilon \theta^1(u) + \mathcal{O}(\varepsilon^2),$$

where $\theta^0 : \mathbb{R} \rightarrow (0, \pi)$ is Lipschitz-continuous.

(A6) If the velocity boundary condition $\mathbf{u}_\text{I}^\varepsilon = \mathbf{u}_\text{in}^\varepsilon$ is used at the inlet $\Gamma_\text{in}^\varepsilon$, the

velocity is given by

$$\mathbf{u}_{\text{in}}^\varepsilon(t, \mathbf{x}) = \begin{pmatrix} 3q(t) \frac{(1+2\lambda^0)-x_2^2}{2+6\lambda^0} + \mathcal{O}(\varepsilon) \\ \mathcal{O}(\varepsilon^2) \end{pmatrix},$$

where $q : [0, \infty) \rightarrow \mathbb{R}$ is a continuous function independent of ε .

As will be seen below, (A1) ensures that the flow remains laminar. Furthermore, (A2) restricts the discussion to moderately viscous liquids. While $M \gg 1$ would result in a highly viscous second fluid which gets immobile as $\varepsilon \rightarrow 0$, we will discuss the case $M \ll 1$ of a extremely mobile fluid like air (compared to water or oil) separately in Section 2.4.3. The asymptotic expansions stated in (A4) and (A5) are crucial for the derivation. As discussed in Section 2.2, slip is necessary to allow the movement of the contact point. Hence, (A3) requires a simple expression of the slip at the pore walls close to the interface to avoid technical complexity, while allowing for the typical no-slip condition at the pore walls away from the interface ($\lambda^0 = 0$). The case of global slip conditions ($\lambda^0 > 0$) generalizes this to applications where the slip length is of the same order as the diameter, e.g., in nano-fluidic devices or for fluids with low viscosity. The assumption of a horizontal wall at the inlet and at the outlet ($\partial_{x_1} w^0(0) = \partial_{x_1} w^0(1) = 0$) in (A4) is used to exclude possible boundary-layer effects caused by non-matching boundary conditions. The inlet velocity in (A6) is then the Hagen–Poiseuille profile incorporating the Navier-slip condition. Assumptions (A4) and (A6) can be relaxed if the boundary conditions (2.18) and (2.19) at $\Gamma_{\text{in}}^\varepsilon$ and $\Gamma_{\text{out}}^\varepsilon$ are replaced appropriately, or if the resulting boundary layer matches the asymptotic solution of the following analysis. We observe that (A4) rules out the possibility that the pore has walls with rapidly oscillatory characteristics (so-called “rough walls”). Such walls can be characterized by a function $w^\varepsilon(x_1) = w^0(x_1) + \varepsilon w^1(x_1/\varepsilon) + \mathcal{O}(\varepsilon)$. Clearly, this would strongly affect the shape and position of the interface. A naive extension of the following results would yield unphysical oscillations of the interface, so that we restrict the discussion to slowly varying walls.

Note that the normal and tangential vectors $\mathbf{n}_\Gamma^\varepsilon$, $\mathbf{t}_\Gamma^\varepsilon$, \mathbf{n}_w^ε and \mathbf{t}_w^ε depend on γ^ε and w^ε , respectively, such that these can be expanded, e.g.

$$\begin{aligned} \mathbf{n}_w^\varepsilon &= \begin{pmatrix} 0 \\ 1 \end{pmatrix} - \varepsilon \begin{pmatrix} \partial_{x_1} w^0 \\ 0 \end{pmatrix} + \mathcal{O}(\varepsilon^2), \\ \mathbf{n}_\Gamma^\varepsilon &= \begin{cases} \begin{pmatrix} 0 \\ -\text{sign}(\partial_s \gamma_1^0) \end{pmatrix} + \varepsilon \frac{1}{|\partial_s \gamma_1^0|} \begin{pmatrix} \partial_s \gamma_2^0 \\ -\partial_s \gamma_1^1 \end{pmatrix} + \mathcal{O}(\varepsilon^2) & \text{for } \partial_s \gamma_1^0 \neq 0, \\ \frac{1}{\sqrt{(\partial_s \gamma_1^1)^2 + (\partial_s \gamma_2^0)^2}} \begin{pmatrix} \partial_s \gamma_2^0 \\ -\partial_s \gamma_1^1 \end{pmatrix} + \varepsilon \frac{1}{\sqrt{(\partial_s \gamma_1^1)^2 + (\partial_s \gamma_2^0)^2}} \begin{pmatrix} \partial_s \gamma_2^1 \\ -\partial_s \gamma_1^2 \end{pmatrix} \\ \quad + \varepsilon \frac{\partial_s \gamma_1^1 \partial_s \gamma_2^1 + \partial_s \gamma_2^0 \partial_s \gamma_1^2}{((\partial_s \gamma_1^1)^2 + (\partial_s \gamma_2^0)^2)^{3/2}} \begin{pmatrix} -\partial_s \gamma_2^0 \\ \partial_s \gamma_1^1 \end{pmatrix} + \mathcal{O}(\varepsilon^2) & \text{otherwise.} \end{cases} \end{aligned} \quad (2.25)$$

In particular, the direction of the normal vector $\mathbf{n}_\Gamma^\varepsilon$ depends on $\partial_s \gamma_1^0$. If $\partial_s \gamma_1^0 \neq 0$ for

some $s \in [0, 1]$, the interface $\Gamma^\varepsilon(t)$ is largely deformed over a region that has a width $\mathcal{O}(\varepsilon^0)$, namely $I = [\min_{s \in [0, 1]} \gamma_1^\varepsilon, \max_{s \in [0, 1]} \gamma_1^\varepsilon]$ with $|I| = \mathcal{O}(\varepsilon^0)$. Therefore, there are both fluids present along a transversal segment at any $x_1 \in I$, and complicated interface dynamics occur in the limit $\varepsilon \rightarrow 0$. On the other hand, if $\partial_s \gamma_1^0 \equiv 0$, only small deformations with $|I| = \mathcal{O}(\varepsilon)$ are possible, and we obtain asymptotically a sharp transition from fluid I to fluid II at γ_1^0 .

2.4.1. Flow in the bulk domains

First, we consider the flow in the bulk domains $\Omega_\alpha^\varepsilon$, $\alpha \in \{I, II\}$, and solve the resulting equations away from the interface. Inserting the homogenization ansatz into (2.13)–(2.20) using (A1)–(A6) and a Taylor expansion around $x_2 = w^0(x_1)$ for (2.20), one obtains

$$\mathcal{O}(\varepsilon) = \partial_{x_1} p_I^0 - \partial_{x_2}^2 u_{I,1}^0 \quad \text{in } \Omega_I^\varepsilon(t), \quad (2.26)$$

$$\mathcal{O}(\varepsilon) = \partial_{x_2} p_I^0 \quad \text{in } \Omega_I^\varepsilon(t), \quad (2.27)$$

$$\mathcal{O}(\varepsilon) = \partial_{x_1} p_{II}^0 - \mathbf{M} \partial_{x_2}^2 u_{II,1}^0 \quad \text{in } \Omega_{II}^\varepsilon(t), \quad (2.28)$$

$$\mathcal{O}(\varepsilon) = \partial_{x_2} p_{II}^0 \quad \text{in } \Omega_{II}^\varepsilon(t), \quad (2.29)$$

$$\mathcal{O}(\varepsilon^2) = \partial_{x_2} u_{\alpha,2}^0 + \varepsilon (\partial_{x_1} u_{\alpha,1}^0 + \partial_{x_2} u_{\alpha,2}^1) \quad \text{in } \Omega_\alpha^\varepsilon(t), \quad (2.30)$$

$$\mathcal{O}(\varepsilon^2) = u_{\alpha,2}^0 + \varepsilon u_{\alpha,2}^1, \quad \mathcal{O}(\varepsilon) = \partial_{x_2} u_{\alpha,1}^0 \quad \text{at } x_2 = 0, \quad (2.31)$$

$$\mathcal{O}(\varepsilon) = \partial_{x_2} p_\alpha^0 \quad \text{at } x_2 = 0, \quad (2.32)$$

$$\mathcal{O}(\varepsilon) = p_I^0 - p_{\text{in}}^0, \quad \mathcal{O}(\varepsilon^2) = u_{I,2}^0 + \varepsilon u_{I,2}^1 \quad \text{or} \quad (2.33)$$

$$\mathcal{O}(\varepsilon^2) = \mathbf{u}_I^0 - \mathbf{u}_{\text{in}}^0 + \varepsilon (\mathbf{u}_I^1 - \mathbf{u}_{\text{in}}^1) \quad \text{at } x_1 = 0, \quad (2.34)$$

$$\mathcal{O}(\varepsilon) = p_{II}^0, \quad \mathcal{O}(\varepsilon^2) = u_{II,2}^0 + \varepsilon u_{II,2}^1 \quad \text{at } x_1 = 1, \quad (2.35)$$

$$\mathcal{O}(\varepsilon) = u_{\alpha,1}^0 + \lambda^0 \partial_{x_2} u_{\alpha,1}^0 \quad \text{at } x_2 = w^0(x_1), \quad (2.36)$$

$$\mathcal{O}(\varepsilon^2) = u_{\alpha,2}^0 + \varepsilon (u_{\alpha,2}^1 + w^1 \partial_{x_2} u_{\alpha,2}^0 - u_{\alpha,1}^0 \partial_{x_1} w^0) \quad \text{at } x_2 = w^0(x_1). \quad (2.37)$$

Note that either (2.33) or (2.34) holds, depending on the choice of the boundary condition at the inlet $\Gamma_{\text{in}}^\varepsilon$.

Since we are interested in the flow behavior away from the interface $\Gamma^\varepsilon(t)$, we define

$$G_I(t) := \min_{s \in [0, 1]} \gamma_1^0(s, t), \quad G_{II}(t) := \max_{s \in [0, 1]} \gamma_1^0(s, t),$$

and investigate the problem for $x_1 < G_I(t)$ in fluid I and for $x_1 > G_{II}(t)$ in fluid II, respectively. In leading order, one obtains $\partial_{x_2} u_{\alpha,2}^0 = 0$ in $\Omega_\alpha^\varepsilon(t)$ for both $\alpha \in \{I, II\}$ by the mass conservation (2.30). The symmetry and wall boundary conditions (2.31) and (2.37) lead to

$$u_{\alpha,2}^0 = 0 \quad \text{for } m = I, x_1 < G_I(t), \text{ and for } m = II, x_1 > G_{II}(t),$$

which agrees with the in- and outflow boundary conditions (2.33)–(2.35). The second component of the momentum balance of fluid I (2.27) yields in leading order $\partial_{x_2} p_I^0 = 0$ in $\Omega_I^\varepsilon(t)$, which is in agreement with the symmetry condition (2.32). We conclude

$$p_I^0 = p_I^0(t, x_1) \quad \text{for } x_1 < G_I(t).$$

Analogously, the second component of the momentum balance of fluid II (2.29) leads to $\partial_{x_2} p_{II}^0 = 0$ in $\Omega_{II}^\varepsilon(t)$ (in agreement with the symmetry condition (2.32)), and thus

$$p_{II}^0 = p_{II}^0(t, x_1) \quad \text{for } x_1 > G_{II}(t).$$

From the first component of the momentum balance of fluid I (2.26) one obtains

$$\partial_{x_1} p_I^0 = \partial_{x_2}^2 u_{I,1}^0 \quad \text{in } \Omega_I^\varepsilon(t).$$

Integrating twice over x_2 using the symmetry and wall boundary conditions (2.31) and (2.36), this leads to

$$u_{I,1}^0(t, \mathbf{x}) = \frac{x_2^2 - w^0(x_1)(w^0(x_1) + 2\lambda^0)}{2} \partial_{x_1} p_I^0(t, x_1) \quad \text{for } x_1 < G_I(t). \quad (2.38)$$

In a similar fashion, one obtains for fluid II by (2.28), (2.31), and (2.36)

$$u_{II,1}^0(t, \mathbf{x}) = \frac{x_2^2 - w^0(x_1)(w^0(x_1) + 2\lambda^0)}{2M} \partial_{x_1} p_{II}^0(t, x_1) \quad \text{for } x_1 > G_{II}(t). \quad (2.39)$$

Integrating (2.38) and (2.39) over $x_2 \in [0, w^0(x_1)]$ for any $x_1 < G_I$ and $x_1 > G_{II}$, respectively, and using Remark 2.2 yields

$$\begin{aligned} q(t) &= \int_0^{w^0(a)} u_{I,1}^0(t, \mathbf{x})|_{x_1=a} dx_2 = -\frac{(w^0(x_1))^2(w^0(x_1) + 3\lambda^0)}{3} \partial_{x_1} p_I^0(t, x_1), \\ q(t) &= \int_0^{w^0(a)} u_{II,1}^0(t, \mathbf{x})|_{x_1=a} dx_2 = -\frac{(w^0(x_1))^2(w^0(x_1) + 3\lambda^0)}{3M} \partial_{x_1} p_{II}^0(t, x_1), \end{aligned}$$

where $q(t) := \int_0^1 u_{I,1}^0(t, \mathbf{x}) dx_2$. Note that q is independent of x_1 , and it is equivalent to the one in (A6) if (2.34) is given. Otherwise, q is unknown and must be found in the further solution process. Solving the above equations for p_α^0 , with the outflow boundary condition (2.35) we obtain

$$p_I^0(t, \mathbf{x}) = p_{in}^0(t) - q(t) \int_0^{x_1} \frac{3}{(w^0(\xi))^2(w^0(\xi) + 3\lambda^0)} d\xi \quad \text{for } x_1 < G_I(t), \quad (2.40)$$

$$p_{II}^0(t, \mathbf{x}) = q(t) \int_{x_1}^1 \frac{3M}{(w^0(\xi))^2(w^0(\xi) + 3\lambda^0)} d\xi \quad \text{for } x_1 > G_{II}(t). \quad (2.41)$$

Here, the inlet pressure $p_{in}^0(t)$ is either given by the inlet boundary condition (2.33),

or has to be found in the further solution process. Note that since the inlet boundary condition is either (2.33) or (2.34), this means that either q or p_{in}^0 is given, while the other still must be determined. Inserting (2.40) and (2.41) into (2.38) and (2.39) yields

$$u_{\text{I},1}^0(t, \mathbf{x}) = 3q(t) \frac{w^0(x_1)(w^0(x_1) + 2\lambda^0) - x_2^2}{2(w^0(x_1))^2(w^0(x_1) + 3\lambda^0)} \quad \text{for } x_1 < G_{\text{I}}(t), \quad (2.42)$$

$$u_{\text{II},1}^0(t, \mathbf{x}) = 3q(t) \frac{w^0(x_1)(w^0(x_1) + 2\lambda^0) - x_2^2}{2(w^0(x_1))^2(w^0(x_1) + 3\lambda^0)} \quad \text{for } x_1 > G_{\text{II}}(t). \quad (2.43)$$

Using (2.42) and (2.43) in the mass conservation (2.30), the first order equations become

$$\partial_{x_2} u_{\alpha,2}^1 = q(t) \left(\frac{1}{2(w^0(x_1) + 3\lambda^0)^2} + \frac{1}{(w^0(x_1))^2} - \frac{9(w^0(x_1) + 2\lambda^0)x_2^2}{2(w^0(x_1))^3(w^0(x_1) + 3\lambda^0)^2} \right) \partial_{x_1} w^0(x_1),$$

for $\alpha \in \{\text{I}, \text{II}\}$. Integration over x_2 using the symmetry condition (2.31) yields

$$u_{\text{I},2}^1(t, \mathbf{x}) = q(t) \left(\frac{x_2}{2(w^0(x_1) + 3\lambda^0)^2} + \frac{x_2}{(w^0(x_1))^2} - \frac{3(w^0(x_1) + 2\lambda^0)x_2^3}{2(w^0(x_1))^3(w^0(x_1) + 3\lambda^0)^2} \right) \partial_{x_1} w^0(x_1) \quad \text{for } x_1 < G_{\text{I}}(t),$$

$$u_{\text{II},2}^1(t, \mathbf{x}) = q(t) \left(\frac{x_2}{2(w^0(x_1) + 3\lambda^0)^2} + \frac{x_2}{(w^0(x_1))^2} - \frac{3(w^0(x_1) + 2\lambda^0)x_2^3}{2(w^0(x_1))^3(w^0(x_1) + 3\lambda^0)^2} \right) \partial_{x_1} w^0(x_1) \quad \text{for } x_1 > G_{\text{II}}(t),$$

which is in agreement with the boundary conditions (2.33)–(2.35) and (2.37).

Summarizing, we obtain the following solution in the bulk domains. There holds

$$\mathbf{u}_{\text{I}}^\varepsilon(t, \mathbf{x}) = q(t) \cdot \left(\begin{aligned} &3 \frac{w^0(x_1)(w^0(x_1) + 2\lambda^0) - x_2^2}{2(w^0(x_1))^2(w^0(x_1) + 3\lambda^0)} + \mathcal{O}(\varepsilon) \\ &\varepsilon \left(\frac{x_2}{2(w^0(x_1) + 3\lambda^0)^2} + \frac{x_2}{(w^0(x_1))^2} - \frac{3(w^0(x_1) + 2\lambda^0)x_2^3}{2(w^0(x_1))^3(w^0(x_1) + 3\lambda^0)^2} \right) \partial_{x_1} w^0(x_1) + \mathcal{O}(\varepsilon^2) \end{aligned} \right), \quad (2.44)$$

$$p_{\text{I}}^\varepsilon(t, \mathbf{x}) = p_{\text{in}}^0(t) - q(t) \int_0^{x_1} \frac{3}{(w^0(\xi))^2(w^0(\xi) + 3\lambda^0)} d\xi + \mathcal{O}(\varepsilon), \quad (2.45)$$

for $x_1 < G_I(t)$, while for $x_1 > G_{II}(t)$ one gets

$$\mathbf{u}_{II}^\varepsilon(t, \mathbf{x}) = q(t) \cdot \left(\begin{array}{c} 3 \frac{w^0(x_1)(w^0(x_1)+2\lambda^0)-x_2^2}{2(w^0(x_1))^2(w^0(x_1)+3\lambda^0)} + \mathcal{O}(\varepsilon) \\ \varepsilon \left(\frac{x_2}{2(w^0(x_1)+3\lambda^0)^2} + \frac{x_2}{(w^0(x_1))^2} - \frac{3(w^0(x_1)+2\lambda^0)x_2^3}{2(w^0(x_1))^3(w^0(x_1)+3\lambda^0)^2} \right) \partial_{x_1} w^0(x_1) + \mathcal{O}(\varepsilon^2) \end{array} \right), \quad (2.46)$$

$$p_{II}^\varepsilon(t, \mathbf{x}) = q(t) \int_{x_1}^1 \frac{3M}{(w^0(\xi))^2(w^0(\xi) + 3\lambda^0)} d\xi + \mathcal{O}(\varepsilon). \quad (2.47)$$

This means that the solution in the bulk domains is of Hagen–Poiseuille type. Depending on the chosen inlet boundary condition (2.33) or (2.34), either the inlet pressure p_{in}^0 or the total flux q is given. The other coefficient will be determined in the following subsection via the coupling at the interface $\Gamma^\varepsilon(t)$. For upscaled models, we emphasize that the total flux q is independent of the position x_1 and that the pressures p_α^0 , $\alpha \in \{I, II\}$, depend linearly on q with a coefficient that only depends on the geometry (w^0), the viscosity ratio M and the slip length λ^0 .

2.4.2. Interface with small deformations

We continue the analysis for the interface region around $\Gamma^\varepsilon(t)$. We first show that the bulk solutions are not compatible with the interface conditions (2.21)–(2.24). However, introduction of a suitable scaling allows to find the asymptotic solution in the boundary layer around the interface $\Gamma^\varepsilon(t)$, which connects the bulk domain solutions. Additionally to (A1)–(A6), we make the following assumptions.

(A7) The leading order interface position in x_1 is constant, i.e., $\partial_s \gamma_1^0 \equiv 0$.

(A8) The capillary number is given by $Ca = \varepsilon^\beta \bar{Ca}$ for some $\beta \in \mathbb{N}_0$. Here, \bar{Ca} denotes the effective capillary number and is independent of ε .

Note that (A7) means that the fluid-fluid interface Γ^ε has only small deformations, such that $G_I(t) = \gamma_1^0(t) = G_{II}(t)$. Furthermore, (A8) is used to distinguish whether interfacial tension is relevant or even dominating the interface movement, see also Remark 2.3. In the alternative case of a largely deformed interface ($\partial_s \gamma_1^0 \neq 0$), both fluids are present along a transversal segment since the interface is partly horizontal, see also (2.25). This leads to complicated interface dynamics and requires a detailed analysis of further boundary layers due to the symmetry and boundary conditions (2.23) and (2.24), which yield $\partial_s \gamma_1^0(t, s) = 0$ for $s \in \{0, 1\}$. However, this lies outside the scope of this manuscript.

Inserting the homogenization ansatz into the kinematic interface condition (2.21) gives

$$(\partial_t \gamma_1^0 - u_{I,1}^0) \partial_s \gamma_2^0 + u_{I,2}^0 \partial_s \gamma_1^1 = \mathcal{O}(\varepsilon).$$

Since γ_1^0 is constant in the parameter s , a non-singular parameterization requires $\partial_s \gamma_2^0 > 0$. Inserting the bulk solution (2.44), where $u_{1,2}^0 = 0$, yields in leading order

$$\partial_t \gamma_1^0 = 3q \frac{w^0(\gamma_1^0)(w^0(\gamma_1^0) + 2\lambda^0) - (\gamma_2^0)^2}{2(w^0(\gamma_1^0))^2(w^0(\gamma_1^0) + 3\lambda^0)},$$

which contradicts the assumption that γ_1^0 does not depend on s , except for the trivial case $q(t) = 0$. Therefore, we expect the existence of a boundary layer around the interface $\Gamma^\varepsilon(t)$. Here, the idea of the matched asymptotic expansion method is to find an asymptotic solution of the problem in rescaled, so-called inner coordinates close to the interface (the boundary layer). This solution must satisfy the interface conditions and match the previously derived, so-called outer solution (2.44)–(2.47) in the bulk regions. The combination of inner and outer solutions then solves the problem in the whole domain. For a detailed introduction to matched asymptotic expansion method we refer to [317].

To resolve the boundary layer, we apply the inner scaling

$$X_1(t, x_1) := (x_1 - \gamma_1^0(t))/\varepsilon, \quad X_2 := x_2$$

and use the rescaled variables and domains (see also Table 2.1)

$$\begin{aligned} \mathbf{Y}^\varepsilon &:= \left(\frac{\gamma_1^\varepsilon - \gamma_1^0}{\gamma_2^\varepsilon} \right), \quad U_\alpha^\varepsilon(t, \mathbf{X}) := \mathbf{u}_\alpha^\varepsilon(t, \mathbf{x}), \quad P_\alpha^\varepsilon(t, \mathbf{X}) := p_\alpha^\varepsilon(t, \mathbf{x}), \\ \Omega_{\mathbf{X}}^\varepsilon(t) &:= \{\mathbf{X} \in \mathbb{R}^2 \mid 0 < X_2 < w^\varepsilon(\gamma_1^0(t) + \varepsilon X_1)\}, \quad \Gamma_{\mathbf{X}}^\varepsilon(t) := \{\mathbf{Y}^\varepsilon(t, s) \mid s \in [0, 1]\}, \\ \Omega_{\mathbf{X}, \text{I}}^\varepsilon(t) &:= \{\mathbf{X}(t, \mathbf{x}) \mid \mathbf{x} \in \Omega_{\text{I}}^\varepsilon\}, \quad \Omega_{\mathbf{X}, \text{II}}^\varepsilon(t) := \{\mathbf{X}(t, \mathbf{x}) \mid \mathbf{x} \in \Omega_{\text{II}}^\varepsilon\}, \\ \Gamma_{\mathbf{X}, \text{w}, \alpha}^\varepsilon(t) &:= \{\mathbf{X} \in \partial\Omega_{\mathbf{X}, \alpha}^\varepsilon(t) \mid X_2 = w^\varepsilon(\gamma_1^0(t) + \varepsilon X_1)\}. \end{aligned}$$

The matching conditions between inner expansion in terms of \mathbf{X} and outer expansion in terms of \mathbf{x} require the equivalence in the limit, i.e., for any outer quantity $a_\alpha^\varepsilon(t, \mathbf{x})$ with inner expansion $A_\alpha^\varepsilon(t, \mathbf{X})$ there must hold

$$\lim_{x_1 \rightarrow \gamma_1^0} a_\alpha^\varepsilon(t, \mathbf{x}) = \lim_{X_1 \rightarrow (-1)^\alpha \infty} A_\alpha^\varepsilon(t, \mathbf{X})|_{X_2=x_2}.$$

With the rescaled coordinates, (2.13)–(2.17) and (2.20)–(2.24) become

$$\varepsilon^2 \text{Re}(\varepsilon \partial_t U_{\text{I}}^\varepsilon - \partial_{X_1} U_{\text{I}}^\varepsilon \partial_t \gamma_1^0 + (U_{\text{I}}^\varepsilon \cdot \nabla_{\mathbf{X}}) U_{\text{I}}^\varepsilon) + \nabla_{\mathbf{X}} P_{\text{I}}^\varepsilon = \varepsilon \Delta_{\mathbf{X}} U_{\text{I}}^\varepsilon \quad \text{in } \Omega_{\mathbf{X}, \text{I}}^\varepsilon(t), \quad (2.48)$$

$$\varepsilon^2 \text{RRe}(\varepsilon \partial_t U_{\text{II}}^\varepsilon - \partial_{X_1} U_{\text{II}}^\varepsilon \partial_t \gamma_1^0 + (U_{\text{II}}^\varepsilon \cdot \nabla_{\mathbf{X}}) U_{\text{II}}^\varepsilon) + \nabla_{\mathbf{X}} P_{\text{II}}^\varepsilon = M \varepsilon \Delta_{\mathbf{X}} U_{\text{II}}^\varepsilon \quad \text{in } \Omega_{\mathbf{X}, \text{II}}^\varepsilon(t), \quad (2.49)$$

$$\nabla_{\mathbf{X}} \cdot U_\alpha^\varepsilon = 0 \quad \text{in } \Omega_{\mathbf{X}, \alpha}^\varepsilon(t), \quad (2.50)$$

$$U_\alpha^\varepsilon \cdot \mathbf{n}_{\text{sym}} = 0, \quad t_{\text{sym}} \cdot \nabla_{\mathbf{X}} U_\alpha^\varepsilon \mathbf{n}_{\text{sym}} = 0 \quad \text{at } X_2 = 0, \quad (2.51)$$

$$\nabla_{\mathbf{X}} P_\alpha^\varepsilon \cdot \mathbf{n}_{\text{sym}} = 0, \quad \text{at } X_2 = 0, \quad (2.52)$$

$$\mathbf{T}_{\text{w}}^\varepsilon \cdot (U_\alpha^\varepsilon + 2\lambda^\varepsilon \mathbf{D}_{\mathbf{X}}(U_\alpha^\varepsilon) \mathbf{N}_{\text{w}}^\varepsilon) = 0, \quad U_\alpha^\varepsilon \cdot \mathbf{N}_{\text{w}}^\varepsilon = 0 \quad \text{on } \Gamma_{\mathbf{X}, \text{w}, \alpha}^\varepsilon(t), \quad (2.53)$$

$$\partial_t \gamma_1^0 N_{\Gamma,1}^\varepsilon + \varepsilon \partial_t \mathbf{Y}^\varepsilon \cdot \mathbf{N}_\Gamma^\varepsilon = \mathbf{U}_I^\varepsilon \cdot \mathbf{N}_\Gamma^\varepsilon, \quad \mathbf{U}_I^\varepsilon = \mathbf{U}_\Pi^\varepsilon \quad \text{on } \Gamma_\mathbf{x}^\varepsilon(t), \quad (2.54)$$

$$-(P_I^\varepsilon - P_\Pi^\varepsilon) \mathbf{N}_\Gamma^\varepsilon + 2\varepsilon (\mathbf{D}_\mathbf{x}(\mathbf{U}_I^\varepsilon) - \mathbf{M} \mathbf{D}_\mathbf{x}(\mathbf{U}_\Pi^\varepsilon)) \mathbf{N}_\Gamma^\varepsilon = \frac{\varepsilon}{\text{Ca}} K^\varepsilon \mathbf{N}_\Gamma^\varepsilon \quad \text{on } \Gamma_\mathbf{x}^\varepsilon(t), \quad (2.55)$$

$$\mathbf{N}_\Gamma^\varepsilon \cdot \mathbf{n}_{\text{sym}} = 0 \quad \text{at } s = 0, \quad (2.56)$$

$$\cos(\theta^\varepsilon(-\partial_t(\gamma_1^0 T_{w,1}^\varepsilon + \varepsilon \mathbf{Y}^\varepsilon \cdot \mathbf{T}_w^\varepsilon)|_{X_1=Y_1^\varepsilon})) = \mathbf{T}_\Gamma^\varepsilon \cdot \mathbf{T}_w^\varepsilon|_{X_1=Y_1^\varepsilon} \quad \text{at } s = 1. \quad (2.57)$$

The transformed normal and tangential vectors are given by

$$\begin{aligned} \mathbf{T}_w^\varepsilon &= \mathbf{t}_w^\varepsilon|_{x_1=\gamma_1^0+\varepsilon X_1}, & \mathbf{N}_w^\varepsilon &= \mathbf{n}_w^\varepsilon|_{x_1=\gamma_1^0+\varepsilon X_1}, \\ \mathbf{T}_\Gamma^\varepsilon &= \frac{1}{\sqrt{(\partial_s Y_1^\varepsilon)^2 + (\partial_s Y_2^\varepsilon)^2}} \partial_s \mathbf{Y}^\varepsilon, & \mathbf{N}_\Gamma^\varepsilon &= \frac{1}{\sqrt{(\partial_s Y_1^\varepsilon)^2 + (\partial_s Y_2^\varepsilon)^2}} \begin{pmatrix} \partial_s Y_2^\varepsilon \\ -\partial_s Y_1^\varepsilon \end{pmatrix}, \end{aligned}$$

and the rescaled curvature K^ε is

$$K^\varepsilon = \frac{\partial_s Y_1^\varepsilon \partial_s^2 Y_2^\varepsilon - \partial_s Y_2^\varepsilon \partial_s^2 Y_1^\varepsilon}{((\partial_s Y_1^\varepsilon)^2 + (\partial_s Y_2^\varepsilon)^2)^{3/2}}.$$

Inserting the homogenization ansatz into (2.48)–(2.57) using (A1)–(A5), (A7), (A8) and a Taylor expansion around $X_2 = w^0(\gamma_1^0(t))$ for (2.53), one obtains

$$\mathcal{O}(\varepsilon^2) = \nabla_\mathbf{x} P_I^0 + \varepsilon (\nabla_\mathbf{x} P_I^1 - \Delta_\mathbf{x} \mathbf{U}_I^0) \quad \text{in } \Omega_{\mathbf{x},I}^\varepsilon(t), \quad (2.58)$$

$$\mathcal{O}(\varepsilon^2) = \nabla_\mathbf{x} P_\Pi^0 + \varepsilon (\nabla_\mathbf{x} P_\Pi^1 - \mathbf{M} \Delta_\mathbf{x} \mathbf{U}_\Pi^0) \quad \text{in } \Omega_{\mathbf{x},\Pi}^\varepsilon(t), \quad (2.59)$$

$$\mathcal{O}(\varepsilon) = \nabla_\mathbf{x} \cdot \mathbf{U}_\alpha^0 \quad \text{in } \Omega_{\mathbf{x},\alpha}^\varepsilon(t), \quad (2.60)$$

$$\mathcal{O}(\varepsilon) = U_{\alpha,2}^0, \quad \mathcal{O}(\varepsilon) = \partial_{X_2} U_{\alpha,1}^0 \quad \text{at } X_2 = 0, \quad (2.61)$$

$$\mathcal{O}(\varepsilon^2) = \partial_{X_2} P_\alpha^0 + \varepsilon \partial_{X_2} P_\alpha^1 \quad \text{at } X_2 = 0, \quad (2.62)$$

$$\mathcal{O}(\varepsilon) = U_{\alpha,1}^0 + (\lambda^0 + \lambda_e \exp(-|X_1|)) \quad (2.63)$$

$$\begin{aligned} &\cdot (\partial_{X_2} U_{\alpha,1}^0 + \partial_{X_1} U_{\alpha,2}^0) \quad \text{at } X_2 = w^0(\gamma_1^0(t)), \\ \mathcal{O}(\varepsilon) &= U_{\alpha,2}^0 \quad \text{at } X_2 = w^0(\gamma_1^0(t)), \end{aligned} \quad (2.64)$$

$$\mathcal{O}(\varepsilon) = (\partial_t \gamma_1^0 - U_{1,1}^0) \partial_s Y_2^0 + U_{1,2}^0 \partial_s Y_1^0 \quad \text{on } \Gamma_\mathbf{x}^\varepsilon(t), \quad (2.65)$$

$$\mathcal{O}(\varepsilon) = \mathbf{U}_I^0 - \mathbf{U}_\Pi^0 \quad \text{on } \Gamma_\mathbf{x}^\varepsilon(t), \quad (2.66)$$

$$\mathcal{O}(\varepsilon^{\min(1,2-\beta)}) = (P_I^0 - P_\Pi^0) + \frac{\varepsilon^{1-\beta}}{\text{Ca}} \frac{\partial_s Y_1^0 \partial_s^2 Y_2^0 - \partial_s Y_2^0 \partial_s^2 Y_1^0}{((\partial_s Y_1^0)^2 + (\partial_s Y_2^0)^2)^{3/2}} \quad \text{on } \Gamma_\mathbf{x}^\varepsilon(t), \quad (2.67)$$

$$\mathcal{O}(\varepsilon) = \partial_s \mathbf{Y}^0 \cdot (\mathbf{D}_\mathbf{x}(\mathbf{U}_I^0) - \mathbf{M} \mathbf{D}_\mathbf{x}(\mathbf{U}_\Pi^0)) \begin{pmatrix} \partial_s Y_2^0 \\ -\partial_s Y_1^0 \end{pmatrix} \quad \text{on } \Gamma_\mathbf{x}^\varepsilon(t), \quad (2.68)$$

$$\mathcal{O}(\varepsilon) = \partial_s Y_1^0 \quad \text{at } s = 0, \quad (2.69)$$

$$\mathcal{O}(\varepsilon) = \frac{\partial_s Y_1^0}{\sqrt{(\partial_s Y_1^0)^2 + (\partial_s Y_2^0)^2}} + \cos(\theta^0(\partial_t \gamma_1^0)) \quad \text{at } s = 1. \quad (2.70)$$

The leading order terms in the momentum equations (2.58) and (2.59) yield $\nabla_\mathbf{x} P_\alpha^0 = \mathbf{0}$ in $\Omega_{\mathbf{x},\alpha}^\varepsilon(t)$ for $\alpha \in \{I, \Pi\}$. This is in agreement with the symmetry condi-

tion (2.62). By matching with the outer solution we obtain

$$P_\alpha^0(t, \mathbf{X}) = p_\alpha^0(t, \gamma_1^0(t)) \quad \text{for all } \mathbf{X} \in \Omega_{\mathbf{x}, \alpha}^\varepsilon(t). \quad (2.71)$$

Remark 2.3. Recall that we assume $\text{Ca} = \varepsilon^\beta \overline{\text{Ca}}$ for some $\beta \in \mathbb{N}_0$. Considering (2.67), one must distinguish the cases $\beta < 1$, $\beta = 1$ and $\beta > 1$. For $\beta < 1$, the interface tension force is negligible in leading order, such that the pressures P_I^0 and P_{II}^0 are equal. Formally, this allows to determine the leading order solution of the outer bulk-flow problem. However, this also means that the interface $\Gamma_{\mathbf{x}}^\varepsilon(t)$ is not stabilized by surface tension, but part of the first order solution, such that we cannot guarantee solvability. Furthermore, one might expect the occurrence of topological changes due to e.g. formation of bubbles, thin films, etc. which are not part of this model. In the case $\beta > 1$, the interfacial tension force is dominating (2.67), so that the leading order curvature K^0 of the interface is zero. Due to the boundary conditions (2.69) and (2.70), this can only happen if the leading order contact angle $\theta^0(\partial_t \gamma_1^0)$ is $\pi/2$ for any $\gamma_1^0(t)$, i.e., for a constant contact-angle model for perfectly mixed-wet materials. Even worse, due to (2.71), the leading order solution of the outer bulk-flow problem then depends on the first order solution, such that we cannot assure the solvability in this case either. We therefore consider in what follows only the case $\beta = 1$. Then the pressure difference is balanced by the surface tension force in (2.67). This leads to a solution for the outer bulk-flow problem as well as for the interface shape.

In the regime $\beta = 1$, plugging the constant pressures (2.71) into the interfacial force balance (2.67) yields a constant leading-order curvature K^0 given by

$$K^0 = \frac{\partial_s Y_2^0 \partial_s^2 Y_1^0 - \partial_s Y_1^0 \partial_s^2 Y_2^0}{((\partial_s Y_1^0)^2 + (\partial_s Y_2^0)^2)^{3/2}} = \overline{\text{Ca}}(p_{II}^0 - p_I^0)|_{x_1=\gamma_1^0}. \quad (2.72)$$

Therefore, the interface is a circular arc. By the contact-angle condition (2.70), one obtains

$$K^0 = -\frac{\cos(\theta^0(\partial_t \gamma_1^0))}{w^0(\gamma_1^0)}. \quad (2.73)$$

Combining (2.72) and (2.73) and plugging in the bulk pressure solutions (2.45) and (2.47) leads to

$$\begin{aligned} p_{\text{in}}^0 - q & \left(\int_0^{\gamma_1^0} \frac{3}{(w^0(x_1))^2 (w^0(x_1) + 3\lambda^0)} dx_1 + \int_{\gamma_1^0}^1 \frac{3M}{(w^0(x_1))^2 (w^0(x_1) + 3\lambda^0)} dx_1 \right) \\ & = \frac{\cos(\theta^0(\partial_t \gamma_1^0))}{\overline{\text{Ca}} w^0(\gamma_1^0)}. \end{aligned} \quad (2.74)$$

Due to the constant curvature (2.73) and the symmetry condition (2.69), the leading order interface $\Gamma_{\mathbf{x}}^0(t) := \{\mathbf{Y}^0(t, s) | s \in [0, 1]\}$ is given (up to a reparametriza-

tion) by

$$\mathbf{Y}^0(t, s) = \begin{cases} \frac{w^0(\gamma_1^0)}{\cos(\theta^0(\partial_t \gamma_1^0))} \begin{pmatrix} \cos((\frac{\pi}{2} - \theta^0(\partial_t \gamma_1^0))s) - \sin(\theta^0(\partial_t \gamma_1^0)) \\ \sin((\frac{\pi}{2} - \theta^0(\partial_t \gamma_1^0))s) \end{pmatrix} & \text{for } \theta^0 \neq \pi/2, \\ w^0(\gamma_1^0(t)) \begin{pmatrix} 0 \\ s \end{pmatrix} & \text{for } \theta^0 = \pi/2. \end{cases}$$

Analogously to [Remark 2.2](#), by the mass conservation [\(2.15\)](#), the interface velocity [\(2.54\)](#) and the outer velocity solution [\(2.44\)](#), we obtain

$$\begin{aligned} 0 &= \int_{\Omega_1^\varepsilon} \nabla^\varepsilon \cdot \mathbf{u}_1^\varepsilon d\mathbf{x} = \int_{\Gamma^\varepsilon} \mathbf{u}_1^\varepsilon \cdot \mathbf{n}_{\Gamma^\varepsilon} dl - \int_0^1 u_{1,1}^\varepsilon|_{x_1=0} dx_1 \\ &= \int_{\Gamma^\varepsilon} \partial_t \gamma_1^0 N_{\Gamma,1}^\varepsilon + \varepsilon \partial_t \mathbf{Y}^\varepsilon \cdot \mathbf{N}_\Gamma^\varepsilon dl - q + \mathcal{O}(\varepsilon) = \int_0^1 \partial_t \gamma_1^0 \partial_s Y_2^\varepsilon ds - q + \mathcal{O}(\varepsilon) \\ &= \partial_t \gamma_1^0 w^0(\gamma_1^0) - q + \mathcal{O}(\varepsilon). \end{aligned}$$

Therefore, the leading order position γ_1^0 of the interface fulfills

$$\partial_t \gamma_1^0(t) = \frac{q(t)}{w^0(\gamma_1^0(t))}. \quad (2.75)$$

To find the solution for \mathbf{u}_α^0 , p_α^0 ($\alpha \in \{\text{I}, \text{II}\}$), which is given by [\(2.44\)–\(2.47\)](#), one has to determine γ_1^0 , q and p_{in}^0 . The derivation depends on the chosen inlet boundary condition. For a given inlet velocity $\mathbf{u}_1^\varepsilon = \mathbf{u}_{\text{in}}^\varepsilon$ at $\Gamma_{\text{in}}^\varepsilon$, the value of q is known. Plugging q into [\(2.75\)](#) and solving for γ_1^0 yields

$$\gamma_1^0(t) = \mathcal{W}^{-1} \left(\mathcal{W}(\gamma_1^0|_{t=0}) + \int_0^t q(\tau) d\tau \right),$$

where $\mathcal{W}(\xi) := \int_0^\xi w^0(x_1) dx_1$. Note that $\mathcal{W}' = w^0 > 0$ by [\(A4\)](#), such that the inverse function \mathcal{W}^{-1} is well-defined. Finally, p_{in}^0 can be found by [\(2.74\)](#).

For a given inlet pressure $p_1^\varepsilon = p_{\text{in}}^\varepsilon$ at $\Gamma_{\text{in}}^\varepsilon$, the value of p_{in}^0 is known. Then, the differential algebraic system [\(2.74\)](#) and [\(2.75\)](#) has index 1 and can be solved for q and γ_1^0 . Inserting [\(2.75\)](#) into [\(2.74\)](#) and applying the implicit function theorem to find q depending on γ_1^0 , a sufficient condition for solvability is

$$\begin{aligned} &\sin \left(\theta^0 \left(\frac{q}{w^0(\gamma_1^0)} \right) \right) (\theta^0)' \left(\frac{q}{w^0(\gamma_1^0)} \right) \\ &\neq \overline{\text{Ca}}(w^0(\gamma_1^0))^2 \left(\int_0^{\gamma_1^0} \frac{3}{(w^0(x_1))^2 (w^0(x_1) + 3\lambda^0)} dx_1 + \int_{\gamma_1^0}^1 \frac{3\mathbf{M}}{(w^0(x_1))^2 (w^0(x_1) + 3\lambda^0)} dx_1 \right), \end{aligned}$$

where $(\theta^0)'$ denotes the derivative of θ^0 . Note that the righthand side is always positive, so that any contact-angle model which fulfills $(\theta^0)' \leq 0$ for $\theta^0 < \pi/2$ and $(\theta^0)' > 0$ for $\theta^0 < 0$ yields solvable differential algebraic equations.

Furthermore, from [\(2.58\)–\(2.66\)](#) and [\(2.68\)](#), the velocity close to the interface is

given by two coupled Stokes problems. More precisely, these problems are defined in the domains

$$\begin{aligned}\Omega_{\mathbf{x},\text{I}}^0(t) &= \{\mathbf{X} \in \mathbb{R} \times (0, w^0(\gamma_1^0(t))) \mid \exists s \in [0, 1] : X_1 < Y_1^0(t, s) \wedge X_2 = Y_2^0(t, s)\}, \\ \Omega_{\mathbf{x},\text{II}}^0(t) &= \{\mathbf{X} \in \mathbb{R} \times (0, w^0(\gamma_1^0(t))) \mid \exists s \in [0, 1] : X_1 > Y_1^0(t, s) \wedge X_2 = Y_2^0(t, s)\}.\end{aligned}$$

With this, the two problems are ($\alpha \in \{\text{I}, \text{II}\}$)

$$\begin{aligned}0 &= \nabla_{\mathbf{x}} P_{\text{I}}^1 - \Delta_{\mathbf{x}} U_{\text{I}}^0 && \text{in } \Omega_{\mathbf{x},\text{I}}^0(t), \\ 0 &= \nabla_{\mathbf{x}} P_{\text{II}}^1 - M \Delta_{\mathbf{x}} U_{\text{II}}^0 && \text{in } \Omega_{\mathbf{x},\text{II}}^0(t), \\ 0 &= \nabla_{\mathbf{x}} \cdot \mathbf{U}_{\alpha}^0 && \text{in } \Omega_{\mathbf{x},\alpha}^0(t), \\ 0 &= U_{\alpha,2}^0, \quad 0 = \partial_{X_2} U_{\alpha,1}^0, \quad 0 = \partial_{X_2} P_{\alpha}^1 && \text{at } X_2 = 0, \\ 0 &= U_{\alpha,1}^0 + (\lambda^0 + \lambda_e \exp(-|X_1|)) \partial_{X_2} U_{\alpha,1}^0, \quad 0 = U_{\alpha,2}^0 && \text{at } X_2 = w^0(\gamma_1^0(t)), \\ 0 &= (\partial_t \gamma_1^0 - U_{\text{I},1}^0) \partial_s Y_2^0 + U_{\text{I},2}^0 \partial_s Y_1^0 && \text{on } \Gamma_{\mathbf{x}}^0(t), \\ 0 &= U_{\text{I}}^0 - U_{\text{II}}^0 && \text{on } \Gamma_{\mathbf{x}}^0(t), \\ 0 &= \partial_s \mathbf{Y}^0 \cdot (\mathbf{D}_{\mathbf{x}}(U_{\text{I}}^0) - M \mathbf{D}_{\mathbf{x}}(U_{\text{II}}^0)) \begin{pmatrix} \partial_s Y_2^0 \\ -\partial_s Y_1^0 \end{pmatrix} && \text{on } \Gamma_{\mathbf{x}}^0(t), \\ 0 &= \lim_{X_1 \rightarrow -\infty} U_{\text{I}}^0 - \mathbf{u}_{\text{I}}^0|_{x_1=\gamma_1^0, x_2=X_2}, \\ 0 &= \lim_{X_1 \rightarrow \infty} U_{\text{II}}^0 - \mathbf{u}_{\text{II}}^0|_{x_1=\gamma_1^0, x_2=X_2}.\end{aligned}$$

2.4.3. Unsaturated flow limit

In (A2) we assumed the viscosity ratio $M = \mathcal{O}(\varepsilon^0)$. Here, we investigate the case when the viscosity of fluid II is much smaller than that of fluid I, like in a system consisting of water and air. Hence, we replace (A2) by:

(A9) The viscosity ratio satisfies $M \leq \mathcal{O}(\varepsilon)$.

Following the same steps as in the previous subsections, we obtain a model which only includes the flow of fluid I, while the flow of fluid II can be omitted. In other words, the upscaled model is an unsaturated flow in the thin strip. Furthermore, the effective solution for fluid I will coincide with the one obtained when letting $M \rightarrow 0$ in (2.44), (2.45), (2.74), and (2.75) derived previously.

To this end, we use the same asymptotic expansions and (A1), (A3)–(A8) and (A9) instead of (A2). For fluid I, we obtain again (2.26), (2.27), (2.30)–(2.32), (2.36), and (2.37) and work with either (2.33) or (2.34) as inlet condition. Therefore, the solution for fluid I is again (2.44) and (2.45), where p_{in}^0 and q are given by the interface region and the inlet condition.

For fluid II, the leading order momentum balance equations become

$$\mathcal{O}(\varepsilon) = \partial_{x_1} p_{\text{II}}^0, \quad \mathcal{O}(\varepsilon) = \partial_{x_2} p_{\text{II}}^0 \quad \text{in } \Omega_{\text{II}}^{\varepsilon}(t).$$

Together with the leading order outflow condition $\mathcal{O}(\varepsilon) = p_{\text{II}}^0$ at $x_1 = 1$, we conclude that $p_{\text{II}}^0(t, \mathbf{x}) = 0$ in $\Omega_{\text{II}}^\varepsilon(t)$. Rescaling the interface region as in [Section 2.4.2](#) and taking [\(A7\)](#) and [\(A8\)](#) into account, the leading order equations for fluid I are again [\(2.58\)](#) and [\(2.60\)–\(2.64\)](#). Since $p_{\text{II}}^0 \equiv 0$, the interface conditions are [\(2.63\)–\(2.65\)](#) and [\(2.69\)](#), as well as

$$\begin{aligned} \mathcal{O}(\varepsilon^{\min(1, 2-\beta)}) &= P_I^0 + \frac{\varepsilon^{1-\beta}}{\overline{\text{Ca}}} \frac{\partial_s Y_1^0 \partial_s^2 Y_2^0 - \partial_s Y_2^0 \partial_s^2 Y_1^0}{((\partial_s Y_1^0)^2 + (\partial_s Y_2^0)^2)^{3/2}} && \text{on } \Gamma_{\mathbf{x}}^\varepsilon(t), \\ \mathcal{O}(\varepsilon) &= \partial_s \mathbf{Y}^0 \cdot \mathbf{D}_{\mathbf{x}}(\mathbf{U}_I^0) \begin{pmatrix} \partial_s Y_2^0 \\ -\partial_s Y_1^0 \end{pmatrix} && \text{on } \Gamma_{\mathbf{x}}^\varepsilon(t). \end{aligned}$$

In the regime $\beta = 1$, this yields a constant leading-order curvature, implying

$$p_{\text{in}}^0 - q \int_0^{\gamma_1^0} \frac{3}{(w^0(x_1))^2 (w^0(x_1) + 3\lambda^0)} dx_1 = \frac{\cos(\theta^0(\partial_t \gamma_1^0))}{\overline{\text{Ca}} w^0(\gamma_1^0)}, \quad (2.76)$$

$$\partial_t \gamma_1^0(t) = \frac{q(t)}{w^0(\gamma_1^0(t))}. \quad (2.77)$$

2.4.4. Hysteretic contact-angle model

The previous analysis requires that the dynamic contact angle relation is continuous, as expressed in [\(A5\)](#). However, experiments suggest the occurrence of contact angle hysteresis, see e.g. the reviews [\[42, 265\]](#) discussing this as a result of surface wettability and roughness. This means that static contact angles are not unique, but can vary due to pinning. Here, we allow that the contact angle relation θ^ε involves a multi-valued graph if the velocity of the contact line is zero. To still obtain a well-defined contact-angle law, we reformulate the respective condition under the following assumption, which replaces [\(A5\)](#).

(A10) Restricted to $\mathbb{R} \setminus \{0\}$, θ^ε is a Lipschitz-continuous and strictly monotonic function into $(0, \pi)$. For a zero velocity, it can take any values as follows.

$$\theta^\varepsilon(0) \in \begin{cases} [\lim_{u \nearrow 0} \theta^\varepsilon(u), \lim_{u \searrow 0} \theta^\varepsilon(u)] & \text{if } \theta^\varepsilon \text{ is increasing,} \\ [\lim_{u \searrow 0} \theta^\varepsilon(u), \lim_{u \nearrow 0} \theta^\varepsilon(u)] & \text{otherwise.} \end{cases}$$

Using the monotonicity of θ^ε , one can invert the relation with respect to the velocity. For this, let $\zeta^\varepsilon := (\cos(\theta^\varepsilon))^{-1}$ be the inverse of $\cos \theta^\varepsilon$. By [\(A10\)](#), ζ^ε is well-defined and Lipschitz-continuous. As before, we assume that ζ^ε depends regularly on ε .

(A11) ζ^ε has a uniform expansion

$$\zeta^\varepsilon(a) = \zeta^0(a) + \varepsilon \zeta^1(a) + \mathcal{O}(\varepsilon^2),$$

where $\zeta^0 : (-1, 1) \rightarrow \mathbb{R}$ is Lipschitz-continuous.

With this, we study the Navier–Stokes system for two-phase flow (2.13)–(2.23), but replace (2.24) by the following, inverted contact angle condition

$$\zeta^\varepsilon \left(\mathbf{t}_\Gamma^\varepsilon|_{s=1} \cdot \mathbf{t}_w^\varepsilon|_{x_1=\gamma_1^\varepsilon} \right) = \partial_t \gamma_1^\varepsilon. \quad (2.78)$$

Since the analysis in Section 2.4.1 is independent of the interface region, and in particular does not use (A5) or the non-hysteretic contact angle relation (2.24), the derived bulk solutions (2.44)–(2.47) remain unchanged.

Using (A1)–(A4), (A6)–(A8) and (A11) instead of (A5), we repeat the analysis close to the interface $\Gamma^\varepsilon(t)$ from Section 2.4.2. Following the same steps, we obtain a circular interface with constant curvature K^0 , which is then implicitly given by

$$\partial_t \gamma_1^0 = \zeta^0 (w^0(\gamma_1^0) K^0).$$

Combining this, the pressure balance (2.72), and the outer pressure solution (2.45) and (2.47), one obtains

$$\partial_t \gamma_1^0 = \zeta^0 (w^0(\gamma_1^0) \overline{\text{Ca}} (p_{\text{in}}^0 - qJ(\gamma_1^0))), \quad (2.79)$$

where

$$J(\gamma_1^0) := \int_0^{\gamma_1^0} \frac{3}{(w^0(x_1))^2 (w^0(x_1) + 3\lambda^0)} dx_1 + \int_{\gamma_1^0}^1 \frac{3M}{(w^0(x_1))^2 (w^0(x_1) + 3\lambda^0)} dx_1.$$

Together with (2.75), this forms a differential algebraic system of two equations for the two unknowns γ_1^0 and either p_{in}^0 or q . Furthermore, the Stokes problem for finding the velocity close to the interface remains unchanged as well.

The solution process depends again on the chosen inlet boundary condition, analogously to the discussion in Section 2.4.2. As before, it is sufficient to obtain γ_1^0 , p_{in}^0 and q , since these are the unknown coefficients for the bulk solutions \mathbf{u}_α^0 and p_α^0 ($\alpha \in \{\text{I}, \text{II}\}$) given by (2.44)–(2.47). For an inlet velocity boundary condition $\mathbf{u}_1^\varepsilon = \mathbf{u}_{\text{in}}^\varepsilon$ at $\Gamma_{\text{in}}^\varepsilon$, the value of q is given. Hence, plugging this into (2.75) yields γ_1^0 , and thus one can solve (2.79) for p_{in}^0 . However, the solution of the inlet pressure p_{in}^0 is not unique if the contact angle relation θ^ε is multi-valued at velocity $u = 0$. On the other hand, for an inlet pressure condition $p_1^\varepsilon = p_{\text{in}}^\varepsilon$, the value of p_{in}^0 is known. Then, the differential algebraic system (2.75) and (2.79) has index 1 and can be solved for q and γ_1^0 . Inserting (2.75) into (2.79) and applying the implicit function theorem to find q depending on γ_1^0 , a sufficient condition for solvability is

$$(\zeta^0)' (w^0(\gamma_1^0) \overline{\text{Ca}} (p_{\text{in}}^0 - qJ(\gamma_1^0))) \neq \frac{1}{\overline{\text{Ca}} (w^0(\gamma_1^0))^2 J(\gamma_1^0)}.$$

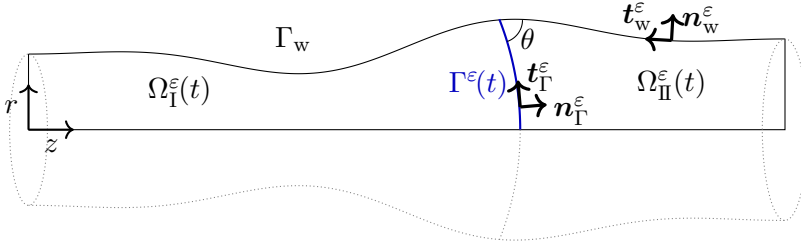


Figure 2.2.: Sketch of the axisymmetric, thin tube Ω filled by two fluids with interface $\Gamma^\epsilon(t)$ at time t .

2.5. Upscaling for a thin cylindrical tube

So far, we have considered the upscaling in a two-dimensional thin strip. In this section, we extend this to the similar setting of an three-dimensional, thin tube. Assuming axisymmetry for all quantities, the dependency on the angular component can be suppressed everywhere, so that the derivation of the upscaled model is for the most part identical with the previous sections. However, we additionally incorporate gravity as external force. In the following, we present the derivation with special attention given to the changes compared to the two-dimensional case.

2.5.1. Non-dimensional model

We use a cylindrical coordinate system oriented along the symmetry axis of the three-dimensional, thin tube. Then, the axial and radial components of a vector are denoted by \cdot_z and \cdot_r , while we suppress the angular component. For a point x , we write $z = x_z$ and $r = x_r$. Furthermore, the unit vectors in axial and radial direction are denoted e_z and e_r , respectively. We directly state the non-dimensional model, where all quantities are scaled as before in [Section 2.3](#), see [Table 2.1](#).

The axisymmetric tube is depicted in [Fig. 2.2](#). We consider the non-dimensional radius to be a given smooth function $w : [0, 1] \rightarrow (0, \infty)$, which is independent of $\varepsilon = \hat{w}(0)/L$ (\hat{w} being the dimensional radius) to simplify the presentation. This satisfies [\(A4\)](#), and higher order terms in ε would not affect the leading order flow solution, as shown previously for the thin strip. Therefore, the non-dimensional tube domain is $\Omega := \{x \in (0, 1) \times (0, \infty) \mid r < w(z)\}$ and its outer wall boundary is given by $\Gamma_w := \{(z, w(z)) \mid z \in [0, 1]\}$. The axisymmetric fluid-fluid interface appears as a free boundary and is given by $\Gamma^\epsilon(t) = \{\gamma^\epsilon(t, s) \mid s \in [0, 1]\}$ with the parametrization γ^ϵ . Therefore, the normal and tangential unit vectors are given by

$$\begin{aligned} t_\Gamma^\epsilon &= \frac{1}{\sqrt{(\partial_s \gamma_z^\epsilon)^2 + (\varepsilon \partial_s \gamma_r^\epsilon)^2}} \partial_s \gamma^\epsilon, & n_\Gamma^\epsilon &= \frac{1}{\sqrt{(\partial_s \gamma_z^\epsilon)^2 + (\varepsilon \partial_s \gamma_r^\epsilon)^2}} (\varepsilon \partial_s \gamma_r^\epsilon e_z - \partial_s \gamma_z^\epsilon e_r), \\ t_w^\epsilon &= -\frac{1}{\sqrt{1 + (\varepsilon \partial_z w)^2}} (e_z + \varepsilon \partial_z w e_r), & n_w^\epsilon &= \frac{1}{\sqrt{1 + (\varepsilon \partial_z w)^2}} (-\varepsilon \partial_z w e_z + e_r). \end{aligned}$$

The non-dimensional differential operators in cylindrical coordinates are

$$\nabla^\varepsilon = \mathbf{e}_z \partial_z + \varepsilon^{-1} \mathbf{e}_r \partial_r, \quad \Delta^\varepsilon = \partial_z^2 + \varepsilon^{-2} r^{-1} \partial_r (r \partial_r), \quad \mathbf{D}^\varepsilon(\mathbf{u}^\varepsilon) = \frac{1}{2} (\nabla^\varepsilon \mathbf{u}^\varepsilon + (\nabla^\varepsilon \mathbf{u}^\varepsilon)^T),$$

and the divergence is scaled accordingly.

The flow of the two immiscible phases in the sub-domains $\Omega_I^\varepsilon(t)$ and $\Omega_{II}^\varepsilon(t)$ is governed by the incompressible Navier–Stokes equations (without angular flow),

$$\varepsilon^2 \text{Re}(\partial_t \mathbf{u}_I^\varepsilon + (\mathbf{u}_I^\varepsilon \cdot \nabla^\varepsilon) \mathbf{u}_I^\varepsilon) = -\nabla^\varepsilon p_I^\varepsilon + \varepsilon^2 \Delta^\varepsilon \mathbf{u}_I^\varepsilon - \text{Ge}_z \quad \text{in } \Omega_I^\varepsilon(t), \quad (2.80)$$

$$\varepsilon^2 \text{Re}(\partial_t \mathbf{u}_{II}^\varepsilon + (\mathbf{u}_{II}^\varepsilon \cdot \nabla^\varepsilon) \mathbf{u}_{II}^\varepsilon) = -\nabla^\varepsilon p_{II}^\varepsilon + \text{M} \varepsilon^2 \Delta^\varepsilon \mathbf{u}_{II}^\varepsilon - \text{RGe}_z \quad \text{in } \Omega_{II}^\varepsilon(t), \quad (2.81)$$

$$\nabla^\varepsilon \cdot \mathbf{u}_\alpha^\varepsilon = 0 \quad \text{in } \Omega_\alpha^\varepsilon(t), \quad (2.82)$$

where $\mathbf{u}_\alpha^\varepsilon(t, \mathbf{x})$ and $p_\alpha^\varepsilon(t, \mathbf{x})$ are the velocity and pressure of the phase α . Here, we include the effect of gravity in axial direction by G , see [Table 2.1](#) for the scaling. Note that it is straightforward to extend the following analysis to gravitational and other volume forces not aligned with the axial direction, as long as the force \mathbf{f} satisfies $|\mathbf{f}| \leq \mathcal{O}(\varepsilon^0)$ analogously to [\(A13\)](#) below. Together with the assumption of a small capillary number [\(A8\)](#), this implies a small ratio of gravitational to interfacial forces, so that the assumption of small deformation of the interface [\(A7\)](#) still applies. Similarly as before, the boundary conditions are given by

$$p_I^\varepsilon = p_{\text{in}}, \quad u_{I,r}^\varepsilon = 0 \quad \text{or} \quad \mathbf{u}_I^\varepsilon = \mathbf{u}_{\text{in}} \quad \text{at } z = 0, \quad (2.83)$$

$$p_{II}^\varepsilon = 0, \quad u_{II,r}^\varepsilon = 0 \quad \text{at } z = 1, \quad (2.84)$$

$$u_{\alpha,r}^\varepsilon = 0, \quad \partial_r u_{\alpha,z}^\varepsilon = 0, \quad \partial_r p_\alpha^\varepsilon = 0 \quad \text{at } r = 0, \quad (2.85)$$

$$\mathbf{u}_\alpha^\varepsilon \cdot \mathbf{n}_w^\varepsilon = 0, \quad \mathbf{t}_w^\varepsilon \cdot (\mathbf{u}_\alpha^\varepsilon + 2\varepsilon \lambda^\varepsilon \mathbf{D}^\varepsilon(\mathbf{u}_\alpha^\varepsilon) \mathbf{n}_w^\varepsilon) = 0 \quad \text{on } \Gamma_w, \quad (2.86)$$

$$\mathbf{u}_I^\varepsilon = \mathbf{u}_{II}^\varepsilon, \quad \partial_t (\gamma_z^\varepsilon \mathbf{e}_z + \varepsilon \gamma_r^\varepsilon \mathbf{e}_r) \cdot \mathbf{n}_I^\varepsilon = \mathbf{u}_I^\varepsilon \cdot \mathbf{n}_I^\varepsilon \quad \text{on } \Gamma^\varepsilon(t), \quad (2.87)$$

$$-(p_I^\varepsilon - p_{II}^\varepsilon) \mathbf{n}_I^\varepsilon + 2\varepsilon^2 (\mathbf{D}^\varepsilon(\mathbf{u}_I^\varepsilon) - \text{M} \mathbf{D}^\varepsilon(\mathbf{u}_{II}^\varepsilon)) \mathbf{n}_I^\varepsilon = \frac{2\varepsilon^2}{\text{Ca}} \kappa^\varepsilon \mathbf{n}_I^\varepsilon \quad \text{on } \Gamma^\varepsilon(t), \quad (2.88)$$

$$\mathbf{n}_I^\varepsilon \cdot \mathbf{e}_r = 0 \quad \text{at } s = 0, \quad (2.89)$$

$$\cos(\theta^\varepsilon(\partial_t \gamma^\varepsilon \cdot -\mathbf{t}_w^\varepsilon|_{z=\gamma_z^\varepsilon})) = \mathbf{t}_I^\varepsilon \cdot \mathbf{t}_w^\varepsilon|_{z=\gamma_z^\varepsilon} \quad \text{at } s = 1. \quad (2.90)$$

As before, λ^ε denotes the slip length, $\kappa^\varepsilon = \nabla^\varepsilon \cdot \mathbf{n}_I^\varepsilon$ is the local mean curvature of the interface, and $\theta : \mathbb{R} \rightarrow (0, \pi)$ is the velocity-dependent contact angle between the wall Γ_w and the interface $\Gamma^\varepsilon(t)$. The initial conditions for the interface position and for the velocity are omitted. In the following, they are implicitly required to match the asymptotic solutions, to avoid possible initial layer solutions for small times.

Remark 2.4. We denote the total flux (in z -direction) at position z by

$$q^\varepsilon(t, z) := 2\pi \int_0^{w(z)} u_{\alpha,z}^\varepsilon r dr,$$

where $\alpha = \text{I}$ for $x \in \Omega_{\text{I}}^\varepsilon$, and $\alpha = \text{II}$ for $x \in \Omega_{\text{II}}^\varepsilon$. As in Remark 2.2 for the thin-strip case, we integrate (2.82) over $V_a = \{x \in \Omega \mid z < a\}$, $a \in (0, 1)$, using the Gauss theorem. Due to the boundary conditions (2.85) and (2.86) and the continuity of the velocity at the interface (2.87), we obtain that the total flux is independent of z , so we will simply use $q^\varepsilon(t)$ for the subsequent analysis.

2.5.2. Asymptotic expansion

In the following, we derive the formal solution for the two-phase flow system (2.80)–(2.90) in the asymptotic limit as $\varepsilon \rightarrow 0$, i.e., the behavior in the limit when the tube becomes infinitely thin. We use the same asymptotic expansion ansatz as in Section 2.4 assuming that all variables are smooth and depend regularly on ε , starting with the leading order $\mathcal{O}(\varepsilon^0)$. First, we derive the asymptotic solution in the bulk domains $\Omega_\alpha^\varepsilon(t)$, $\alpha \in \{\text{I}, \text{II}\}$, away from the interface $\Gamma^\varepsilon(t)$, where either fluid I or II is present. Subsequently, we show that the bulk solutions are connected by a boundary layer solution in an $\mathcal{O}(\varepsilon)$ -region around the interface $\Gamma^\varepsilon(t)$.

The resulting asymptotic solution is of Hagen–Poiseuille type in the bulk coupled by a dynamic Young–Laplace law at the interface, meaning that the interface position and the total flux are given by differential algebraic equations. The case of vanishing viscosity ratio $M \rightarrow 0$ matches the asymptotic limit for unsaturated one-phase flow, and a reformulation for hysteretic contact-angle models is possible. However, we omit the details, since the arguments and results are identical to those presented in Sections 2.4.3 and 2.4.4 for the thin-strip setting.

We reuse the assumptions (A1)–(A5) and (A7)–(A8) on the model parameters. Additionally, we require the following.

(A12) If the velocity boundary condition $u_{\text{I}}^\varepsilon = u_{\text{in}}$ is used at $z = 0$, the velocity is given by $u_{\text{in},z}^\varepsilon(t, x) = 2q(t) \frac{(1+2\lambda^0)-r^2}{\pi(1+4\lambda^0)} + \mathcal{O}(\varepsilon)$ and $u_{\text{in},r}^\varepsilon = \mathcal{O}(\varepsilon^2)$.

(A13) The gravitational effect G is uniformly bounded, i.e., $G \leq \mathcal{O}(\varepsilon^0)$.

Note that (A12) excludes possible boundary-layer effects caused by non-matching boundary conditions, just as (A6) did in the thin-strip case. Furthermore, (A13) ensures that the leading-order interface parametrization remains axisymmetric, and that the gravitational acceleration along the tube is balanced by the stress.

First, we solve the flow equations in the bulk domains $\Omega_\alpha^\varepsilon$, $\alpha \in \{\text{I}, \text{II}\}$ away from the interface. Inserting the homogenization ansatz into (2.80)–(2.86) using (A1)–

(A5), (A7), (A12) and (A13), one obtains in leading order

$$\mathcal{O}(\varepsilon) = -\partial_z p_I^0 + r^{-1} \partial_r (r \partial_r u_{I,z}^0) - G \quad \text{in } \Omega_I^\varepsilon(t), \quad (2.91)$$

$$\mathcal{O}(\varepsilon) = -\partial_z p_{II}^0 + M r^{-1} \partial_r (r \partial_r u_{II,z}^0) - RG \quad \text{in } \Omega_{II}^\varepsilon(t), \quad (2.92)$$

$$\mathcal{O}(\varepsilon) = \partial_r p_\alpha^0 \quad \text{in } \Omega_\alpha^\varepsilon(t), \quad (2.93)$$

$$\mathcal{O}(\varepsilon) = \partial_r (r u_{\alpha,r}^0) \quad \text{in } \Omega_\alpha^\varepsilon(t), \quad (2.94)$$

$$\mathcal{O}(\varepsilon) = u_{\alpha,r}^0, \quad \mathcal{O}(\varepsilon) = \partial_r u_{\alpha,z}^0, \quad \mathcal{O}(\varepsilon) = \partial_r p_\alpha^0 \quad \text{at } r = 0, \quad (2.95)$$

$$\mathcal{O}(\varepsilon) = p_I^0 - p_{in}, \quad \mathcal{O}(\varepsilon) = u_{I,r}^0 \quad \text{or} \quad (2.96)$$

$$\mathcal{O}(\varepsilon) = u_I^0 - u_{in} \quad \text{at } z = 0, \quad (2.97)$$

$$\mathcal{O}(\varepsilon) = p_{II}^0, \quad \mathcal{O}(\varepsilon) = u_{II,r}^0 \quad \text{at } z = 1, \quad (2.98)$$

$$\mathcal{O}(\varepsilon) = u_{\alpha,z}^0 + \lambda^0 \partial_r u_{\alpha,z}^0, \quad \mathcal{O}(\varepsilon) = u_{\alpha,r}^0 \quad \text{at } r = w(z). \quad (2.99)$$

Note that either (2.96) or (2.97) holds, depending on the choice of the boundary condition at $z = 0$.

Since we are interested in the flow behavior away from the interface, we investigate the problem for $z < \gamma_z^0(t)$ in fluid I and for $z > \gamma_z^0(t)$ in fluid II, respectively. By the mass conservation (2.94) together with the symmetry and wall conditions (2.95) and (2.99), one obtains

$$u_{\alpha,r}^0 \equiv 0 \quad \text{for } \alpha = I, z < \gamma_z^0(t), \text{ and for } \alpha = II, z > \gamma_z^0(t). \quad (2.100)$$

Equation (2.93) yields that p_α^0 is independent of r for both phases. Integrating (2.91) twice over r and using the symmetry and the wall boundary conditions (2.95) and (2.99), one obtains

$$u_{I,z}^0(t, \mathbf{x}) = \frac{r^2 - w(z)(w(z) + 2\lambda^0)}{4} (\partial_z p_I^0(t, z) + G) \quad \text{for } z < \gamma_z^0(t). \quad (2.101)$$

Analogously, one obtains for fluid II by (2.92), (2.95), and (2.99)

$$u_{II,1}^0(t, \mathbf{x}) = \frac{r^2 - w(z)(w(z) + 2\lambda^0)}{4M} (\partial_z p_{II}^0(t, z) + RG) \quad \text{for } z > \gamma_z^0(t). \quad (2.102)$$

Integrating (2.101) and (2.102) over the cross-section yields with Remark 2.4

$$q(t) = 2\pi \int_0^{w(z)} u_{I,z}^0(t, \mathbf{x}) r dr = -\frac{\pi(w(z))^3(w(z) + 4\lambda^0)}{8} (\partial_z p_I(t, \mathbf{x}) + G), \quad (2.103)$$

$$q(t) = 2\pi \int_0^{w(z)} u_{II,z}^0(t, \mathbf{x}) r dr = -\frac{\pi(w(z))^3(w(z) + 4\lambda^0)}{8M} (\partial_z p_{II}(t, \mathbf{x}) + RG), \quad (2.104)$$

where $q(t) := 2\pi \int_0^1 u_{I,z}^0(t, \mathbf{x})|_{z=0} r dr$ is the leading-order total flux. Solving these

equations for p_α^0 , we obtain with the outflow boundary condition (2.98)

$$\begin{aligned} p_I^0(t, \mathbf{x}) &= p_{\text{in}}(t) - \mathbf{G}z - q(t) \int_0^z \frac{8}{\pi(w(\xi))^3(w(\xi) + 4\lambda^0)} d\xi \quad \text{for } z < \gamma_z^0(t), \\ p_{II}^0(t, \mathbf{x}) &= \mathbf{R}\mathbf{G}(1 - z) + q(t) \int_z^1 \frac{8\mathbf{M}}{\pi(w(\xi))^3(w(\xi) + 4\lambda^0)} d\xi \quad \text{for } z > \gamma_z^0(t). \end{aligned}$$

Inserting these expressions into (2.101) and (2.102) results in the following solution in the bulk domains. There holds for $z < \gamma_z^0(t)$

$$\mathbf{u}_I^\varepsilon(t, \mathbf{x}) = 2q(t) \frac{w(z)(w(z) + 2\lambda^0) - r^2}{\pi(w(z))^3(w(z) + 4\lambda^0)} \mathbf{e}_z + \mathcal{O}(\varepsilon), \quad (2.105)$$

$$p_I^\varepsilon(t, \mathbf{x}) = p_{\text{in}}(t) - \mathbf{G}z - q(t) \int_0^z \frac{8}{\pi(w(\xi))^3(w(\xi) + 4\lambda^0)} d\xi + \mathcal{O}(\varepsilon), \quad (2.106)$$

and for $z > \gamma_z^0(t)$

$$\mathbf{u}_{II}^\varepsilon(t, \mathbf{x}) = 2q(t) \frac{w(z)(w(z) + 2\lambda^0) - r^2}{\pi(w(z))^3(w(z) + 4\lambda^0)} \mathbf{e}_z + \mathcal{O}(\varepsilon), \quad (2.107)$$

$$p_{II}^\varepsilon(t, \mathbf{x}) = \mathbf{R}\mathbf{G}(1 - z) + q(t) \int_z^1 \frac{8\mathbf{M}}{\pi(w(\xi))^3(w(\xi) + 4\lambda^0)} d\xi + \mathcal{O}(\varepsilon). \quad (2.108)$$

This means that the solution in the bulk domains is of Hagen–Poiseuille type also in this case. Note that the first order equations for the radial component of the velocities $u_{\alpha,r}^1$ can be derived as in the previous section. However, they are of no interest here and thus omitted.

Depending on the chosen inlet boundary condition (2.96) or (2.97), either the inlet pressure p_{in} or the leading-order total flux q is given. The other coefficient will be determined in the following via the coupling at the interface $\Gamma^\varepsilon(t)$. Exactly as for the thin-strip case, the bulk solutions are not compatible with the interface condition (2.87). We omit the details here and directly introduce the inner scaling, which allows to find the asymptotic solution in the boundary layer around the interface $\Gamma^\varepsilon(t)$. Similar as in Section 2.4.2 (see also Table 2.1), and due to (A7), this inner scaling is given by

$$\begin{aligned} X_z(t, z) &:= \frac{z - \gamma_z^0(t)}{\varepsilon}, \quad X_r := r, \\ \mathbf{Y}^\varepsilon &:= \frac{\gamma_z^\varepsilon - \gamma_z^0}{\varepsilon} \mathbf{e}_z + \gamma_r^\varepsilon \mathbf{e}_r, \quad \mathbf{U}_\alpha^\varepsilon(t, \mathbf{X}) := \mathbf{u}_\alpha^\varepsilon(t, \mathbf{x}), \quad P_\alpha^\varepsilon(t, \mathbf{X}) := p_\alpha^\varepsilon(t, \mathbf{x}). \end{aligned}$$

The geometry becomes $\Omega_{\mathbf{x}}^\varepsilon(t) := \{\mathbf{X}(t, \mathbf{x}) \mid \mathbf{x} \in \Omega\}$, and analogously for $\Gamma_{\mathbf{x}}^\varepsilon(t)$, $\Omega_{\mathbf{x},\alpha}^\varepsilon(t)$, $\Gamma_{\mathbf{x},w,\alpha}^\varepsilon(t)$ for $\alpha \in \{I, II\}$.

Note that analogously to Remark 2.4, by the mass conservation (2.82), the in-

terface velocity (2.87) and assumption (A7), we obtain

$$\begin{aligned} 0 &= \int_{\Omega_1^\varepsilon} \nabla^\varepsilon \cdot \mathbf{u}_1^\varepsilon d\mathbf{x} = \int_{\Gamma^\varepsilon} \mathbf{u}_1^\varepsilon \cdot \mathbf{n}_1^\varepsilon da - 2\pi \int_0^{w(0)} u_{1,z}^\varepsilon|_{z=0} r dr \\ &= \int_{\Gamma^\varepsilon} \partial_t \gamma_z^0 N_{\Gamma,z}^0 da - q + \mathcal{O}(\varepsilon) = \pi (w(\gamma_z^0))^2 \partial_t \gamma_z^0 - q + \mathcal{O}(\varepsilon). \end{aligned}$$

Therefore, the leading order position γ_z^0 of the interface satisfies

$$\partial_t \gamma_z^0(t) = \frac{q(t)}{\pi (w(\gamma_z^0(t)))^2}. \quad (2.109)$$

Inserting the homogenization ansatz into (2.80), (2.81), and (2.88)–(2.90) using (A1), (A2), (A5), (A7), (A8), (A13), and the inner scaling, one obtains

$$\mathcal{O}(\varepsilon) = \nabla_{\mathbf{x}} P_\alpha^0 \quad \text{in } \Omega_{\mathbf{x},\alpha}^\varepsilon(t), \quad (2.110)$$

$$\mathcal{O}(\varepsilon) = (P_I^0 - P_{II}^0) + \frac{2}{\overline{\text{Ca}}} K^0 \quad \text{on } \Gamma_{\mathbf{x}}^\varepsilon(t), \quad (2.111)$$

$$\mathcal{O}(\varepsilon) = \partial_s Y_z^0 \quad \text{at } s = 0, \quad (2.112)$$

$$\mathcal{O}(\varepsilon) = \cos(\theta^0(\partial_t \gamma_z^0)) + \frac{\partial_s Y_z^0}{\sqrt{(\partial_s Y_z^0)^2 + (\partial_s Y_r^0)^2}} \quad \text{at } s = 1, \quad (2.113)$$

where we chose $\text{Ca} = \varepsilon \overline{\text{Ca}}$, see Remark 2.3. Furthermore, K^0 is the scaled leading-order curvature

$$K^0 = \frac{\partial_s Y_z^0 \partial_s^2 Y_r^0 - \partial_s Y_r^0 \partial_s^2 Y_z^0}{((\partial_s Y_z^0)^2 + (\partial_s Y_r^0)^2)^{3/2}}.$$

By (2.110), the leading-order pressures P_α^0 are constant in $\Omega_{\mathbf{x},\alpha}^\varepsilon(t)$ for $\alpha \in \{I, II\}$. By matching with the outer solution, we obtain

$$P_\alpha^0(t, \mathbf{X}) = p_\alpha^0(t, \gamma_z^0(t)) \quad \text{for all } \mathbf{X} \in \Omega_{\mathbf{x},\alpha}^\varepsilon(t).$$

Inserting these constant pressures into the interfacial stress balance (2.111) yields that the leading-order curvature K^0 is constant and given by

$$K^0 = \frac{\overline{\text{Ca}}}{2} (p_{II}^0 - p_I^0)|_{z=\gamma_z^0}. \quad (2.114)$$

Therefore, the interface is in leading order a spherical cap. By the symmetry condition (2.112) and the contact-angle condition (2.113), one obtains

$$K^0 = -\frac{\cos(\theta^0(\partial_t \gamma_z^0))}{w(\gamma_z^0)}. \quad (2.115)$$

Combining (2.114) and (2.115) and inserting the bulk pressure solutions (2.106)

and (2.108), leads to

$$p_{\text{in}} - q \left(\int_0^{\gamma_z^0} \frac{8}{\pi(w(z))^3(w(z) + 4\lambda^0)} dz + \int_{\gamma_z^0}^1 \frac{8M}{\pi(w(z))^3(w(z) + 4\lambda^0)} dz \right) - G(\gamma_z^0 + R(1 - \gamma_z^0)) = \frac{2 \cos(\theta^0(\partial_t \gamma_z^0))}{\overline{\text{Ca}} w(\gamma_z^0)}. \quad (2.116)$$

To find the solution for u_α^0, p_α^0 ($\alpha \in \{\text{I}, \text{II}\}$), which is given by (2.105)–(2.108), one has to determine γ_z^0, q and p_{in} . The derivation depends on the chosen inlet boundary condition, as discussed in Section 2.4.2, so we omit the details here. Furthermore, one can use the $\mathcal{O}(\varepsilon)$ terms of the inner expansion to (2.80)–(2.90) to obtain a Stokes problem for finding the velocity close to the interface.

2.6. Averaged models and effective quantities

Based on the asymptotic solution for pressures and velocities, we continue with the study of averaged models and effective quantities. First, we show that a local, one-dimensional version of Darcy's law holds for the transversally averaged pressures and velocities. In the second part we derive effective quantities based on volume averages. The main result is a capillary pressure - saturation relationship involving dynamic effects.

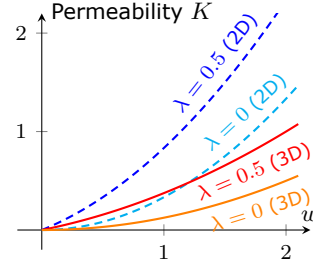
In the following, we are only interested in the leading order relations. To simplify the notation, we thus drop the indices $(\cdot)^\varepsilon$ and $(\cdot)^0$, and neglect higher-order terms. Hence, all following equations should be understood as up to terms of order ε . To distinguish the two-dimensional strip and the three-dimensional tube, we use the index $(\cdot)_2$ or $(\cdot)_3$, respectively. No index is used if the expressions coincide. Furthermore, the axial coordinate is always denoted x_1 (instead of z in three dimensions).

2.6.1. Transversal average: Darcy's law

In the following, we derive the transversal average of the quantities to demonstrate that the one-dimensional descriptions of the thin strip and of the thin tube yield a local version of Darcy's law. Starting with the thin strip, recall that the total flux (in the half strip) $q(t)$ is independent of x_1 as discussed in Remark 2.2. The transversally averaged velocity in x_1 -direction is therefore given by

$$\begin{aligned} \bar{u}(t, x_1) &:= \begin{cases} (w(x_1))^{-1} \int_0^{w(x_1)} u_{\text{I}, \text{I}}(t, \mathbf{x}) dx_2 & \text{for } x_1 < \gamma_1(t), \\ (w(x_1))^{-1} \int_0^{w(x_1)} u_{\text{I}, \text{II}}(t, \mathbf{x}) dx_2 & \text{for } x_1 > \gamma_1(t), \end{cases} \\ &= \frac{q(t)}{w(x_1)}. \end{aligned}$$

Figure 2.3: The local permeability K has a quadratic dependence on the width w and increases for increasing slip length λ .



Since the pressures p_I and p_{II} are independent of x_2 , we obtain by (2.45) and (2.47) for the transversally averaged pressures

$$\begin{aligned}\bar{p}_I(t, x_1) &:= \frac{1}{w(x_1)} \int_0^{w(x_1)} p_I(t, \mathbf{x}) dx_2 \\ &= p_{in}(t) - q(t) \int_0^{x_1} \frac{3}{(w(\xi))^2(w(\xi) + 3\lambda)} d\xi \quad \text{for } x_1 < \gamma_1(t), \\ \bar{p}_{II}(t, x_1) &:= \frac{1}{w(x_1)} \int_0^{w(x_1)} p_{II}(t, \mathbf{x}) dx_2 \\ &= q(t) \int_{x_1}^1 \frac{3M}{(w(\xi))^2(w(\xi) + 3\lambda)} d\xi \quad \text{for } x_1 > \gamma_1(t).\end{aligned}$$

This means that the transversally averaged pressures in the thin strip satisfy a Darcy-type law

$$\bar{u}(t, x_1) = -K(x_1) \partial_{x_1} \bar{p}_I(t, x_1), \quad \bar{u}(t, x_1) = -\frac{K(x_1)}{M} \partial_{x_1} \bar{p}_{II}(t, x_1), \quad (2.117)$$

where the local permeability is given by

$$K_2(x_1) := \frac{1}{3} w(x_1) (w(x_1) + 3\lambda).$$

An analogous calculation for the thin tube using the transversal average $\overline{(\cdot)} = w^{-2} \int_0^w (\cdot) 2r dr$ leads to (2.117) with the local permeability

$$K_3(x_1) := \frac{1}{8} w(x_1) (w(x_1) + 4\lambda).$$

These permeabilities depend only on the local width w of the thin strip and on the slip length λ , see also Fig. 2.3. Note that without slip ($\lambda = 0$) these are the typical relations for single-phase flow: $\bar{u} = \frac{d^2}{12} \partial_{x_1} p$ in a thin strip of diameter $d = 2w$, and $\bar{u} = \frac{R^2}{8} \partial_z p$ in a tube with radius $R = w$. Also note that the permeabilities are non-dimensional due to the chosen scaling of the radial coordinate by $\hat{w}(0)$.

2.6.2. Effective quantities: Dynamic capillary pressure

To obtain effective quantities like the saturation and the intrinsically averaged pressures, we use volume averages. With these, we obtain a capillary pressure - saturation relationship involving dynamic effects. In line with classical volume averaging theory [261, 323], we define the volume average $\langle f_\alpha \rangle$ of a quantity f_α defined in Ω_α , $\alpha \in \{I, II\}$, to be

$$\langle f_\alpha \rangle := \frac{\int_{\Omega_\alpha} f_\alpha d\mathbf{x}}{\int_{\Omega} d\mathbf{x}},$$

while the intrinsic average is

$$\langle f_\alpha \rangle_\alpha := \frac{\int_{\Omega_\alpha} f_\alpha d\mathbf{x}}{\int_{\Omega_\alpha} d\mathbf{x}}.$$

Note that polynomial corrections were discussed in [246, 247], which take the center of mass of each phase into account. This approach includes spatial derivatives $\frac{\partial^k}{\partial \mathbf{x}^k} \langle f_\alpha \rangle_\alpha$ for $k = 1, \dots, K \in \mathbb{N}$ in the locally averaged quantities. This affects the exact value of the effective parameters, but the general structure of the upscaled relations remains the same. For simplicity, we just use the classical volume averages over the whole domain.

We denote the volume of the strip or tube up to x_1 by

$$\mathcal{V}_2(x_1) := \int_0^{x_1} w(\xi) d\xi, \quad \mathcal{V}_3(x_1) := \pi \int_0^{x_1} (w(\xi))^2 d\xi.$$

Then, the volume of the domain Ω_I is given by $\int_{\Omega_I} d\mathbf{x} = \mathcal{V}(\gamma_1)$. Analogously, we have $\int_{\Omega} d\mathbf{x} = \mathcal{V}(1)$ and $\int_{\Omega_{II}} d\mathbf{x} = \mathcal{V}(1) - \mathcal{V}(\gamma_1)$. Therefore, the saturation of fluid I is in leading order given by

$$S(t) := \langle 1_{\Omega_I(t)} \rangle = \frac{\int_{\Omega_I(t)} d\mathbf{x}}{\int_{\Omega} d\mathbf{x}} = \frac{\mathcal{V}(\gamma_1(t))}{\mathcal{V}(1)}. \quad (2.118)$$

Note that we only consider the case when both phases are present, so that $\gamma_1(t) \in (0, 1)$ and $S \in (0, 1)$. For simplicity, we define the functions

$$\gamma(S) := \mathcal{V}^{-1}(\mathcal{V}(1)S), \quad \mathcal{R}(S) := w(\gamma(S)), \quad \mathcal{A}(S) := \begin{cases} \mathcal{R}(S) & d = 2, \\ \pi(\mathcal{R}(S))^2 & d = 3, \end{cases} \quad (2.119)$$

which represent the position of the interface, the local width/radius and the local cross-sectional area, respectively, each depending on the saturation S and on the geometry of the thin strip. Here and in the following, $d \in \{2, 3\}$ denotes the dimension. Note that the thin-strip system (2.74) and (2.75) (setting $G = 0$), as well as the thin-tube system (2.109) and (2.116) can be rewritten in terms of the

saturation as

$$p_{\text{in}} - (\mathcal{V}(1))^2 \left(\int_0^S \frac{1}{(\mathcal{A}(\sigma))^2 K(\gamma(\sigma))} d\sigma + \int_S^1 \frac{\mathbf{M}}{(\mathcal{A}(\sigma))^2 K(\gamma(\sigma))} d\sigma \right) \partial_t S \\ - G(\gamma(S) + R(1 - \gamma(S))) = \frac{(d-1) \cos \left(\theta \left(\frac{\mathcal{V}(1)}{\mathcal{A}(S)} \partial_t S \right) \right)}{\overline{\text{Ca}} \mathcal{R}(S)}.$$

However, this reformulations is less practical, since the function $\gamma(S)$, and thus all functions in (2.119), typically are not closed-form expressions.

Using (2.45), the intrinsically averaged pressure of fluid I in the thin strip is

$$\langle p_I \rangle_I = \frac{1}{\mathcal{V}(\gamma_1)} \int_0^{\gamma_1} w(x_1) \left(p_{\text{in}} - q \int_0^{x_1} \frac{1}{w(\xi) K(\xi)} d\xi \right) dx_1,$$

which can be rewritten after integration by parts as

$$\langle p_I \rangle_I = p_I|_{x_1=\gamma_1} + \frac{q}{\mathcal{V}(\gamma_1)} \int_0^{\gamma_1} \frac{\mathcal{V}(x_1)}{w(x_1) K(x_1)} dx_1.$$

Analogously, (2.47) yields the intrinsically averaged pressure of fluid II to be

$$\langle p_{II} \rangle_{II} = p_{II}|_{x_1=\gamma_1} - \frac{\mathbf{M}q}{\mathcal{V}(1) - \mathcal{V}(\gamma_1)} \int_{\gamma_1}^1 \frac{\mathcal{V}(1) - \mathcal{V}(x_1)}{w(x_1) K(x_1)} dx_1.$$

Using the interface condition (2.74), the difference of the intrinsically averaged pressures, in the following called phase-pressure difference, is given for the thin strip by

$$\langle p_I \rangle_I - \langle p_{II} \rangle_{II} = \frac{\cos(\theta(\partial_t \gamma_1))}{\overline{\text{Ca}} w(\gamma_1)} \\ + q \left(\frac{1}{\mathcal{V}(\gamma_1)} \int_0^{\gamma_1} \frac{\mathcal{V}(\xi)}{w(\xi) K(\xi)} d\xi + \frac{\mathbf{M}}{\mathcal{V}(1) - \mathcal{V}(\gamma_1)} \int_{\gamma_1}^1 \frac{\mathcal{V}(1) - \mathcal{V}(\xi)}{w(\xi) K(\xi)} d\xi \right). \quad (2.120)$$

In the same way, using (2.106), (2.108), and (2.116), one obtains the phase-pressure difference in the thin tube

$$\langle p_I \rangle_I - \langle p_{II} \rangle_{II} = \frac{2 \cos(\theta(\partial_t \gamma_1))}{\overline{\text{Ca}} w(\gamma_1)} + G \left(\int_0^{\gamma_1} \frac{\mathcal{V}(\xi)}{\mathcal{V}(\gamma_1)} d\xi + R \int_{\gamma_1}^1 \frac{\mathcal{V}(1) - \mathcal{V}(\xi)}{\mathcal{V}(1) - \mathcal{V}(\gamma_1)} d\xi \right) \\ + q \left(\frac{1}{\mathcal{V}(\gamma_1)} \int_0^{\gamma_1} \frac{\mathcal{V}(\xi)}{\pi(w(\xi))^2 K(\xi)} d\xi + \frac{\mathbf{M}}{\mathcal{V}(1) - \mathcal{V}(\gamma_1)} \int_{\gamma_1}^1 \frac{\mathcal{V}(1) - \mathcal{V}(\xi)}{\pi(w(\xi))^2 K(\xi)} d\xi \right). \quad (2.121)$$

Using (2.118) and (2.119), the phase-pressure difference (2.120) in the thin strip and (2.121) in the thin tube can be expressed in the form

$$\langle p_I \rangle_I - \langle p_{II} \rangle_{II} = p_{c,\text{loc}}(S, \partial_t S) + p_G(S) + \tau(S) \partial_t S, \quad (2.122)$$

where $p_G \equiv 0$ for the thin strip, as gravity has been neglected. The first righthand term denotes the local capillary pressure $p_{c,\text{loc}} := (p_I - p_{II})|_{x_1=\gamma_1}$ given for both geometries ($d = 2, 3$) by

$$p_{c,\text{loc}}(S, \partial_t S) = \frac{(d-1) \cos(\theta(\mathcal{V}(1)(\mathcal{A}(S))^{-1} \partial_t S))}{\overline{\text{Ca}} \mathcal{R}(S)}. \quad (2.123)$$

The second righthand term in (2.122) is the hydrostatic pressure of the fluids in the thin-tube model given by

$$p_G(S) = G\mathcal{V}(1) \left(\frac{1}{S} \int_0^S \frac{\sigma}{\mathcal{A}(\sigma)} d\sigma + \frac{R}{1-S} \int_S^1 \frac{1-\sigma}{\mathcal{A}(\sigma)} d\sigma \right).$$

The last righthand term in (2.122) can be interpreted as a dynamic capillarity due to the viscous drag. In particular, its coefficient is for both geometries

$$\tau(S) = (\mathcal{V}(1))^2 \left(\frac{1}{S} \int_0^S \frac{\sigma}{(\mathcal{A}(\sigma))^2 K(\gamma(\sigma))} d\sigma + \frac{M}{1-S} \int_S^1 \frac{1-\sigma}{(\mathcal{A}(\sigma))^2 K(\gamma(\sigma))} d\sigma \right), \quad (2.124)$$

which depends on the slip length λ , the viscosity ratio M and the wall function w . Note that under quasi-static conditions, when $q \ll 1$, we have $p_{\text{in}} \approx \langle p_I \rangle_I - \langle p_{II} \rangle_{II} = p_{c,\text{loc}}$, such that the measurement of the inlet pressure yields the (static) capillary pressure–saturation relation. However, under the dynamic conditions studied here, these quantities can considerably differ. This one must be aware of when performing experiments.

The local capillary pressure $p_{c,\text{loc}}$ depends reciprocally on the effective capillary number $\overline{\text{Ca}}$ and on the local width $\mathcal{R}(S)$ of the thin strip or tube. In case of a dynamic contact-angle model of the form $\cos(\theta(u)) = \cos(\theta_s) + \eta \overline{\text{Ca}} u$, the linearized molecular kinetic theory in [41, 42], (2.123) yields

$$p_{c,\text{loc}}^{\text{MKT}}(S, \partial_t S) = \frac{(d-1) \cos(\theta_s)}{\overline{\text{Ca}} \mathcal{R}(S)} + \eta \frac{(d-1) \mathcal{V}(1)}{\mathcal{A}(S) \mathcal{R}(S)} \partial_t S. \quad (2.125)$$

The static and dynamic effects are decoupled in this case. The first term models the static (local) capillary pressure, while the second term is a dynamic contribution.

In case of a constant contact angle $\theta \equiv \theta_s \in (0, \pi)$, (2.123) yields the local capillary pressure

$$p_{c,\text{loc}}^{\text{const}}(S) = \frac{(d-1) \cos(\theta_s)}{\overline{\text{Ca}} \mathcal{R}(S)}.$$

Let $l(t) := \int_{\Gamma_{\mathbf{x}}(t)} ds$ be the length of the circular interface $\Gamma_{\mathbf{x}}(t)$ in the thin strip at time t , and let $a(t) := \int_{\Gamma_{\mathbf{x}}(t)} 2\pi s ds$ be the surface of the spherical interface in the

thin tube. Then, the local capillary pressure becomes

$$p_{c,\text{loc}}^{\text{const}}(l) = \frac{\frac{\pi}{2} - \theta_s}{\text{Ca} l}, \quad p_{c,\text{loc}}^{\text{const}}(a) = \frac{2 \cos(\theta_s) \sqrt{2\pi(1 - |\cos(\theta_s)|)}}{\text{Ca} \sqrt{a}},$$

respectively. Observe that $l(t)$ and $a(t)$ can be assimilated to the interfacial area concept considered in [154, 155]. Note that for a dynamic contact angle, there is no simple closed-form expression of the local capillary pressure as a function of the interface length/area (nor of its derivatives).

2.7. Numerical experiments

To illustrate the theoretical findings, we depict several numerical examples for the two-dimensional thin strip in this section. The case of three-dimensional thin tubes will be considered in detail for the process of capillary rise in Chapter 3. Here, we start with a thin strip of constant width, and afterwards consider a constricted “pore throat” with varying width. After a short discussion of the boundary conditions, we consider the resulting effective quantities. In particular, we study the effect of the slip length and the viscosity ratio and discuss the effect of a dynamic and a hysteretic contact-angle model for both geometries. Additional examples with combinations of these effects are illustrated in Appendix A.

We have implemented the numerical solutions using MATLAB® R2020a [303]. The source code is openly available under the CC-BY license in a GitHub repository at <https://github.com/s-lunowa/AsymptoticThinStripMCLSolver> [215].

2.7.1. Thin strip of constant width

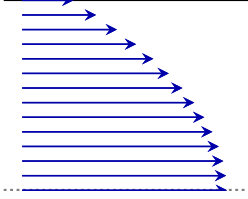
First we consider a simple case, which is a thin strip of constant width $w^\varepsilon \equiv 1$, and study the velocity and pressure distribution of the two phases as well as the movement of the interface. After a short discussion of the effect of different inlet boundary conditions, we will consider the effect of different parameter choices in the following subsections — the slip length in Section 2.7.1, the viscosity ratio in Section 2.7.1, and dynamic and hysteretic contact-angle models in Section 2.7.1, respectively. Except for the varying parameter mentioned in each subsection, all the other ones are fixed, as given in Table 2.2. In particular, the contact-angle model considered when discussing the other parameters is constant, i.e., the contact angle is static and fluid I is non-wetting.

For this geometry, the solution given in (2.44)–(2.47) for the bulk domains is

$$u_1(t, \mathbf{x}) = \begin{pmatrix} 3q(t) \frac{1+2\lambda-x_2^2}{2+6\lambda} \\ 0 \end{pmatrix}, \quad p_1(t, \mathbf{x}) = p_{\text{in}}(t) - q(t) \frac{3x_1}{1+3\lambda}, \quad \text{for } x_1 < \gamma_1(t), \quad (2.126)$$

Parameter		Value
Capillary number	$\overline{\text{Ca}}$	1/2
Contact angle	θ	$\pi/3$
Slip length	λ	1/6
Viscosity ratio	M	1
Initial interface position	$\gamma_1 _{t=0}$	0
Inlet pressure	p_{in}	3

Table 2.2.: Standard parameters for the thin strip of constant width.

Figure 2.4: Velocity profile in the thin strip with constant width ($\lambda = 1/6$).

$$\mathbf{u}_{\text{II}}(t, \mathbf{x}) = \begin{pmatrix} 3q(t) \frac{1+2\lambda-x_2^2}{2+6\lambda} \\ 0 \end{pmatrix}, \quad p_{\text{II}}(t, \mathbf{x}) = q(t) \frac{3M(1-x_1)}{1+3\lambda}, \quad \text{for } x_1 > \gamma_1(t). \quad (2.127)$$

This means that the velocity profiles are of Hagen–Poiseuille type, see also Fig. 2.4. The pressures decrease linearly inside the bulk phases due to the viscous forces. Furthermore, the interface system (2.74) and (2.75) simplifies into

$$p_{\text{in}}(t) - q(t) \frac{3\gamma_1(t) + 3M(1-\gamma_1(t))}{1+3\lambda} = \frac{\cos(\theta(q(t)))}{\overline{\text{Ca}}}, \quad \partial_t \gamma_1(t) = q(t). \quad (2.128)$$

The actual size of the quantities and the movement of the interface depends on the inlet boundary conditions, on the effective capillary number, on the slip length, on the viscosity ratio and on the contact-angle model. Here, we shortly discuss the qualitatively different cases with respect to the inlet boundary conditions and the viscosity ratio, when all other parameters are given by Table 2.2 for simplicity.

- (a) When the inlet velocity is fixed, e.g. $u_{\text{in},1} = 4/3 - x_2^2$, one obtains $q(t) = 1$ and thus the constant (in time) velocities $u_{\alpha,1} = 4/3 - x_2^2$ for $\alpha \in \{\text{I}, \text{II}\}$, so that the interface moves linearly, $\gamma_1(t) = t$. The pressures are then given by

$$p_{\text{I}}(t, \mathbf{x}) = 1 + 2M + 2(1-M)t - 2x_1, \quad p_{\text{II}}(t, \mathbf{x}) = 2M(1-x_1).$$

For $M \neq 1$, the pressure of fluid I is time-dependent, see also Fig. 2.5, while both pressures are constant in time for $M = 1$.

- (b) When the inlet pressure is fixed, e.g. $p_{\text{in}} = 3$, the flow of both fluids is time-

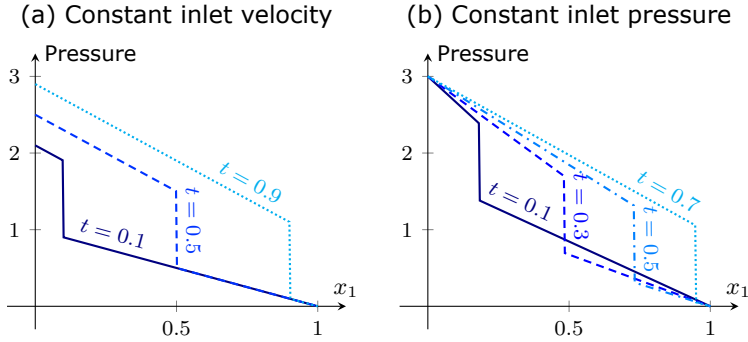


Figure 2.5.: Pressure distribution over length x_1 at various times in the thin strip of constant width for viscosity ratio $M = 0.5$. The solution depends on the inlet boundary condition and shows a more dynamic behavior in case (b) than in case (a).

dependent. For a viscosity ratio $M < 1$, one obtains the solution

$$p_I(t, \mathbf{x}) = 3 - \frac{2(1-M)x_1}{\sqrt{M^2 + 2(1-M)t}}, \quad p_{II}(t, \mathbf{x}) = \frac{2M(1-M)(1-x_1)}{\sqrt{M^2 + 2(1-M)t}},$$

$$u_{\alpha,1}(t, \mathbf{x}) = \frac{(1-M)\left(\frac{4}{3} - x_2^2\right)}{\sqrt{M^2 + 2(1-M)t}}, \quad \gamma_1(t) = \frac{\sqrt{M^2 + 2(1-M)t} - M}{1-M},$$

for $\alpha \in \{I, II\}$, see Fig. 2.5. Analogous behavior can be observed when $M > 1$. Only for $M = 1$, both pressures are constant in time, like in (a).

From these examples, we observe a more dynamic behavior when the inlet pressure is given, which corresponds also to the typical setting for capillary pressure experiments. Thus, we restrict the following discussion to the case of given pressure boundary condition at the inlet.

Due to the constant width, the effective quantities have rather simple algebraic expressions. The saturation S coincides with the interface position, i.e., $S = \gamma_1$. The local permeability is constant and given by

$$K \equiv \frac{1}{3} + \lambda. \quad (2.129)$$

The local capillary pressure, the dynamic coefficient and the phase-pressure difference are

$$p_{c,loc}(S, \partial_t S) = \frac{\cos \theta(\partial_t S)}{\text{Ca}} \quad (2.130)$$

$$\tau(S) = 3 \frac{S + M(1-S)}{2 + 6\lambda}, \quad (2.131)$$

$$\langle p_I \rangle_I - \langle p_{II} \rangle_{II} = \frac{p_{in} + p_{c,loc}(S, \partial_t S)}{2}. \quad (2.132)$$

As direct consequence of the constant contact angle in Table 2.2, we obtain a constant local capillary pressure $p_{c,loc} \equiv 1$ by (2.130) and a constant phase-pressure difference $\langle p_I \rangle_I - \langle p_{II} \rangle_{II} \equiv 2$ by (2.132). Changing the static contact angle $\theta \equiv \theta_s \in (0, \pi)$ or the capillary number \overline{Ca} influences the size of the local capillary pressure and the size of the phase-pressure difference in a straightforward way, while the behavior of the other quantities remains qualitatively the same. For simplicity, we do not discuss their detailed effects. Note that $p_{c,loc}$ and $\langle p_I \rangle_I - \langle p_{II} \rangle_{II}$ do not depend on the slip length nor on the viscosity ratio. Hence, we only consider their behavior for dynamic and hysteretic contact-angle models. Meanwhile, the dynamic coefficient depends on the slip length and the viscosity ratio, which is relevant in case of a inlet velocity condition.

Effect of the slip length

First, we consider the effect of the slip length λ while using all other parameters as above. The velocity at the wall is given by

$$u_{\alpha,1}|_{x_2=1} = q \frac{3\lambda}{1+3\lambda} \quad \text{for } \alpha \in \{I, II\}.$$

It is zero for $\lambda = 0$, increases for an increasing slip length, and approaches q for $\lambda \rightarrow \infty$, which corresponds to a total slip, see Fig. 2.6. This is a result of the decreased friction of the fluid at the wall for an increased slip length. Additionally, this leads to a smaller dynamic coefficient τ , cf. (2.131) and Fig. 2.6. For constant inlet pressure, the decrease of the pressure gradients in (2.126) and (2.127) for an increased slip length λ are compensated by a larger total flux q , and thus a faster movement of the interface position γ_1 , see also Fig. 2.6. The local permeability K shows a similar behavior. Observe that since $w \equiv 1$, it only depends on the slip length. As follows from (2.129) (see also Fig. 2.3), it increases linearly with λ .

Effect of the viscosity ratio

Next, we continue the investigation for various viscosity ratios M . Since the viscous force in fluid II is proportional to the viscosity ratio M , the total flux q decreases when the viscosity ratio M increases, cf. (2.128). In particular, the interface position γ_1 moves faster when the thin strip is mainly filled by the less viscous fluid. Furthermore, we observe that the solutions converge for $M \rightarrow 0$ towards solution of the simplified, unsaturated flow model as discussed in Section 2.4.3, see Fig. 2.7. Note that we use $\gamma_1|_{t=0} = 10^{-3}$ when $M = 0$ to avoid the degeneration of the interface system (2.128).

The dynamic coefficient τ becomes larger for small saturations S , if the viscosity

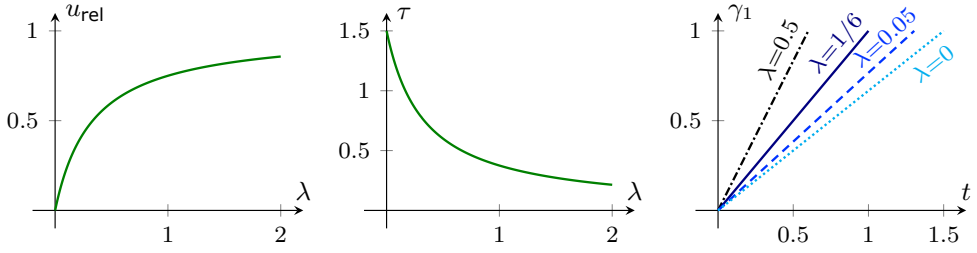


Figure 2.6.: For an increasing slip length λ , the velocity ratio $u_{\text{rel}} = u_{\alpha,1}|_{x_2=1}/q$ at the wall increases (*left*), while the dynamic parameter τ decreases (*center*). The interface position γ_1 moves faster for an increasing slip length λ (*right*).

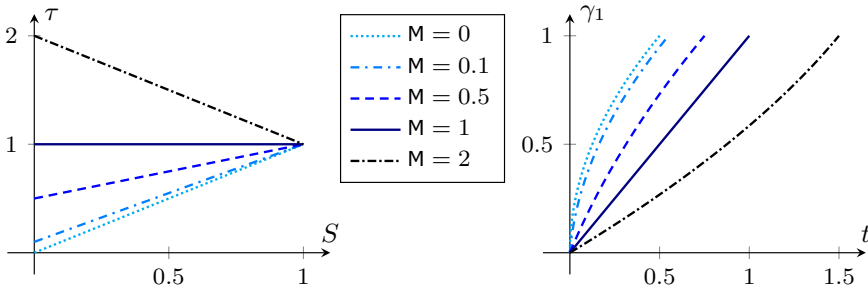


Figure 2.7.: For increasing viscosity ratio M , the dynamic parameter τ increases (*left*), while the interface position γ_1 moves slower (*right*).

ratio is large ($M > 1$), and vice versa for $M < 1$, see (2.131) and Fig. 2.7. Note that one can observe even in this extremely simplified setting that the dynamic coefficient is saturation dependent, except for fluids with the same viscosity ($M = 1$). Additionally, the dynamic coefficient is monotonic in the saturation S for any viscosity ratio.

Effect of a dynamic contact angle

Now, we consider the effect of a dynamic contact-angle model. As we expect the similar qualitative behavior for different dynamic contact-angle models, we restrict the discussion to the model

$$\theta(u) = \arccos \left(\max \left(\min(\cos(\theta_s) + \eta \overline{\text{Ca}} u, 1), -1 \right) \right), \quad (2.133)$$

which is the linearized molecular kinetic theory model (for small velocities) from [41,42,43,79,269,270] restricted to the possible range $[0, \pi]$. Here, the parameter $\eta \geq 0$ models the effective friction at the contact point leading to a dynamic contact angle. For comparability, we fix the static contact angle $\theta_s = \pi/3$ and all the other

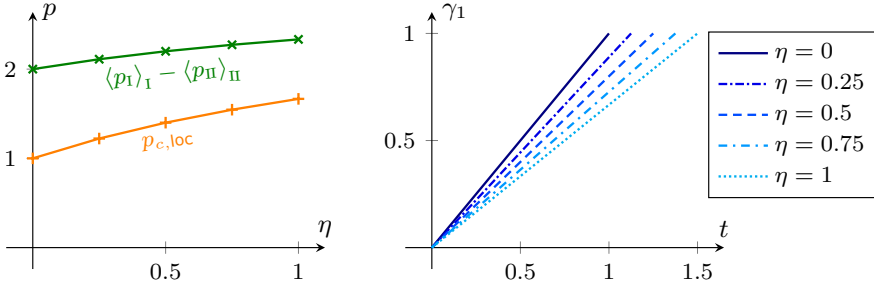


Figure 2.8.: The local capillary pressure $p_{c,loc}$ increases for increasing dynamic contact angle coefficient η (left). Hence, the movement of the interface position γ_1 slows down (right).

parameters as in Table 2.2. Note that for any $\eta \geq 0$, the differential algebraic system (2.128) has a unique solution, since the problem can be rewritten as a separable differential equation.

In contrast to the previous examples, the dynamic contact-angle model does not affect the dynamic coefficient τ , but has an impact on the local capillary pressure $p_{c,loc}$ and the phase-pressure difference $\langle p_I \rangle_I - \langle p_{II} \rangle_{II}$. Recall that the local capillary pressure is given in this case by (2.125). In particular, its dynamic part is proportional to the parameter η . Hence, the interface position γ_1 moves slower when the parameter η increases, see Fig. 2.8. Note that the total flux q is constant, so that γ_1 is linear in time. Since $M = 1$, the local capillary pressure and the phase-pressure difference are constant over S , so that we only show the dependence on η in Fig. 2.8.

Effect of a hysteretic contact angle

Finally, we consider the effect of a hysteretic contact-angle model and compare it to the static and dynamic ones. As before we use the dynamic contact-angle model (2.133) with static contact angle $\theta_s = \pi/3$. For the hysteretic contact-angle model, the advancing and receding contact angles (with respect to fluid I) are chosen $\theta_a = \pi/4$ and $\theta_r = 5\pi/12$, respectively. Together with the same dynamic contact-angle model away from $u = 0$, this yields

$$\zeta(a) = \begin{cases} \frac{a - \cos(\theta_r)}{\eta Ca} & \text{if } a < \cos(\theta_r), \\ \frac{a - \cos(\theta_a)}{\eta Ca} & \text{if } a > \cos(\theta_a), \\ 0 & \text{otherwise.} \end{cases} \quad (2.134)$$

Recall that ζ is the inverse of $\cos \theta$. We consider a drainage and imbibition cycle by choosing the time-dependent inlet pressure $p_{in}(t) = 3 - t$, and stop the simulations when the interface position returns to the inlet. The other parameters are taken

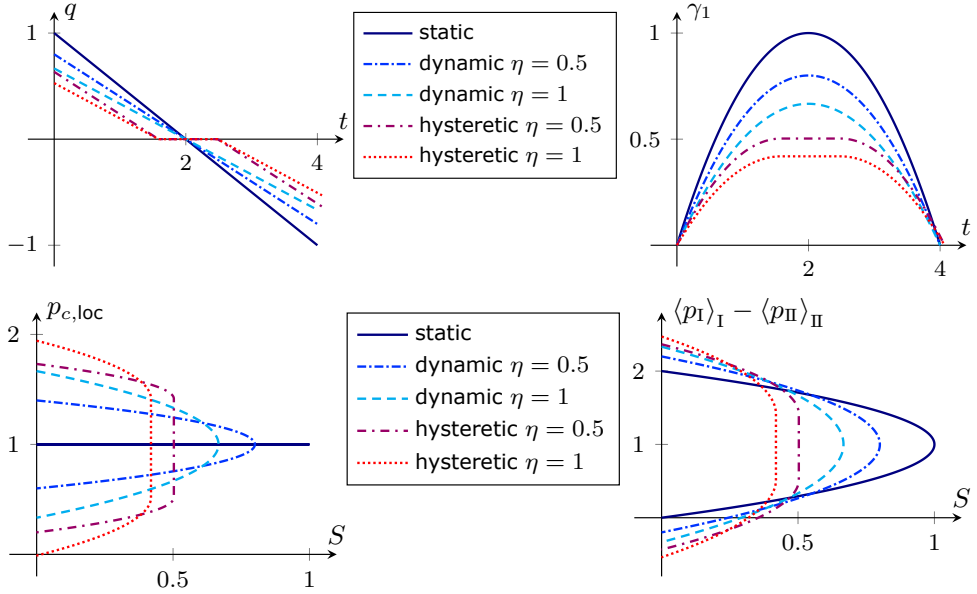


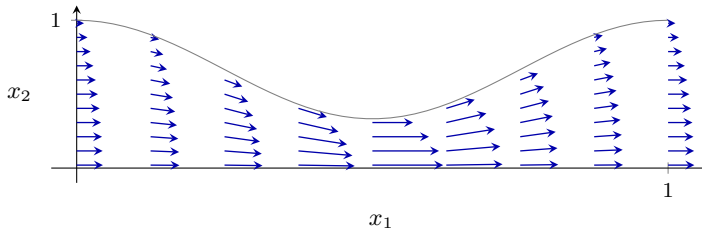
Figure 2.9.: The total flux q (*top-left*) is linear for the static and dynamic contact-angle model, while being zero for some time for the hysteretic model. The interface position γ_1 moves accordingly (*top-right*). In case of the hysteretic model, it is at rest, when the local capillary pressure $p_{c,loc}$ (*bottom-left*) lies in between the (static) capillary pressures for drainage and imbibition, i.e., $p_{c,loc}$ is multi-valued at the maximal reached saturation. For the dynamic models, $p_{c,loc}$ at the maximal saturation is exactly the static capillary pressure. The phase-pressure difference $\langle p_I \rangle_I - \langle p_{II} \rangle_{II}$ (*bottom-right*) shows the same qualitative behavior.

from Table 2.2.

As in the dynamic case, we observe that the movement of the interface position γ_1 is slower when the parameter η is increased, see Fig. 2.9 (top). While the total flux q is linear for the static and dynamic contact-angle model, so that γ_1 is quadratic in time, the hysteretic model leads to a constant interface position when $\theta_a \leq \theta \leq \theta_r$. Therefore, the local capillary pressure $p_{c,loc}$ and the phase-pressure difference $\langle p_I \rangle_I - \langle p_{II} \rangle_{II}$ at the maximal reached saturation is multi-valued taking all values between the (static) drainage and imbibition capillary pressures, see Fig. 2.9 (bottom). On the other hand, for the dynamic contact-angle model, $p_{c,loc}$ and $\langle p_I \rangle_I - \langle p_{II} \rangle_{II}$ at the maximal saturation are given by the static capillary pressure, since $\partial_t S = 0$. Furthermore, the hysteresis leads to higher deviations from the static capillary pressure and thus a smaller maximal saturation. Finally, note that p_{in} is linear and reaches $p_{c,loc}^{\text{const}}$ at $t = 2$ such that all curves with the dynamic contact-angle model are symmetric. Since θ_a and θ_r have the same distance from θ_s , the same holds in the hysteretic cases.

Parameter		Value
Capillary number	$\overline{\text{Ca}}$	1/2
Contact angle	θ	$\pi/3$
Slip length	λ	1/6
Viscosity ratio	M	1
Initial interface position	$\gamma_1 _{t=0}$	0
Inlet pressure	p_{in}	12

Table 2.3.: Standard parameters for the thin strip of varying width.

Figure 2.10.: Velocity profile in the thin strip of varying width ($\lambda = 1/6$).

2.7.2. Constricted “pore throat”

Next, we consider a strip with varying width

$$w(x_1) = \frac{2}{3} + \frac{1}{3} \cos(2\pi x_1),$$

which represents a constricted “pore throat”. As before, we shortly discuss the velocity and pressure distribution of the two phases as well as the movement of the interface, before proceeding with the detailed discussion of the effect of the slip length, of the viscosity ratio and of a dynamic and a hysteretic contact-angle model, varying each individually, while fixing all other parameters as given in [Table 2.3](#). Note that we choose a static contact angle such that fluid I is non-wetting.

While the overall trend is similar to the previous case with constant width, we additionally observe here a strong impact of the geometry on the flow behavior and thus on the effective quantities. In contrast to the constant-width case, the local capillary pressure $p_{c,\text{loc}}$ now depends on the saturation due to the constriction, see [Fig. 2.12](#). Analogously, the phase-pressure difference $\langle p_I \rangle_I - \langle p_{II} \rangle_{II}$ varies in the saturation.

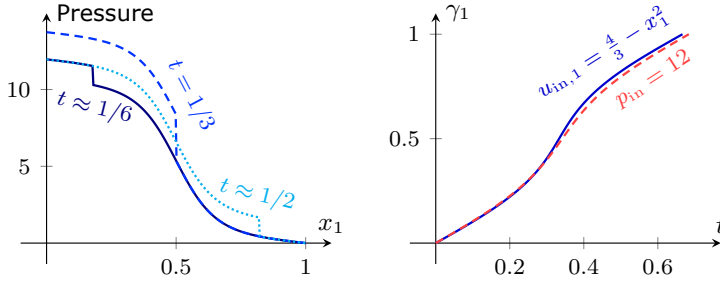


Figure 2.11.: Pressure distribution over length x_1 at various times (*left*) for fixed inlet velocity $u_{in,1} = 4/3 - x_1^2$ and interface position γ_1 over time t (*right*) for fixed inlet velocity $u_{in,1} = 4/3 - x_1^2$ and fixed pressure condition $p_{in} = 12$ for the thin strip of varying width.

The solution in the bulk domains (2.44)–(2.47) for this geometry then reads

$$u_{\alpha,1}(t, \mathbf{x}) = 9q(t) \frac{(c(x_1))^2 + 5c(x_1) + 6 - x_2^2}{(c(x_1) + 2)^2(2c(x_1) + 7)},$$

$$u_{\alpha,2}(t, \mathbf{x}) = \varepsilon 18\pi q(t) \sin(2\pi x_1) \frac{18(c(x_1) + 3)x_2^3 - (c(x_1) + 2)(2(c(x_1) + 3)^2 + 1)x_2}{(c(x_1) + 2)^3(2c(x_1) + 7)^2},$$

for $\alpha \in \{I, II\}$, where $c(x_1) := \cos(2\pi x_1)$, see also Fig. 2.10, while

$$p_I(t, \mathbf{x}) = \frac{3}{c(\gamma_1(t)) + 2} + \frac{9q(t) \sin(2\pi x_1)}{\pi(c(x_1) + 2)} + \frac{24q(t)(\pi H(0.5 - x_1) - \arctan(\frac{\sqrt{5}}{3} \tan(\pi x_1)))}{\pi\sqrt{5}},$$

for $x_1 < \gamma_1(t)$, and

$$p_{II}(t, \mathbf{x}) = \frac{9q(t) \sin(2\pi x_1)}{\pi(c(x_1) + 2)} + \frac{24q(t)(\pi H(0.5 - x_1) - \arctan(\frac{\sqrt{5}}{3} \tan(\pi x_1)))}{\pi\sqrt{5}},$$

for $x_1 > \gamma_1(t)$, where H denotes the Heaviside graph, see also Fig. 2.11. The first velocity component is higher where the width is reduced, while the second component adjusts to the changes in width to maintain the incompressibility, see Fig. 2.10. Note that the second velocity component is of order ε due to the different scaling. Accordingly, the pressure gradients depend on the local width and are steeper around the constriction in the middle. This leads to the s-shaped pressure profiles instead of the linear ones in the constant-width case.

For fixed inlet velocity $u_{in,1} = 4/3 - x_1^2$, i.e., for $q \equiv 1$, the pressure solutions at several times are depicted in Fig. 2.11 together with the evolution of the interface position $\gamma_1(t)$, which is given implicitly by $t = 2\gamma_1(t)/3 + \sin(2\pi\gamma_1(t))/(6\pi)$. Note that the interface position γ_1 moves faster in the vicinity of the constriction, since

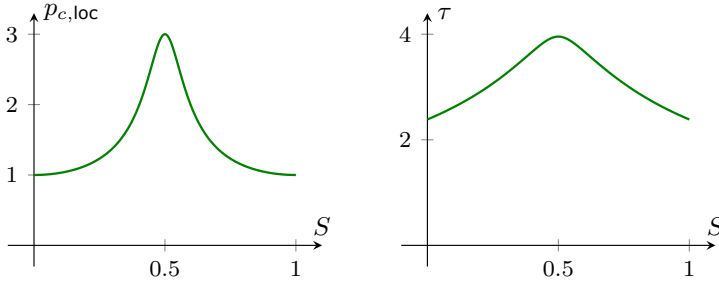


Figure 2.12.: The local capillarity pressure $p_{c,loc}$ (left) and the dynamic coefficient τ (right) increase for saturations below $S = 0.5$, and decreases thereafter. This results from the symmetric constriction of the thin strip.

the average velocity $\bar{u} = q/w$ is higher around the constriction, cf. Fig. 2.10. Furthermore, the movement is very similar to the one obtained with constant inlet pressure $p_{in} \equiv 12$. Hence, we restrict the following discussion to this inlet pressure condition. Note that this larger inlet pressure is necessary to obtain a similar total flux as in the constant-width case, since the width is reduced.

For this geometry, we still can derive relations for the effective quantities obtained in Section 2.6.2. We obtain for the saturation

$$S = \gamma_1 + \frac{1}{4\pi} \sin(2\pi\gamma_1), \quad \partial_t S = \frac{3}{2} q.$$

Since this function $S(\gamma_1)$ has no analytical inverse, there is no closed-form expression for the local capillary pressure $p_{c,loc}$ (2.123) nor for the dynamic coefficient τ (2.124). Their numeric approximations are depicted in Fig. 2.12. Both have a peak at $S = 0.5$, where the interface passes the position $x_1 = 0.5$ with the smallest width. For the local capillary pressure this results from the reciprocal dependence on the local width, while the dynamic coefficient is symmetric due to the symmetric wall and the viscosity ratio $M = 1$. Note that the dynamic effects are much stronger than in the constant-width setting due to the reduced width, which requires larger pressure gradients to maintain the flow. Hence, we conclude that the wall shape has a significant impact, especially on the dynamic effects.

Effect of the slip length

We begin the investigation for various slip lengths λ . As in the previous, constant-width case, the movement of the interface position γ_1 is faster when the slip length is increased, see Fig. 2.13. However, the total flux q is drastically reduced while the interface passes through the constriction due to the higher capillary pressure, cf. Fig. 2.13.

The dynamic coefficient τ is lower when the slip length increases, as shown in Fig. 2.14. In contrast to the constant-width case, it is non-monotonic in the

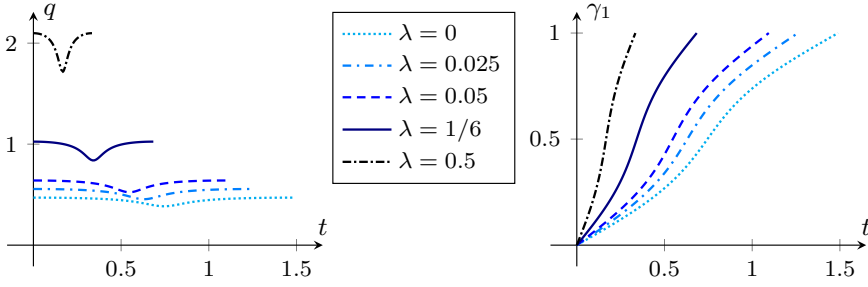


Figure 2.13.: The total flux q is drastically reduced while the interface passes through the constriction due to the larger capillary pressure (*left*). It increases when the slip length λ is increased, so that the movement of the interface position γ_1 is faster (*right*).

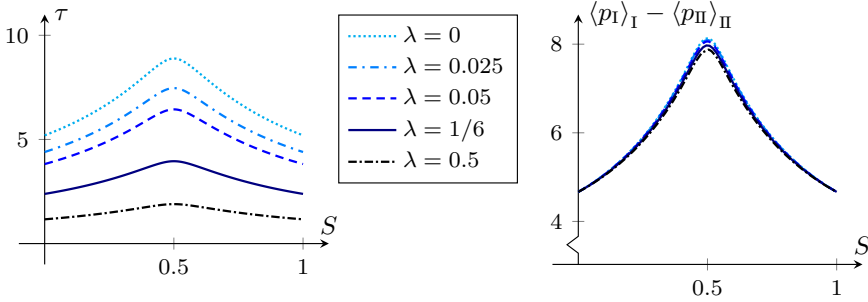


Figure 2.14.: The dynamic coefficient τ decreases for increasing slip length λ (*left*). It is non-monotonic in the saturation. The resulting phase-pressure difference $\langle p_I \rangle_I - \langle p_{II} \rangle_{II}$ is also non-monotonic, but almost the same for all slip lengths (*right*).

saturation, and maximal around $S = 0.5$, i.e., when the interface passes through the constriction around $x_1 = 0.5$. Note that the combination of higher velocity with lower dynamic coefficient leads to almost no changes in the phase-pressure difference $\langle p_I \rangle_I - \langle p_{II} \rangle_{II}$ for all slip lengths, see Fig. 2.14.

Effect of the viscosity ratio

Next, we consider the effect of the viscosity ratio M . As in the previous, constant-wall case, the total flux q is smaller when the viscosity ratio M increases, see also Fig. 2.15. Especially at early times t , one can observe large total fluxes q , when the viscosity ratio is very small ($M \leq 0.1$), since the strip is filled with the extremely mobile fluid II. On the other hand, the total flux is reduced while the interface passes through the constriction, but this effect is very small compared to the effect of viscosity for $M < 1$. As before, the solutions converge for $M \rightarrow 0$ towards the simplified, unsaturated flow model as discussed in Section 2.4.3, see Fig. 2.15.

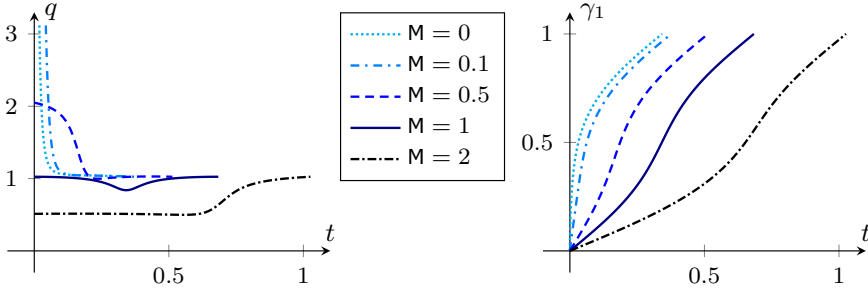


Figure 2.15.: The total flux q is high when the thin strip is mainly filled with the less viscous fluid (*left*). It is smaller while the interface passes through the constriction. When the viscosity ratio M is increased, the interface position γ_1 moves generally slower (*right*).

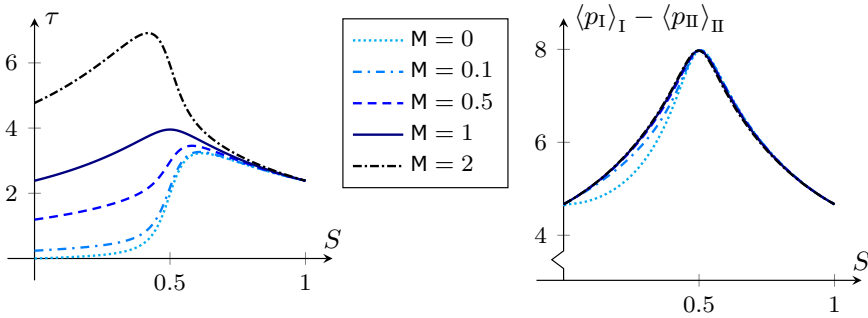


Figure 2.16.: The dynamic parameter τ increases for increasing viscosity ratio M (*left*). It is non-monotonic in the saturation. The resulting phase-pressure difference $\langle p_I \rangle_I - \langle p_{II} \rangle_{II}$ is also non-monotonic, but almost the same for all moderate viscosity ratios (*right*).

Note that we use $\gamma_1|_{t=0} = 10^{-3}$ when $M = 0$ to avoid the degeneration of the interface system (2.74) and (2.75).

The dynamic coefficient τ becomes larger for small saturations S , if the viscosity ratio is larger ($M > 1$), and vice versa for $M < 1$, as shown in Fig. 2.16. The rapid change close to $S = 0.5$ is due to the strong influence of the region around $x_1 = 0.5$, where the thin strip has its minimal width. Note that for small viscosity ratio $M \leq 0.1$ and saturation below 0.4, the dynamic coefficient is almost zero. Furthermore, we observe here non-monotonic behavior of the dynamic coefficient τ for every viscosity ratio, while it is monotonic in the constant-width case. This is due to the interplay between the constricted geometry and the nonlinear dynamic effect (2.124). Finally, note that the combination of higher velocity with lower dynamic coefficient leads to almost no changes in the phase-pressure difference $\langle p_I \rangle_I - \langle p_{II} \rangle_{II}$ for all moderate viscosity ratios, see Fig. 2.16. Only for a very small viscosity ratio $M \leq 0.1$, the phase-pressure difference is slightly lower for

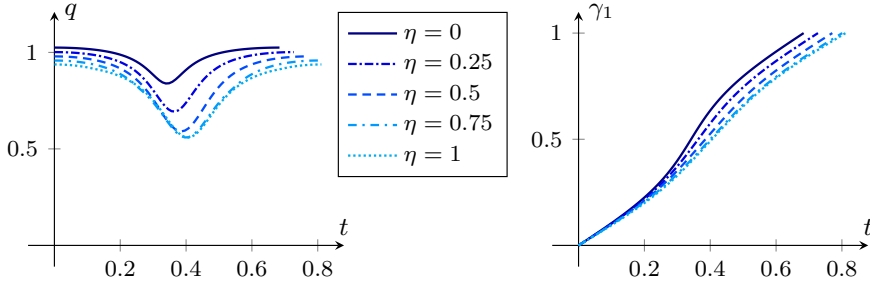


Figure 2.17.: The total flux q decreases for higher values of η , since the (dynamic) local capillary pressure increases (*left*). Accordingly, the interface position γ_1 moves slower (*right*). Due to the constriction, the effect is maximal for $\gamma_1 = 0.5$.

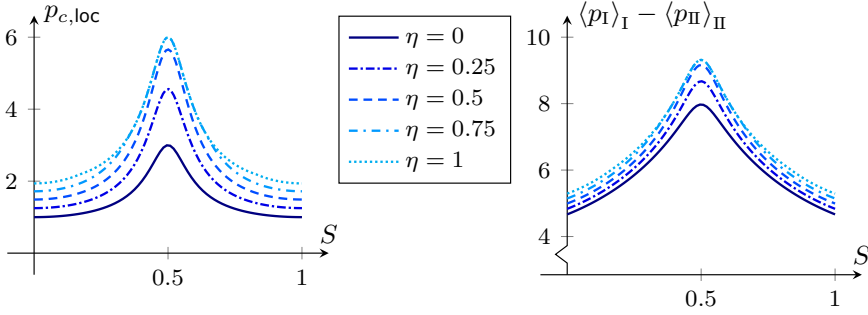


Figure 2.18.: The local capillary pressure $p_{c,loc}$ (*left*) and the phase-pressure difference $\langle p_I \rangle_I - \langle p_{II} \rangle_{II}$ (*right*) increase for increasing dynamic contact angle coefficient η . They attain their maximum at $S = 0.5$, when the interface passes the minimal width.

saturations between 0 and 0.5.

Effect of a dynamic contact angle

We consider the effect of a dynamic contact-angle model. As for the constant-width case, we use (2.133) with $\theta_s = \pi/3$. The total flux q is smaller when η is increased, see Fig. 2.17. This effect is amplified while the interface passes through the constriction.

Although the total flux is smaller, the local capillary pressure $p_{c,loc}$ and the phase-pressure difference $\langle p_I \rangle_I - \langle p_{II} \rangle_{II}$ increase for increasing η , see Fig. 2.18. The maximum is attained at $S = 0.5$, when the interface passes the minimal width. There, the dynamic effect is also the highest. Note that the curves for $\eta = 0.75$ and $\eta = 1$ partly coincide because the dynamic contact angle reaches π in both cases. In a laboratory experiment, this could lead to instabilities and the formation of bubbles or a thin residual film. However, such behavior is beyond the scope of the model

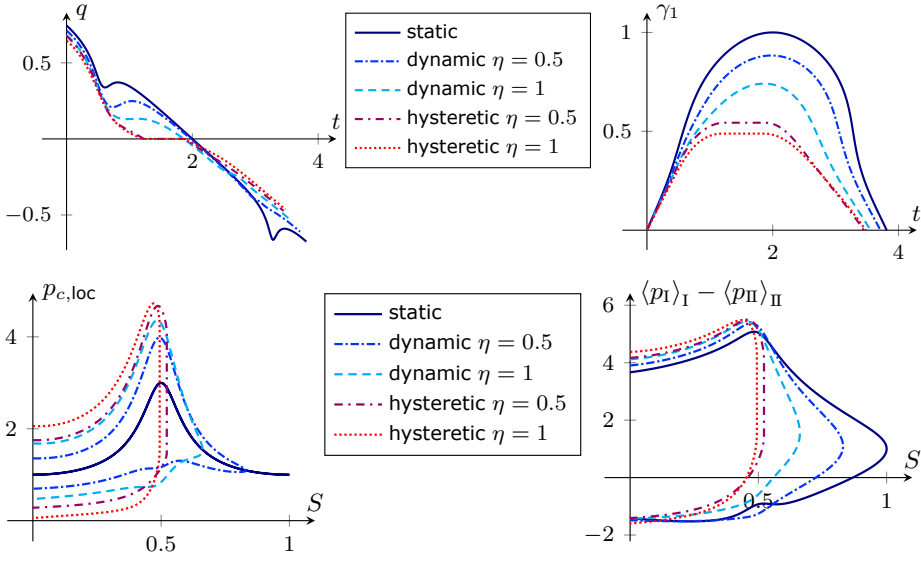


Figure 2.19.: The total flux q (top-left) decreases faster when the interface passes through the constriction. In case of the hysteretic contact-angle model, the interface position γ_1 (top-right) stops in the constriction when the local capillary pressure $p_{c,loc}$ (bottom-left) lies in between the (static) capillary pressures for drainage and imbibition, whereas $p_{c,loc}$ at the maximal saturation is exactly the static capillary pressure for the dynamic models. The phase-pressure difference $\langle p_I \rangle_I - \langle p_{II} \rangle_{II}$ (bottom-right) shows the same qualitative behavior.

presented here.

Effect of a hysteretic contact angle

Finally, we consider the effect of a hysteretic contact-angle model and compare it to the static and dynamic ones. As in the constant-width case, we use the dynamic contact-angle model (2.133) with $\theta_s = \pi/3$ and the hysteretic contact-angle model (2.134) with $\theta_a = \pi/4$ and $\theta_r = 5\pi/12$. We consider a drainage and imbibition cycle by choosing the time-dependent inlet pressure $p_{in}(t) = 9 - 4t$, and stop the simulations when the interface position returns to the inlet. The other parameters are taken from Table 2.3.

As before, the total flux q decreases faster, when the interface passes through the constriction, see Fig. 2.19 (top). Note that the higher capillary pressure when passing the constriction counteracts the drainage, while it increases the imbibition speed. This results in a more negative velocity. In case of the hysteretic contact-angle model, the interface position γ_1 stops in the constriction, while the pressure lies in between the (static) capillary pressures for drainage and imbibition, so that the local capillary pressure $p_{c,loc}$ and the phase-pressure difference $\langle p_I \rangle_I - \langle p_{II} \rangle_{II}$

are multi-valued at the maximal saturation. In contrast, the dynamic model yields a direct switching between drainage and imbibition, when $p_{c,\text{loc}}$ is exactly the static capillary pressure (at the maximal saturation), see Fig. 2.19 (bottom). Hence, hysteresis also leads to higher deviations from the static capillary pressure and thus a smaller maximal saturation.

2.8. Conclusion

We have formally derived the asymptotic solution for the flow of two immiscible fluids in a two-dimensional thin strip and a three-dimensional thin tube of varying width, where the fluid-fluid interface is treated as a free boundary. The obtained effective models form a system of differential algebraic equations for the interface position and the total flux, and are applicable to a wide range of viscosity ratios M , of slip lengths λ , as well as contact angle models. The resulting effective relations are a Darcy-type equation for the local flow, and a capillary pressure - saturation relationship involving dynamic effects.

We have discussed the effects of a varying pore width, of the viscosity ratio, of the slip length as well as of having a dynamic and a hysteretic contact-angle law through numerical experiments. In particular, the results for a varying pore width show that the geometry has a large influence on the effective quantities and their behavior. While dynamic effects occur even for a static contact-angle model, hysteresis in the capillary pressure is only present when a hysteretic contact-angle model is used.

The presented models and effective relations can be generalized to asymmetric domains with heterogeneities in the contact angle. Furthermore, rough walls of type $w^\varepsilon(x_1) = w(x_1) + \varepsilon w^1(x_1/\varepsilon) + \mathcal{O}(\varepsilon)$ would strongly affect the shape and position of the interface. This needs to be investigated in the future. Additionally, it remains to validate the effective models by a direct comparison with numerical simulations of the full model or with experiments in single pores. The latter will be presented in the following chapter for the capillary rise of fluids in circular tubes. Furthermore, the effective models can be used in pore-network models or for upscaling in a bundle-of-tubes model.

Dynamic effects during the capillary rise of fluids in cylindrical tubes

This chapter is based on the following publication [218]:

- S. B. Lunowa, A. Mascini, C. Bringedal, T. Bultreys, V. Cnudde, I. S. Pop, *Dynamic effects during the capillary rise of fluids in cylindrical tubes*, *Langmuir* 38 (2022), pp. 1680–1688. doi.org/10.1021/acs.langmuir.1c02680
Copyright © 2022, American Chemical Society. Reprinted with permission.
Available at pubs.acs.org/articlesonrequest/AOR-G5CA7SBN7FQCRKI7ISQ

The numerical examples were obtained using the following software [216]:

- S. B. Lunowa, *Software for Fitting the Upscaled and Extended Model of Capillary Rise to Experimental Data*, GitHub repository (2021).
github.com/s-lunowa/dynamic-capillary-rise

3.1. Introduction

One hundred years ago, the classical works of Lucas [213], Washburn [322], Rideal [272], and Bosanquet [47] laid the foundation for the description of the capillary-driven flow of fluids in porous structures. Since then, this field of research has gained attention because of its various applications, ranging from water transport in soil and plants, over printing with ink, to oil recovery and CO₂ sequestration. To understand the flow processes in a porous medium, knowledge about the fluid dynamics within its fundamental structures, the single pores, is needed. In these, the surface tension leads to capillary-driven flow. An overview on the topic can be found in the recent review [64].

The model of Lucas and Washburn describes the balance between capillary and hydrostatic pressure, leading to viscous flow until equilibrium at the so-called

Jurin's height is reached. In [109], a formulation for the solution of the Lucas–Washburn equation was derived that remains valid also at late times. The resulting flow close to the fluid-air interface was studied in detail in [206], assuming a spherical meniscus and low Reynolds numbers. Although these basic mechanisms are well-understood, the complex wetting effects lead to a dynamic evolution of the interface, in particular of both its shape and position. An important feature is the contact angle formed between the fluid-air interface and the pore wall. In the aforementioned works, this contact angle is assumed constant. However, experimental results invalidate this assumption, in particular at early times [160, 326]. This is discussed in [223, 224] based on molecular dynamics simulations and the molecular kinetics theory. This theory was also used in [150] to discuss the effect of a dynamic contact angle as a source of interface retardation and viscous dissipation. In [77, 256] several dynamic contact-angle models are compared when applied to the Lucas–Washburn equation.

Furthermore, inertial effects are relevant for early times of capillary rise, as discussed in detail in [260], and for low viscous fluids they can even lead to (damped) oscillations around Jurin's height at late times. Additionally, the end effect at the reservoir (sink flow) was considered for parallel plates and tubes in [325], and a double Dirichlet series representation of the solution was derived. An overview of the different regimes was given in [110, 330]. However, all these models are based on the assumption of a static contact angle.

To incorporate and quantify the influence of the different effects of the dynamic contact angle and of inertia, one should start with a derivation based on the fundamental description within the tube. Considering this detailed pore-scale model, and under suitable assumptions on the non-dimensional parameters like the Reynolds and capillary number, one can employ asymptotic expansion techniques to derive an effective, so-called upscaled model for the relevant quantities like flux, pressure, and rise height. The result is an upscaled model that describes the effective behavior of the relevant physical quantities, which can be validated using experimental data. Thereby, the dynamics of the capillary rise including the detailed evolution of the contact angle becomes predictable. Furthermore, the application of these extended models helps to reduce the observed discrepancy [160] between the experiments and the classical Lucas–Washburn model.

In this chapter, the upscaling of the capillary-driven flow in cylindrical tubes is discussed first. The result is an upscaled model, which is a nonlinear first-order differential equation of the Lucas–Washburn type. This is solved analytically to obtain directly usable solutions. While capillary-rise models with dynamic contact angle have been described in the literature, to the best of the authors' knowledge, this work is the first to derive such a model rigorously by upscaling. The upscaled model is then extended to incorporate inertial effects. To validate the theory, the solutions to the upscaled and to the extended model are compared to the experi-

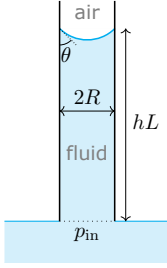


Figure 3.1: Sketch of the tube with radius R . The contact angle θ is formed between the tube wall and the fluid-air interface at rise height hL . The inlet pressure p_{in} is attained between tube and reservoir.

mental results reported in [160]. This includes the simultaneous comparison to the provided height and contact-angle data for different fluids and several radii, which has not been presented before. Finally, the results of the comparison including uncertainties and limitations are discussed. Additional details of the comparison are presented in [Appendix B](#).

3.2. Mathematical models

First, the upscaled model for the capillary-driven flow in a cylindrical tube and its analytical solution are discussed. This is based on the detailed derivation in [Section 2.5](#). In particular, the model includes a dynamic contact angle and slip. Subsequently, the upscaled model is extended to incorporate inertial effects.

3.2.1. Upscaled model and analytic solution

The flow of a fluid in a thin, vertical tube, driven by the surface tension at the fluid-air interface, can be modeled by the Navier-Stokes equations defined in a time-dependent domain, where the fluid-air interface is a free boundary, see [Fig. 3.1](#). Under the assumptions given in [Section 2.5](#), in particular assuming a moderate Reynolds number, one can derive the solution by a matched asymptotic expansion for the limit of a vanishing radius-to-length ratio $\varepsilon = R/L \ll 1$ (R being the tube radius and L Jurin's height). The result is Hagen-Poiseuille flow driven by the difference between the surface tension and the hydrostatic pressure. In the dimensionless form, the evolution of the fluid rise height h is then governed by [\(2.109\)](#) and [\(2.116\)](#). In the context considered here, there holds (approximately)

$$h = \gamma_z, \quad w \equiv 1, \quad \mathbf{M} = 0, \quad \mathbf{R} = 0,$$

so that [\(2.109\)](#) and [\(2.116\)](#) simplify into

$$p_{in} - Gh - \frac{8h}{1 + 4\lambda} \frac{dh}{dt} = -\frac{2 \cos(\theta(\frac{dh}{dt}))}{\text{Ca}}. \quad (3.1)$$

Here p_{in} is the pressure at the inlet (bottom, see Fig. 3.1), λ denotes the slip length at the tube wall, G and $\overline{\text{Ca}}$ are the effective gravitational and capillary number. Note that the dynamic contact angle θ is measured in the fluid (thus the change in sign compared to (2.116)). Furthermore, it may depend on the velocity of the interface. Furthermore, (3.1) resembles the relation derived by Washburn [322], based on macroscopic arguments. However, Washburn discussed only the case of a static contact angle, whereas here a dynamic contact-angle model is incorporated.

In the context of capillary rise experiments, the pressure at the inlet is approximately atmospheric, i.e., $p_{\text{in}} = 0$. The typical length scale is given by the equilibrium or Jurin's height $L = 2\sigma \cos(\theta_s)/(\rho g R)$, attained as $t \rightarrow \infty$, and which is depending on the fluid-air surface tension σ , the static contact angle θ_s , the density ρ of the fluid, the gravitational acceleration $g = 9.81 \text{ m/s}^2$, and the tube radius R . The characteristic (viscous) velocity scale is $U = \rho g R^2/\mu$. These characteristic scales yield (cf. Table 2.1)

$$\varepsilon = \rho g R^2/(2\sigma \cos(\theta_s)), \quad \text{Re} = 2\rho\sigma R \cos(\theta_s)/\mu^2, \quad G = 1, \quad \overline{\text{Ca}} = 2 \cos(\theta_s).$$

Therefore, (3.1) becomes

$$\frac{8h}{1+4\lambda} \frac{dh}{dt} = \frac{\cos\left(\theta\left(\frac{dh}{dt}\right)\right)}{\cos(\theta_s)} - h, \quad (3.2)$$

for all $t > 0$. Clearly, the solution $h = h(t)$ depends on the contact-angle model. However, the specific choice of this model is uncertain without much reference data, because the differences resulting after fitting the different models are typically very small [42, 256]. For simplicity, a linear model in the velocity is considered here, which was also used frequently as a simplification of the molecular kinetics theory [42, 150, 151, 223, 224, 256, 266], valid at low velocities. Specifically,

$$\cos(\theta(v)) = \cos(\theta_s) - \eta \overline{\text{Ca}} v,$$

where the dynamic parameter $\eta \geq 0$ denotes the strength of the linear response due to the interface velocity $v = \frac{dh}{dt}$. Note that this model arises naturally for all possible contact-angle models after linearization using the relation $\cos(\tilde{\theta}(v)) \approx \cos(\tilde{\theta}(0)) - \sin(\tilde{\theta}(0)) \frac{d\tilde{\theta}}{dv}(0) v$ and therefore is generic. Other models could be used as well; however, the advantage of the linear model is that the resulting equation can be solved analytically, as discussed in the following. With this contact-angle model, the rise model (3.2) becomes

$$\left(\frac{8h}{1+4\lambda} + 2\eta \right) \frac{dh}{dt} = 1 - h, \quad (3.3)$$

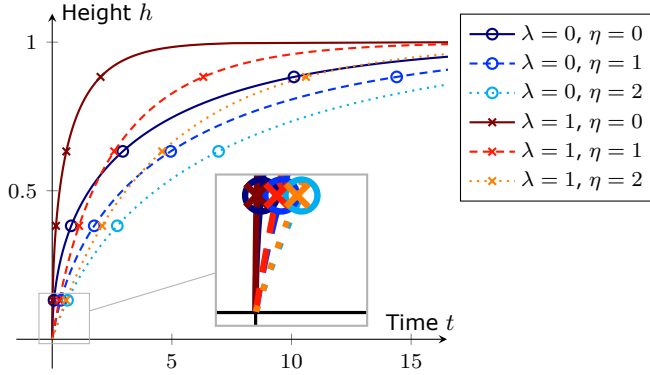


Figure 3.2.: The height of the capillary rise given by (3.5) increases faster for higher slip length λ . The dynamic parameter η retards the rise and determines the initial velocity at time $t = 0$.

for all $t > 0$. A natural initial condition is

$$h(0) = 0. \quad (3.4)$$

Observe that, because $h \equiv 1$ is an equilibrium solution to (3.3), the solution to the initial value problem (3.3)–(3.4) remains below 1 for all times t . Moreover, h is increasing. By separation of variables, the solution to (3.3)–(3.4) is obtained in implicit form

$$(1 - h(t)) \exp\left(\frac{4h(t)}{(1 + 4\lambda)\eta + 4}\right) = \exp\left(-\frac{(1 + 4\lambda)t}{2(1 + 4\lambda)\eta + 8}\right). \quad (3.5)$$

Because h is monotone, using (3.5) one can express t as a function of h , namely

$$t = t(h) = -\frac{8h}{1 + 4\lambda} - \frac{2(1 + 4\lambda)\eta + 8}{1 + 4\lambda} \ln(1 - h).$$

At early times, this yields

$$t \approx 2\eta h + \left(\eta + \frac{4}{1 + 4\lambda}\right) h^2.$$

If $\eta = 0$, this resembles the classical Lucas–Washburn equation. If $\eta > 0$, the first term implies a linear time–height relation at early times, when $h \ll 1$, and therefore, quadratic terms can be neglected. Figure 3.2 illustrates possible solutions. The dynamic parameter η determines the velocity of the rise in the beginning, because (3.3) yields $\frac{dh}{dt}(0) = \frac{1}{2\eta}$. In particular, it is singular if $\eta = 0$, because inertial terms and the movement of the air are neglected. On the other hand, the influence of the slip length λ on the velocity increases with increasing height h . Furthermore, for $\eta > 0$, this yields an initial contact angle $\theta = 90^\circ$ at time $t = 0$.

3.2.2. Extended model including inertial effects

The upscaled model described above requires the Reynolds number to be small. In case of a low viscosity, or when the tube radius increases, the Reynolds number becomes large, so that one cannot neglect inertial effects. In that situation, the up-scaling procedure does not yield a closed expression for the height of the capillary rise, as the system remains fully coupled. Instead, an empirical extension of the up-scaled model is used, based on macroscopic considerations [47, 110, 150, 266, 330]. In these references, the balance between hydrostatic, inertial and capillary forces was considered assuming Hagen–Poiseuille flow and a spherical meniscus. In this context, the resulting balance reads

$$\mathcal{I} \frac{d}{dt} \left(h \frac{dh}{dt} \right) + \left(\frac{8h}{1+4\lambda} + 2\eta \right) \frac{dh}{dt} = 1 - h, \quad (3.6)$$

where $\mathcal{I} = \varepsilon^2 \text{Re} = \rho^3 g^2 R^5 / (2\mu^2 \sigma \cos(\theta_s))$ is the inertial coefficient (cf. also (2.80)). Note that the denominator $(1 + 4\lambda)$ accounts for slip, and the term $2\eta \frac{dh}{dt}$ is due to the linearized contact-angle model. Note that this extended model (3.6) is closely related to the modified Lucas–Washburn equation discussed in [223, 224]. However, they considered a model that does not account for a slip length λ .

With (3.4), this nonlinear second-order differential equation (3.6) becomes degenerate. Furthermore, one needs to specify a second initial condition, similar to the initial velocity. For this purpose, one can use an asymptotic analysis carried out for $t \rightarrow 0$ with ansatz $h(t) = ct^\alpha + o(t^\alpha)$ [266, 330]. Equating the leading order terms yields $h(t) \sim t/(\eta + \sqrt{\eta^2 + \mathcal{I}})$, and hence

$$\left. \frac{dh}{dt} \right|_{t=0} = \frac{1}{\eta + \sqrt{\eta^2 + \mathcal{I}}}. \quad (3.7)$$

To solve the initial value problem (3.4), (3.6), and (3.7) numerically, it is reformulated as a system of nonlinear first-order differential equations in the variables $w := h^2$ and $v := \frac{dw}{dt}$. Equation (3.6) then becomes

$$\frac{dw}{dt} = v, \quad \frac{dv}{dt} = \frac{2}{\mathcal{I}} \left(1 - \sqrt{w} - \left(\frac{4}{1+4\lambda} + \frac{\eta}{\sqrt{w}} \right) v \right).$$

To avoid the singularity at $w = 0$, the initial conditions used here are $w(0) = 10^{-12}$ and $v(0) = 2\sqrt{w(0)}(\sqrt{\eta^2 + \mathcal{I}} - \eta)/\mathcal{I}$. Note that this choice does not significantly affect the result as long as $w(0)$ is sufficiently small. The implementation of the numerical solver [216] is done in Python using the packages NumPy 1.21.0 [152] and SciPy 1.3.3 [320]. The chosen time integrator is an implicit multi-step variable-order (1–5) BDF method.

Fluid	ρ [kg/m ³]	μ [Pa s]	σ [N/m]	R [mm]	θ_s [deg]
Glycerol	1260	1.0111	0.06347	0.250, 0.500, 1.000	5.63
Soltrol 170	774	0.0026	0.02483	0.375, 0.500, 0.650	9.79
Water	997	0.0011	0.07280	0.375, 0.500, 0.650	9.99

Table 3.1.: Density ρ , viscosity μ , surface tension σ of the fluids, and the experimental tube radii R reported in [160], and the static contact angle θ_s extracted from late-time data.

3.3. Comparison with experimental data

To validate the suggested models, the solutions are compared to the experimental data reported by Heshmati and Piri [160], where the capillary rise of glycerol, Soltrol 170, and water in vertical glass tubes with constant radii was investigated. These results include both the rise height and the contact angle over time.

The comparison with experimental data is done in three steps. First, the reported physical properties are used for the dimensionless scaling (see also Table 3.1). Note that the scale ratio ε was below 0.1 in all cases. Second, the late-time data is assumed to be near equilibrium, so that the static contact angle can be extracted from it for each of the three fluids. Note that the resulting static angles ($< 10^\circ$) hardly influence the rise height ($< 2\%$), but strongly affect the dynamic contact angle. In the third step, the solutions of the suggested models are matched to the experimental data by fitting the remaining parameters, namely, the dynamic contact-angle parameter η and the slip length λ . For this, for each fluid and each radius separately, a non-linear least-squares fitting of the rise height (h -fit), of the contact angle (θ -fit), and of both at the same time (both-fit) is performed. Thereby, one can compare the parameter values obtained for the different fits as well as for the different radii to investigate the predictive abilities of the suggested models. The implementation of the procedure [216] is done in Python using the packages pandas 1.3.0 [268] and LMFIT 1.0.2 [240].

To illustrate the effect of the dynamic contact-angle model, the classical Lucas-Washburn (LW) solution is also provided. It is obtained from (3.5) when taking $\eta = 0$ and $\lambda = 0$, using the dimensionless scaling and static contact angle found in the first and second step for the comparison.

3.3.1. Glycerol

In the first set of measurements, glycerol was used as the rising fluid. Because of the high viscosity, the inertial effects are negligible ($\mathcal{I} < 1.5 \cdot 10^{-3}$), so that the solutions to the upscaled model (3.5) and to the extended one (3.6) coincide. Therefore, only the results for the upscaled model are presented in Table 3.2. Note that the simultaneous fitting of the parameters η and λ results in dimensionless

R [mm]	h -fit		θ -fit		both-fit	
	η	χ^2_ν	η	χ^2_ν	η	χ^2_ν
0.25	0.402 ± 0.010	0.059	0.525 ± 0.008	0.647	0.519 ± 0.006	0.388
0.50	2.356 ± 0.066	0.327	2.151 ± 0.069	2.105	2.183 ± 0.049	1.203
1.00	5.935 ± 0.383	1.226	10.077 ± 0.613	3.985	8.787 ± 0.461	4.053

Table 3.2.: Best-fit parameter η (\pm estimated standard deviation) and the reduced residual χ^2_ν when fitting the upscaled model to the experimental data of the height (h -fit), the contact angle (θ -fit) and both (both-fit), for the glycerol experiments.

slip lengths $\lambda < 10^{-2}$, except for the both-fit at the radius 1.0 mm, which yields the highly uncertain $\lambda = 0.026 \pm 0.109$ (value \pm estimated standard deviation). Hence, slip is negligible and ignored in the further discussion.

The comparison of the experimental data with the fitted upscaled model (3.3) and the classical Lucas–Washburn model in Fig. 3.3 illustrates the relevance of the dynamic contact angle. While both models match the late-time data when the static contact angle is approached, only the upscaled model with dynamic contact angle agrees with the early-time data. In particular, it matches reasonably both the rise height and the contact angle for all three radii. Note that the three fit-types (h , θ , both) yield different parameters, but the resulting solutions only differ on the scale of the scatter in the experimental data (cf. Appendix B). Note that the increase in η with increasing radius is expected, as the dimensional dynamic parameter should be approximately constant. This effect is discussed below for all fluids.

3.3.2. Soltrol 170

In the second set of measurements, Soltrol 170 was used as the rising fluid. In contrast to the previous case, the extended model differs from the upscaled one ($\mathcal{I} = 1.0, 4.2, 15.7$), but for all radii the best-fit parameters coincide within 1.5 standard deviations ($< 5\%$ difference), while the residuals are rather lower (-40% to $+30\%$ difference, avg. -6%). The minor differences are illustrated in Fig. 3.4, and the results for both models are reported in Table 3.3. Note that the fit of the dimensionless slip length yields $\lambda < 10^{-6}$ in all cases, which is again negligible and thus ignored.

For Soltrol, the fitted upscaled model (3.5) matches the experimental data almost perfectly, while the classical Lucas–Washburn model predicts only the stationary solution well (see Fig. 3.4). In particular, the upscaled model with dynamic contact angle agrees with the data of both the rise height and the contact angle for all three radii and at all times. For more details, see also Appendix B. The fit of the extended model coincides with that of the upscaled model. Only at very early times (until 0.05 s) does the extended model predict a slightly lower contact angle. These

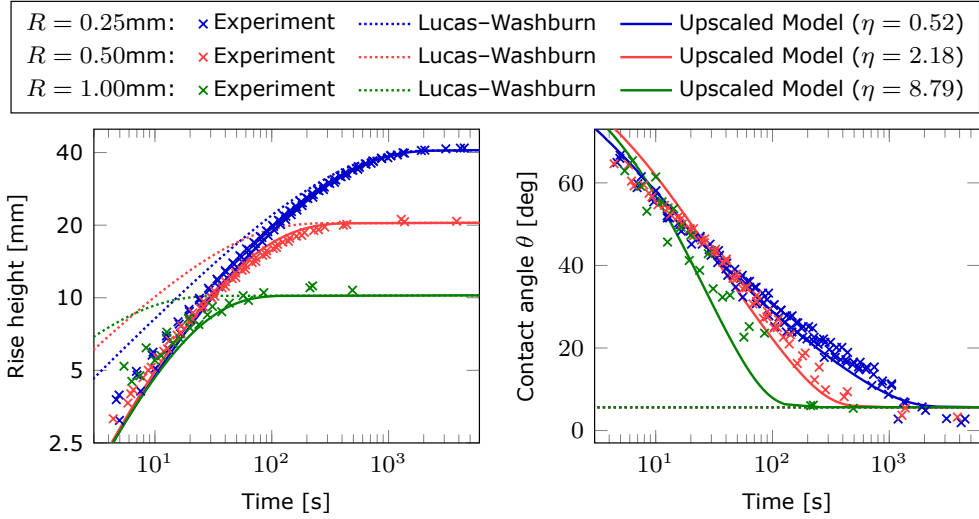


Figure 3.3.: The experimental data for glycerol is matched well by the upscaled model (both-fit). Especially at early times, the representation of the rise is much better than the one for the classical Lucas-Washburn model.

R [mm]	h -fit		θ -fit		both-fit	
	η	χ^2_ν	η	χ^2_ν	η	χ^2_ν
0.375	1.464 ± 0.067	0.313	1.250 ± 0.058	2.153	1.273 ± 0.042	1.232
0.500	2.521 ± 0.080	0.196	2.358 ± 0.081	1.042	2.386 ± 0.056	0.603
0.650	4.588 ± 0.162	0.414	3.963 ± 0.143	1.370	4.098 ± 0.108	0.951
0.375	1.437 ± 0.005	0.340	1.241 ± 0.027	2.239	1.261 ± 0.044	1.275
0.500	2.430 ± 0.075	0.207	2.309 ± 0.062	0.623	2.330 ± 0.045	0.403
0.650	4.370 ± 0.016	0.537	3.830 ± 0.024	1.183	3.944 ± 0.122	0.899

Table 3.3.: Best-fit parameter η (\pm estimated standard deviation) and the reduced residual χ^2_ν when fitting the upscaled model (*top rows*) and the extended model (*bottom rows*) to the experimental data of the height (h -fit), the contact angle (θ -fit) and both (both-fit), for the Soltrol 170 experiments.

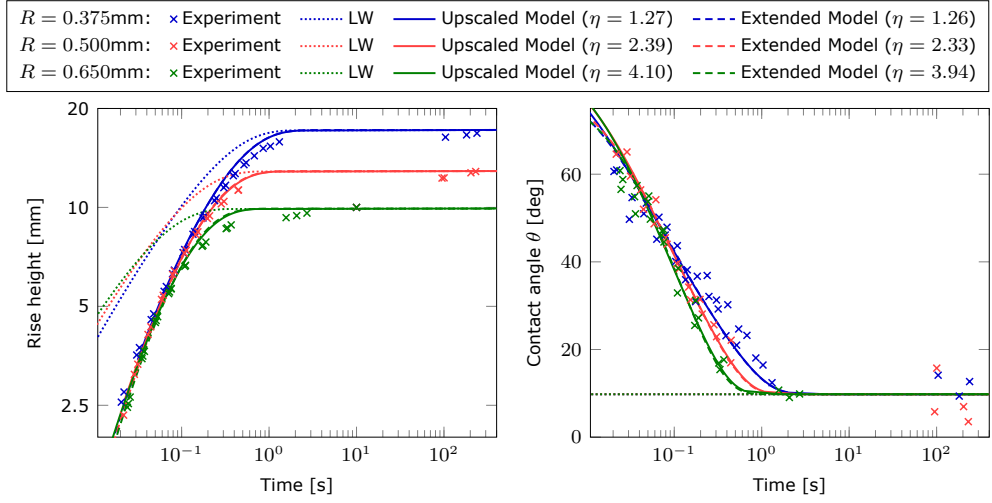


Figure 3.4.: The experimental data for Soltrol 170 is matched almost perfectly by the upscaled model (both-fit), while the classical Lucas–Washburn model (LW) describes only the stationary solution well (after 1 s). For the upscaled and the extended models after fitting, the solutions practically coincide.

early-time dynamics are especially relevant for larger radii and less viscous fluids like water, as shown and discussed below.

3.3.3. Water

In the last set of measurements, distilled water was used as the rising fluid. In contrast to the previous cases, the extended model differs significantly from the upscaled one ($\mathcal{I} = 4.1, 17, 64$), see Fig. 3.5. The upscaled model (both-fit) matches only the contact angle and late-time height (after ≈ 0.05 s). The experimental data is much better represented by the extended model; hence, only these results are reported in Table 3.4. More details and the results of the upscaled model can be found in Appendix B. Note that the fit of the dimensionless slip length was inconsistent ($\lambda < 0.15$) with generally large standard deviation. For the θ -fits, the slip was negligible ($\lambda < 10^{-9}$), while the other fits suggest the occurrence of an effective slip, which might be due to pre-wetting films, as discussed below.

For water, the fitted extended model matches reasonably the experimental data, although the rise height is slightly overpredicted (+10%) for the radius $R = 0.65$ mm, see Fig. 3.5. In particular, note that the model predicts an overshoot (between 0.2 and 0.4 s). The experimental data does not show this behavior. Instead, the rise seems delayed compared to the other experiments (3.4 mm vs. 6.5–7.4 mm at time 0.016 s).

R [mm]	h -fit		θ -fit		both-fit	
	η	χ^2_ν	η	χ^2_ν	η	χ^2_ν
0.375	0.162 ± 0.005	0.058	0.377 ± 0.017	2.054	0.367 ± 0.013	1.143
0.500	0.111 ± 0.020	0.153	0.498 ± 0.037	3.914	0.476 ± 0.026	2.249
0.650	2.849 ± 0.064	0.234	1.052 ± 0.079	4.595	1.248 ± 0.079	4.203

Table 3.4.: Best-fit parameter η (\pm standard deviation) and the reduced residual χ^2_ν when fitting the extended model (without slip) to the experimental data of the height (h -fit), the contact angle (θ -fit) and both (both-fit), for the water experiments.

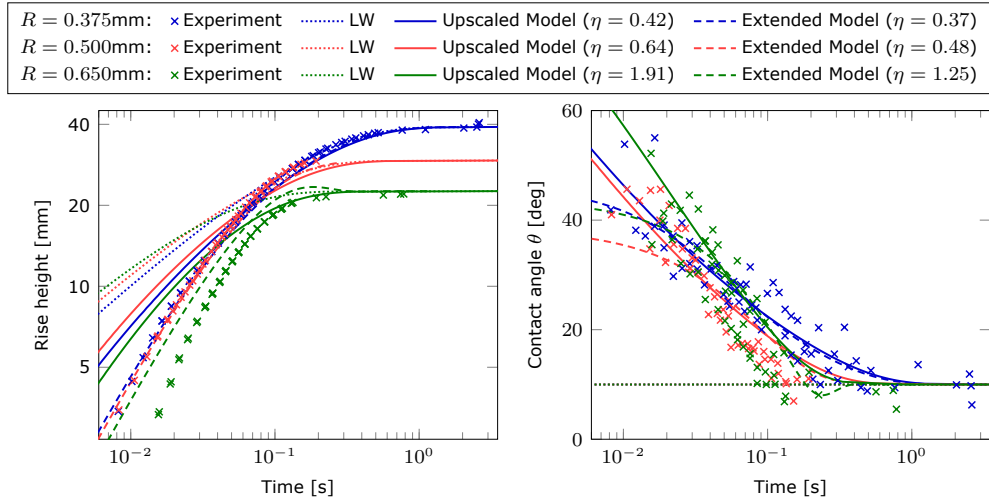


Figure 3.5.: The experimental data for water is matched well by the extended model (both-fit), while the upscaled model (both-fit) matches only the contact angle and late-time data (after ≈ 0.05 s). The classical Lucas-Washburn (LW) model describes only the stationary solution well (after 0.1 s).

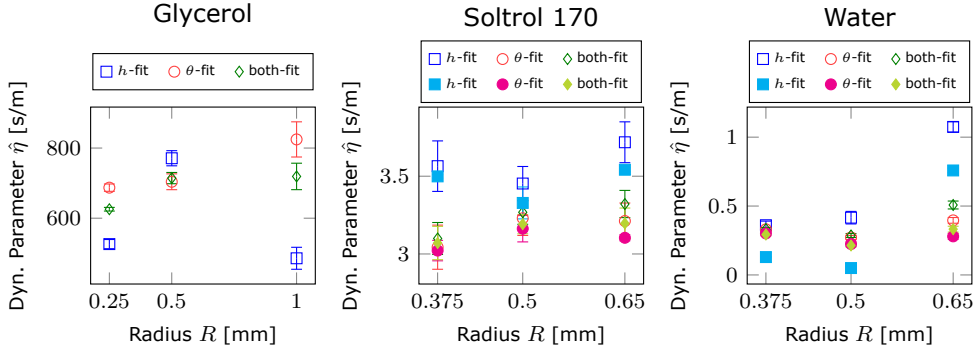


Figure 3.6.: The dimensional dynamic parameter $\hat{\eta} = \eta/U$ of the models (*empty*: upscaled, *filled*: extended) fitted to the experimental data of the height (h -fit), the contact angle (θ -fit) and both (both-fit). Observe that these parameters vary significantly from one fluid to another, but appear to not depend on the tube radius.

3.4. Discussion

In the following, the physical basis of the fitted dynamical parameter is elaborated, and further aspects that might have an impact on the experimental and theoretical data are discussed. In particular, the influence of the initial transient regime and of the meniscus shape are considered, as well as possible wetting films and resulting slip in the case of water. Finally, the uncertainty and limitations of the suggested models and of the fitting are addressed.

3.4.1. The dynamic parameter as physical property

The dynamic parameter η obtained by fitting can be interpreted as a physical property of the fluid system. For this, we use dimensional quantities denoted by a hat. Although the different fitting criteria, namely, the height, the contact angle, or both, provide optimal parameters with significant variation, the dynamic parameter $\hat{\eta}$ [s/m] (scaling $\mu/(\rho g R^2)$) seems to be independent of the tube radius, see Fig. 3.6. This agrees with the results reported in [150, 151], where the Lucas–Washburn equation with dynamic contact angle was compared with experiments of ethanol, water and silicon oil in glass tubes, and those obtained in [224] for molecular dynamics simulations. Further experimental data considering a larger range of radii and hence velocities are necessary to confirm this hypothesis.

Note that the closely related linearized molecular-kinetic theory [42, 150, 151, 223, 224, 266] yields the dynamic contact-angle model

$$\cos(\theta_s) - \cos(\theta) = \xi \hat{v},$$

where \hat{v} denotes the contact line velocity. Here, the intrinsic friction coefficient ξ [s/m] is proportional to the ratio μ/σ of the viscosity to the fluid-air surface tension. Therefore, one expects an almost constant ratio $\hat{\eta}\sigma/\mu$ for all fluids, which is also found for the fitted parameter $\hat{\eta}$, because the ratio is ca. 30–70 for glycerol, ca. 25–35 for Soltrol 170 and ca. 5–50 for water. Finally, it was demonstrated in [223] that neglecting the dynamic parameter can lead to significant underestimation of the effective pore radius in porous media.

3.4.2. The influence of the initial transient regime

At the start of the experiment, the tube touches the surface of the fluid in the reservoir. This topological change initiates the rise and the meniscus shape, which are hence strongly affected by the (touch) speed and the exact (nanometric) surface of the tube tip. In the suggested models, this initial transient regime is neglected, and a stable Hagen–Poiseuille flow profile and a spherical meniscus are assumed to form quasi-instantaneously. To understand the details better, accurate micro-scale analysis and simulations in the initial stage are necessary. For micro-gravity experiments, three successive phases were found in [297]: a quadratic dependence of the meniscus height on time ($h \sim t^2$), followed by a linear increase ($h \sim t$), and, finally, the Lucas–Washburn behavior ($h^2 \sim t$).

However, the fitting results suggest that the initial transient regime is indeed negligible here, especially for glycerol and Soltrol 170 (cf. the above comparison), for which one could even neglect inertia. Nevertheless, for large radii, as well as less viscous fluids, such as water, these effects might be significant. In particular, the water experiment with largest radius ($R = 0.65$ mm) shows deviations from an initially linear height-time relation (see Fig. 3.5 and Appendix B). Additionally, for such regimes, the proper choice of the (numerical) initial conditions for the extended model (3.6) might be important. Here, we used asymptotic analysis to approach $t = 0$, and a sufficiently small numerical regularization with negligible impact on the solution. Further investigation can lead to conditions (or extensions) that include the transient effect.

3.4.3. The meniscus shape

The meniscus shape is assumed spherical for the experimental measurement of the contact angle, as well as for the discussed models. However, this shape might be deformed due to the influence of the inertia and gravity. For glycerol and Soltrol 170, the agreement of the experimental contact-angle data and the fitted upscaled model gives confidence that these effects can be neglected. For water, the experimental contact-angle data has a rather large scatter, and the differences between experiments and fitted models are higher (cf. Fig. 3.5 and Appendix B). For experiments with water in glass tubes of lower radius ($R = 0.15$ mm and

$R = 0.2$ mm), it was reported in [326] that the rise velocity is too high to have a spherical meniscus shape. Therefore, the obtained results for the contact angle of water should be treated with caution.

3.4.4. Wetting films and slip

For glycerol and Soltrol 170, the tubes used in [160] were vacuum-dried immediately before the experiments, so that no pre-wetting films were present. The model fitting resulted accordingly in negligible slip lengths, $\lambda < 10^{-2}$, which translates into a dimensional slip length below 1 μm . In contrast, the tubes for the experiments with water were only partially dried using a paper filter, to avoid a contamination affecting the contact angle and the equilibrium rise [160]. Hence, heterogeneous pre-wetting films of water could possibly be present in the tubes. This can influence the contact angle and the meniscus shape and induces difficulties for the measurements and the modeling, so that a direct comparison becomes more involved.

Additionally, the presence of wetting films would reduce the dissipation from the formation of water-glass interfacial area. Hence, the water rises faster, which corresponds to an effective slip in the presented models. In the fitting of the extended model using the height data (h -fit and both-fit), indeed, a relevant slip length up to 0.15 (dimensional about 0.1 mm, cf. Appendix B) was observed. However, the dynamic coefficient η and the slip length λ are strongly correlated, such that the slip length in the model is difficult to relate to the physical behavior.

Furthermore, note that negative effective slip was observed for nanometric pores [329]. There, the effective slip length depends on the wettability and the viscosity, which considerably differs for confined water near walls and for bulk water. Here, however, the fitting did not allow for negative slip lengths, since these effects were found to be only relevant for radii on nanometer scale [329].

3.4.5. Uncertainty and limitations of the models and of the fitting

Because the suggested models are derived in leading order for $\varepsilon \ll 1$, errors in the order of ε are expected (here $\varepsilon < 10^{-2}$). Furthermore, a linearized dynamic contact-angle model is chosen here for simplicity. A higher accuracy can be obtained using a more sophisticated contact-angle model, which, itself, needs further investigation and validation [42, 256]. Additionally, a Hagen–Poiseuille flow is assumed for the extended model. Deviations due to inertial effects are ignored, but might affect the inertial coefficient \mathcal{I} . This could explain the overshoot observed for the extended model in the case of water with tube radius $R = 0.65$ mm (cf. Fig. 3.5), which is not present in the experiment.

Furthermore, the static contact angle is highly sensitive to the used materials. In contrast to the total wetting ($\theta = 0^\circ$) assumed in [160], the values extracted from

the experiments range between 5° and 10° . Note that, for water-air-glass systems, even a static contact angle of 20° to 30° was reported in [207]. Although this has only a minor influence on the rise height, it affects the fitting for the dynamic contact angle.

3.5. Conclusion

The upscaled model of capillary-driven flow in circular cylindrical tubes extends the classical Lucas–Washburn theory by incorporating a dynamic contact angle. Using a simple relation between the contact angle and the velocity of the moving contact line, an analytical expression for the capillary rise over time was derived. Based on empirical arguments, the mathematical model was extended to account for inertial effects.

To validate the models, the solutions were compared to the experimental data observed in [160]. In contrast to the Lucas–Washburn model, the models with dynamic contact angle do match the experimental data, both the rise height and the contact angle, even at early times. The fitting procedure requires only one parameter for the dynamic contact angle. In particular, the findings suggest that this parameter depends only on the physical properties of the involved fluids (and of the tube), but is independent of geometrical features, such as the radius of the tube. Therefore, the presented models can be used to predict capillary-driven flow in tubular systems upon knowledge of the underlying dynamic contact-angle relation.

PART II

Numerical Methods at the Darcy Scale

Linearized domain decomposition methods for two-phase porous media flow models involving dynamic capillarity and hysteresis

This chapter originated from the master's thesis [214] and is based on the following publications [219, 220]:

- S. B. Lunowa, I. S. Pop, B. Koren, *Linearized domain decomposition methods for two-phase porous media flow models involving dynamic capillarity and hysteresis*, Computer Methods in Applied Mechanics and Engineering, 372 (2020), 113364. doi.org/10.1016/j.cma.2020.113364
Copyright © 2020, Elsevier B.V.
- S. B. Lunowa, I. S. Pop, B. Koren, *A linear domain decomposition method for non-equilibrium two-phase flow models*, in: Numerical Mathematics and Advanced Applications ENUMATH 2019, Springer, Cham (2021), pp. 145–153. doi.org/10.1007/978-3-030-55874-1_13
Copyright © 2021, Springer Nature.

4.1. Introduction

The mathematical models for porous-media flow at the Darcy scale typically consist of coupled nonlinear differential equations, which may degenerate and change type in an a-priori unknown manner, depending on the solution itself. While the complexity increases further when dynamic and hysteretic effects are incorporated, largely varying or even discontinuous physical properties pose additional difficul-

ties. There is a strong demand for the mathematical design and analysis of suitable, robust computational methods.

Newton based solvers cannot be applied directly to these problems due to severe constraints on the time step sizes to ensure convergence [264]. A simple fixed-point iteration, the L-scheme, has been proposed as robust, but only linearly convergent alternative, see Section 1.5.3. The method is independent of the spatial discretization. It is combined with the (mixed) finite element method in [70, 254] for Richards' equation with equilibrium capillary pressure and two-phase flow with dynamic capillarity, respectively. In [187], the L-scheme is used together with a discontinuous Galerkin method for the two-phase system with dynamic effects, neglecting hysteresis. A multi-point flux approximation finite volume method is applied in [71] for two-phase flow incorporating dynamic capillarity.

For layered soil, it seems natural to additionally apply a domain decomposition method to decouple the essentially different layers and thereby speeding up the convergence. Domain decomposition methods have been used and optimized for a wide range of applications, see Section 1.5.4. Such methods can be used after temporal discretization for porous media equations, as proposed in [37, 65] for a simplistic setting, while Richards' equation and the two-phase flow equations are considered in [4, 6], where a-posteriori error estimates and multi-rate time stepping methods are derived. In [285, 286], the domain decomposition is integrated in the linearization process for both Richards' equation and two-phase flow, and the convergence is proven rigorously. For single-phase flow in a fractured medium, a domain decomposition method is used together with the L-scheme in [5] to solve the mixed-dimensional problem.

Here, we propose two linearization and domain decomposition schemes for two-phase flow in block-heterogeneous porous media. The model includes dynamic effects and hysteresis in the capillary pressure formulation. These methods are independent of the concrete space discretization and avoid the use of derivatives as in Newton based iterations. By maintaining the formulation of the equations in physical variables like saturation and pressure, instead of using the Kirchhoff transformation, these schemes are particularly accessible for direct application in the engineering context.

This chapter is structured in the following way: The two-phase flow model, the notation and the assumptions are introduced in Section 4.2. In Section 4.3, the temporal discretization by the θ -scheme is stated. Based on this, the iterative schemes for finding the solutions to the nonlinear semi-discrete equations are derived. The analysis in Section 4.4 contains proofs for the existence of unique solutions to the problems defining the linear iterations and for the convergence of the iterative solutions. Section 4.5 addresses the numerical validation of the theoretical results by several examples in two spatial dimensions. Finally, Section 4.6 completes this chapter with a discussion and outlook.

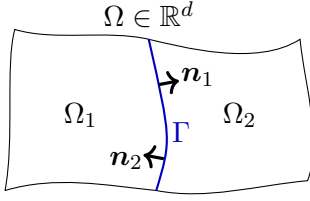


Figure 4.1: Schematic sketch of a block-heterogeneous domain $\Omega = \Omega_1 \cup \Gamma \cup \Omega_2$ with interface Γ .

4.2. Modeling of non-equilibrium two-phase flow in porous media

Let the domain $\Omega \subset \mathbb{R}^d$ for $d \in \mathbb{N}$ with a Lipschitz boundary $\partial\Omega$ and the final time $T > 0$ be fixed. The domain is partitioned into two disjoint sub-domains Ω_1 and Ω_2 with Lipschitz boundaries $\partial\Omega_l$ and outer normal vectors \mathbf{n}_l for $l \in \{1, 2\}$, which henceforth denotes the sub-domain index. Furthermore, the sub-domains are separated by the interface $\Gamma = \Omega \setminus (\Omega_1 \cup \Omega_2)$, which is assumed to be a $(d-1)$ -dimensional manifold (see also Fig. 4.1). Note that the extension of this and all the following to more than two sub-domains is straightforward, see [285, Rem. 3 & Sect. 4.4]. All the following quantities can depend on their position in the domain, but we suppress this dependence for the ease of presentation. In each sub-domain Ω_l , the dimensionless formulation for flow of two immiscible, incompressible phases through a stationary, rigid porous medium is governed by the mass balance equations

$$-\phi_l \partial_t S_l + \nabla \cdot \mathbf{u}_{n,l} = q_{n,l} \quad \text{in } \Omega_l \times (0, T), \quad (4.1)$$

$$\phi_l \partial_t S_l + \nabla \cdot \mathbf{u}_{w,l} = q_{w,l} \quad \text{in } \Omega_l \times (0, T), \quad (4.2)$$

where $\phi_l \in (0, 1)$ is the medium porosity and S_l is the saturation of the wetting phase (note that in a two-phase system $S_n + S_w = 1$, so that only one saturation is necessary). The source rate of the α -phase ($\alpha \in \{n, w\}$) is denoted by $q_{\alpha,l}$. The specific discharge $\mathbf{u}_{\alpha,l}$ of the α -phase incorporates the intrinsic permeability \mathbf{K}_l , and the relative mobility $\lambda_{\alpha,l}$ due to the extended Darcy law,

$$\mathbf{u}_{\alpha,l} = -\lambda_{\alpha,l}(S_l) \mathbf{K}_l \nabla p_{\alpha,l} \quad \text{in } \Omega_l \times (0, T). \quad (4.3)$$

Here, $p_{\alpha,l}$ denotes the pressure in the α -phase.

At the interface Γ separating the two sub-domains, we assume that the normal flux and the pressure of each phase are continuous, i.e., for $\alpha \in \{n, w\}$

$$\mathbf{u}_{\alpha,1} \cdot \mathbf{n}_1 = -\mathbf{u}_{\alpha,2} \cdot \mathbf{n}_2, \quad p_{\alpha,1} = p_{\alpha,2} \quad \text{on } \Gamma \times (0, T). \quad (4.4)$$

Remark 4.1 (Interface conditions). The continuity of the normal fluxes follows directly from mass conservation. The continuity of the phase pressure is valid, if the phase is present at both sides of the interface. This is not necessarily valid any

more for so-called entry-pressure models, when the non-wetting phase is absent at one side of the interface, as shown in [62, 68, 314] for standard models and in [310] for dynamic capillary pressure. To the best of our knowledge, conditions for entry-pressure models including both dynamic and hysteretic effects have not yet been proposed or derived.

Based on the discussion in Section 1.3.1, we consider the play-type hysteresis model proposed in [32, 154],

$$p_{n,l} - p_{w,l} \in p_{c,l}(S_l) - \gamma_l \operatorname{sign}(\partial_t S_l) - \tau_l(S_l) \partial_t S_l, \quad (4.5)$$

where $\gamma_l \geq 0$ and the non-negative function τ_l are used to model the effects due to hysteresis and dynamic capillarity, respectively. Below, we will use a regularization $\Phi_{\delta,l}$ of the scaled sign function to obtain a single-valued relation and to ensure strict monotonicity. For fixed, small parameter $\delta > 0$ and $l \in \{1, 2\}$, the regularization is

$$\Phi_{\delta,l}(\xi) = \begin{cases} \gamma_l \operatorname{sign}(\xi) & \text{if } |\xi| \geq \delta, \\ \gamma_l \frac{\xi}{\delta} & \text{if } |\xi| < \delta. \end{cases}$$

The regularized non-equilibrium capillary pressure condition then becomes

$$p_{n,l} - p_{w,l} = p_{c,l}(S_l) - \Phi_{\delta,l}(\partial_t S_l) - \partial_t T_l(S_l) \quad \text{in } \Omega_l \times (0, T), \quad (4.6)$$

where T_l denotes the primitive of τ_l .

Alternatively, the multi-valued equation (4.5) can be inverted. As discussed in Section 1.3.1, this yields a single-valued relation $\partial_t S_l = \hat{\Psi}_l(S_l, p_{n,l} - p_{w,l})$. Here, we consider the inverse capillary pressure condition only for constant $\tau_l > 0$, which then becomes

$$\partial_t S_l = \Psi_l(p_{n,l} - p_{w,l} - p_{c,l}(S_l)) \quad \text{in } \Omega_l \times (0, T), \quad (4.7)$$

where

$$\Psi_l(p) = \begin{cases} \frac{-p + \gamma_l}{\tau_l} & \text{if } p \geq \gamma_l, \\ 0 & \text{if } |p| < \gamma_l, \\ \frac{-p - \gamma_l}{\tau_l} & \text{if } p \leq -\gamma_l. \end{cases}$$

A regularization of Ψ_l matching $\Phi_{\delta,l}$ is used in [191, 201, 275, 282] to prove the existence of weak solutions for $\delta \rightarrow 0$, and to develop appropriate numerical schemes. Moreover, it is possible to only include hysteresis and no dynamic effects. Then, Ψ_l has to be regularized by including e.g. a small dynamic effect, namely taking $\tau_l = \varepsilon > 0$.

Remark 4.2. Richards' equation models unsaturated flow in porous media [271], based on the simplification that the non-wetting pressure p_n is constant, such that

(4.1) can be neglected. Although this manuscript focuses on the general two-phase flow equations, the results can be directly transferred to Richards' equation.

4.2.1. Notation

We denote by $L^2(X)$, $H^1(X)$, $H_0^1(X)$ and $H^{\text{div}}(X)$ the standard Hilbert spaces on $X \in \{\Omega, \Omega_1, \Omega_2\}$. $H^{1/2}(\Gamma)$ consists of all traces of functions in $H^1(\Omega)$. This trace on Γ of $w \in H^1(\Omega)$ is denoted by $w|_\Gamma$. For any function $f \in L^2(\Omega)$, $f_l := f|_{\Omega_l}$ denotes the restriction to Ω_l for $l \in \{1, 2\}$. Vice versa, a pair of functions $(f_1, f_2) \in L^2(\Omega_1) \times L^2(\Omega_2)$ is identified with the natural L^2 -extension f on the whole domain Ω . For simplicity, we only consider homogeneous Dirichlet boundary conditions at $\partial\Omega$ for the pressures, so that the following spaces will be used

$$\mathcal{W}_l := \{w \in H^1(\Omega_l) : w|_{\partial\Omega_l \cap \partial\Omega} \equiv 0\}, \quad \mathcal{W} := L^2(\Omega) \times [\mathcal{W}_1 \times \mathcal{W}_2]^2.$$

At the expense of additional technical effort, it is possible to extend the results in this chapter to other types of boundary conditions. Since $\partial\Omega \cap \partial\Omega_l$ is either empty or has positive $(d-1)$ -measure, the functions in \mathcal{W}_l vanish on this common part of the boundary. Note that $w \in H_0^1(\Omega)$ is equivalent to $(w_1, w_2) \in \mathcal{W}_1 \times \mathcal{W}_2$ with $w_1|_\Gamma \equiv w_2|_\Gamma$. This is a direct consequence of the trace theorem. For the continuity of the pressure across the interface Γ , we introduce the space

$$\mathcal{V} := L^2(\Omega) \times [H_0^1(\Omega)]^2.$$

Moreover, the space for the interface conditions on Γ is given by

$$H_{00}^{1/2}(\Gamma) := \{w \in H^{1/2}(\Gamma) : \exists v \in H_0^1(\Omega) : v|_\Gamma \equiv w\}.$$

It is a Hilbert space as the quotient space $H_0^1(\Omega)/\ker(\cdot|_\Gamma)$, see [38, Proposition 2.3]. The L^2 inner product and norm on $X \in \{\Omega_1, \Omega_2, \Gamma\}$ are denoted by $(\cdot, \cdot)_X$ and $\|\cdot\|_X$. Analogously, $\langle \cdot, \cdot \rangle_\Gamma$ stands for the dual pairing on $H_{00}^{1/2}(\Gamma)$ with $H_{00}^{1/2}(\Gamma)'$ via the Gelfand triple with $L^2(\Gamma)$. Here and in the following, the dual of a Banach space B is denoted by B' .

4.2.2. Assumptions on the coefficient functions

In the following, we summarize all assumptions on the coefficient functions, which are mostly also found in realistic physical systems. Note that we explicitly exclude the degeneration of the equations by requiring positive mobilities λ_α and a Lipschitz-continuous equilibrium capillary pressure p_c . This is necessary to ensure that the pressures p_w, p_n based on (4.1)–(4.3) are well-defined even if one phase is not present due to $S = 0, 1$. In realistic applications, where these assumptions do not hold, one can use a regularization like in [72, 74, 232, 234, 280], where the convergence of the solutions of the regularized equations towards the solution

of the degenerated equations and the existence of the latter solutions are proven. Note that we allow discontinuities of the coefficient functions at the interface Γ .

Assumption 4.1. For $l \in \{1, 2\}$ and $\alpha \in \{n, w\}$, assume that

- $\mathbf{K}_l : \Omega_l \rightarrow \mathbb{R}^{d \times d}$ is symmetric, and constants $\underline{K}_l, \overline{K}_l \in \mathbb{R}^+ = (0, \infty)$ exist such that $\underline{K}_l \|\xi\|_{\mathbb{R}^d}^2 \leq \xi^T \mathbf{K}_l(x) \xi \leq \overline{K}_l \|\xi\|_{\mathbb{R}^d}^2$ for all $x \in \Omega_l$ and $\xi \in \mathbb{R}^d$,
- $\lambda_{\alpha,l} : \mathbb{R} \rightarrow \mathbb{R}^+$, is Lipschitz-continuous with Lipschitz constant $L_{\lambda_{\alpha,l}}$, and constants $m_{\lambda_{\alpha,l}}, M_{\lambda_{\alpha,l}} \in \mathbb{R}^+$ exist such that $m_{\lambda_{\alpha,l}} \leq \lambda_{\alpha,l}(s) \leq M_{\lambda_{\alpha,l}}$ for all $s \in \mathbb{R}$,
- $q_{\alpha,l} : [0, T] \rightarrow L^2(\Omega_l)$ is continuous,
- $p_{c,l} : \mathbb{R} \times \Omega_l \rightarrow \mathbb{R}$ is strictly monotonically decreasing in the first variable, Lipschitz-continuous, and constants $m_{p_{c,l}}, L_{p_{c,l}} \in \mathbb{R}^+$ exist such that $m_{p_{c,l}}|r - s| \leq |p_{c,l}(r, x) - p_{c,l}(s, x)| \leq L_{p_{c,l}}|r - s|$ for all $r, s \in \mathbb{R}$ and $x \in \Omega_l$,
- $\tau_l : \mathbb{R} \rightarrow \mathbb{R}^+$ is measurable, and constants $m_{T,l}, L_{T,l} \in \mathbb{R}^+$ exist such that $m_{T,l} < \tau_l(s) < L_{T,l}$ for all $s \in \mathbb{R}$; we call its primitive $T_l : \mathbb{R} \rightarrow \mathbb{R}$,
- $\gamma_l : \Omega_l \rightarrow [0, \infty)$ is Lipschitz-continuous and bounded by a constant $M_{\gamma,l} \in \mathbb{R}^+$.

Remark 4.3. The extension of $\lambda_{\alpha,l}$, $p_{c,l}$ and τ_l to any value $s \in \mathbb{R}$ is necessary because the non-degenerated, non-equilibrium model does not satisfy a maximum principle due to possible overshoots. The solutions of the degenerated model remain (essentially) bounded, see [74, 232]. These extensions can be constructed naturally, only assuming Lipschitz continuity on $[0, 1]$.

Remark 4.4. By Assumption 4.1, $\Phi_{\delta,l} : \mathbb{R} \times \Omega_l \rightarrow \mathbb{R}$ is monotonically increasing in the first variable and Lipschitz-continuous with Lipschitz constant $L_{\Phi_{\delta,l}} = M_{\gamma,l}/\delta$. Furthermore for constant $\tau_l > 0$, $\Psi_l : \mathbb{R} \times \Omega_l \rightarrow \mathbb{R}$ is Lipschitz-continuous, monotonically decreasing in the first variable, and it holds $|\Psi_l(p, x) - \Psi_l(q, x)| \leq L_{\Psi,l}|p - q|$ for all $p, q \in \mathbb{R}$ and $x \in \Omega_l$, where $L_{\Psi,l} = \tau_l^{-1}$.

The system of nonlinear equations (4.1)–(4.4) with either (4.6) or (4.7) forms an initial-boundary-value problem in the primary variables S , p_n and p_w for given initial data $S|_{t=0} = S^0 \in L^\infty(\Omega; [0, 1])$.

Remark 4.5 (Existence and boundedness of unique weak solutions). For the existence of unique weak solutions to (4.1)–(4.4) under either condition (4.6) or (4.7), with respect to initial and boundary conditions, we refer to [72, 73, 191]. The existence of solutions is proven in [191], while the uniqueness of the solutions to these equations for $\delta = 0$ is derived in [72, 73]. Note that additional assumptions on the regularity of the coefficient functions and the domain are necessary for this. Furthermore, the sequence of solutions to the regularized equations converge (weakly) towards the solution of the original equations for $\delta \rightarrow 0$, as shown in [201].

For the main theorems Theorems 4.1 and 4.2 in this work we assume the existence

of time-discrete solutions with bounded pressure gradients. This has been proven in the time-continuous case e.g. in [72, Lemma 1], where $S \in L^\infty(0, T; C^{0,\beta}(\overline{\Omega}))$ and $p_n, p_w \in L^\infty(0, T; C^{1,\beta}(\overline{\Omega}))$ is obtained under the above mentioned additional regularity assumptions that the coefficient functions are independent of x , that $p_c \in C^1$ and $S^0 \in C^{0,\beta}(\Omega)$, and that Ω is a $C^{1,\beta}$ -domain.

4.3. Temporal discretization and iterative schemes

First, we present the discretization in time by the θ -scheme. In particular, we are interested in the unconditionally stable situation when $\theta \geq 1/2$. For $\theta = 1$, this boils down to the first-order backward Euler method, while $\theta = 1/2$ coincides with the second-order Crank–Nicolson method. The resulting semi-discrete equations are nonlinear, and thus iterative methods are necessary to find the solutions. We propose two linearization and domain decomposition schemes (LDD-schemes).

4.3.1. Discretization in time

For given $K \in \mathbb{N}$, let the fixed time step length be $\Delta t := \frac{T}{K}$. At time $t^k := k\Delta t$, the approximations of the saturation, pressures and source terms are denoted by $S^k, p_\alpha^k, q_\alpha^k$. With this, the auxiliary quantities at time t^k are

$$\mathbf{u}_{\alpha,l}^k := -\lambda_{\alpha,l}(S_l^k) \mathbf{K}_l \nabla p_{\alpha,l}^k, \quad p_{c,l}^k := p_{c,l}(S_l^k), \quad \Psi_l^k := \Psi_l(p_{n,l}^k - p_{w,l}^k - p_{c,l}^k).$$

For $\theta \in (0, 1]$, the θ -averaged quantities are defined by $(\cdot)^{k,\theta} := \theta(\cdot)^k + (1-\theta)(\cdot)^{k-1}$, e.g. $\mathbf{u}_{\alpha,l}^{k,\theta} = \theta \mathbf{u}_{\alpha,l}^k + (1-\theta) \mathbf{u}_{\alpha,l}^{k-1}$. Then, the interface conditions (4.4) directly become

$$\mathbf{u}_{\alpha,1}^{k,\theta} \cdot \mathbf{n}_1 = -\mathbf{u}_{\alpha,2}^{k,\theta} \cdot \mathbf{n}_2, \quad p_{\alpha,1}^k = p_{\alpha,2}^k \quad \text{on } \Gamma. \quad (4.8)$$

The time-discrete counterparts of (4.1) and (4.2) are tested with $\xi_n, \xi_w \in H_0^1(\Omega)$. After partial integration using (4.8) and summation over $l \in \{1, 2\}$, the time-discrete, weak equations read

$$\sum_{l=1}^2 \left(-\phi_l \left(\frac{S_l^k - S_l^{k-1}}{\Delta t}, \xi_{n,l} \right)_{\Omega_l} - \left(\mathbf{u}_{n,l}^{k,\theta}, \nabla \xi_{n,l} \right)_{\Omega_l} \right) = \left(q_{n,l}^{k,\theta}, \xi_n \right)_\Omega, \quad (4.9)$$

$$\sum_{l=1}^2 \left(\phi_l \left(\frac{S_l^k - S_l^{k-1}}{\Delta t}, \xi_{w,l} \right)_{\Omega_l} - \left(\mathbf{u}_{w,l}^{k,\theta}, \nabla \xi_{w,l} \right)_{\Omega_l} \right) = \left(q_{w,l}^{k,\theta}, \xi_w \right)_\Omega. \quad (4.10)$$

Additionally, the time-discrete counterparts of either the regularized non-equilibrium capillary pressure equation (4.6)

$$p_{n,l}^{k,\theta} - p_{w,l}^{k,\theta} = p_{c,l}^{k,\theta} - \Phi_{\delta,l} \left(\frac{S_l^k - S_l^{k-1}}{\Delta t} \right) - \frac{T_l(S_l^k) - T_l(S_l^{k-1})}{\Delta t} \quad \text{in } L^2(\Omega_l) \text{ for } l \in \{1, 2\}, \quad (4.11)$$

or of the inverse capillary pressure equation (4.7)

$$\frac{S_l^k - S_l^{k-1}}{\Delta t} = \theta \Psi_l^k + (1 - \theta) \Psi_l^{k-1} \quad \text{in } L^2(\Omega_l) \text{ for } l \in \{1, 2\}, \quad (4.12)$$

will be used below, yielding the following two semi-discrete formulations.

Problem 4.1 (Semi-discrete weak formulation I). Given $(S^{k-1}, p_n^{k-1}, p_w^{k-1}) \in \mathcal{V}$, find $(S^k, p_n^k, p_w^k) \in \mathcal{V}$ such that (4.9)–(4.11) hold for all $\xi_n, \xi_w \in H_0^1(\Omega)$.

Problem 4.2 (Semi-discrete weak formulation II). Given $(S^{k-1}, p_n^{k-1}, p_w^{k-1}) \in \mathcal{V}$, find $(S^k, p_n^k, p_w^k) \in \mathcal{V}$ such that (4.9), (4.10), and (4.12) hold for all $\xi_n, \xi_w \in H_0^1(\Omega)$.

In particular, the second formulation is well suited for hysteretic models since it avoids the regularization of the sign function, and thus additional errors. In the absence of hysteresis, the first formulation is more natural and can be straightforwardly used even for vanishing τ . Note that both weak semi-discrete problems are well defined.

Remark 4.6. If $(S^k, p_n^k, p_w^k) \in \mathcal{V}$ is a solution of Problem 4.1 or Problem 4.2, then $p_{\alpha,1}^k|_\Gamma = p_{\alpha,2}^k|_\Gamma$ holds by the definition of \mathcal{V} . Since $S_l^k, S_l^{k-1}, q_{\alpha,l}^{k,\theta} \in L^2(\Omega_l)$, testing (4.9) and (4.10) with arbitrary $\xi_{\alpha,l} \in C_0^\infty(\Omega_l)$ implies $\nabla \cdot \mathbf{u}_{\alpha,l}^{k,\theta} \in L^2(\Omega_l)$, i.e., $\mathbf{u}_{\alpha,l}^{k,\theta} \in H^{\text{div}}(\Omega_l)$. This shows that

$$\nabla \cdot \mathbf{u}_{n,l}^{k,\theta} = \phi_l \frac{S_l^k - S_l^{k-1}}{\Delta t} + q_{n,l}^{k,\theta}, \quad \nabla \cdot \mathbf{u}_{w,l}^{k,\theta} = -\phi_l \frac{S_l^k - S_l^{k-1}}{\Delta t} + q_{w,l}^{k,\theta} \quad \text{in } L^2(\Omega_l). \quad (4.13)$$

Therefore, the normal trace lemma [55, Lemma III.1.1] yields $\mathbf{u}_{\alpha,l}^{k,\theta} \cdot \mathbf{n}_l \in H^{1/2}(\partial\Omega_l)'$ and integration by parts in (4.9) and (4.10) implies $\mathbf{u}_{\alpha,1}^{k,\theta} \cdot \mathbf{n}_1 = -\mathbf{u}_{\alpha,2}^{k,\theta} \cdot \mathbf{n}_2$ in $H_{00}^{1/2}(\Gamma)'$.

Problems 4.1 and 4.2 are nonlinear systems of mixed elliptic algebraic equations with possibly discontinuous coefficients. This is evident when (4.12) is substituted into (4.9) and (4.10). One may prove the existence of (unique) solutions analogously to the time-continuous case (Remark 4.5) or the fully discrete case in [106] for equilibrium capillary pressure. By this, the time-discrete pressure gradients should be bounded – corresponding to the results in [72, 106]. However, this lies out of the scope of this manuscript. In the following, we will assume that solutions to Problems 4.1 and 4.2 with bounded gradients exist.

4.3.2. Linearization and domain decomposition schemes

To decouple the problems on the sub-domains, and thereby to account for the possible discontinuities at the interface Γ , we introduce a non-overlapping domain decomposition method. Following the ideas in [88, 209], we combine the interface conditions (4.8) by a (to be freely chosen) parameter $\mathcal{L}_\Gamma \in (0, \infty)$ to define

$$g_{\alpha,l}^k := \mathbf{u}_{\alpha,l}^{k,\theta} \cdot \mathbf{n}_l - \mathcal{L}_\Gamma p_{\alpha,l}^k \quad \text{for } l \in \{1, 2\}.$$

With these Robin type expressions, the interface conditions (4.8) at Γ read

$$g_{\alpha,3-l}^k = -2\mathcal{L}_\Gamma p_{\alpha,l}^k - g_{\alpha,l}^k.$$

This formulation is equivalent to (4.8) for any $\mathcal{L}_\Gamma \neq 0$, cf. [285, Remark 1].

Lemma 4.1. *Let $k \in \mathbb{N}$ be fixed and assume that $(S^k, p_n^k, p_w^k) \in \mathcal{W}$ and $g_{\alpha,l}^k \in H_{00}^{1/2}(\Gamma)'$ exist for $l \in \{1, 2\}$ and $\alpha \in \{n, w\}$, such that it holds*

$$-\phi_l \left(\frac{S_l^k - S_l^{k-1}}{\Delta t}, \xi_{n,l} \right)_{\Omega_l} - \left(\mathbf{u}_{n,l}^{k,\theta}, \nabla \xi_{n,l} \right)_{\Omega_l} + \langle \mathcal{L}_\Gamma p_{n,l}^k + g_{n,l}^k, \xi_{n,l} \rangle_\Gamma = \left(q_{n,l}^{k,\theta}, \xi_{n,l} \right)_{\Omega_l}, \quad (4.14)$$

$$\phi_l \left(\frac{S_l^k - S_l^{k-1}}{\Delta t}, \xi_{w,l} \right)_{\Omega_l} - \left(\mathbf{u}_{w,l}^{k,\theta}, \nabla \xi_{w,l} \right)_{\Omega_l} + \langle \mathcal{L}_\Gamma p_{w,l}^k + g_{w,l}^k, \xi_{w,l} \rangle_\Gamma = \left(q_{w,l}^{k,\theta}, \xi_{w,l} \right)_{\Omega_l}, \quad (4.15)$$

$$\langle g_{\alpha,l}^k, \xi_{\alpha,l} \rangle_\Gamma = \langle -2\mathcal{L}_\Gamma p_{\alpha,3-l}^k - g_{\alpha,3-l}^k, \xi_{\alpha,l} \rangle_\Gamma, \quad (4.16)$$

for $l \in \{1, 2\}$ and all $\xi_n, \xi_w \in H_0^1(\Omega)$, as well as either (4.11) or (4.12). Then, the interface conditions $\mathbf{u}_{\alpha,1}^{k,\theta} \cdot \mathbf{n}_1 = -\mathbf{u}_{\alpha,2}^{k,\theta} \cdot \mathbf{n}_2$ in $H_{00}^{1/2}(\Gamma)'$ and $p_{\alpha,1}^k|_\Gamma = p_{\alpha,2}^k|_\Gamma$ are satisfied, and thus $(S^k, p_n^k, p_w^k) \in \mathcal{V}$ is a solution of Problem 4.1 or Problem 4.2, respectively. Moreover, it holds $g_{\alpha,l}^k = \mathbf{u}_{\alpha,l}^{k,\theta} \cdot \mathbf{n}_l - \mathcal{L}_\Gamma p_{\alpha,l}^k$ in $H_{00}^{1/2}(\Gamma)'$.

Vice versa, if $(S^k, p_n^k, p_w^k) \in \mathcal{V}$ is a solution of Problem 4.1 or Problem 4.2, and we define

$$g_{\alpha,l}^k := \mathbf{u}_{\alpha,l}^{k,\theta} \cdot \mathbf{n}_l - \mathcal{L}_\Gamma p_{\alpha,l}^k \quad \text{in } H_{00}^{1/2}(\Gamma)', \quad (4.17)$$

then (S^k, p_n^k, p_w^k) and $g_{\alpha,l}^k$, $l \in \{1, 2\}$ and $\alpha \in \{n, w\}$, solve the system (4.14)–(4.16).

Proof. Subtracting the equations (4.16) for $l \in \{1, 2\}$ directly yields $p_{\alpha,1}^k|_\Gamma = p_{\alpha,2}^k|_\Gamma$, whereas adding up these equations leads to $g_{\alpha,1}^k + g_{\alpha,2}^k = -\mathcal{L}_\Gamma (p_{\alpha,1}^k + p_{\alpha,2}^k)$. Using this in the sum of (4.14) over $l \in \{1, 2\}$ gives (4.9). Analogously, one obtains (4.10) from (4.15). Together with (4.11) or (4.12), this is equivalent to Problem 4.1 or Problem 4.2, respectively. Furthermore, integration by parts in (4.14) and (4.15), using (4.13), leads to $g_{\alpha,l}^k = \mathbf{u}_{\alpha,l}^{k,\theta} \cdot \mathbf{n}_l - \mathcal{L}_\Gamma p_{\alpha,l}^k$ in $H_{00}^{1/2}(\Gamma)'$.

Conversely, if (S^k, p_n^k, p_w^k) solves Problem 4.1 or Problem 4.2, then the continuity of pressures and normal fluxes at Γ holds, and thus one gets

$$g_{\alpha,l}^k = \mathbf{u}_{\alpha,l}^{k,\theta} \cdot \mathbf{n}_l - \mathcal{L}_\Gamma p_{\alpha,l}^k = -\mathbf{u}_{\alpha,3-l}^{k,\theta} \cdot \mathbf{n}_{3-l} - \mathcal{L}_\Gamma p_{\alpha,3-l}^k = -2\mathcal{L}_\Gamma p_{\alpha,3-l}^k - g_{\alpha,3-l}^k$$

in $H_{00}^{1/2}(\Gamma)'$. Finally, (4.14) and (4.15) follow from integration by parts of (4.9) and (4.10) using (4.13) and the definition of $g_{\alpha,l}^k$. \square

The above-shown equivalence of Lemma 4.1 can also be observed for Richards' equation [285]. We will use the system (4.14)–(4.16) and either (4.11) or (4.12)

instead of the equivalent semi-discrete [Problems 4.1](#) and [4.2](#) to prove that the solutions to the LDD-schemes converge towards the solutions of [Problems 4.1](#) and [4.2](#), respectively.

The two problems only differ in the used capillary pressure relation, but this will result in different iterative schemes, as will be seen below. The common idea is to linearize the capillary pressure equations [\(4.11\)](#) and [\(4.12\)](#) using the L-scheme discussed in [Section 1.5.3](#). This means to add stabilization terms of the form

$$\mathcal{L}(\text{solution of current iteration} - \text{solution of last iteration}),$$

which vanish in the limit if the sequence converges. Here, the parameter $\mathcal{L} > 0$ takes the place of the Jacobian which would be used in the Newton method.

Assuming that for some $i \in \mathbb{N}$ the approximations $(S_l^{k,i-1}, p_n^{k,i-1}, p_w^{k,i-1}) \in \mathcal{W}$ and $g_{\alpha,l}^{k,i-1} \in L^2(\Gamma)$ for $l \in \{1, 2\}$ and $\alpha \in \{n, w\}$ are known, the linearized fluxes and interface conditions are defined by

$$\mathbf{u}_{\alpha,l}^{k,\theta,i} := -\theta \lambda_{\alpha,l}(S_l^{k,j}) \mathbf{K}_l \nabla p_{\alpha,l}^{k,i} + (1 - \theta) \mathbf{u}_{\alpha,l}^{k-1}, \quad g_{\alpha,l}^{k,i} := -2\mathcal{L}_\Gamma p_{\alpha,3-l}^{k,i-1} - g_{\alpha,3-l}^{k,i-1},$$

where $j = i - 1$ for the following LDD-scheme I, while $j = i$ for the LDD-scheme II. With these, [\(4.9\)](#) and [\(4.10\)](#) become linear and decouple into

$$\begin{aligned} -\phi_l \left(\frac{S_l^{k,i} - S_l^{k-1}}{\Delta t}, \xi_{n,l} \right)_{\Omega_l} - \left(\mathbf{u}_{n,l}^{k,\theta,i}, \nabla \xi_{n,l} \right)_{\Omega_l} \\ + \left(\mathcal{L}_\Gamma p_{n,l}^{k,i} + g_{n,l}^{k,i}, \xi_{n,l} \right)_\Gamma = \left(q_{n,l}^{k,\theta}, \xi_{n,l} \right)_{\Omega_l}, \end{aligned} \quad (4.18)$$

$$\begin{aligned} \phi_l \left(\frac{S_l^{k,i} - S_l^{k-1}}{\Delta t}, \xi_{w,l} \right)_{\Omega_l} - \left(\mathbf{u}_{w,l}^{k,\theta,i}, \nabla \xi_{w,l} \right)_{\Omega_l} \\ + \left(\mathcal{L}_\Gamma p_{w,l}^{k,i} + g_{w,l}^{k,i}, \xi_{w,l} \right)_\Gamma = \left(q_{w,l}^{k,\theta}, \xi_{w,l} \right)_{\Omega_l}, \end{aligned} \quad (4.19)$$

$$g_{\alpha,l}^{k,i} = -2\mathcal{L}_\Gamma p_{\alpha,3-l}^{k,i-1} - g_{\alpha,3-l}^{k,i-1} \quad \text{in } L^2(\Gamma). \quad (4.20)$$

If the limit exists, we expect for [\(4.18\)](#)–[\(4.20\)](#) to iteratively find the solution of the formal limit system [\(4.14\)](#)–[\(4.16\)](#) as $i \rightarrow \infty$. Although this convergence is independent of the initial guess, as shown below in [Theorems 4.1](#) and [4.2](#), note that the natural choice for the first iteration is the solution at the previous time step,

$$S_l^{k,0} = S_l^{k-1}, \quad p_{\alpha,l}^{k,0} = p_{\alpha,l}^{k-1}, \quad g_{\alpha,l}^{k,0} = g_{\alpha,l}^{k-1}.$$

Note that the Robin condition formulated in [\(4.20\)](#) removes the necessity to calculate the fluxes at the interface Γ in favor of evaluating the pressure. This has the advantage that the regularity can be improved ($g_{\alpha,l}^{k,i} \in L^2(\Gamma)$ instead of $\mathbf{u}_{\alpha,l}^{k,\theta,i} \cdot \mathbf{n}_l \in H_{00}^{1/2}(\Gamma)'$) and that no post-processing is required for finite element methods and other pressure-based spatial discretization schemes.

For **Problem 4.1**, we use the stabilization parameters $\mathcal{L}_{p,l}, \mathcal{L}_{\Phi,l}, \mathcal{L}_{T,l} \geq 0$, which must satisfy some mild constraints to guarantee convergence, as shown below in **Theorem 4.1**. With these, the stabilized linearization of (4.11) becomes

$$\begin{aligned} p_{n,l}^{k,\theta,i} - p_{w,l}^{k,\theta,i} + \left(\mathcal{L}_{p,l} + \frac{\mathcal{L}_{T,l} + \mathcal{L}_{\Phi,l}}{\Delta t} \right) (S_l^{k,i} - S_l^{k,i-1}) \\ = \theta p_{c,l}(S_l^{k,i-1}) + (1 - \theta) p_{c,l}^{k-1} - \Phi_{\delta,l} \left(\frac{S_l^{k,i-1} - S_l^{k-1}}{\Delta t} \right) - \frac{T_l(S_l^{k,i-1}) - T_l(S_l^{k-1})}{\Delta t} \end{aligned} \quad (4.21)$$

in $L^2(\Omega_l)$, for $l \in \{1, 2\}$, where $p_{\alpha,l}^{k,\theta,i} := \theta p_{\alpha,l}^{k,i} + (1 - \theta) p_{\alpha,l}^{k-1}$. Clearly, the stabilizing term in (4.21) vanishes in the case of convergence, and hence the formal limit is (4.11). The iteration reduces to solving the following problem.

Problem LDD-1 (Weak formulation of the LDD-scheme I).

Given $(S^{k-1}, p_n^{k-1}, p_w^{k-1}) \in \mathcal{V}$, $(S^{k,i-1}, p_n^{k,i-1}, p_w^{k,i-1}) \in \mathcal{W}$ and $g_{\alpha,l}^{k,i-1} \in L^2(\Gamma)$ for $l \in \{1, 2\}$, $\alpha \in \{n, w\}$, find $(S^{k,i}, p_n^{k,i}, p_w^{k,i}) \in \mathcal{W}$ and $g_{\alpha,l}^{k,i} \in L^2(\Gamma)$ for $l \in \{1, 2\}$ and $\alpha \in \{n, w\}$, such that the equations (4.18)–(4.21) hold for all $\xi_{n,l}, \xi_{w,l} \in \mathcal{W}_l$ and $l \in \{1, 2\}$.

For **Problem 4.2**, we define the semi-linearized inverted capillary pressure equation based on (4.12) and $\Psi_l^{k,i} := \Psi_l(p_n^{k,i-1} - p_w^{k,i-1} - p_{c,l}(S_l^{k,i}))$ by

$$\frac{S_l^{k,i} - S_l^{k-1}}{\Delta t} = \theta \Psi_l^{k,i} + (1 - \theta) \Psi_l^{k-1} \quad \text{in } L^2(\Omega_l) \text{ for } l \in \{1, 2\}. \quad (4.22)$$

Note that $S_l^{k,i}$ still arises implicitly. However, (4.22) defines a contraction, as shown in **Lemma 4.3**. Therefore, it can be easily solved by directly applying the associated fixed-point iteration or any other suited method such as the Newton-Raphson iteration.

Note that this allows to use $S_l^{k,i}$ for the definition of the flux

$$\mathbf{u}_{\alpha,l}^{k,\theta,i} := -\theta \lambda_{\alpha,l}(S_l^{k,i}) \mathbf{K}_l \nabla p_{\alpha,l}^{k,i} + (1 - \theta) \mathbf{u}_{\alpha,l}^{k-1}$$

in the second LDD-scheme. Substitution of (4.22) into (4.18) and (4.19) leads then to a nonlinear elliptic system of equations in $p_{n,l}$ and $p_{w,l}$. Therefore, we stabilize these equations using only one stabilization parameter $\mathcal{L}_{p,l} > 0$, which again must satisfy a mild constraint discussed in **Section 4.4.2**. In particular, the term $\mathcal{L}_{p,l}(p_{n,l}^{k,i} - p_{n,l}^{k,i-1} - p_{w,l}^{k,i} + p_{w,l}^{k,i-1})$ is added to (4.18) and subtracted from (4.19). Again, this term vanishes in case of convergence. Altogether, the second LDD-scheme is constituted by iteratively solving the following problem.

Problem LDD-2 (Weak formulation of the LDD-scheme II).

Given $(S^{k-1}, p_n^{k-1}, p_w^{k-1}) \in \mathcal{V}$, $(S^{k,i-1}, p_n^{k,i-1}, p_w^{k,i-1}) \in \mathcal{W}$ and $g_{\alpha,l}^{k,i-1} \in L^2(\Gamma)$ for $l \in \{1, 2\}$, $\alpha \in \{n, w\}$, find $(S^{k,i}, p_n^{k,i}, p_w^{k,i}) \in \mathcal{W}$ and $g_{\alpha,l}^{k,i} \in L^2(\Gamma)$ for $l \in \{1, 2\}$,

$\alpha \in \{n, w\}$, such that it holds

$$\begin{aligned} & -\phi_l \left(\frac{S_l^{k,i} - S_l^{k-1}}{\Delta t}, \xi_{n,l} \right)_{\Omega_l} + \mathcal{L}_{p,l} \left(p_{n,l}^{k,i} - p_{n,l}^{k,i-1} - p_{w,l}^{k,i} + p_{w,l}^{k,i-1}, \xi_{n,l} \right)_{\Omega_l} \\ & - \left(\mathbf{u}_{n,l}^{k,\theta,i}, \nabla \xi_{n,l} \right)_{\Omega_l} + \left(\mathcal{L}_\Gamma p_{n,l}^{k,i} + g_{n,l}^{k,i}, \xi_{n,l} \right)_\Gamma = \left(q_{n,l}^{k,\theta}, \xi_{n,l} \right)_{\Omega_l}, \end{aligned} \quad (4.23)$$

$$\begin{aligned} & \phi_l \left(\frac{S_l^{k,i} - S_l^{k-1}}{\Delta t}, \xi_{w,l} \right)_{\Omega_l} - \mathcal{L}_{p,l} \left(p_{n,l}^{k,i} - p_{n,l}^{k,i-1} - p_{w,l}^{k,i} + p_{w,l}^{k,i-1}, \xi_{w,l} \right)_{\Omega_l} \\ & - \left(\mathbf{u}_{w,l}^{k,\theta,i}, \nabla \xi_{w,l} \right)_{\Omega_l} + \left(\mathcal{L}_\Gamma p_{w,l}^{k,i} + g_{w,l}^{k,i}, \xi_{w,l} \right)_\Gamma = \left(q_{w,l}^{k,\theta}, \xi_{w,l} \right)_{\Omega_l}, \end{aligned} \quad (4.24)$$

$$g_{\alpha,l}^{k,i} = -2\mathcal{L}_\Gamma p_{\alpha,3-l}^{k,i-1} - g_{\alpha,3-l}^{i-1} \quad \text{in } L^2(\Gamma), \quad (4.25)$$

$$\frac{S_l^{k,i} - S_l^{k-1}}{\Delta t} = \theta \Psi_l^{k,i} + (1 - \theta) \Psi_l^{k-1} \quad \text{in } L^2(\Omega_l), \quad (4.26)$$

for all $\xi_{n,l}, \xi_{w,l} \in \mathcal{W}_l$ and $l \in \{1, 2\}$.

4.4. Existence and convergence of the iterative solutions

In the following, [Problems LDD-1](#) and [LDD-2](#) defining the LDD-schemes are analyzed. The existence of unique solutions to these problems and the convergence towards the solutions of the semi-discrete equations is rigorously proven. The ideas of the proofs are based on [\[187, 285, 286\]](#), where similar models are discussed, in which either hysteresis or both dynamic capillarity and hysteresis are absent. In comparison to [\[214\]](#), the improved convergence proofs state sharper bounds on the stabilization parameters and on the time-step size. The LDD-scheme I is presented first, the second one afterwards.

4.4.1. LDD-scheme I

The existence of a unique solution to [Problem LDD-1](#) is a direct consequence of the linearization.

Lemma 4.2. *[Problem LDD-1](#) has a unique solution if [Assumption 4.1](#) is fulfilled and $\theta \in (0, 1]$.*

Proof. Since $p_{\alpha,l}^{k,i-1}|_\Gamma \in L^2(\Gamma)$, [\(4.20\)](#) yields unique $g_{\alpha,l}^{k,i} \in L^2(\Gamma)$ for $l \in \{1, 2\}$ and $\alpha \in \{n, w\}$. Furthermore, [\(4.21\)](#) can be rewritten as

$$\frac{S_l^{k,i} - S_l^{k-1}}{\Delta t} = -\beta_l \theta (p_{n,l}^{k,i} - p_{w,l}^{k,i}) + \beta_l f_l^i \quad \text{in } L^2(\Omega_l), \quad (4.27)$$

where $\beta_l = (\mathcal{L}_{p,l}\Delta t + \mathcal{L}_{T,l} + \mathcal{L}_{\Phi,l})^{-1} > 0$, and

$$f_l^i = \theta p_{c,l}(S_l^{k,i-1}) + (1-\theta)p_{c,l}^{k-1} - (1-\theta) \left(p_{n,l}^{k-1} - p_{w,l}^{k-1} \right) \\ - \Phi_{\delta,l} \left(\frac{S_l^{k,i-1} - S_l^{k-1}}{\Delta t} \right) - \frac{T_l(S_l^{k,i-1}) - T_l(S_l^{k-1})}{\Delta t}$$

is independent of any quantity at the iteration i . Inserting this into the sum of (4.18) and (4.19) leads to

$$\phi_l \beta_l \theta \left(p_{n,l}^{k,i} - p_{w,l}^{k,i}, \xi_{n,l} - \xi_{w,l} \right)_{\Omega_l} + \theta \sum_{\alpha \in \{n,w\}} \left(\lambda_{\alpha,l}(S_l^{k,i-1}) \mathbf{K}_l \nabla p_{\alpha,l}^{k,i}, \nabla \xi_{\alpha,l} \right)_{\Omega_l} \\ + \sum_{\alpha \in \{n,w\}} \mathcal{L}_{\Gamma} \left(p_{\alpha,l}^{k,i}, \xi_{\alpha,l} \right)_{\Gamma} = \phi_l \beta_l \left(f_l^i, \xi_{n,l} - \xi_{w,l} \right)_{\Omega_l} + (1-\theta) \sum_{\alpha \in \{n,w\}} \left(\mathbf{u}_{\alpha,l}^{k-1}, \nabla \xi_{\alpha,l} \right)_{\Omega_l} \\ + \sum_{\alpha \in \{n,w\}} \left(q_{\alpha,l}^{k,\theta}, \xi_{\alpha,l} \right)_{\Omega_l} - \sum_{\alpha \in \{n,w\}} \left(g_{\alpha,l}^{k,i}, \xi_{\alpha,l} \right)_{\Gamma}.$$

Note that the righthand side is independent of any quantity at iteration i except the known $g_{\alpha,l}^{k,i}$ in the last term. With respect to the product space $[\mathcal{W}_l]^2$, the first term on the lefthand side is positive semi-definite. The remaining terms of the lefthand side are a symmetric, coercive and continuous bilinear form on $[\mathcal{W}_l]^2$ by [Assumption 4.1](#), $\theta > 0$ and $\mathcal{L}_{\Gamma} > 0$. The righthand side is a continuous linear functional on $[\mathcal{W}_l]^2$, hence by the Lax–Milgram lemma, a unique solution $(p_{n,l}^{k,i}, p_{w,l}^{k,i}) \in [\mathcal{W}_l]^2$ exists for $l \in \{1, 2\}$. Finally, $S_l^{k,i} \in L^2(\Omega_l)$ is uniquely determined by (4.27). \square

To prove the convergence of the LDD-scheme I, we derive a-priori estimates for the errors between the solution to [Problem LDD-1](#) and the solution of the limit equations. These estimates yield the convergence for any initial guess.

Theorem 4.1 (Convergence of the LDD-scheme I). *Let [Assumption 4.1](#) be fulfilled and $\theta \in (0, 1]$. Assume that a solution $(S^k, p_n^k, p_w^k) \in \mathcal{V}$ of [Problem 4.1](#) exists and satisfies $\|\mathbf{K}_l^{1/2} \nabla p_{\alpha,l}^k\|_{L^\infty(\Omega_l)} \leq M_{p_{\alpha,l}}$ and $\mathbf{u}_{\alpha,l}^{k,\theta} \cdot \mathbf{n}_l \in L^2(\Gamma)$. If the stabilization parameters are sufficiently large and the time step is small enough, i.e.,*

$$\mathcal{L}_{p,l} \geq \theta L_{p_{c,l}}, \quad \mathcal{L}_{T,l} \geq \frac{L_{T,l}}{2}, \quad \mathcal{L}_{\Phi,l} \geq \frac{L_{\Phi_{\delta,l}}}{2} \quad \text{and} \quad \Delta t < \frac{\phi_l m_{p_{c,l}}}{\sum_{\alpha \in \{n,w\}} \frac{\theta L_{\lambda_{\alpha,l}}^2 M_{p_{\alpha,l}}^2}{m_{\lambda_{\alpha,l}}}},$$

for $l \in \{1, 2\}$, the sequence of solutions of [Problem LDD-1](#) converges towards the solution of [Problem 4.1](#) independently of the initial guess $(S^{k,0}, p_n^{k,0}, p_w^{k,0}) \in \mathcal{W}$ and $g_{\alpha,l}^{k,0} \in L^2(\Gamma)$ for $l \in \{1, 2\}$ and $\alpha \in \{n, w\}$. More precisely, it holds

$$S_l^{k,i} \rightarrow S_l^k \text{ in } L^2(\Omega_l), \quad p_{\alpha,l}^{k,i} \rightarrow p_{\alpha,l}^k \text{ in } \mathcal{W}_l, \quad g_{\alpha,l}^{k,i} \rightarrow g_{\alpha,l}^k \text{ in } L^2(\Gamma)$$

for $l \in \{1, 2\}$ and $\alpha \in \{n, w\}$ as $i \rightarrow \infty$.

Remark 4.7. Due to the regularized sign-function, one has $L_{\Phi,\delta,l} = M_{\gamma,l}/\delta$. This means that the stabilization parameters and the time step can be chosen independently of the regularization, except for $\mathcal{L}_{\Phi,l} \geq M_{\gamma,l}/(2\delta)$.

Remark 4.8. Note that we assume the solution of the semi-discrete [Problem 4.1](#) to exist and to be sufficiently smooth. Given the additional regularity assumptions mentioned in [Remark 4.5](#), this holds for the continuous problem. In particular, following the proof of Lemma 1 in [72], the same arguments yield $S_l^k \in C^0(\overline{\Omega_l})$ and $p_{\alpha,l}^k \in C^1(\overline{\Omega_l})$ in the semi-discrete case under these assumptions. Then, one would have $\mathbf{u}_{\alpha,l}^{k,\theta} \in C^0(\overline{\Omega_l})$ and hence the regularity assumptions would be fulfilled. However, this remains an open problem if only [Assumption 4.1](#) is fulfilled. Furthermore, the existence of the semi-discrete solutions remains unclear in both cases.

Proof of Theorem 4.1. The iteration errors are defined by

$$e_{S,l}^i := S_l^{k,i} - S_l^k \in L^2(\Omega_l), \quad e_{p_{\alpha},l}^i := p_{\alpha,l}^{k,i} - p_{\alpha,l}^k \in \mathcal{W}_l, \quad e_{g_{\alpha},l}^i := g_{\alpha,l}^{k,i} - g_{\alpha,l}^k \in L^2(\Gamma).$$

Subtracting the limit equations (4.14)–(4.16) and (4.11) from (4.18)–(4.21) leads to

$$\begin{aligned} -\phi_l \left(\frac{e_{S,l}^i}{\Delta t}, \xi_{n,l} \right)_{\Omega_l} + \theta \left(\lambda_{n,l}(S_l^{k,i-1}) \mathbf{K}_l \nabla p_{n,l}^{k,i} - \lambda_{n,l}(S_l^k) \mathbf{K}_l \nabla p_{n,l}^k, \nabla \xi_{n,l} \right)_{\Omega_l} \\ + (\mathcal{L}_{\Gamma} e_{p_{n,l}}^i + e_{g_{n,l}}^i, \xi_{n,l})_{\Gamma} = 0, \end{aligned} \quad (4.28)$$

$$\begin{aligned} \phi_l \left(\frac{e_{S,l}^i}{\Delta t}, \xi_{w,l} \right)_{\Omega_l} + \theta \left(\lambda_{w,l}(S_l^{k,i-1}) \mathbf{K}_l \nabla p_{w,l}^{k,i} - \lambda_{w,l}(S_l^k) \mathbf{K}_l \nabla p_{w,l}^k, \nabla \xi_{w,l} \right)_{\Omega_l} \\ + (\mathcal{L}_{\Gamma} e_{p_{w,l}}^i + e_{g_{w,l}}^i, \xi_{w,l})_{\Gamma} = 0, \end{aligned} \quad (4.29)$$

$$e_{g_{\alpha},l}^i = -2\mathcal{L}_{\Gamma} e_{p_{\alpha},3-l}^{i-1} - e_{g_{\alpha},3-l}^{i-1} \quad \text{in } L^2(\Gamma), \quad (4.30)$$

$$\begin{aligned} \theta(e_{p_{n,l}}^i - e_{p_{w,l}}^i) + \left(\mathcal{L}_{p,l} + \frac{\mathcal{L}_{T,l} + \mathcal{L}_{\Phi,l}}{\Delta t} \right) (e_{S,l}^i - e_{S,l}^{i-1}) \\ = \theta(p_{c,l}(S_l^{k,i-1}) - p_{c,l}(S_l^k)) - \frac{T_l(S_l^{k,i-1}) - T_l(S_l^k)}{\Delta t} \\ - \left(\Phi_{\delta,l} \left(\frac{S_l^{k,i-1} - S_l^{k-1}}{\Delta t} \right) - \Phi_{\delta,l} \left(\frac{S_l^k - S_l^{k-1}}{\Delta t} \right) \right) \quad \text{in } L^2(\Omega_l). \end{aligned} \quad (4.31)$$

In the following, we derive estimates for the errors at iteration i depending on those of the previous iteration $i-1$. This is done separately for each of the equations (4.28)–(4.31) using the monotonicity of the coefficient functions. Combining these estimates, we observe absolute convergence of the series of errors, and conclude the convergence of the solution.

Error estimate on the interface conditions. Using (4.30), the norm of $e_{g_{\alpha},l}^i$ is

$$\|e_{g_{\alpha},l}^i\|_{\Gamma}^2 = 4\mathcal{L}_{\Gamma} \left(\mathcal{L}_{\Gamma} e_{p_{\alpha},3-l}^{i-1} + e_{g_{\alpha},3-l}^{i-1}, e_{p_{\alpha},3-l}^{i-1} \right)_{\Gamma} + \|e_{g_{\alpha},3-l}^{i-1}\|_{\Gamma}^2$$

and thus by index shifting i to $i + 1$ and l to $3 - l$

$$(\mathcal{L}_\Gamma e_{p_\alpha, l}^i + e_{g_\alpha, l}^i, e_{p_\alpha, l}^i)_\Gamma = -\frac{1}{4\mathcal{L}_\Gamma} \left(\|e_{g_\alpha, l}^i\|_\Gamma^2 - \|e_{g_\alpha, 3-l}^{i+1}\|_\Gamma^2 \right). \quad (4.32)$$

Error estimate on the non-wetting pressure. Testing (4.28) with $\xi_{n, l} = e_{p_n, l}^i$ yields

$$\begin{aligned} & -\phi_l \left(\frac{e_{S, l}^i}{\Delta t}, e_{p_n, l}^i \right)_{\Omega_l} + \theta \left(\lambda_{n, l} (S_l^{k, i-1}) \mathbf{K}_l \nabla e_{p_n, l}^i, \nabla e_{p_n, l}^i \right)_{\Omega_l} \\ & + (\mathcal{L}_\Gamma e_{p_n, l}^i + e_{g_n, l}^i, e_{p_n, l}^i)_\Gamma + \theta \left((\lambda_{n, l} (S_l^{k, i-1}) - \lambda_{n, l} (S_l^k)) \mathbf{K}_l \nabla p_{n, l}^k, \nabla e_{p_n, l}^i \right)_{\Omega_l} = 0. \end{aligned}$$

Since $\lambda_{n, l}$ has the lower bound $m_{\lambda_{n, l}}$ and is Lipschitz-continuous, one obtains by the Cauchy–Schwarz inequality and (4.32)

$$\begin{aligned} & -\phi_l \left(\frac{e_{S, l}^i}{\Delta t}, e_{p_n, l}^i \right)_{\Omega_l} + \theta m_{\lambda_{n, l}} \left\| \mathbf{K}_l^{1/2} \nabla e_{p_n, l}^i \right\|_{\Omega_l}^2 - \frac{1}{4\mathcal{L}_\Gamma} \left(\|e_{g_\alpha, l}^i\|_\Gamma^2 - \|e_{g_\alpha, 3-l}^{i+1}\|_\Gamma^2 \right) \\ & \leq \theta L_{\lambda_{n, l}} \left\| \mathbf{K}_l^{1/2} \nabla p_{n, l}^k \right\|_{L^\infty(\Omega_l)} \|e_{S, l}^{i-1}\|_{\Omega_l} \left\| \mathbf{K}_l^{1/2} \nabla e_{p_n, l}^i \right\|_{\Omega_l}. \end{aligned}$$

By Young’s inequality and the bound on the pressure gradient, one gets

$$\begin{aligned} & -\phi_l \left(\frac{e_{S, l}^i}{\Delta t}, e_{p_n, l}^i \right)_{\Omega_l} + \frac{\theta m_{\lambda_{n, l}}}{2} \left\| \mathbf{K}_l^{1/2} \nabla e_{p_n, l}^i \right\|_{\Omega_l}^2 + \frac{1}{4\mathcal{L}_\Gamma} \|e_{g_\alpha, 3-l}^{i+1}\|_\Gamma^2 \\ & \leq \frac{\theta L_{\lambda_{n, l}}^2 M_{p_n, l}^2}{2m_{\lambda_{n, l}}} \|e_{S, l}^{i-1}\|_{\Omega_l}^2 + \frac{1}{4\mathcal{L}_\Gamma} \|e_{g_\alpha, l}^i\|_\Gamma^2. \quad (4.33) \end{aligned}$$

Error estimate on the wetting pressure. Testing (4.29) with $\xi_{w, l} = e_{p_w, l}^i$ and following the same steps as for the non-wetting pressure equation yields

$$\begin{aligned} & \phi_l \left(\frac{e_{S, l}^i}{\Delta t}, e_{p_w, l}^i \right)_{\Omega_l} + \frac{\theta m_{\lambda_{w, l}}}{2} \left\| \mathbf{K}_l^{1/2} \nabla e_{p_w, l}^i \right\|_{\Omega_l}^2 + \frac{1}{4\mathcal{L}_\Gamma} \|e_{g_w, 3-l}^{i+1}\|_\Gamma^2 \\ & \leq \frac{\theta L_{\lambda_{w, l}}^2 M_{p_w, l}^2}{2m_{\lambda_{w, l}}} \|e_{S, l}^{i-1}\|_{\Omega_l}^2 + \frac{1}{4\mathcal{L}_\Gamma} \|e_{g_w, l}^i\|_\Gamma^2. \quad (4.34) \end{aligned}$$

Error estimate on the pressure difference. Testing (4.31) with $e_{S, l}^i$ and using the identity $a(a - b) = \frac{1}{2}(a^2 - b^2 + (a - b)^2)$ for the stabilization term yields

$$\theta (e_{p_n, l}^i - e_{p_w, l}^i, e_{S, l}^i)_{\Omega_l} + \left(\frac{\mathcal{L}_{p, l}}{2} + \frac{\mathcal{L}_{T, l} + \mathcal{L}_{\Phi, l}}{2\Delta t} \right) \left(\|e_{S, l}^i\|_{\Omega_l}^2 - \|e_{S, l}^{i-1}\|_{\Omega_l}^2 + \|e_{S, l}^i - e_{S, l}^{i-1}\|_{\Omega_l}^2 \right)$$

$$\begin{aligned}
&= \left(\theta \left(p_{c,l}(S_l^{k,i-1}) - p_{c,l}(S_l^k) \right) - \frac{T_l(S_l^{k,i-1}) - T_l(S_l^k)}{\Delta t}, e_{S,l}^{i-1} \right)_{\Omega_l} \\
&\quad - \left(\Phi_{\delta,l} \left(\frac{S_l^{k,i-1} - S_l^{k-1}}{\Delta t} \right) - \Phi_{\delta,l} \left(\frac{S_l^k - S_l^{k-1}}{\Delta t} \right), e_{S,l}^{i-1} \right)_{\Omega_l} \\
&\quad + \left(\theta \left(p_{c,l}(S_l^{k,i-1}) - p_{c,l}(S_l^k) \right) - \frac{T_l(S_l^{k,i-1}) - T_l(S_l^k)}{\Delta t}, e_{S,l}^i - e_{S,l}^{i-1} \right)_{\Omega_l} \\
&\quad - \left(\Phi_{\delta,l} \left(\frac{S_l^{k,i-1} - S_l^{k-1}}{\Delta t} \right) - \Phi_{\delta,l} \left(\frac{S_l^k - S_l^{k-1}}{\Delta t} \right), e_{S,l}^i - e_{S,l}^{i-1} \right)_{\Omega_l}.
\end{aligned}$$

The last two terms on the righthand side can be bounded by Cauchy–Schwarz inequality and Young’s inequality, which yields

$$\begin{aligned}
&\theta (e_{p_n,l}^i - e_{p_w,l}^i, e_{S,l}^i)_{\Omega_l} + \left(\frac{\mathcal{L}_{p,l}}{2} + \frac{\mathcal{L}_{T,l} + \mathcal{L}_{\Phi,l}}{2\Delta t} \right) \left(\|e_{S,l}^i\|_{\Omega_l}^2 - \|e_{S,l}^{i-1}\|_{\Omega_l}^2 \right) \\
&\leq \left(\theta \left(p_{c,l}(S_l^{k,i-1}) - p_{c,l}(S_l^k) \right) - \frac{T_l(S_l^{k,i-1}) - T_l(S_l^k)}{\Delta t}, e_{S,l}^{i-1} \right)_{\Omega_l} \\
&\quad - \left(\Phi_{\delta,l} \left(\frac{S_l^{k,i-1} - S_l^{k-1}}{\Delta t} \right) - \Phi_{\delta,l} \left(\frac{S_l^k - S_l^{k-1}}{\Delta t} \right), e_{S,l}^{i-1} \right)_{\Omega_l} \\
&\quad + \frac{\theta^2}{2\mathcal{L}_{p,l}} \|p_{c,l}(S_l^{k,i-1}) - p_{c,l}(S_l^k)\|_{\Omega_l}^2 + \frac{\Delta t}{2\mathcal{L}_{T,l}} \left\| \frac{T_l(S_l^{k,i-1}) - T_l(S_l^k)}{\Delta t} \right\|_{\Omega_l}^2 \\
&\quad + \frac{\Delta t}{2\mathcal{L}_{\Phi,l}} \left\| \Phi_{\delta,l} \left(\frac{S_l^{k,i-1} - S_l^{k-1}}{\Delta t} \right) - \Phi_{\delta,l} \left(\frac{S_l^k - S_l^{k-1}}{\Delta t} \right) \right\|_{\Omega_l}^2.
\end{aligned}$$

For a Lipschitz-continuous and monotonically increasing function $f : \mathbb{R} \rightarrow \mathbb{R}$, it holds $(f(a) - f(b))(a - b) \geq \frac{1}{L_f} |f(a) - f(b)|^2$ for all $a, b \in \mathbb{R}$, where L_f denotes the Lipschitz constant of f . Since $p_{c,l}$, T_l and $\Phi_{\delta,l}$ are Lipschitz-continuous and monotone, one thereby gets

$$\begin{aligned}
&\theta (e_{p_n,l}^i - e_{p_w,l}^i, e_{S,l}^i)_{\Omega_l} + \left(\frac{\mathcal{L}_{p,l}}{2} + \frac{\mathcal{L}_{T,l} + \mathcal{L}_{\Phi,l}}{2\Delta t} \right) \left(\|e_{S,l}^i\|_{\Omega_l}^2 - \|e_{S,l}^{i-1}\|_{\Omega_l}^2 \right) \\
&+ \frac{\theta}{2} \left(|p_{c,l}(S_l^{k,i-1}) - p_{c,l}(S_l^k)|, |e_{S,l}^{i-1}| \right)_{\Omega_l} \leq \left(\frac{\theta^2}{2\mathcal{L}_{p,l}} - \frac{\theta}{2L_{p_c,l}} \right) \|p_{c,l}(S_l^{k,i-1}) - p_{c,l}(S_l^k)\|_{\Omega_l}^2 \\
&\quad + \left(\frac{\Delta t}{2\mathcal{L}_{T,l}} - \frac{\Delta t}{L_{T,l}} \right) \left\| \frac{T_l(S_l^{k,i-1}) - T_l(S_l^k)}{\Delta t} \right\|_{\Omega_l}^2 \\
&\quad + \left(\frac{\Delta t}{2\mathcal{L}_{\Phi,l}} - \frac{\Delta t}{L_{\Phi_{\delta,l}}} \right) \left\| \Phi_{\delta,l} \left(\frac{S_l^{k,i-1} - S_l^{k-1}}{\Delta t} \right) - \Phi_{\delta,l} \left(\frac{S_l^k - S_l^{k-1}}{\Delta t} \right) \right\|_{\Omega_l}^2.
\end{aligned}$$

Since $\mathcal{L}_{p,l} \geq \theta L_{p_c,l}$, $\mathcal{L}_{T,l} \geq L_{T,l}/2$ and $\mathcal{L}_{\Phi,l} \geq L_{\Phi_{\delta,l}}/2$ by assumption, the right-hand side can be neglected. Furthermore, using the bound $m_{p_c,l} |S_l^{k,i-1} - S_l^k| \leq$

$|p_{c,l}(S_l^{k,i-1}) - p_{c,l}(S_l^k)|$ from [Assumption 4.1](#), one obtains

$$\begin{aligned} \theta (e_{p_n,l}^i - e_{p_w,l}^i, e_{S,l}^i)_{\Omega_l} + \frac{\theta m_{p_c,l}}{2} \|e_{S,l}^{i-1}\|_{\Omega_l}^2 \\ + \left(\frac{\mathcal{L}_{p,l}}{2} + \frac{\mathcal{L}_{T,l} + \mathcal{L}_{\Phi,l}}{2\Delta t} \right) \left(\|e_{S,l}^i\|_{\Omega_l}^2 - \|e_{S,l}^{i-1}\|_{\Omega_l}^2 \right) \leq 0. \end{aligned}$$

Multiplication with $\phi_l(\theta\Delta t)^{-1}$ finally leads to

$$\begin{aligned} \phi_l \left(e_{p_n,l}^i - e_{p_w,l}^i, \frac{e_{S,l}^i}{\Delta t} \right)_{\Omega_l} + \frac{\phi_l m_{p_c,l}}{2\Delta t} \|e_{S,l}^{i-1}\|_{\Omega_l}^2 \\ \leq \frac{\phi_l}{\theta\Delta t} \left(\frac{\mathcal{L}_{p,l}}{2} + \frac{\mathcal{L}_{T,l} + \mathcal{L}_{\Phi,l}}{2\Delta t} \right) \left(\|e_{S,l}^{i-1}\|_{\Omega_l}^2 - \|e_{S,l}^i\|_{\Omega_l}^2 \right). \quad (4.35) \end{aligned}$$

Combined error estimate. Summation of the estimates (4.33)–(4.35) yields

$$\begin{aligned} \sum_{\alpha \in \{n,w\}} \frac{\theta m_{\lambda_\alpha,l}}{2} \|\mathbf{K}_l^{1/2} \nabla e_{p_\alpha,l}^i\|_{\Omega_l}^2 + C_l(\Delta t) \|e_{S,l}^{i-1}\|_{\Omega_l}^2 \\ \leq \frac{1}{4\mathcal{L}_\Gamma} \sum_{\alpha \in \{n,w\}} \left(\|e_{g_\alpha,l}^i\|_\Gamma^2 - \|e_{g_\alpha,3-l}^{i+1}\|_\Gamma^2 \right) \\ + \frac{\phi_l}{\theta\Delta t} \left(\frac{\mathcal{L}_{p,l}}{2} + \frac{\mathcal{L}_{T,l} + \mathcal{L}_{\Phi,l}}{2\Delta t} \right) \left(\|e_{S,l}^{i-1}\|_{\Omega_l}^2 - \|e_{S,l}^i\|_{\Omega_l}^2 \right), \end{aligned}$$

where by assumption

$$C_l(\Delta t) = \frac{\phi_l m_{p_c,l}}{2\Delta t} - \sum_{\alpha \in \{n,w\}} \frac{\theta L_{\lambda_\alpha,l}^2 M_{p_\alpha,l}^2}{2m_{\lambda_\alpha,l}} > 0.$$

By summing the estimates for $l \in \{1, 2\}$ and $i = 1, 2, \dots, r$, one gets

$$\begin{aligned} \sum_{i=1}^r \sum_{l=1}^2 \sum_{\alpha \in \{n,w\}} \frac{\theta m_{\lambda_\alpha,l}}{2} \|\mathbf{K}_l^{1/2} \nabla e_{p_\alpha,l}^i\|_{\Omega_l}^2 + \sum_{i=1}^r \sum_{l=1}^2 C_l(\Delta t) \|e_{S,l}^{i-1}\|_{\Omega_l}^2 \\ \leq \frac{1}{4\mathcal{L}_\Gamma} \sum_{l=1}^2 \sum_{\alpha \in \{n,w\}} \|e_{g_\alpha,l}^1\|_\Gamma^2 + \frac{\phi_l}{\theta\Delta t} \sum_{l=1}^2 \left(\frac{\mathcal{L}_{p,l}}{2} + \frac{\mathcal{L}_{T,l} + \mathcal{L}_{\Phi,l}}{2\Delta t} \right) \|e_{S,l}^0\|_{\Omega_l}^2. \end{aligned}$$

Since the righthand side is independent of r , we conclude that the series on the left are absolutely convergent. Therefore, $S_l^{k,i} \rightarrow S_l^k$ in $L^2(\Omega_l)$ and the Poincaré inequality implies $p_{\alpha,l}^{k,i} \rightarrow p_{\alpha,l}^k$ in \mathcal{W}_l . To show the convergence of the $g_{\alpha,l}^{k,i}$, we consider again (4.28) and (4.29), and take the limit $i \rightarrow \infty$. By continuity one obtains

$$\lim_{i \rightarrow \infty} (e_{g_\alpha,l}^i, \xi_{\alpha,l})_\Gamma = 0$$

for any $\xi_{\alpha,l} \in \mathcal{W}_l$. Since the trace operator is surjective onto $H_{00}^{1/2}(\Gamma)$, which is dense in $L^2(\Gamma)$, we conclude $e_{g_{\alpha,l}}^i \rightharpoonup 0$ in $L^2(\Gamma)$ as $i \rightarrow \infty$. Additionally, one can directly obtain $e_{g_{\alpha,l}}^i + e_{g_{\alpha,3-l}}^{i-1} \rightarrow 0$ in $L^2(\Gamma)$ by (4.30). \square

4.4.2. LDD-scheme II

The existence of a unique solution to [Problem LDD-2](#) is again a consequence of the linearization, but using additionally the contraction property in (4.26).

Lemma 4.3. *Problem LDD-2 has a unique solution if Assumption 4.1 is fulfilled, $\theta \in (0, 1]$, and it holds $\Delta t < \frac{1}{\theta L_{\Psi,l} L_{p_{c,l}}}$.*

Proof. Since $p_{\alpha,l}^{k,i-1}|_{\Gamma} \in L^2(\Gamma)$, (4.20) uniquely provides $g_{\alpha,l}^{k,i} \in L^2(\Gamma)$ for $\alpha \in n, w$ and $l \in \{1, 2\}$. After multiplying (4.26) by Δt and adding S_l^{k-1} , the lefthand side is $S_l^{k,i}$, while the righthand side, considered as function

$$F_l(S_l^{k,i}) := S_l^{k-1} + \Delta t \theta \Psi_l \left(p_{n,l}^{k,i-1} - p_{w,l}^{k,i-1} - p_{c,l}(S_l^{k,i}) \right) + \Delta t (1 - \theta) \Psi_l^{k-1}, \quad (4.36)$$

maps $L^2(\Omega_l)$ into itself. Moreover, for $s, r \in L^2(\Omega_l)$, it holds

$$\|F_l(s) - F_l(r)\|_{\Omega_l} \leq \Delta t \theta L_{\Psi,l} L_{p_{c,l}} \|s - r\|_{\Omega_l}.$$

By assumption $\Delta t \theta L_{\Psi,l} L_{p_{c,l}} < 1$, so F_l is a contraction, and the Banach fixed-point theorem yields the existence of a unique solution $S_l^{k,i} \in L^2(\Omega_l)$ to (4.26). Reordering of the sum of (4.23) and (4.24) leads to

$$\begin{aligned} & \mathcal{L}_{p,l} \left(p_{n,l}^{k,i} - p_{w,l}^{k,i}, \xi_{n,l} - \xi_{w,l} \right)_{\Omega_l} + \theta \sum_{\alpha \in \{n,w\}} \left(\lambda_{\alpha,l}(S_l^{k,i}) \mathbf{K}_l \nabla p_{\alpha,l}^{k,i}, \nabla \xi_{\alpha,l} \right)_{\Omega_l} \\ & + \sum_{\alpha \in \{n,w\}} \mathcal{L}_{\Gamma} \left(p_{\alpha,l}^{k,i}, \xi_{\alpha,l} \right)_{\Gamma} = \sum_{\alpha \in \{n,w\}} \left(q_{\alpha,l}^{k,\theta}, \xi_{\alpha,l} \right)_{\Omega_l} + \phi_l \left(\frac{S_l^{k,i} - S_l^{k-1}}{\Delta t}, \xi_{n,l} - \xi_{w,l} \right)_{\Omega_l} \\ & + \mathcal{L}_{p,l} \left(p_{n,l}^{k,i-1} - p_{w,l}^{k,i-1}, \xi_{n,l} - \xi_{w,l} \right)_{\Omega_l} \\ & + (1 - \theta) \sum_{\alpha \in \{n,w\}} \left(\mathbf{u}_{\alpha,l}^{k,i-1}, \nabla \xi_{\alpha,l} \right)_{\Omega_l} - \sum_{\alpha \in \{n,w\}} \left(g_{\alpha,l}^{k,i}, \xi_{\alpha,l} \right)_{\Gamma}, \end{aligned}$$

where the righthand side is independent of $p_{n,l}^{k,i}$ and $p_{w,l}^{k,i}$. As before for the first scheme, the first term on the lefthand side is positive semi-definite with respect to the product space $[\mathcal{W}_l]^2$, while the remaining terms of the lefthand side form a symmetric, coercive and continuous bilinear form on $[\mathcal{W}_l]^2$ by [Assumption 4.1](#), $\theta > 0$ and $\mathcal{L}_{\Gamma} > 0$. The righthand side is a continuous linear functional on $[\mathcal{W}_l]^2$, hence by the Lax–Milgram lemma, a unique solution $(p_{n,l}^{k,i}, p_{w,l}^{k,i}) \in [\mathcal{W}_l]^2$ exists for $l \in \{1, 2\}$. \square

To prove the convergence of the LDD-scheme II, we derive a-priori estimates

for the errors between the solution to [Problem LDD-2](#) and the solution of the limit equations. These estimates then yield the convergence for any initial guess.

Theorem 4.2 (Convergence of the LDD-scheme II). *Let [Assumption 4.1](#) be fulfilled, and let $\theta \in (0, 1]$ and $\tau_l > 0$ be fixed. Assume that a solution $(S^k, p_n^k, p_w^k) \in \mathcal{V}$ of [Problem 4.2](#) exists and satisfies $\|\mathbf{K}_l^{1/2} \nabla p_{\alpha,l}^k\|_{L^\infty(\Omega_l)} \leq M_{p_{\alpha,l}}$ and $\mathbf{u}_{\alpha,l}^{k,\theta} \cdot \mathbf{n}_l \in L^2(\Gamma)$. If the stabilization parameter is sufficiently large and the time step is small enough,*

$$\mathcal{L}_{p,l} > 2\phi_l \theta L_{\Psi,l}, \quad \Delta t \leq \frac{1}{2\theta L_{\Psi,l} L_{p_{c,l}}}, \quad \Delta t \leq \sqrt{\frac{\frac{1}{2\theta \phi_l L_{\Psi,l}} - \frac{1}{\mathcal{L}_{p,l}}}{\sum_{\alpha \in \{n,w\}} \left(\frac{2\theta L_{\Psi,l}^2 L_{p_{c,l}}^2 C_{\Omega_l}^2}{m_{\lambda_{\alpha,l}} \underline{K}_l} + \frac{\theta L_{\lambda_{\alpha,l}}^2 M_{p_{\alpha,l}}^2}{\phi_l^2 m_{\lambda_{\alpha,l}}} \right)}}$$

for $l \in \{1, 2\}$, the sequence of solutions of [Problem LDD-2](#) converges towards the solution of [Problem 4.2](#) independently of the initial guess $(S^{k,0}, p_n^{k,0}, p_w^{k,0}) \in \mathcal{W}$ and $g_{\alpha,l}^{k,0} \in L^2(\Gamma)$ for $l \in \{1, 2\}$ and $\alpha \in \{n, w\}$. More precisely, it holds

$$S_l^{k,i} \rightarrow S_l^k \text{ in } L^2(\Omega_l), \quad p_{\alpha,l}^{k,i} \rightarrow p_{\alpha,l}^k \text{ in } \mathcal{W}_l, \quad g_{\alpha,l}^{k,i} \rightarrow g_{\alpha,l}^k \text{ in } L^2(\Gamma)$$

for $l \in \{1, 2\}$, $\alpha \in \{n, w\}$ as $i \rightarrow \infty$.

Proof. We define the iteration errors by

$$e_{S,l}^i := S_l^{k,i} - S_l^k \in L^2(\Omega_l), \quad e_{p_{\alpha,l}}^i := p_{\alpha,l}^{k,i} - p_{\alpha,l}^k \in \mathcal{W}_l, \quad e_{g_{\alpha,l}}^i := g_{\alpha,l}^{k,i} - g_{\alpha,l}^k \in L^2(\Gamma), \\ e_{p_{c,l}}^i := e_{p_{n,l}}^i - e_{p_{w,l}}^i \in \mathcal{W}_l, \quad e_{\Psi,l}^i := \Psi_l^{k,i} - \Psi_l(p_{n,l}^k - p_{w,l}^k - p_{c,l}(S_l^{k,i})) \in L^2(\Gamma).$$

Subtracting the limit equations (4.14)–(4.16) and (4.12) from (4.23)–(4.26) gives

$$-\phi_l \left(\frac{e_{S,l}^i}{\Delta t}, \xi_{n,l} \right)_{\Omega_l} + \mathcal{L}_{p,l} \left(e_{p_{c,l}}^i - e_{p_{c,l}}^{i-1}, \xi_{n,l} \right)_{\Omega_l} - \left(\mathbf{u}_{n,l}^{k,\theta,i} - \mathbf{u}_{n,l}^{k,\theta}, \nabla \xi_{n,l} \right)_{\Omega_l} \\ + (\mathcal{L}_{\Gamma} e_{p_{n,l}}^i + e_{g_{n,l}}^i, \xi_{n,l})_{\Gamma} = 0, \quad (4.37)$$

$$\phi_l \left(\frac{e_{S,l}^i}{\Delta t}, \xi_{w,l} \right)_{\Omega_l} - \mathcal{L}_{p,l} \left(e_{p_{c,l}}^i - e_{p_{c,l}}^{i-1}, \xi_{w,l} \right)_{\Omega_l} - \left(\mathbf{u}_{w,l}^{k,\theta,i} - \mathbf{u}_{w,l}^{k,\theta}, \nabla \xi_{w,l} \right)_{\Omega_l} \\ + (\mathcal{L}_{\Gamma} e_{p_{w,l}}^i + e_{g_{w,l}}^i, \xi_{w,l})_{\Gamma} = 0, \quad (4.38)$$

$$e_{g_{\alpha,l}}^i = -2\mathcal{L}_{\Gamma} e_{p_{\alpha,3-l}}^{i-1} - e_{g_{\alpha,3-l}}^{i-1} \text{ in } L^2(\Gamma), \quad (4.39)$$

$$\frac{e_{S,l}^i}{\Delta t} = \theta (\Psi_l^{k,i} - \Psi_l^k) \text{ in } L^2(\Omega_l). \quad (4.40)$$

As for the proof of [Theorem 4.1](#), we derive estimates for the errors at iteration i depending on those of the previous iteration $i - 1$. This is done separately for (4.37), (4.38), and (4.40) using the monotonicity of the coefficient functions. For (4.39) we use the estimate (4.32) from the proof of [Theorem 4.1](#). Combining the estimates, the convergence of the solution follows from the absolute convergence of the series of errors.

Error estimate on the saturation. Equation (4.40) yields

$$\begin{aligned} \frac{1}{\Delta t} \|e_{S,l}^i\|_{\Omega_l} &= \theta \left\| \Psi_l^{k,i} - \Psi_l^k \right\|_{\Omega_l} \leq \theta \left\| \Psi_l^{k,i} - \Psi_l(p_{n,l}^k - p_{w,l}^k - p_{c,l}(S_l^{k,i})) \right\|_{\Omega_l} \\ &\quad + \theta \left\| \Psi_l(p_{n,l}^k - p_{w,l}^k - p_{c,l}(S_l^{k,i})) - \Psi_l^k \right\|_{\Omega_l} \\ &\leq \theta \|e_{\Psi,l}^i\|_{\Omega_l} + \theta L_{\Psi,l} L_{p_{c,l}} \|e_{S,l}^i\|_{\Omega_l}. \end{aligned}$$

In the last step, the Lipschitz continuity of Ψ_l and $p_{c,l}$ is used. Multiplying by Δt and using $\Delta t \leq (2\theta L_{\Psi,l} L_{p_{c,l}})^{-1}$ yields

$$\|e_{S,l}^i\|_{\Omega_l} \leq 2\theta \Delta t \|e_{\Psi,l}^i\|_{\Omega_l}. \quad (4.41)$$

Error estimate on the non-wetting pressure. Note that (4.39) again leads to (4.32). Therefore, testing (4.37) with $\xi_{n,l} = e_{p_{n,l}}^i$ yields

$$\begin{aligned} &-\phi_l \left(\frac{e_{S,l}^i}{\Delta t}, e_{p_{n,l}}^i \right)_{\Omega_l} + \mathcal{L}_{p,l} \left(e_{p_{c,l}}^i - e_{p_{c,l}}^{i-1}, e_{p_{n,l}}^i \right)_{\Omega_l} + \theta \left(\lambda_{n,l}(S_l^{k,i}) \mathbf{K}_l \nabla e_{p_{n,l}}^i, \nabla e_{p_{n,l}}^i \right)_{\Omega_l} \\ &= -\theta \left((\lambda_{n,l}(S_l^{k,i}) - \lambda_{n,l}(S_l^k)) \mathbf{K}_l \nabla p_{n,l}^k, \nabla e_{p_{n,l}}^i \right)_{\Omega_l} + \frac{1}{4\mathcal{L}_\Gamma} \left(\|e_{g_{n,l}}^{i+1}\|_\Gamma^2 - \|e_{g_{n,3-l}}^i\|_\Gamma^2 \right). \end{aligned}$$

By the lower bound $m_{\lambda_{n,l}}$ on $\lambda_{n,l}$, the Lipschitz continuity of $\lambda_{n,l}$ and the bound on the pressure gradient, one obtains with the Cauchy–Schwarz inequality

$$\begin{aligned} &-\phi_l \left(\frac{e_{S,l}^i}{\Delta t}, e_{p_{n,l}}^i \right)_{\Omega_l} + \mathcal{L}_{p,l} \left(e_{p_{c,l}}^i - e_{p_{c,l}}^{i-1}, e_{p_{n,l}}^i \right)_{\Omega_l} + \theta m_{\lambda_{n,l}} \left\| \mathbf{K}_l^{1/2} \nabla e_{p_{n,l}}^i \right\|_{\Omega_l}^2 \\ &\leq \theta L_{\lambda_{n,l}} M_{p_{n,l}} \|e_{S,l}^i\|_{\Omega_l} \left\| K^{1/2} \nabla e_{p_{n,l}}^i \right\|_{\Omega_l} + \frac{1}{4\mathcal{L}_\Gamma} \left(\|e_{g_{n,l}}^{i+1}\|_\Gamma^2 - \|e_{g_{n,3-l}}^i\|_\Gamma^2 \right). \end{aligned}$$

Young's inequality and estimate (4.41) lead to

$$\begin{aligned} &-\phi_l \left(\frac{e_{S,l}^i}{\Delta t}, e_{p_{n,l}}^i \right)_{\Omega_l} + \mathcal{L}_{p,l} \left(e_{p_{c,l}}^i - e_{p_{c,l}}^{i-1}, e_{p_{n,l}}^i \right)_{\Omega_l} + \frac{\theta m_{\lambda_{n,l}}}{2} \left\| \mathbf{K}_l^{1/2} \nabla e_{p_{n,l}}^i \right\|_{\Omega_l}^2 \\ &\leq \frac{2\Delta t^2 \theta^3 L_{\lambda_{n,l}}^2 M_{p_{n,l}}^2}{m_{\lambda_{n,l}}} \|e_{\Psi,l}^i\|_{\Omega_l}^2 + \frac{1}{4\mathcal{L}_\Gamma} \left(\|e_{g_{n,l}}^{i+1}\|_\Gamma^2 - \|e_{g_{n,3-l}}^i\|_\Gamma^2 \right). \quad (4.42) \end{aligned}$$

Error estimate on the wetting pressure. Testing (4.29) with $\xi_{w,l} = e_{p_{w,l}}^i$ and following the same steps as for the non-wetting pressure equation yields

$$\begin{aligned} &\phi_l \left(\frac{e_{S,l}^i}{\Delta t}, e_{p_{w,l}}^i \right)_{\Omega_l} - \mathcal{L}_{p,l} \left(e_{p_{c,l}}^i - e_{p_{c,l}}^{i-1}, e_{p_{w,l}}^i \right)_{\Omega_l} + \frac{\theta m_{\lambda_{w,l}}}{2} \left\| \mathbf{K}_l^{1/2} \nabla e_{p_{w,l}}^i \right\|_{\Omega_l}^2 \\ &\leq \frac{2\Delta t^2 \theta^3 L_{\lambda_{w,l}}^2 M_{p_{w,l}}^2}{m_{\lambda_{w,l}}} \|e_{\Psi,l}^i\|_{\Omega_l}^2 + \frac{1}{4\mathcal{L}_\Gamma} \left(\|e_{g_{w,l}}^i\|_\Gamma^2 - \|e_{g_{w,3-l}}^{i+1}\|_\Gamma^2 \right). \quad (4.43) \end{aligned}$$

Combined error estimate Addition of the pressure estimates (4.42) and (4.43) yields by the identity $(a - b)a = \frac{1}{2}(a^2 - b^2 + (a - b)^2)$

$$\begin{aligned} & -\phi_l \left(\frac{e_{S,l}^i}{\Delta t}, e_{p_c,l}^i \right)_{\Omega_l} + \frac{\mathcal{L}_{p,l}}{2} \left(\|e_{p_c,l}^i\|_{\Omega_l}^2 - \|e_{p_c,l}^{i-1}\|_{\Omega_l}^2 + \|e_{p_c,l}^i - e_{p_c,l}^{i-1}\|_{\Omega_l}^2 \right) \\ & + \sum_{\alpha \in \{n,w\}} \frac{\theta m_{\lambda_\alpha,l}}{2} \|\mathbf{K}_l^{1/2} \nabla e_{p_\alpha,l}^i\|_{\Omega_l}^2 \leq \frac{1}{4\mathcal{L}_\Gamma} \sum_{\alpha \in \{n,w\}} \left(\|e_{g_\alpha,l}^i\|_\Gamma^2 - \|e_{g_\alpha,l}^{i+1}\|_\Gamma^2 \right) \\ & + \sum_{\alpha \in \{n,w\}} \frac{2\Delta t^2 \theta^3 L_{\lambda_\alpha,l}^2 M_{p_\alpha,l}^2}{m_{\lambda_\alpha,l}} \|e_{\Psi,l}^i\|_{\Omega_l}^2. \quad (4.44) \end{aligned}$$

The first term on the lefthand side can be estimated as follows. Using (4.40) and $\Psi^* := \Psi_l(p_{n,l}^k - p_{w,l}^k - p_{c,l}(S_l^{k,i}))$, one obtains

$$\begin{aligned} \left(\frac{e_{S,l}^i}{\Delta t}, e_{p_c,l}^i \right)_{\Omega_l} &= \left(\frac{e_{S,l}^i}{\Delta t}, e_{p_c,l}^i - e_{p_c,l}^{i-1} \right)_{\Omega_l} + \theta \left(\Psi_l^{k,i} - \Psi^* + \Psi^* - \Psi_l^k, e_{p_c,l}^{i-1} \right)_{\Omega_l} \\ &\leq \frac{1}{\Delta t} \|e_{S,l}^i\|_{\Omega_l} \|e_{p_c,l}^i - e_{p_c,l}^{i-1}\|_{\Omega_l} + \theta \left(e_{\Psi,l}^i, e_{p_c,l}^{i-1} \right)_{\Omega_l} \\ &\quad + \theta \left(\Psi^* - \Psi_l(p_{n,l}^k - p_{w,l}^k - p_{c,l}(S_l^k)), e_{p_c,l}^{i-1} \right)_{\Omega_l}. \end{aligned}$$

Since Ψ_l and $p_{c,l}$ are decreasing and Lipschitz-continuous, one gets

$$\begin{aligned} \left(\frac{e_{S,l}^i}{\Delta t}, e_{p_c,l}^i \right)_{\Omega_l} &\leq \frac{1}{\Delta t} \|e_{S,l}^i\|_{\Omega_l} \|e_{p_c,l}^i - e_{p_c,l}^{i-1}\|_{\Omega_l} - \frac{\theta}{L_{\Psi,l}} \|e_{\Psi,l}^i\|_{\Omega_l}^2 \\ &\quad + \theta L_{\Psi,l} L_{p_c,l} \|e_{S,l}^i\|_{\Omega_l} \sum_{\alpha \in \{n,w\}} \|e_{p_\alpha,l}^{i-1}\|_{\Omega_l}. \end{aligned}$$

With the estimate (4.41), Young's inequality yields for $\epsilon_\alpha > 0$

$$\begin{aligned} \left(\frac{e_{S,l}^i}{\Delta t}, e_{p_c,l}^i \right)_{\Omega_l} &\leq \left(\frac{2\phi_l \theta^2}{\mathcal{L}_{p,l}} + \sum_{\alpha \in \{n,w\}} \frac{\Delta t^2 \theta^4 L_{\Psi,l}^2 L_{p_c,l}^2}{\epsilon_\alpha} - \frac{\theta}{L_{\Psi,l}} \right) \|e_{\Psi,l}^i\|_{\Omega_l}^2 \\ &\quad + \frac{\mathcal{L}_{p,l}}{2\phi_l} \|e_{p_c,l}^i - e_{p_c,l}^{i-1}\|_{\Omega_l}^2 + \sum_{\alpha \in \{n,w\}} \epsilon_\alpha \|e_{p_\alpha,l}^{i-1}\|_{\Omega_l}^2. \end{aligned}$$

The Poincaré inequality (with C_{Ω_l} the domain dependent constant) leads to

$$\begin{aligned} \left(\frac{e_{S,l}^i}{\Delta t}, e_{p_c,l}^i \right)_{\Omega_l} &\leq \left(\frac{2\phi_l \theta^2}{\mathcal{L}_{p,l}} + \sum_{\alpha \in \{n,w\}} \frac{\Delta t^2 \theta^4 L_{\Psi,l}^2 L_{p_c,l}^2}{\epsilon_\alpha} - \frac{\theta}{L_{\Psi,l}} \right) \|e_{\Psi,l}^i\|_{\Omega_l}^2 \\ &\quad + \frac{\mathcal{L}_{p,l}}{2\phi_l} \|e_{p_c,l}^i - e_{p_c,l}^{i-1}\|_{\Omega_l}^2 + \sum_{\alpha \in \{n,w\}} \frac{\epsilon_\alpha C_{\Omega_l}^2}{\underline{K}_l} \|\mathbf{K}_l^{1/2} \nabla e_{p_\alpha,l}^{i-1}\|_{\Omega_l}^2. \end{aligned}$$

Multiplying this estimate by ϕ_l , choosing $\epsilon_\alpha = \theta m_{\lambda_\alpha, l} \underline{K}_l (4\phi_l C_{\Omega_l}^2)^{-1}$, and adding to (4.44), one is left with

$$\begin{aligned} & \frac{\mathcal{L}_{p,l}}{2} \left(\|e_{p_\alpha, l}^i\|_{\Omega_l}^2 - \|e_{p_\alpha, l}^{i-1}\|_{\Omega_l}^2 \right) + \sum_{\alpha \in \{n, w\}} \frac{\theta m_{\lambda_\alpha, l}}{2} \left\| \mathbf{K}_l^{1/2} \nabla e_{p_\alpha, l}^i \right\|_{\Omega_l}^2 + C_l(\Delta t) \|e_{\Psi, l}^i\|_{\Omega_l}^2 \\ & \leq \frac{1}{4\mathcal{L}_\Gamma} \sum_{\alpha \in \{n, w\}} \left(\|e_{g_\alpha, l}^i\|_\Gamma^2 - \|e_{g_\alpha, l}^{i+1}\|_\Gamma^2 \right) + \sum_{\alpha \in \{n, w\}} \frac{\theta m_{\lambda_\alpha, l}}{4} \left\| \mathbf{K}_l^{1/2} \nabla e_{p_\alpha, l}^{i-1} \right\|_{\Omega_l}^2, \end{aligned}$$

where

$$C_l(\Delta t) = \frac{\phi_l \theta}{L_{\Psi, l}} - \frac{2\phi_l^2 \theta^2}{\mathcal{L}_{p, l}} - \Delta t^2 \theta^3 \sum_{\alpha \in \{n, w\}} \left(\frac{4\phi_l^2 L_{\Psi, l}^2 L_{p_\alpha, l}^2 C_{\Omega_l}^2}{m_{\lambda_\alpha, l} \underline{K}_l} + \frac{2L_{\lambda_\alpha, l}^2 M_{p_\alpha, l}^2}{m_{\lambda_\alpha, l}} \right).$$

By assumption, $\mathcal{L}_{p, l} > 2\phi_l \theta L_{\Psi, l}$ and Δt is small enough, such that $C_l(\Delta t) \geq 0$. Then, summation of the estimates for $l \in \{1, 2\}$ and $i = 1, 2, \dots, r$ yields

$$\begin{aligned} & \sum_{i=1}^r \sum_{l=1}^2 \sum_{\alpha \in \{n, w\}} \frac{\theta m_{\lambda_\alpha, l}}{4} \left\| \mathbf{K}_l^{1/2} \nabla e_{p_\alpha, l}^i \right\|_{\Omega_l}^2 + \sum_{i=1}^r \sum_{l=1}^2 C_l(\Delta t) \|e_{\Psi, l}^i\|_{\Omega_l}^2 \\ & \leq \frac{1}{4\mathcal{L}_\Gamma} \sum_{l=1}^2 \sum_{\alpha \in \{n, w\}} \|e_{g_\alpha, l}^1\|_\Gamma^2 + \sum_{l=1}^2 \frac{\mathcal{L}_{p, l}}{2} \|e_{p_\alpha, l}^0\|_{\Omega_l}^2 \\ & \quad + \sum_{l=1}^2 \sum_{\alpha \in \{n, w\}} \frac{\theta m_{\lambda_\alpha, l}}{4} \left\| \mathbf{K}_l^{1/2} \nabla e_{p_\alpha, l}^0 \right\|_{\Omega_l}^2. \end{aligned}$$

Since the righthand side is independent of r , we conclude that the series on the left is absolutely convergent. By the Poincaré inequality and estimate (4.41), we obtain $p_{\alpha, l}^{k, i} \rightarrow p_{\alpha, l}^k$ in \mathcal{W}_l and $S_l^{k, i} \rightarrow S_l^k$ in $L^2(\Omega_l)$. The weak convergence $e_{g_\alpha, l}^i \rightharpoonup 0$ in $L^2(\Gamma)$ can be shown exactly as in Theorem 4.1 by the limit $i \rightarrow \infty$ in (4.37) and (4.38). \square

4.5. Numerical experiments

For the numerical validation of the previous theoretical results, we present several numerical studies in two spatial dimensions. We focus on three aspects: the convergence behavior in space and time of the whole method, the convergence behavior of the LDD-schemes within single time steps, and the choice of the parameters. Three examples with manufactured solution are presented, followed by a realistic application.

The theoretical results above are independent of the spatial discretization, and thus hold true for all. For Richards' equation and two-phase flow models with equilibrium capillary pressure as well as dynamic capillarity, the (mixed) finite element

method is used in [70,210,254], the discontinuous Galerkin method in [102,187] and the finite volume method in [51,53,71,99]. General gradient schemes are considered in [96,106]. Since the pressure equations are elliptic, we choose here a standard finite element method (Q_2) on a uniform, rectangular mesh of width Δx matching at the interface Γ . Note that this choice is in general not possible for the saturation which lies in $L^2(\Omega_l)$. However, in light of (4.12), the regularity of the saturation is inherited from the initial condition up to $S_l^0 \in H^1(\Omega_l)$. This restriction of the initial data is used for the following numerical examples to allow the use of Lagrange finite elements. We use the Crank–Nicolson method ($\theta = 1/2$) in time, so that discretization errors of order $\mathcal{O}(\Delta t^2 + \Delta x^2)$ are expected for sufficiently smooth solutions. At each time step, the LDD-schemes are stopped, when the relative L^2 -norm of the difference of subsequent iterative solutions drops below 10^{-8} . To obtain the implicitly given saturation in the LDD-scheme II, the fixed-point iteration discussed in the proof of Lemma 4.3 is used up to a residual of 10^{-12} . For simplicity, we take the same linearization parameters on both sub-domains, $\mathcal{L}_a := \mathcal{L}_{a,1} = \mathcal{L}_{a,2}$ for $a \in \{p, T, \Phi\}$.

The implementation is done in C++ using the library deal.II 9.0 [19]. All calculations are performed on a Linux octa-core system.

Note that the mobility functions used in the following examples are not bounded away from zero as required by Assumption 4.1. However, the initial and boundary conditions are chosen in such a way that a degeneracy does not occur since the saturation solutions are bounded away from 0 and 1. The same results are obtained, when the mobility functions are replaced by a regularization $\lambda_{\alpha,l}^\varepsilon(s) = \max\{\varepsilon, \lambda_{\alpha,l}(s)\}$ for some small $\varepsilon > 0$.

4.5.1. Analytic test cases

For the three examples with manufactured solution, one can explicitly compute the errors and thereby the experimental order of convergence (EOC). For simplicity, we assume an isotropic and constant absolute permeability $\mathbf{K}_1 = \mathbf{K}_2 = \mathbf{1}$ on the whole domain and a constant porosity $\phi_1 = \phi_2 = 1$. Note that these values have no actual physical meaning here, and are taken to simplify the manufactured solutions. We set the final time $T = 1$, and decompose the domain $\Omega = (-1, 1) \times (0, 1)$ at the interface $\Gamma = \{0\} \times (0, 1)$ into $\Omega_1 = (-1, 0) \times (0, 1)$ and $\Omega_2 = (0, 1) \times (0, 1)$.

Note that for an anisotropic absolute permeability \mathbf{K}_l a suitable spatial discretization is necessary to avoid the discretization errors to depend on the ratio between the largest and the smallest eigenvalue of \mathbf{K}_l . Furthermore, the direction of the anisotropy affects the flux across the interface Γ and thus the optimal choice of the parameter \mathcal{L}_Γ .

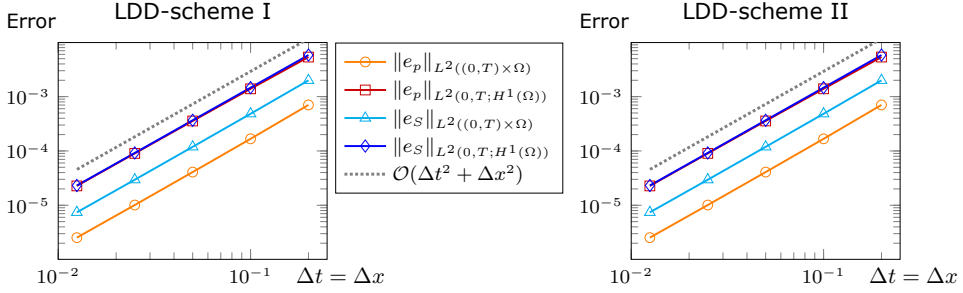


Figure 4.2.: Second order convergence in time step size Δt and mesh width Δx of pressure and saturation is observed for both LDD-schemes in the case with linear coefficients, but no hysteresis.

Linear coefficient functions without hysteresis

We consider a simple nonlinear problem with linear coefficient functions, but no hysteresis. These functions are therefore chosen

$$\lambda_n(S) = 1 - S, \quad \lambda_w(S) = S, \quad p_c(S, \mathbf{x}) = 0.2 - S, \quad \tau \equiv 1, \quad \gamma \equiv 0.$$

The righthand side terms are selected such that the analytic solution is given by

$$p_n(\mathbf{x}, t) = \frac{(1 - x_1)(1 + x_1)^2}{2(1 + t)^2}, \quad p_w(\mathbf{x}, t) = \frac{(1 - x_1)(1 + x_1)^2}{2(1 + t)},$$

$$S(\mathbf{x}, t) = \frac{(1 - x_1)(1 + x_1)^2}{2(1 + t)} + 0.2.$$

This corresponds to homogeneous Dirichlet boundary conditions at $x_1 = \pm 1$ and homogeneous Neumann boundary conditions at $x_2 \in \{0, 1\}$. Note that in this special case, the two schemes almost coincide, since they only differ in the inverted capillary pressure equation, which is a linear transformation here, and thus the results are very similar.

First, we study the convergence order of the two methods with respect to the time step size Δt and the mesh width Δx . For the LDD-scheme I, the parameters are $\mathcal{L}_p = 0.5$, $\mathcal{L}_T = 1$ and $\mathcal{L}_\Gamma = 0.375$ ($\mathcal{L}_\Phi = 0$), while for the LDD-scheme II, the parameters are $\mathcal{L}_p = 0.5$ and $\mathcal{L}_\Gamma = 0.375$. Second order convergence of pressure and saturation is observed for both schemes, as clearly shown in Fig. 4.2 and Tables 4.1 and 4.2. This even holds for the saturation in the $L^2(0, T; H^1(\Omega))$ norm, which is not covered by the above theoretical results. Note that the results of both schemes are almost identical because the particular combination of the parameter functions and the linearization parameters incidentally yields almost equivalent algorithms.

With decreasing time step size Δt , the average iteration number per time step and thus the convergence rate stay almost constant for $\Delta t \geq 0.025$. This pre-

Δt	Δx	$\ e_p\ _{L^2(0,T;H^1(\Omega))}$	EOC _p	$\ e_S\ _{L^2(0,T;H^1(\Omega))}$	EOC _S	Avg.-Iter.
0.2	0.2	$5.352 \cdot 10^{-3}$		$5.824 \cdot 10^{-3}$		13
0.1	0.1	$1.394 \cdot 10^{-3}$	1.94	$1.463 \cdot 10^{-3}$	1.993	12.3
0.05	0.05	$3.564 \cdot 10^{-4}$	1.968	$3.670 \cdot 10^{-4}$	1.995	12
0.025	0.025	$9.013 \cdot 10^{-5}$	1.983	$9.192 \cdot 10^{-5}$	1.997	11.5
0.0125	0.0125	$2.273 \cdot 10^{-5}$	1.987	$2.312 \cdot 10^{-5}$	1.991	15.5

Table 4.1.: Convergence study and average number of LDD-iterations per time step of the LDD-scheme I for varying time step size Δt and mesh width Δx in the case with linear coefficients, but no hysteresis.

Δt	Δx	$\ e_p\ _{L^2(0,T;H^1(\Omega))}$	EOC _p	$\ e_S\ _{L^2(0,T;H^1(\Omega))}$	EOC _S	Avg.-Iter.
0.2	0.2	$5.352 \cdot 10^{-3}$		$5.824 \cdot 10^{-3}$		13
0.1	0.1	$1.394 \cdot 10^{-3}$	1.94	$1.463 \cdot 10^{-3}$	1.993	12
0.05	0.05	$3.564 \cdot 10^{-4}$	1.968	$3.670 \cdot 10^{-4}$	1.995	12
0.025	0.025	$9.013 \cdot 10^{-5}$	1.983	$9.192 \cdot 10^{-5}$	1.997	11.3
0.0125	0.0125	$2.273 \cdot 10^{-5}$	1.987	$2.312 \cdot 10^{-5}$	1.991	16.2

Table 4.2.: Convergence study and average number of LDD-iterations per time step of the LDD-scheme II for varying time step size Δt and mesh width Δx in the case with linear coefficients, but no hysteresis.

asymptotic, constant regime seems to end around $\Delta t = 0.025$, followed by an increase of the average iteration number per time step at $\Delta t = 0.0125$. This increase is expected, since the convergence rate asymptotically deteriorates for both the L-scheme and the domain decomposition method. For L-schemes, the convergence rate typically is $\sqrt{C/(C + \Delta t)}$ for some $C > 0$ (see e.g. [210, 254]), and for the domain decomposition method with optimal parameter, one obtains convergence rates of $1 - \mathcal{O}(\sqrt{\Delta t})$ (see e.g. [116, 119]).

Moreover, the analysis provides convergence independently of the initial guess. This can also be observed, when the initial guess in each time step is fixed to $p_n^{k,0} = p_w^{k,0} \equiv 1$ and $S^{k,0} \equiv 0.75$ for the above simulations with $\Delta t = \Delta x = 0.05$. In this case, the resulting errors $\|e_p\|_{L^2(0,T;H^1(\Omega))}$ and $\|e_S\|_{L^2(0,T;H^1(\Omega))}$ are the same as in the studies above ($\pm 0.1\%$), only the average number of LDD-iterations per time step increases by about 20%.

Next, the convergence properties within one time step are considered. Therefore, the relative differences in pressure and saturation between consecutive iterations

$$d_p^i := \left(\sum_{\alpha \in \{n,w\}} \left\| \frac{p_\alpha^{k,i} - p_\alpha^{k,i-1}}{p_\alpha^{k,i}} \right\|_{L^2(\Omega)}^2 \right)^{1/2}, \quad d_S^i := \left\| \frac{S^{k,i} - S^{k,i-1}}{S^{k,i}} \right\|_{L^2(\Omega)},$$

are plotted in Fig. 4.3 for the last time step of the above simulations with $\Delta t =$

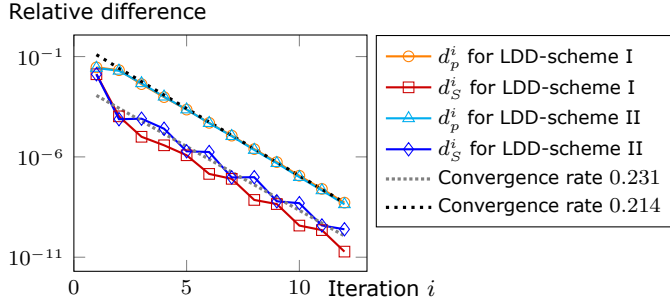


Figure 4.3.: The LDD-schemes converge very fast and linearly in the last time step of the case with linear coefficient functions, but no hysteresis. Plotted are the relative differences of pressure and saturation between consecutive iterations, together with the fitted convergence rates.

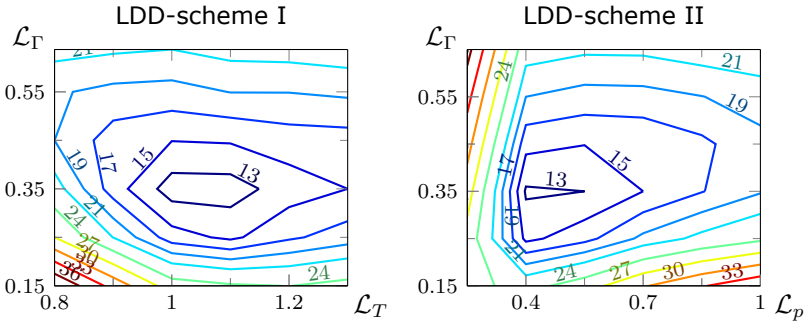


Figure 4.4.: Parameter dependence of the average number of LDD-iterations per time step for $\Delta t = \Delta x = 0.05$ in the case with linear coefficients, but no hysteresis. For simplicity, $\mathcal{L}_p = 0$ for LDD-scheme I.

$\Delta x = 0.05$. Note that the smooth decline of the relative difference in pressure might be due to the aggregated measure d_p^i involving the non-wetting and wetting-pressures. Since the method includes domain decomposition and some linearization parameters for the L-scheme are below the Lipschitz constants of the coefficient functions, monotone convergence cannot be expected, as also visible for the relative saturation differences d_S^i . Nevertheless, the results indicate a very fast, linear convergence. This fast convergence depends on a proper choice of the parameters. To analyze the dependence, we compute the average number of LDD-iterations per time step for several simulations with varying values of \mathcal{L}_p , \mathcal{L}_T and \mathcal{L}_Γ , while $\Delta t = \Delta x = 0.05$ is fixed. The average number of LDD-iterations per time step is minimal for a specific set of parameters and increases drastically for small deviations from that, see Fig. 4.4. The linearization parameters typically should be chosen as small as possible, but big enough to ensure convergence (see e.g. [210, 254, 285]). Here, this means that lower bounds from our analy-

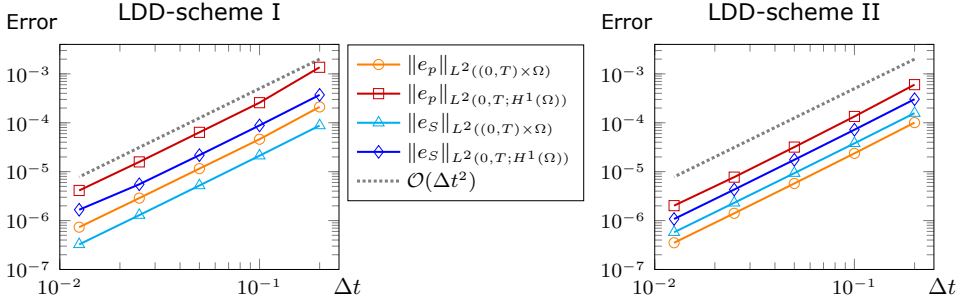


Figure 4.5.: Second order convergence in the time step size Δt of pressure and saturation is observed for both LDD-schemes in the case with nonlinear coefficients, but no hysteresis.

sis (see [Theorems 4.1](#) and [4.2](#)) should be good predictions. They are $\mathcal{L}_p \geq 1/2$ and $\mathcal{L}_T \geq 1/2$ for the first scheme and $\mathcal{L}_p > 1$ for the second one, and they are indeed very close to the optimal ones. On the other hand, theoretical prediction of the domain decomposition parameter \mathcal{L}_Γ is usually based on the Fourier transformation [[65](#), [116](#), [119](#)], which cannot be directly applied to nonlinear problems. Therefore, there are no such predictions available yet for this type of nonlinear equations.

Nonlinear coefficient functions without hysteresis

Next, we consider a problem with nonlinear coefficient functions, again excluding hysteresis. These functions are

$$\lambda_n(S) = (1 - S)^2, \quad \lambda_w(S) = S^2, \quad p_c(S, \mathbf{x}) = -S^2, \quad \tau(S) = S, \quad \gamma \equiv 0.$$

The righthand sides are chosen in such a way that the analytic solution is given by

$$p_n(\mathbf{x}, t) = 1 - \frac{(3 - 2t)(3 + 2(x_2 - x_1))^2}{400}, \quad p_w(\mathbf{x}, t) = 1 + \frac{(3 - 2t)(3 + 2(x_2 - x_1))^2}{400},$$

$$S(\mathbf{x}, t) = \frac{(3 + 2(x_2 - x_1))\sqrt{1 + t}}{10},$$

where the corresponding boundary conditions are for simplicity the given exact values, i.e., inhomogeneous Dirichlet values on the whole boundary $\partial\Omega$. Note, that the solutions are polynomials of degree two, and thus the spatial discretization (Q_2) is exact, so that the mesh width $\Delta x = 0.05$ is fixed in the following. The parameters are $\mathcal{L}_p = 0.5$, $\mathcal{L}_T = 0.55$ and $\mathcal{L}_\Gamma = 2.65$ ($\mathcal{L}_\Phi = 0$) for the LDD-scheme I, while $\mathcal{L}_p = 1.5$ and $\mathcal{L}_\Gamma = 2.65$ for the LDD-scheme II.

As before, second order convergence in Δt is achieved by both schemes, again even for the saturation in the $L^2(0, T; H^1(\Omega))$ norm (see [Fig. 4.5](#) and [Tables 4.3](#) and [4.4](#)). The average number of LDD-iterations per time step is two times big-

Δt	$\ e_p\ _{L^2(0,T;H^1(\Omega))}$	EOC _p	$\ e_S\ _{L^2(0,T;H^1(\Omega))}$	EOC _S	Avg.-Iter.
0.2	$1.363 \cdot 10^{-3}$		$3.712 \cdot 10^{-4}$		51.8
0.1	$2.573 \cdot 10^{-4}$	2.405	$8.829 \cdot 10^{-5}$	2.072	46.6
0.05	$6.370 \cdot 10^{-5}$	2.014	$2.174 \cdot 10^{-5}$	2.022	43.2
0.025	$1.584 \cdot 10^{-5}$	2.007	$5.519 \cdot 10^{-6}$	1.978	41.6
0.0125	$4.126 \cdot 10^{-6}$	1.941	$1.665 \cdot 10^{-6}$	1.729	41.1

Table 4.3.: Convergence study and average number of LDD-iterations per time step of the LDD-scheme I for varying time step size Δt in the case with nonlinear coefficients, but no hysteresis.

Δt	$\ e_p\ _{L^2(0,T;H^1(\Omega))}$	EOC _p	$\ e_S\ _{L^2(0,T;H^1(\Omega))}$	EOC _S	Avg.-Iter.
0.2	$6.017 \cdot 10^{-4}$		$3.036 \cdot 10^{-4}$		49.6
0.1	$1.345 \cdot 10^{-4}$	2.162	$7.200 \cdot 10^{-5}$	2.076	44.5
0.05	$3.181 \cdot 10^{-5}$	2.08	$1.750 \cdot 10^{-5}$	2.04	40.1
0.025	$7.733 \cdot 10^{-6}$	2.04	$4.305 \cdot 10^{-6}$	2.023	36.6
0.0125	$2.020 \cdot 10^{-6}$	1.937	$1.076 \cdot 10^{-6}$	2	33.6

Table 4.4.: Convergence study and average number of LDD-iterations per time step of the LDD-scheme II for varying time step size Δt in the case with nonlinear coefficients, but no hysteresis.

ger than in the previous example due to the stronger nonlinearities. This time, it even decreases for decreasing time step size Δt , which indicates here an early pre-asymptotic regime, where the smaller differences between solutions of consecutive time steps lead to a smaller number of necessary iterations. Fixing the initial guess ($S \equiv 0.25$ and $p_n = p_w \equiv 2$) results in the same errors $\|e_p\|_{L^2(0,T;H^1(\Omega))}$ and $\|e_S\|_{L^2(0,T;H^1(\Omega))}$ ($\pm 0.3\%$) as in the above studies with $\Delta t = 0.05$, but in a significantly increased number of iterations per time step (an increase of 71% and 89% for LDD-scheme I and II, respectively).

Next, the convergence properties of the methods within one time step are discussed. In the last time step of the above simulations with $\Delta t = 0.05$, we observe again a fast and almost linear convergence (see Fig. 4.6). The dependence of the average number of LDD-iterations per time step when varying the LDD-parameters \mathcal{L}_p , \mathcal{L}_T and \mathcal{L}_Γ is computed for several simulations where $\Delta t = 0.05$ is fixed. As visible in Fig. 4.7, the parameter dependence shows a different behavior in this case. Only the second scheme has an optimal parameter set, whereas the first one shows improving convergence for decreasing $\mathcal{L}_T \searrow 0.6$, until it suddenly does not converge any more. The latter agrees very well with the theory, which predicts $\mathcal{L}_p \geq 1$ and $\mathcal{L}_T \geq 1/2$ for the LDD-scheme I, while $\mathcal{L}_p > 1$ for the second one is again very close to the optimum at 1.5. Furthermore, small deviations from the optima have less impact than in the previous example.

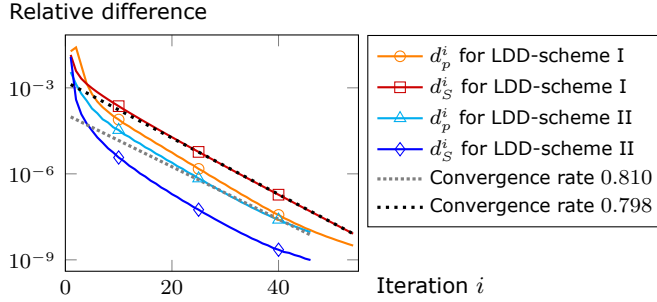


Figure 4.6.: The LDD-schemes converge fast and almost linearly in the last time step of the case with nonlinear coefficient functions, but no hysteresis. Plotted are the relative differences of pressure and saturation between consecutive iterations, together with the fitted convergence rates.

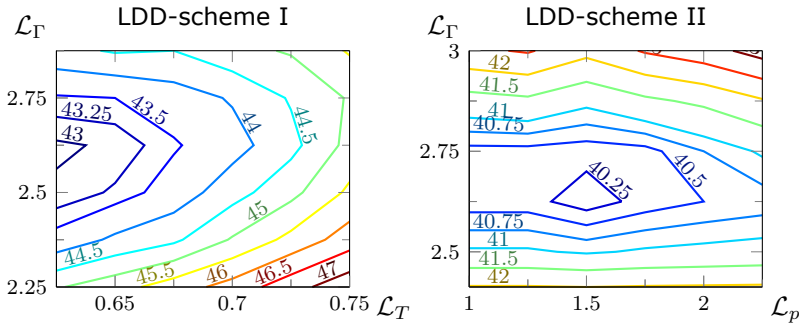


Figure 4.7.: Parameter dependence of the average number of LDD-iterations per time step for $\Delta t = 0.05$ in the case with nonlinear coefficients, but no hysteresis. For simplicity, $\mathcal{L}_p = 0$ for LDD-scheme I.

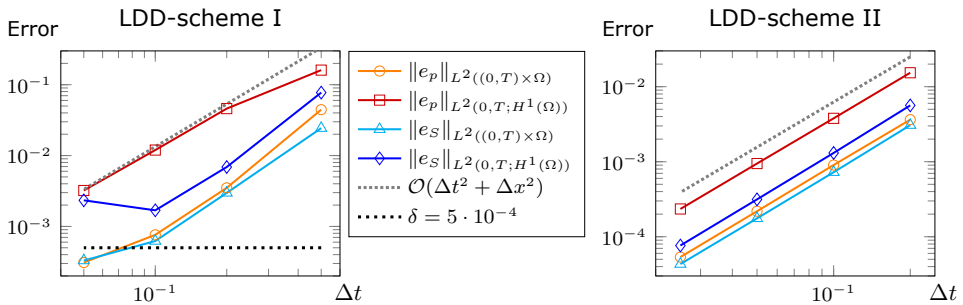


Figure 4.8.: Second order convergence in time step size Δt and mesh width Δx of pressure and saturation is observed for both LDD-schemes in the case with linear coefficients, including hysteresis. The accuracy of the first scheme is limited by the regularization (parameter δ), as visible for e.g. the saturation. The mesh width is $\Delta x = \Delta t/2$ for LDD-scheme I and $\Delta x = \Delta t/4$ for LDD-scheme II.

Linear coefficient functions including hysteresis

Finally, we consider a problem including hysteresis, where the linear coefficient functions are

$$\lambda_n(S) = 1 - S, \quad \lambda_w(S) = S, \quad p_c(S, \mathbf{x}) = -S, \quad \tau \equiv 1, \quad \gamma \equiv 1.$$

Since hysteresis occurs during the change between imbibition and drainage, we construct righthand side terms which yield the following manufactured solution

$$\begin{aligned} S(\mathbf{x}, t) &= \begin{cases} \frac{1}{2} \cos((t_0(\mathbf{x}) - t)^2) & \text{if } t < t_0(\mathbf{x}), \\ \frac{1}{2} & \text{if } t_0(\mathbf{x}) \leq t \leq t_1(\mathbf{x}), \\ \frac{1}{2} \cos((t - t_1(\mathbf{x}))^2) & \text{if } t_1(\mathbf{x}) < t, \end{cases} \\ p_n(\mathbf{x}, t) &= \begin{cases} 1 - \frac{1}{2} \cos((t_0(\mathbf{x}) - t)^2) & \text{if } t < t_0(\mathbf{x}), \\ 6\xi^5(t, \mathbf{x}) - 15\xi^4(t, \mathbf{x}) + 10\xi^3(t, \mathbf{x}) + \frac{1}{2} & \text{if } t_0(\mathbf{x}) \leq t \leq t_1(\mathbf{x}), \\ 2 - \frac{1}{2} \cos((t - t_1(\mathbf{x}))^2) & \text{if } t_1(\mathbf{x}) < t, \end{cases} \\ p_w(\mathbf{x}, t) &= \begin{cases} 2 + \sqrt{(t_0(\mathbf{x}) - t)^2} \sin((t_0(\mathbf{x}) - t)^2) & \text{if } t < t_0(\mathbf{x}), \\ -6\xi^5(t, \mathbf{x}) + 15\xi^4(t, \mathbf{x}) - 10\xi^3(t, \mathbf{x}) + 2 & \text{if } t_0(\mathbf{x}) \leq t \leq t_1(\mathbf{x}), \\ 1 - \sqrt{(t - t_1(\mathbf{x}))^2} \sin((t - t_1(\mathbf{x}))^2) & \text{if } t_1(\mathbf{x}) < t, \end{cases} \end{aligned}$$

where

$$t_0(\mathbf{x}) := \frac{10x_1 + 7}{20}, \quad t_1(\mathbf{x}) := t_0(\mathbf{x}) + \frac{3}{10} = \frac{10x_1 + 13}{20}, \quad \xi(t, \mathbf{x}) := \frac{t - t_0(\mathbf{x})}{t_1(\mathbf{x}) - t_0(\mathbf{x})}.$$

The corresponding boundary conditions are simply chosen to be of inhomogeneous Dirichlet type at $x_1 = \pm 1$, and of homogeneous Neumann type at $x_2 \in \{0, 1\}$. For the LDD-scheme I, the regularization parameter is chosen $\delta = 5 \cdot 10^{-4}$ and the LDD-parameters are $\mathcal{L}_p = 0.5$, $\mathcal{L}_T = 2$, $\mathcal{L}_\Phi = 10^3$ and $\mathcal{L}_\Gamma = 0.375$. In this case, we use a reduced stopping criterion for the LDD-scheme of 10^{-7} . For the LDD-scheme II, the parameters are $\mathcal{L}_p = 0.33$ and $\mathcal{L}_\Gamma = 0.375$.

As before, second order convergence with respect to the time step size Δt and mesh width Δx is observed for both schemes, until the errors due to regularization are dominating in the first scheme (see Fig. 4.8 and Tables 4.5 and 4.6). Here, the inverted formulation of the second scheme is clearly advantageous. While the first scheme needs a huge parameter \mathcal{L}_Φ for a moderate regularization parameter δ due to the steep slope in the capillary pressure equation near zero, the second scheme has no such restriction due to the inverted formulation. Therefore, the average number of iterations per time step for the LDD-scheme I is huge, which makes this scheme unpractical for such problems. In contrast, the average number of iteration for the LDD-scheme II is much lower, which again shows that the latter is the preferable method for this type of applications. As before, we observe the iteration

Δt	Δx	$\ e_p\ _{L^2(0,T;H^1(\Omega))}$	EOC _p	$\ e_S\ _{L^2(0,T;H^1(\Omega))}$	EOC _S	Avg.-Iter.
0.5	0.25	0.161		$7.739 \cdot 10^{-2}$		5,525
0.2	0.1	$4.600 \cdot 10^{-2}$	1.364	$6.891 \cdot 10^{-3}$	2.64	4,890
0.1	0.05	$1.196 \cdot 10^{-2}$	1.943	$1.688 \cdot 10^{-3}$	2.029	4,380
0.05	0.025	$3.215 \cdot 10^{-3}$	1.895	$2.336 \cdot 10^{-3}$	-0.469	3,900

Table 4.5.: Convergence study and average number of LDD-iterations per time step of the LDD-scheme I for varying time step in the full analytical case with linear coefficients including hysteresis.

Δt	Δx	$\ e_p\ _{L^2(0,T;H^1(\Omega))}$	EOC _p	$\ e_S\ _{L^2(0,T;H^1(\Omega))}$	EOC _S	Avg.-Iter.
0.2	0.05	$1.534 \cdot 10^{-2}$		$5.631 \cdot 10^{-3}$		17.8
0.1	0.025	$3.788 \cdot 10^{-3}$	2.018	$1.309 \cdot 10^{-3}$	2.105	17
0.05	0.0125	$9.454 \cdot 10^{-4}$	2.002	$3.147 \cdot 10^{-4}$	2.056	16.5
0.025	0.0063	$2.345 \cdot 10^{-4}$	2.011	$7.640 \cdot 10^{-5}$	2.042	15.6

Table 4.6.: Convergence study and average number of LDD-iterations per time step of the LDD-scheme II for varying time step in the full analytical case with linear coefficients including hysteresis.

number to decrease for decreasing time step size due to the pre-asymptotic regime. Furthermore, if the initial guess is fixed to $S^{k,0} \equiv 0.75$ and $p_n^{k,0} = p_w^{k,0} \equiv 1$ in each time step, the errors are similar to those in the original studies with $\Delta t = 0.1$, (+35% for LDD-scheme I, $\pm 0.1\%$ for LDD-scheme II).

The convergence is almost linear for both schemes, but only the LDD-scheme II is fast (see Fig. 4.9). The first scheme has a convergence rate of 0.999 and thus should not be used for applications including hysteresis, or at least needs to be improved by e.g. localizing the LDD-parameter. Nevertheless, it has good convergence properties within the first few iterations, and hence could be used as a preconditioner. The dependence of the average number of iterations per time step on the LDD-parameters \mathcal{L}_Φ , \mathcal{L}_p and \mathcal{L}_Γ based on several simulations with fixed discretization is similar to the previous example. Only the LDD-scheme II has a clear optimal parameter set, whereas the first one shows almost no dependence on the domain decomposition parameter \mathcal{L}_Γ (see Fig. 4.10). The lower bounds from our analysis are in this case $\mathcal{L}_p \geq 1/2$, $\mathcal{L}_T \geq 1/2$ and $\mathcal{L}_\Phi \geq 10^3$ for LDD-scheme I and $\mathcal{L}_p > 1$ for the second one. For the first scheme, this coincides very well with the observed optimum, while the bound for the second one is too restrictive for this application, but a good indicator of the optimal region.

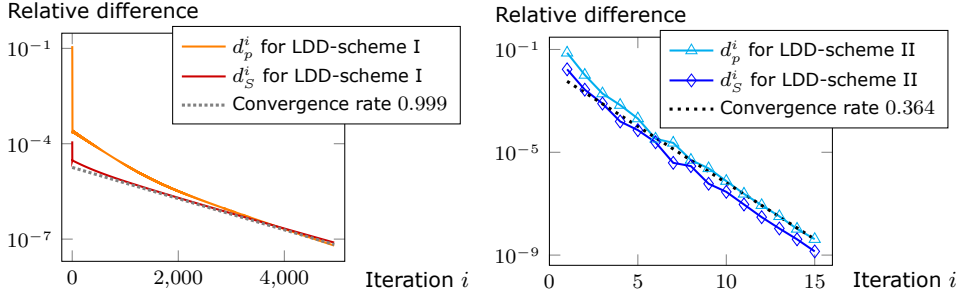


Figure 4.9.: Both LDD-schemes converge almost linearly, but only the second one is fast in the last time step of the case with linear coefficient functions including hysteresis, for $\Delta t = 0.05$ and $\Delta x = 0.025$ (left) or $\Delta x = 0.0125$ (right). Plotted are the relative differences of pressure and saturation between consecutive iterations, and the fitted convergence rates.

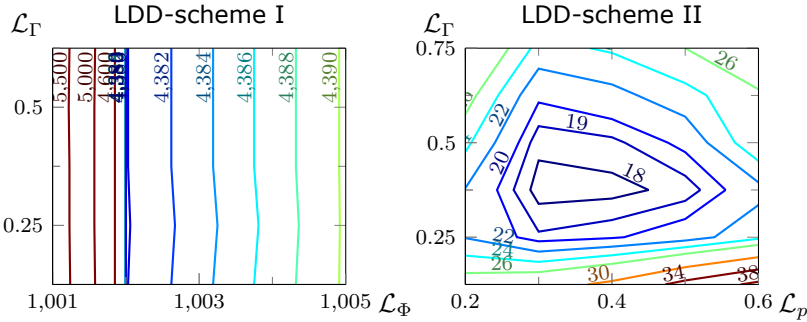


Figure 4.10.: Parameter dependence of the average number of iterations per time step in the case with linear coefficients including hysteresis. *Left:* $\delta = 5 \cdot 10^{-4}$, $\Delta t = 0.1$, $\Delta x = 0.05$. For simplicity $\mathcal{L}_p = \mathcal{L}_T = 0$. *Right:* $\Delta t = 0.1$, $\Delta x = 0.025$.

Parameter	Symbol	Value		Unit
		Ω_1	Ω_2	
Porosity	ϕ	0.4	0.3	m^2
Absolute permeability	\tilde{K}	$3.0 \cdot 10^{-10}$	$5.0 \cdot 10^{-10}$	m^2
Material-specific pressure	P	$1.25 \cdot 10^3$	$1.0 \cdot 10^3$	Pa
Retention exponent	m	0.8	0.7	—
Residual saturation, non-wetting phase	S_{nr}	0.1	0.05	—
Residual saturation, wetting phase	S_{wr}	0.1	0.05	—
Typical redistribution parameter	$\tilde{\tau}$	$2.0 \cdot 10^3$	$1.5 \cdot 10^3$	Pa s
Hysteresis pressure parameter	$\tilde{\gamma}$	200	100	Pa
Density of the non-wetting phase	ρ_n	1.0		kg/m^3
Density of the wetting phase	ρ_w	$1.0 \cdot 10^3$		kg/m^3
Gravity (positive x_1 -direction)	g	9.81		m/s^2
Viscosity of the non-wetting phase	μ_n	$2.0 \cdot 10^{-5}$		Pa s
Viscosity of the wetting phase	μ_w	$1.0 \cdot 10^{-3}$		Pa s

Table 4.7.: Parameters of the van-Genuchten–Mualem model in the two sub-domains for the realistic case.

4.5.2. Realistic test case

This last subsection is dedicated to the study of a realistic problem including gravity. To this end, we choose a van-Genuchten–Mualem parameterization [318], with the relative permeabilities and the equilibrium capillary pressure given by

$$k_n(S) := \sqrt{1 - S_{\text{eff}}} \left(1 - S_{\text{eff}}^{1/m}\right)^{2m}, \quad k_w(S) := \sqrt{S_{\text{eff}}} \left(1 - \left(1 - S_{\text{eff}}^{1/m}\right)^m\right)^2,$$

$$\tilde{p}_c(S, \mathbf{x}) := P \left(S_{\text{eff}}^{-1/m} - 1\right)^{1-m} - (\rho_n - \rho_w)gx_1, \quad S_{\text{eff}} := \frac{S - S_{wr}}{1 - S_{wr} - S_{nr}},$$

where the effective saturation S_{eff} accounts for the residual saturations S_{nr} and S_{wr} . The capillary pressure is scaled by a material-specific pressure P , and the retention exponent $m > 0$ determines the steepness of the S-shaped curve. Note that this choice of \tilde{p}_c limits the possible range of S to $(S_{wr}, 1 - S_{nr}]$. Since $\tilde{p}_c(s, \mathbf{x}) \rightarrow -(\rho_n - \rho_w)gx_1$ as $S \rightarrow 1 - S_{nr}$, while $\tilde{p}_c(s, \mathbf{x}) \rightarrow \infty$ as $S \rightarrow S_{wr}$ independently of the chosen parameters P and m , this excludes the occurrence of entry-pressures as discussed in Remark 4.1. Furthermore, we include dynamic capillarity and hysteresis by constant τ and γ within each sub-domain. All the parameters are listed in Table 4.7 and inspired by the choices made in [277].

To obtain the non-dimensional equations (4.1)–(4.6), we choose the scaling parameters $L = 1 \text{ m}$, $p^* = 2.5 \cdot 10^3 \text{ Pa}$ and $\tau^* = 1.5 \cdot 10^3 \text{ Pa s}$ and

$$\lambda_\alpha(S) = \frac{\tau^*}{\mu_\alpha} k_\alpha(S), \quad K = \frac{\tilde{K}}{L^2}, \quad p_c(S) = \frac{\tilde{p}_c(S)}{p^*}, \quad \tau = \frac{\tilde{\tau}}{\tau^*}, \quad \gamma = \frac{\tilde{\gamma}}{p^*}.$$

The domain $\Omega = (-0.5, 0.5) \times (0, 1)$ is decomposed into two sub-domains at the interface $\Gamma = \{0\} \times (0, 1)$. We choose the final time $T = 400$ (real time 240 s) and initial conditions with almost constant saturation given by

$$p_n^0(\mathbf{x}) = 0.75 - \frac{\rho_n g L}{p^*} x_1 = 0.75 - 0.003924 x_1, \quad p_w^0(\mathbf{x}) = -\frac{\rho_w g L}{p^*} x_1 = -3.924 x_1,$$

$$S^0(\mathbf{x}) = p_c^{-1}(p_n^0(\mathbf{x}) - p_w^0(\mathbf{x})) \approx \begin{cases} 0.2431 & \text{if } x_1 < 0, \\ 0.2414 & \text{if } x_1 > 0. \end{cases}$$

The boundary conditions at $x_1 = \pm 0.5$ are of constant Dirichlet type, to match the initial conditions, except for p_w at $x_1 = -0.5$ given by

$$p_w|_{x_1=-0.5} = 1.962 + \begin{cases} 0.015t & \text{if } t < 25, \\ 0.375 & \text{if } 25 \leq t < 100, \\ 0.015(125 - t) & \text{if } 100 \leq t < 130, \\ -0.075 & \text{if } 125 \leq t, \end{cases}$$

whereas the boundary conditions at $x_2 \in \{0, 1\}$ are of homogeneous Neumann type. By this choice, we simulate an imbibition and drainage cycle. The order of the spatial discretization is reduced to one, i.e., piece-wise linear, and the tolerance for the LDD-schemes is 10^{-6} , since the solution is less smooth than in the analytical cases. In contrast to the manufactured examples above, we only study the convergence of the LDD-schemes within the time steps. Therefore, the mesh width $\Delta x = 0.02$ and $\Delta t = 0.1$ are fixed. Note that the time step size here is about 100 times larger than in [277]. This might partially be a consequence of the different parameters and scaling, but also due to the L-scheme, whereas the Newton method is used in [277].

The choice of the parameters and the results are shown in Table 4.8, and the obtained solutions for $\mathcal{L}_\Gamma = 0.25$ at time $t \in \{100, 200, 400\}$ are depicted in Fig. 4.11. The solutions of both methods are very similar and the imbibition and drainage cycle can be clearly observed. The small small peaks near $x_1 = 0$ probably result from the hysteresis. Due to the higher permeability in the second domain, the latter imbibes the wetting phase from the first domain, such that the region in the first domain close to the interface is rather draining. Together with the different equilibrium capillary pressure, this leads to a saturation discontinuity at the interface. Note that the $L^2((0, T) \times \Gamma)$ -norm of the flux jumps due to the domain decomposition is below 10^{-3} , and thus smaller than the expected discretization errors. Furthermore, they decrease when the time step size and the mesh width are reduced, although at a sub-linear rate (see Table 4.8). The norms of the jump in the pressures remain one magnitude lower. Hence, the possibility of numerical artifacts cannot be excluded with certainty. Again, the huge parameter \mathcal{L}_Φ slows down the LDD-scheme I, whereas the second scheme has no such restriction. Al-

$\mathcal{L}_\Gamma = 0.25$	Δt	Δx	Avg.-Iter.	$\ [p_\alpha] \ _{L^2((0,T) \times \Gamma)}$	$\ [\mathbf{u}_\alpha \cdot \mathbf{n}] \ _{L^2((0,T) \times \Gamma)}$
LDD-scheme I	0.5	0.1	1480.3	$6.22 \cdot 10^{-5}$	$1.68 \cdot 10^{-3}$
	0.2	0.05	954.8	$8.29 \cdot 10^{-5}$	$1.32 \cdot 10^{-3}$
	0.1	0.02	626.5	$1.13 \cdot 10^{-4}$	$9.89 \cdot 10^{-4}$
LDD-scheme II	0.5	0.1	410.8	$9.77 \cdot 10^{-6}$	$1.61 \cdot 10^{-3}$
	0.2	0.05	212.7	$1.65 \cdot 10^{-5}$	$1.06 \cdot 10^{-3}$
	0.1	0.02	69.9	$3.65 \cdot 10^{-5}$	$4.42 \cdot 10^{-4}$
$\mathcal{L}_\Gamma = 0.01$	Δt	Δx	Avg.-Iter.	$\ [p_\alpha] \ _{L^2((0,T) \times \Gamma)}$	$\ [\mathbf{u}_\alpha \cdot \mathbf{n}] \ _{L^2((0,T) \times \Gamma)}$
LDD-scheme I	0.5	0.1	147.4	$5.31 \cdot 10^{-5}$	$1.67 \cdot 10^{-3}$
	0.2	0.05	134.4	$5.76 \cdot 10^{-5}$	$1.33 \cdot 10^{-3}$
	0.1	0.02	128.5	$8.60 \cdot 10^{-5}$	$1.00 \cdot 10^{-3}$
LDD-scheme II	0.5	0.1	393.4	$1.72 \cdot 10^{-5}$	$1.65 \cdot 10^{-3}$
	0.2	0.05	209.8	$2.21 \cdot 10^{-5}$	$1.21 \cdot 10^{-3}$
	0.1	0.02	77.7	$1.54 \cdot 10^{-5}$	$1.05 \cdot 10^{-3}$

Table 4.8.: Average number of iterations per time step and $L^2((0,T) \times \Gamma)$ -norm of the jump in pressures and of the jump in the fluxes for the realistic problem for varying time step Δt and mesh width Δx with two parameters $\mathcal{L}_\Gamma = 0.25$ (top) and $\mathcal{L}_\Gamma = 0.01$ (bottom). The other parameters of the LDD-scheme I are $\mathcal{L}_p = 1.0$, $\mathcal{L}_T = 1.3$, $\mathcal{L}_\Phi = 40$ and $\delta = 10^{-3}$. The other parameter of the second scheme is $\mathcal{L}_p = 2.0$.

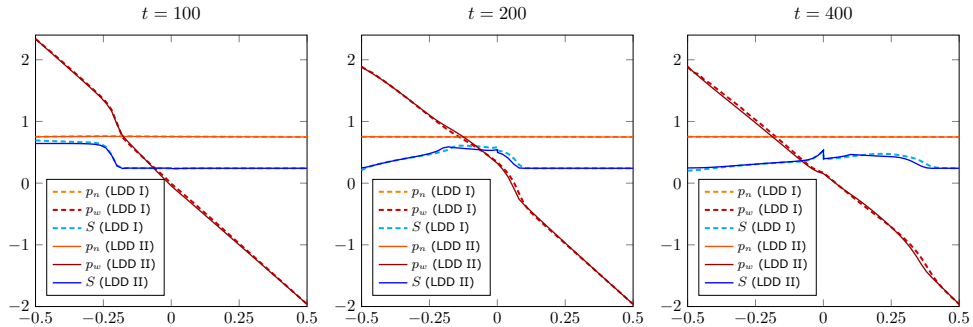


Figure 4.11.: Numerical solution for the realistic case over x_1 , at $x_2 = 0.5$ and the times $t = 100$ (left), $t = 200$ (center) and $t = 400$ (right). Dashed: LDD-scheme I. Solid: LDD-scheme II.

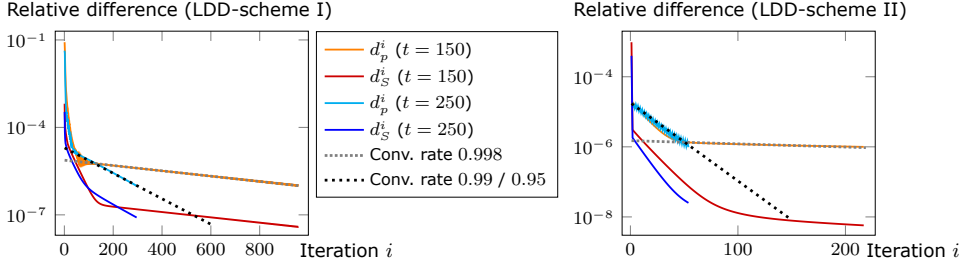


Figure 4.12.: Both LDD-schemes converge very slowly and rather monotonous, at times $t = 150$ and $t = 250$ of the realistic case for $\Delta t = 0.1$ and $\Delta x = 0.02$ with $\mathcal{L}_\Gamma = 0.25$. Plotted are the relative differences of pressure and saturation between consecutive iterations, together with the fitted convergence rates.

though the average number of iterations per time step for the LDD-scheme I is much smaller than in the last example, the average number of iterations per time step for the LDD-scheme II is up to eight times smaller for small time step sizes. Note that both schemes are used with smaller linearization parameters than those required by our analysis in [Section 4.4](#), but give rise to better results than the required ones.

This time, we consider the convergence properties of the methods within one time step at the times $t = 150$ and $t = 250$. The first is shortly before the flow passes Γ , while the process switches at Γ from imbibition to drainage around the latter time. For both schemes, we observe convergence rates close to one (see [Fig. 4.12](#)), such that both schemes are slow and should be improved by e.g. localized linearization parameters. Nevertheless, the convergence is almost monotonous, and the differences again decrease rapidly at the beginning. Since such problems would require different parameters for the two sub-domains, which makes a proper choice even more challenging, here we do not study the effect of varying parameters. However, note that the choice of \mathcal{L}_Γ strongly affects the efficiency of the first LDD-scheme, while the second one seems rather robust.

4.6. Conclusion

Linearization and domain decomposition can be combined into one iteration, the LDD-scheme. For the considered non-equilibrium two-phase model, the proposed LDD-schemes lead to unique solutions, which converge towards the semi-discrete solutions of the model, as proven in [Section 4.4](#). This convergence is global, i.e., independent of the initial guess, and requires only a mild restriction on the time step, independent of the spatial discretization. The inverted formulation for the capillary pressure in the LDD-scheme II avoids the necessary regularization for the original formulation in the LDD-scheme I.

The stability and robustness of both LDD-schemes were numerically verified for several spatially two-dimensional cases. The convergence rate can be improved significantly by a proper choice of the LDD-parameters. In particular, we pointed out the practical advantages of the second scheme, when hysteresis is present. While the analysis leads to good estimates for the linearization parameters, an estimate for the domain decomposition parameter is still an open problem.

The methods can be generalized, when the porosity ϕ and the dynamic capillarity coefficient τ are spatially variable, and when the hysteresis coefficient γ depends on the saturation S . Furthermore, the required regularity of the parameter functions may be relaxed to Hölder continuity as in [48, 262]. The degenerated cases $\lambda_w(0) = 0$ and $\lambda_n(1) = 0$ involve difficulties which need to be investigated in future, as well as vanishing dynamic capillarity $\tau = 0$. Nonlinear interface conditions for entry-pressure models can be studied as soon as extensions for the case of dynamic and hysteretic capillarity are available.

The convergence properties of the schemes can be further improved by choosing the LDD-parameters depending on the position or the current solution. Finally, an a-posteriori error analysis can lead to estimates for efficient and adaptive stopping criteria, which would increase the performance even more.

Consistent and asymptotic-preserving finite-volume Robin transmission conditions for singularly perturbed elliptic equations

This chapter is based on the following publication [125]:

- M. J. Gander, S. B. Lunowa, C. Rohde, *Consistent and Asymptotic-Preserving Finite-Volume Robin Transmission Conditions for Singularly Perturbed Elliptic Equations*, in: Domain Decomposition Methods in Science and Engineering XXVI, Springer (2022), pp. 419–426. In press.

link.springer.com/book/9783030950248

Copyright © 2022, Springer Nature. Reproduced with permission.

5.1. Introduction

Adaptive Dirichlet–Neumann and Robin–Neumann algorithms for singularly-perturbed advection-diffusion equations were introduced in [75], accounting for transport along characteristics, see also [130] for the discrete setting and damped versions using a modified quadrature rule to recover the hyperbolic limit. Non-overlapping Schwarz domain decomposition methods (DDM) with Robin transmission conditions applied to advection-diffusion equations were analyzed in [35, 239] and a stabilized finite-element method for singularly perturbed problems was discussed in [212], see also [120, 121] and references therein for heterogeneous couplings. However, the behavior of these DDMs in the limit of vanishing diffusion has not been addressed.

Our goal is to develop finite volume Robin transmission conditions such that the

associated non-overlapping DDM is consistent *and* asymptotic-preserving. Consistent here means that, for fixed mesh size, the discrete DDM iterates converge to the discrete solution on the entire domain, and asymptotic-preserving means that the singular limit in the DDM yields a convergent limit DDM (for more on asymptotic-preserving methods, see e.g. [176]). We first show that the continuous DDM is only asymptotic-preserving under a strict condition on the Robin transmission parameter, see [Theorem 5.1](#). In contrast, our new discrete DDM is asymptotic-preserving without restriction on this parameter, see [Theorem 5.3](#), and fast convergence is automatically recovered in the hyperbolic limit. While our analysis is in one dimension, we show numerical experiments also in two dimensions; for the nonlinear space-time case with triangular meshes, see [124].

5.2. The continuous problem and non-overlapping DDM

We consider for $\nu \geq 0$, $a > 0$ and $f \in L^2(-1, 1)$ the stationary advection-diffusion equation with homogeneous Dirichlet boundary conditions, i.e.,

$$\nu \partial_{xx} u - a \partial_x u = f \quad \text{in } \Omega := (-1, 1), \quad u(-1) = 0, \quad \nu u(1) = 0. \quad (5.1)$$

In the singular limit $\nu = 0$, the partial differential equation in (5.1) becomes (trivially) advective, and the boundary condition collapses into the inflow condition $u(-1) = 0$ only. It is easy to see that there exists a unique weak solution $u \in H^1(-1, 1)$ of (5.1) for $\nu \geq 0$.

We apply a non-overlapping DDM with two sub-domains $\Omega_1 = (-1, 0)$ and $\Omega_2 = (0, 1)$ to (5.1). The problem (5.1) is then rewritten using at $x = 0$ the Robin transmission conditions

$$\mathcal{B}_1(u) = \nu \partial_x u - au + \lambda u, \quad \mathcal{B}_2(u) = -\nu \partial_x u + au + \lambda u, \quad \lambda > 0. \quad (5.2)$$

Definition 5.1 (Continuous DDM). Let $u_2^0 \in H^1(\Omega_2)$ be given. For $i \in \mathbb{N}$, the i -th continuous DDM-iterate $(u_1^i, u_2^i) \in H^1(\Omega_1) \times H^1(\Omega_2)$ is given as solution of

$$\nu \partial_{xx} u_l^i - a \partial_x u_l^i = f \quad \text{in } \Omega_l, \quad l = 1, 2, \quad (5.3)$$

$$u_1^i(-1) = 0, \quad \nu u_2^i(1) = 0, \quad (5.4)$$

$$\nu \mathcal{B}_1(u_1^i) = \nu \mathcal{B}_1(u_2^{i-1}), \quad \mathcal{B}_2(u_2^i) = \mathcal{B}_2(u_1^i) \quad \text{at } x = 0. \quad (5.5)$$

Here, the iteration is sequential starting on the left sub-domain following the direction of the advection. Alternatively, it can be started on the right sub-domain or in a parallel manner, and the analysis below applies then analogously. Note that (5.3)–(5.5) is equivalent to (5.1) in the limit $i \rightarrow \infty$. In the limit when $\nu \rightarrow 0$, we get the stationary advection equation, and the two Robin transmission conditions (5.5) degenerate into one Dirichlet transmission condition. Therefore, the multiplication

of \mathcal{B}_1 by ν is necessary to remove the transmission condition in the limit $\nu \rightarrow 0$.

The errors $e_l^i := u|_{\Omega_l} - u_l^i$ satisfy (5.3)–(5.5) with $f \equiv 0$ due to linearity. Therefore, we obtain the explicit solution

$$\begin{aligned} e_1^i(x) &= A_1^i(e^{ax/\nu} - e^{-a/\nu}), & e_2^i(x) &= A_2^i(1 - e^{a(x-1)/\nu}) & \text{if } \nu > 0, \\ e_1^i &\equiv 0, & e_2^i &\equiv 0 & \text{if } \nu = 0, \end{aligned}$$

where $A_1^i, A_2^i \in \mathbb{R}$ satisfy the recurrence relations

$$A_1^i = \frac{-a + \lambda(1 - e^{-a/\nu})}{ae^{-a/\nu} + \lambda(1 - e^{-a/\nu})} A_2^{i-1}, \quad A_2^i = \frac{-ae^{-a/\nu} + \lambda(1 - e^{-a/\nu})}{a + \lambda(1 - e^{-a/\nu})} A_1^i.$$

This yields the following convergence result.

Theorem 5.1 (Convergence and asymptotic-preserving property of the continuous DDM). *The sequence of continuous DDM-iterates $\{(u_1^i, u_2^i)\}_{i \in \mathbb{N}}$ from (5.3)–(5.5) converges point-wise to $(u|_{\Omega_1}, u|_{\Omega_2})$. For $\nu > 0$, the convergence is linear with convergence factor*

$$\rho = \left| \frac{(a - \lambda) + \lambda e^{-a/\nu}}{(a + \lambda) - \lambda e^{-a/\nu}} \right| \left| \frac{\lambda - (a + \lambda)e^{-a/\nu}}{\lambda + (a - \lambda)e^{-a/\nu}} \right| < 1. \quad (5.6)$$

Convergence in one iteration is achieved iff $\lambda = \frac{a}{1 - e^{-a/\nu}}$ or in the case $\nu = 0$.

The continuous DDM (5.3)–(5.5) is asymptotic-preserving iff $\lambda = \lambda(\nu)$ satisfies $|\lambda(\nu) - a| = o(1)$ as $\nu \rightarrow 0$.

5.3. Cell-centered finite volume discretization

We discretize (5.1) and (5.3)–(5.5) by a cell-centered finite volume method. For given $M \in \mathbb{N}$, define the step-width $h := 1/M$ and the volumes $V_m := [mh, (m+1)h]$ for $-M \leq m < M$. Furthermore, let $f_m := \int_{V_m} f(x) dx$. We denote the constant, cell-centered approximation of u in V_m by u_m , and encapsulate these for all V_m in the vector $\mathbf{u} := (u_m)_{m=-M}^{M-1} \in \mathbb{R}^{2M}$. Using centered differences for the diffusion and upwind fluxes for the advection, the discrete version of problem (5.1) reads

$$\frac{\nu}{h}(u_{m-1} - 2u_m + u_{m+1}) + a(u_{m-1} - u_m) = f_m \quad \text{for } -M < m < M-1, \quad (5.7)$$

$$\frac{\nu}{h}(-3u_{-M} + u_{-M+1}) - 2au_{-M} = f_{-M}, \quad (5.8)$$

$$\frac{\nu}{h}(u_{M-2} - 3u_{M-1}) + a(u_{M-2} - u_{M-1}) = f_{M-1}. \quad (5.9)$$

Here, we eliminated the ghost values u_{-M-1} and u_M using a linear interpolation of the boundary conditions. Analogously, one obtains the discrete version of (5.3) and (5.4), while (5.5) becomes

$$B_1(\mathbf{u}_1^i) = B_1(\mathbf{u}_2^{i-1}), \quad B_2(\mathbf{u}_2^i) = B_2(\mathbf{u}_1^i). \quad (5.10)$$

Note that there is no multiplication of B_1 by ν in (5.10). This avoids the indefinite limit case for $\nu = 0$, which would require a reformulation. Instead, we will use a particular type of discretization for B_1 and B_2 , which ensures the correct limit as $\nu \rightarrow 0$ (for an appropriate choice of the coefficients). In particular, we use centered differences for the diffusion and linear combinations of the values in V_{-1} and V_0 for the other terms of the transmission condition (5.2) to obtain

$$B_1(\mathbf{u}) = \frac{\nu}{h}(u_0 - u_{-1}) - a((1 - \alpha_1)u_{-1} + \alpha_1 u_0) + \lambda((1 - \beta_1)u_{-1} + \beta_1 u_0), \quad (5.11)$$

$$B_2(\mathbf{u}) = -\frac{\nu}{h}(u_0 - u_{-1}) + a((1 - \alpha_2)u_{-1} + \alpha_2 u_0) + \lambda((1 - \beta_2)u_{-1} + \beta_2 u_0), \quad (5.12)$$

for some $\alpha_1, \alpha_2, \beta_1, \beta_2 \in [0, 1]$. Note that $\alpha_l = \beta_l = 0$, $l = 1, 2$, is an upwind discretization, while the centered choice $\alpha_l = \beta_l = 1/2$, $l = 1, 2$, is typically used in the diffusion-dominated case $\nu \gg a$ to obtain second-order convergence in h .

To eliminate the ghost values $u_{1,0}$ and $u_{2,-1}$ in (5.7), we solve (5.11) for u_0 and (5.12) for u_{-1} . To eliminate $u_{2,-1}$ in (5.11) and $u_{1,0}$ in (5.12), we solve (5.7) for $u_{1,0}$ and $u_{2,-1}$. Inserting the resulting expressions and using (5.10), we obtain the following discrete DDM iteration.

Definition 5.2 (Discrete DDM). For given $\mathbf{u}_2^0 \in \mathbb{R}^M$, let $\tilde{B}_1(\mathbf{u}_2^0) := \frac{\nu B_1(\mathbf{u}_2^0)}{\nu - ah\alpha_1 + \lambda h\beta_1}$. For $i \in \mathbb{N}$, the i -th discrete DDM-iterate $(\mathbf{u}_1^i, \mathbf{u}_2^i) \in (\mathbb{R}^M)^2$ satisfies

$$\frac{\nu}{h}(u_{l,m-1}^i - 2u_{l,m}^i + u_{l,m+1}^i) + a(u_{l,m-1}^i - u_{l,m}^i) = f_m, \quad (5.13)$$

for $l = 1$, $-M < m < -1$ and for $l = 2$, $0 < m < M - 1$, and

$$\frac{\nu}{h}(-3u_{1,-M}^i + u_{1,-M+1}^i) - 2au_{1,-M}^i = f_{-M}, \quad (5.14)$$

$$\frac{\nu}{h}(u_{2,M-2}^i - 3u_{2,M-1}^i) + a(u_{2,M-2}^i - u_{2,M-1}^i) = f_{M-1}, \quad (5.15)$$

$$\frac{\nu}{h}(u_{1,-2}^i - 2u_{1,-1}^i) + a(u_{1,-2}^i - u_{1,-1}^i) + \frac{\nu}{h}c_1 u_{1,-1}^i = f_{-1} - \tilde{B}_1(\mathbf{u}_2^{i-1}), \quad (5.16)$$

$$\frac{\nu}{h}(-2u_{2,0}^i + u_{2,1}^i) - au_{2,0}^i + \left(\frac{\nu}{h} + a\right)c_2 u_{2,0}^i = f_0 - \tilde{B}_2(\mathbf{u}_1^i), \quad (5.17)$$

where

$$\tilde{B}_1(\mathbf{u}_2^i) = \frac{\nu}{h}u_{2,0}^i - \frac{\nu}{\nu + ah}c_1 \left(f_0 - \frac{\nu}{h}(-2u_{2,0}^i + u_{2,1}^i) + au_{2,0}^i\right), \quad (5.18)$$

$$\tilde{B}_2(\mathbf{u}_1^i) = \left(\frac{\nu}{h} + a\right)u_{1,-1}^i - \frac{\nu + ah}{\nu}c_2 \left(f_{-1} - \frac{\nu}{h}(u_{1,-2}^i - 2u_{1,-1}^i) - a(u_{1,-2}^i - u_{1,-1}^i)\right), \quad (5.19)$$

$$c_1 = \frac{\frac{\nu}{h} + a(1 - \alpha_1) - \lambda(1 - \beta_1)}{\frac{\nu}{h} - a\alpha_1 + \lambda\beta_1}, \quad c_2 = \frac{\frac{\nu}{h} - a\alpha_2 - \lambda\beta_2}{\frac{\nu}{h} + a(1 - \alpha_2) + \lambda(1 - \beta_2)}. \quad (5.20)$$

Note that (5.13)–(5.19) is uniquely solvable for all $\nu \geq 0$ iff $c_1 = \mathcal{O}(1/\nu)$ and $c_2 = \mathcal{O}(\nu)$ as $\nu \rightarrow 0$. The resulting system matrix for \mathbf{u}_2^i is weakly chained diagonally dominant, and thus non-singular. The same holds for \mathbf{u}_1^i if $c_1 \leq 1$. Further note that \tilde{B}_1 and \tilde{B}_2 in (5.16)–(5.19) are discrete Robin-to-Dirichlet operators, so that $c_1 = c_2 = 0$ corresponds to Dirichlet transmission conditions, which do not lead to

convergence without overlap.

5.3.1. Consistency of the discrete domain decomposition method

We next investigate how the coefficients α_l, β_l , $l = 1, 2$, must be chosen to obtain a discrete DDM that is consistent with (5.7)–(5.9). Since the discretization (5.13)–(5.15) is the same as (5.7)–(5.9), consistency follows iff the solution to (5.16)–(5.19) in the limit when $i \rightarrow \infty$ satisfies (5.7) and vice versa. The solution u of (5.7)–(5.9) solves (5.16)–(5.19), as can be directly seen when inserting it into (5.16)–(5.19) using (5.7) for $m = -1, 0$. This only requires that νc_1 and c_2/ν are well-defined for all $\nu \geq 0$ and all $\lambda > 0$. On the other hand, combining (5.16) and (5.18) as well as (5.17) and (5.19) yields

$$\begin{aligned} & \frac{\nu}{h}(u_{1,-2} - 2u_{1,-1} + u_{2,0}) + a(u_{1,-2} - u_{1,-1}) \\ &= f_{-1} + \frac{\nu}{\nu+ah}c_1(f_0 - \frac{\nu}{h}(u_{1,-1} - 2u_{2,0} + u_{2,1}) - a(u_{1,-1} - u_{2,0})), \\ & \frac{\nu}{h}(u_{1,-1} - 2u_{2,0} + u_{2,1}) + a(u_{1,-1} - u_{2,0}) \\ &= f_0 + \frac{\nu+ah}{\nu}c_2(f_{-1} - \frac{\nu}{h}(u_{1,-2} - 2u_{1,-1} + u_{2,0}) - a(u_{1,-2} - u_{1,-1})). \end{aligned}$$

We obtain equivalence with (5.7) iff $1 \neq c_1 c_2$. Hence, we have proved the following theorem which provides choices for the transmission condition parameters $\alpha_1, \alpha_2, \beta_1, \beta_2$ that ensure consistency for all $\lambda > 0$ and $\nu \geq 0$.

Theorem 5.2 (Consistency of the discrete DDM). *The limit of the discrete DDM iterates (5.13)–(5.19) as $i \rightarrow \infty$ is equal to the solution of (5.7)–(5.9) for all $\lambda > 0$ if the following conditions hold:*

- (C1) $\alpha_1 < \frac{\nu}{ah}$ (or equal if $\beta_1 > 0$), and
- (C2) $\nu c_1 = \mathcal{O}(1)$ as $\nu \rightarrow 0$, i.e. by (C1), $\nu = \mathcal{O}(\nu - ah\alpha_1 + \lambda h\beta_1)$, and
- (C3) $c_2 = \mathcal{O}(\nu)$ as $\nu \rightarrow 0$, i.e., $\alpha_2 + \beta_2 = \mathcal{O}(\nu)$, and
- (C4) $c_1 c_2 \neq 1$, i.e., $0 \neq a^2(\alpha_2 - \alpha_1) + \lambda(\frac{2\nu}{h} + a(\beta_1 + \beta_2 - \alpha_1 - \alpha_2)) + \lambda^2(\beta_1 - \beta_2)$.

Remark 5.1. Note that the simplest choice of the coefficients, which satisfies Theorem 5.2 is $\alpha_1 = \alpha_2 = \beta_2 = 0$ and $\beta_1 = 1/2$. As shown below, this also yields convergence for any positive discrete Péclet number $Pe := ah/\nu > 0$. Furthermore, this choice ensures that the discrete DDM is asymptotic-preserving as $\nu \rightarrow 0$ for any $\lambda > 0$, as we show next.

5.3.2. Convergence of the discrete domain decomposition method

We split the convergence analysis of the discrete DDM into two regimes due to the different types of solutions: the elliptic case $\nu > 0$ and the singular limit $\nu = 0$. For this, let $e^i := u - (u_1^i, u_2^i)$ be the error of the discrete DDM at iteration i . By linearity, e^i satisfies the discrete DDM (5.13)–(5.19) with $f = 0$.

The elliptic case $\nu > 0$

Then, (5.13)–(5.15) for e^i yield the solution

$$e^i = \left(A_1^i \left(\xi^{(m+1)h} - \left(1 + \frac{\text{Pe}}{2} \right) \xi^{-1} \right)_{m=-M}^{-1}, A_2^i \left(1 + \frac{\text{Pe}}{2} - \xi^{(m+1)h-1} \right)_{m=0}^{M-1} \right),$$

where we defined $\xi := (1 + \text{Pe})^M$. The constants $A_1^i, A_2^i \in \mathbb{R}$ are determined by (5.16)–(5.19), which yield the recurrence relations

$$\begin{aligned} A_1^i &= - \frac{\lambda - a + (a\alpha_1 - \lambda(\text{Pe}^{-1} + \beta_1)) \frac{2\text{Pe}}{2+\text{Pe}} \xi^{-1}}{(a\alpha_1 - \lambda(\text{Pe}^{-1} + \beta_1)) \frac{2\text{Pe}}{2+\text{Pe}} + (\lambda - a) \xi^{-1}} A_2^{i-1}, \\ A_2^i &= \frac{a\alpha_2 + \lambda(\text{Pe}^{-1} + \beta_2) - (\lambda + a) \frac{2+\text{Pe}}{2\text{Pe}} \xi^{-1}}{(\lambda + a) \frac{2+\text{Pe}}{2\text{Pe}} - (a\alpha_2 + \lambda(\text{Pe}^{-1} + \beta_2)) \xi^{-1}} A_1^i. \end{aligned}$$

Therefore, the iteration is linearly convergent iff

$$\rho = \left| \frac{\lambda - a + (a\alpha_1 - \lambda(\text{Pe}^{-1} + \beta_1)) \frac{2\text{Pe}}{2+\text{Pe}} \xi^{-1}}{\lambda + a - (a\alpha_2 + \lambda(\text{Pe}^{-1} + \beta_2)) \frac{2\text{Pe}}{2+\text{Pe}} \xi^{-1}} \right| \left| \frac{a\alpha_2 + \lambda(\text{Pe}^{-1} + \beta_2) - (\lambda + a) \frac{2+\text{Pe}}{2\text{Pe}} \xi^{-1}}{a\alpha_1 - \lambda(\text{Pe}^{-1} + \beta_1) + (\lambda - a) \frac{2+\text{Pe}}{2\text{Pe}} \xi^{-1}} \right| < 1. \quad (5.21)$$

Note that convergence in one iteration is possible for the choice

$$\lambda = \lambda_{\text{opt}} := \frac{2\nu + ah - 2\alpha_1 ah \xi^{-1}}{2\nu + ah - 2(\nu + \beta_1 ah) \xi^{-1}} a \xrightarrow{h \rightarrow 0} \frac{a}{1 - e^{-a/\nu}}, \quad (5.22)$$

which is almost mesh independent when $\alpha_1 = 0$ and $\beta_1 = 1/2$. This is consistent with the continuous DDM and also yields $\lambda_{\text{opt}} \rightarrow a$ as $\nu \rightarrow 0$.

Furthermore, note that (5.21) for $\alpha_1 = \alpha_2 = 0$ and $\beta_1 = \beta_2 = 1/2$ is satisfied for all $\lambda > 0$. But $\beta_2 = 1/2$ does not satisfy (C3) of Theorem 5.2, so that \tilde{B}_2 (and thus ρ) degenerates when $\nu \rightarrow 0$. However, choosing $\alpha_1 = \alpha_2 = \beta_2 = 0$ and $\beta_1 = 1/2$, Theorem 5.2 and (5.21) are satisfied for all $\nu > 0$ and for all $\lambda > 0$ due to $\text{Pe} > 0$.

The singular limit $\nu = 0$

Then, (5.13)–(5.15) for e^i yields

$$e^i = \left((0)_{m=-M}^{-2}, A_1^i, (A_2^i)_{m=0}^{M-1} \right),$$

with $A_1^i, A_2^i \in \mathbb{R}$ determined by (5.16)–(5.19). To obtain $A_1^1 = 0$, i.e., the correct solution in Ω_1 , this requires by (5.16)

$$0 = A_1^1 = \frac{-\tilde{B}_1(e^0)}{\frac{\nu}{h} c_1 - a}, \quad \tilde{B}_1(e^0) = \frac{\nu B_1(e^0)}{\nu - ah\alpha_1 + \lambda h\beta_1}.$$

Since $\nu c_1 = \mathcal{O}(1)$ as $\nu \rightarrow 0$ by (C2), this holds iff $\lim_{\nu \rightarrow 0} \nu c_1 \neq ah$ and $\lim_{\nu \rightarrow 0} \nu/(\nu - ah\alpha_1 + \lambda h\beta_1) = 0$. Using (C1) of Theorem 5.2, this simplifies to $\nu/\beta_1 = o(1)$ as $\nu \rightarrow 0$ and implies $c_1 = o(1)$. For A_2^1 , we then obtain by (5.17)–(5.19) and (C3) that $A_2^1 = 0$, i.e., convergence in one iteration. Then, $A_1^i = A_2^i = 0$ for all $i > 2$ follows by induction using (5.16)–(5.19).

Summarizing the above analysis, we obtain the following result.

Theorem 5.3 (Convergence and asymptotic-preserving property of the discrete DDM). *Let (C1)–(C4) from Theorem 5.2 be satisfied. The sequence of discrete DDM iterates $\{(\mathbf{u}_1^i, \mathbf{u}_2^i)\}_{i \in \mathbb{N}}$ from (5.13)–(5.19) converges linearly to the solution of (5.7)–(5.9) for $\nu > 0$ iff (5.21) is satisfied.*

Convergence in one iteration is achieved if λ satisfies (5.22) or for $\nu = 0$ if the limit discrete DDM for $\nu/\beta_1 = o(1)$ as $\nu \rightarrow 0$ is used.

The discrete DDM (5.13)–(5.19) is asymptotic-preserving if $|\lambda(\nu) - a| = o(1)$ or $\nu/\beta_1 = o(1)$ as $\nu \rightarrow 0$.

Note that as shown above, the choice $\alpha_1 = \alpha_2 = 0$ and $\beta_1 = \beta_2 = 1/2$ yields linear convergence for $\nu > 0$, but the convergence rate degenerates for $\nu \rightarrow 0$. The choice $\alpha_1 = \alpha_2 = \beta_2 = 0$ and $\beta_1 = 1/2$ leads to linear convergence for $\nu > 0$ uniformly in ν with 1-step convergence for $\nu = 0$, and thus is asymptotic-preserving.

Remark 5.2 (Convergence order and mass conservation). As the iterates of the discrete DDM converge to the solution of (5.7)–(5.9), which is a first-order convergent finite volume method (uniform in ν and a), the same holds for the discrete DDM at convergence (and before as soon as $e^i = \mathcal{O}(h)$). Furthermore, the finite volume method is locally mass conservative, such that mass conservation holds in each sub-domain of the discrete DDM. At the interface between the sub-domains, mass conservation is ensured at convergence, since the discrete DDM recovers the (implicit) mono-domain finite volume formulation. In contrast, methods based on an explicit splitting at the interface (see e.g. [208, 331]) directly ensure mass conservation, but require the usual time-step restriction of CFL-type when the diffusion vanishes ($\nu \rightarrow 0$).

5.4. Numerical examples

We now study numerically the convergence properties of the discrete DDM as $\nu \rightarrow 0$ for various choices of the parameters in the discrete Robin transmission conditions. Since $\alpha_l = \mathcal{O}(\nu)$, $l = 1, 2$, is required for convergence, we restrict our study to $\alpha_1 = \alpha_2 = 0$ and vary only β_1 , β_2 and λ . We consider (5.1) for

$$f(x) = -\nu(k\pi)^2 \sin(k\pi x) - ak\pi \cos(k\pi x),$$

which leads to the exact solution $u(x) = \sin(k\pi x)$. We fix $a = 1$, $k = 3$, $B_1(u_2^0) = 1$ and $M = 100$, and study the number of iterations required to reach an error of

$\|e^i\|_\infty < 10^{-12}$, see Fig. 5.1. As discussed above, the choice $\beta_1 = \beta_2 = 1/2$ leads to a degeneration as $\nu \rightarrow 0$, while the choice $\beta_1 = \beta_2 = \min(1/2, \nu/(ah))$ yields linear convergence, but is only asymptotic-preserving for $\lambda \rightarrow a$. As predicted by Theorem 5.3, the convergence improves for all choices such that $\nu/\beta_1 = o(1)$ and $\beta_2 = \mathcal{O}(\nu)$ as $\nu \rightarrow 0$. In particular, the number of iterations decreases faster when β_1 is large, which illustrates well the convergence factor ρ in (5.21), which satisfies

$$\rho = \frac{|\lambda - a|}{\lambda + a} \mathcal{O}\left(\frac{\nu}{\nu + \beta_1}\right) + \mathcal{O}(\nu^{M-1}).$$

Note that the finite volume method permits a straightforward extension of the discrete DDM to higher dimensions. For our two-dimensional example with equidistant rectangular mesh, the two-point fluxes across the edges on the interface between the sub-domains can be constructed exactly as in one dimension based on the transmission conditions and ghost values. We consider the two-dimensional problem

$$\begin{aligned} \nu \Delta u - \nabla \cdot u &= f \quad \text{in } (-1, 1) \times (0, 1), \\ u(-1, y) &= u(x, 0) = \nu u(1, y) = \nu u(x, 1) = 0, \end{aligned}$$

where f is chosen such that the exact solution is $u(x, y) = \sin(3\pi x) \sin(3\pi y)$. Using the same discretization parameters as in the previous case, the resulting iteration numbers show the same behavior as those in one dimension, see Fig. 5.2.

5.5. Conclusion

The continuous non-overlapping DDM with Robin transmission conditions applied to singularly-perturbed advection-diffusion problems is asymptotic-preserving only when the transmission parameter λ tends to the advection speed as $\nu \rightarrow 0$. We showed that a much better result can be obtained for a discrete DDM based on a cell-centered finite volume method: in contrast to the continuous algorithm, a proper, but asymmetric choice of the discrete parameters $(\alpha_l, \beta_l, l = 1, 2)$ in the Robin transmission conditions yields the asymptotic-preserving property without any restriction on the transmission parameter λ . We illustrated the theoretical results by numerical examples in one and two spatial dimensions. The technique developed here can also be used for robust DDMs for nonlinear time-dependent advection-diffusion equations in space-time on triangular meshes, as shown in the following Chapter 6.

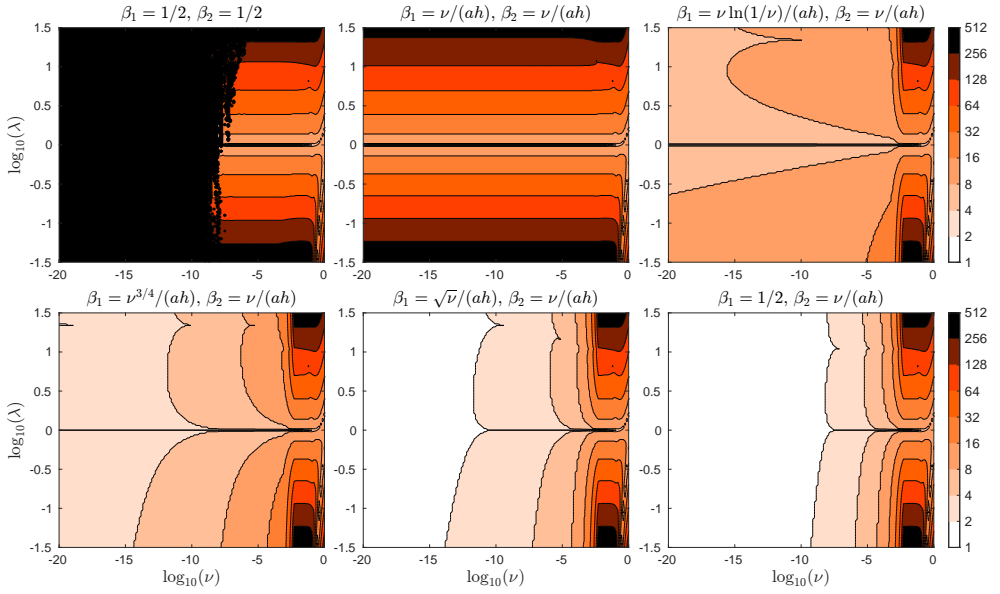


Figure 5.1.: Number of DDM-iterations for various β_1 and β_2 in one dimension.

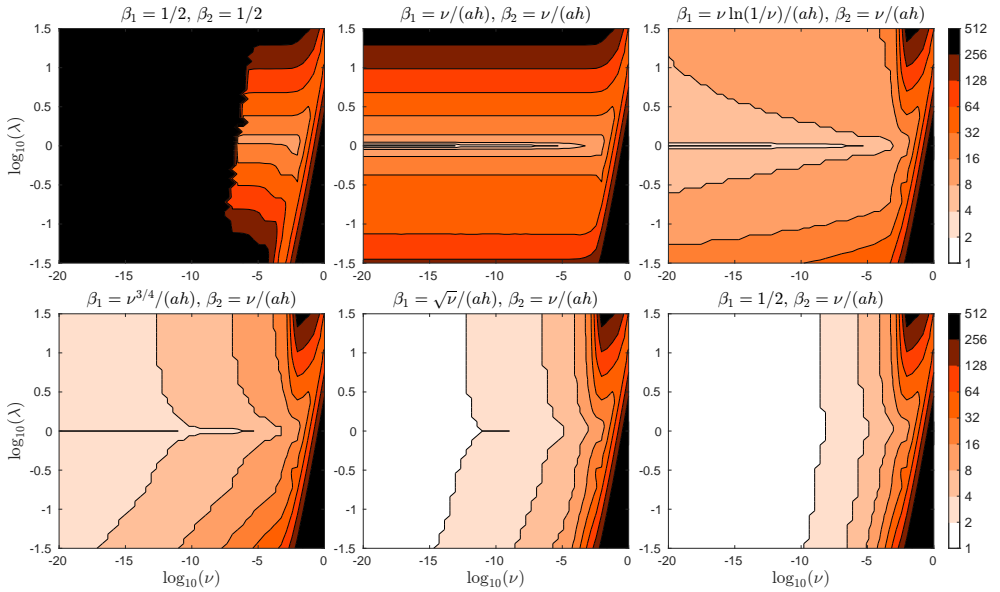


Figure 5.2.: Number of DDM-iterations for various β_1 and β_2 in two dimensions.

Non-overlapping Schwarz waveform-relaxation for nonlinear advection-diffusion equations

This chapter is based on the following submitted manuscript [124]:

- M. J. Gander, S. B. Lunowa, C. Rohde, *Non-overlapping Schwarz waveform-relaxation for nonlinear advection-diffusion equations*, submitted in revised form to SIAM Journal of Scientific Computing (03/2022), UHasselt CMAT Preprint UP-21-03 (2021): www.uhasselt.be/media/mufgoyse/up2103.pdf

6.1. Introduction

Nonlinear advection-diffusion equations often arise in the modeling of transport processes, especially in porous media. The precise formulation of the underlying nonlinear advection-diffusion equations can involve strong heterogeneities due to largely varying physical properties and parameters. In turn, this raises significant mathematical and computational problems, such that the development and analysis of robust discretization methods becomes a non-trivial challenge.

To still reach reasonable performance, a typical approach is the parallelization by a domain decomposition method, see [Section 1.5.4](#) and references therein. Here we focus on Schwarz Waveform-Relaxation (SWR) methods, which are time-parallel time integration methods [115] based on waveform-relaxation techniques invented in [204] for the design of large scale integrated circuits, and use domain decomposition in space following the seminal work of Schwarz [278] for the parallelization. SWR methods have been studied over the past three decades for many evolution problems, starting with [40, 111, 128, 133] for linear parabolic problems with typical superlinear convergence, and [118, 123] for hyperbolic problems,

where these algorithms typically converge in a finite number of steps, and also optimal and optimized transmission conditions were introduced, based on [122]. Such transmission conditions are crucial for good performance, which has been demonstrated e.g. in [117, 225] for the two-dimensional linear advection-reaction-diffusion equation. Asymptotic expressions for the optimal parameters in the transmission conditions have been analyzed in [35, 36, 119] for linear equations by the Fourier transform, see also [212, 239] for steady advection-diffusion problems with a non-overlapping domain decomposition with Robin transmission conditions. Less is known for the case of nonlinear problems: superlinear convergence was proved in [112] for classical overlapping SWR for semi-linear reaction diffusion, and for advection-dominated nonlinear conservation laws in [127]. An analysis of non-overlapping SWR for semi-linear wave propagation can be found in [149]. Optimized transmission conditions were explored for nonlinear reactive transport in [144, 145], the latter also containing Newton acceleration. This approach was numerically explored for the Navier-Stokes equations in [81], see also [140, 141] with transmission conditions from [60] for the error analysis of a (discrete) domain-decomposition algorithm. To the best of our knowledge there are so far no rigorous convergence results for non-overlapping SWR algorithms applied to fully nonlinear advection-diffusion equations.

The purpose of this chapter is to provide a theory for non-overlapping SWR algorithms with Robin transmission conditions applied to nonlinear advection-diffusion problems in time and space, see problem (6.1)–(6.3). For the resulting algorithm on two sub-domains we prove rigorously convergence. Our approach exploits the weak solution concept as it has been established for quasi-linear elliptic-parabolic equations in the seminal work by Alt and Luckhaus [18]. In this way we work in the most general framework induced by the generic energy estimates on nonlinear advection-diffusion equations. Our convergence analysis follows the one in [63], where non-overlapping SWR algorithms were considered for nonlinear reaction-diffusion equations. There, the higher-order regularity results are combined with fixed-point arguments. Here, no higher-order regularity results are available (cf. Remark 6.1), but the chosen concept of weak solutions still allows us to prove convergence, without requiring fixed-point arguments.

This chapter is structured as follows: we first present the problem on the entire domain, the non-overlapping SWR algorithm and weak solution concepts in Section 6.2. In Section 6.3, we deal with the existence and (imposing stronger assumptions on data) uniqueness of weak solutions for the SWR problems. On this basis, we proceed in Section 6.4 with the proof of the convergence of these solutions towards the solution of the problem on the entire domain. This main result is formulated in Theorem 6.3. In Section 6.5, we present the numerical treatment of the equations and a fully-discrete SWR algorithm that relies on a finite volume approach on triangular meshes in two spatial dimensions. In particular, our design

of the discrete Robin transmission conditions is asymptotic-preserving, i.e., in the hyperbolic limit, we recover the desired fast hyperbolic convergence of the method in a finite number of iterations. Finally, in [Section 6.6](#) we illustrate the theoretical convergence results by numerical examples and provide numerical simulations for two-phase flow in porous media, including problems with strong nonlinearities.

6.2. Problem formulation and the non-overlapping SWR algorithm

For $d \in \mathbb{N}$ let $\Omega \in \mathbb{R}^d$ be a bounded domain with Lipschitz boundary $\partial\Omega$ and let $T \in (0, \infty)$. We consider for the unknown $u = u(\mathbf{x} = (x_1, \dots, x_d)^T, t) : \Omega \times [0, T] \rightarrow \mathbb{R}$ an initial boundary value problem for nonlinear advection-diffusion equations given by

$$\partial_t u + \nabla \cdot \mathbf{f}(u) - \nabla \cdot (p(u) \nabla u) = 0 \quad \text{in } \Omega \times (0, T), \quad (6.1)$$

$$u|_{t=0} = u_0 \quad \text{in } \Omega, \quad (6.2)$$

$$u = 0 \quad \text{on } \partial\Omega \times (0, T). \quad (6.3)$$

Here, $p : \mathbb{R} \rightarrow (0, \infty)$ is a positive diffusion coefficient, $\mathbf{f} = (f_1, \dots, f_d)^T : \mathbb{R} \rightarrow \mathbb{R}^d$ is the advective flux and $u_0 : \Omega \rightarrow \mathbb{R}$ is the initial data. Necessary requirements on these given functions will be summarized in [Assumption 6.1](#) below. Working with a weak solution concept gives rise to define the function space

$$\mathcal{H} := H^1(0, T; H^{-1}(\Omega)) \cap L^2(0, T; H_0^1(\Omega)).$$

Definition 6.1 (Weak solution to (6.1)–(6.3)). A function $u \in \mathcal{H}$ is called a weak solution to problem (6.1)–(6.3) iff $u|_{t=0} = u_0$ almost everywhere in Ω and

$$\int_0^T \langle \partial_t u, \xi \rangle_\Omega + (p(u) \nabla u - \mathbf{f}(u), \nabla \xi)_\Omega dt = 0 \quad (6.4)$$

for all $\xi \in L^2(0, T; H_0^1(\Omega))$.

Here, we denote by $\langle \cdot, \cdot \rangle_\Omega$ the dual pairing between $H^{-1}(\Omega)$ and $H_0^1(\Omega)$, and by $(\cdot, \cdot)_\Omega$ the inner product on $L^2(\Omega)$. Note that for $u \in \mathcal{H}$, we also have $u \in C([0, T]; L^2(\Omega))$ by e.g. [103, Ch. 5.9, Thm. 3], such that the equality $u|_{t=0} = u_0$ is well defined in $L^2(\Omega)$.

We apply a non-overlapping SWR algorithm to approximate the solution u of the problem (6.1)–(6.3) as proposed in [63] for the reaction-diffusion equation. For the analysis, we restrict ourselves to the two-sub-domain case, the generalization to multiple sub-domains is straightforward as long as the normal derivative of the weak solution to (6.1)–(6.3) exists as trace on the sub-domain boundaries, cf. [Theorem 4.1](#). More precisely, the domain Ω is partitioned into two non-overlapping

sub-domains Ω_1 and Ω_2 , such that both have Lipschitz boundaries $\partial\Omega_1, \partial\Omega_2$. We denote the common interface by $\Gamma := \partial\Omega_1 \cap \partial\Omega_2$, and by \mathbf{n}_1 and \mathbf{n}_2 the unit outward normal vectors to Ω_1 and Ω_2 . The non-overlapping SWR algorithm is then given by iteratively solving for $i \in \mathbb{N}$ and $l \in \{1, 2\}$ the problems

$$\partial_t u_l^i + \nabla \cdot \mathbf{f}(u_l^i) - \nabla \cdot (p(u_l^i) \nabla u_l^i) = 0 \quad \text{in } \Omega_l \times (0, T), \quad (6.5)$$

$$u_l^i|_{t=0} = u_0 \quad \text{in } \Omega_l, \quad (6.6)$$

$$u_l^i = 0 \quad \text{on } (\partial\Omega_l \setminus \Gamma) \times (0, T), \quad (6.7)$$

$$\mathfrak{B}_l(u_l^i) = \mathfrak{B}_l(u_{3-l}^{i-1}) \quad \text{on } \Gamma \times (0, T). \quad (6.8)$$

Note that the index $3-l$ refers just to the other sub-domain, as $3-l = 2, 1$ for $l = 1, 2$. The differential transmission operators \mathfrak{B}_l are chosen as linear combination of the normal flux across the interface and of the solution, resulting in nonlinear Robin transmission conditions given for a fixed transmission parameter $\lambda > 0$ by

$$\mathfrak{B}_l(u) = (p(u) \nabla u - \mathbf{f}(u)) \cdot \mathbf{n}_l + \lambda u. \quad (6.9)$$

This choice ensures the continuity of the solution and of the normal flux across the interface in the limit $i \rightarrow \infty$. The iteration over $i \in \mathbb{N}$ is initialized by a given initial guess g_l of $\mathfrak{B}_l(u_{3-l}^0)$, i.e., (6.8) for $i = 1$ is replaced by $\mathfrak{B}_l(u_l^1) = g_l$ on $\Gamma \times (0, T)$. These transmission operators are the nonlinear counterparts of the linear ones, which have been studied e.g. in [36, 63, 119, 126] as optimized approximations of the Dirichlet to Neumann operator, see [113] for an introduction, and [129] for a comprehensive review. Before we proceed, let us note that the evaluation of the transmission operator can be expressed for $i > 1$ and $l \in \{1, 2\}$ by the shift relation

$$\begin{aligned} \mathfrak{B}_l(u_l^i) &= \mathfrak{B}_l(u_{3-l}^{i-1}) \\ &= (p(u_{3-l}^{i-1}) \nabla u_{3-l}^{i-1} - \mathbf{f}(u_{3-l}^{i-1})) \cdot \mathbf{n}_l + \lambda u_{3-l}^{i-1} \\ &= 2\lambda u_{3-l}^{i-1} - (p(u_{3-l}^{i-1}) \nabla u_{3-l}^{i-1} - \mathbf{f}(u_{3-l}^{i-1})) \cdot \mathbf{n}_{3-l} - \lambda u_{3-l}^{i-1} \\ &= 2\lambda u_{3-l}^{i-1} - \mathfrak{B}_{3-l}(u_{3-l}^{i-1}). \end{aligned} \quad (6.10)$$

For a weak definition of the iterative solutions of the SWR algorithm, we introduce the function spaces

$$\mathcal{W}_l := \{v \in H^1(\Omega_l) : v|_{\partial\Omega_l \setminus \Gamma} = 0\},$$

$$\mathcal{H}_l := H^1(0, T; \mathcal{W}_l') \cap L^2(0, T; \mathcal{W}_l),$$

denoting by \mathcal{W}_l' the dual of \mathcal{W}_l for $l \in \{1, 2\}$. In our analysis, we make use of the following assumption on the problem and the SWR iteration data. Most notably we require (6.1) to be non-degenerate.

Assumption 6.1.

- The initial data u_0 satisfies $u_0 \in H_0^1(\Omega)$.

- The flux function \mathbf{f} is in $C_b^{0,1}(\mathbb{R}, \mathbb{R}^d)$, i.e., bounded and Lipschitz-continuous with Lipschitz constant $L_f > 0$.
- The diffusion coefficient $p \in C_b^{0,1}(\mathbb{R})$ with Lipschitz constant $L_p > 0$ satisfies for some $\bar{p} > 0$ the condition $p(v) \geq \bar{p}$ for all $v \in \mathbb{R}$.
- The initial guesses of the transmission condition g_1 and g_2 are in $L^2(0, T; L^2(\Gamma))$.
- The transmission parameter λ is positive.

Note that the assumption applies for two-phase flow in porous media (in the non-degenerate regime), and also for the nonlinear viscous Burgers equation (cf. [Section 6.6](#)), since the solution is bounded, so that e.g. $\mathbf{f}(u) = v \min(u^2, u_{\max}^2)$ and $p(u) = \max(u_{\min}, \min(u, u_{\max}))$ can be used to obtain bounded and Lipschitz-continuous functions. We use now [\(6.10\)](#) to avoid the evaluation of traces of gradients on Γ (see also [\[63, 126\]](#)) and are led to

Definition 6.2 (Weak solution to the SWR algorithm [\(6.5\)–\(6.8\)](#)). Let [Assumption 6.1](#) hold. For $l \in \{1, 2\}$ and $i \in \mathbb{N}$ the functions $u_l^i \in \mathcal{H}_l$ are called a weak solution to the SWR algorithm [\(6.5\)–\(6.9\)](#) iff $u_l^i|_{t=0} = u_0$ almost everywhere in Ω_l and

$$\int_0^T \langle \partial_t u_l^i, \xi \rangle_{\Omega_l} + (p(u_l^i) \nabla u_l^i - \mathbf{f}(u_l^i), \nabla \xi)_{\Omega_l} dt = \int_0^T (\mathfrak{B}_l^i - \lambda u_l^i, \xi)_{\Gamma} dt \quad (6.11)$$

for all $\xi \in L^2(0, T; \mathcal{W}_l)$. Here $\mathfrak{B}_l^i \in L^2(0, T; L^2(\Gamma))$ are given by $\mathfrak{B}_l^1 = g_l$, and iteratively for $i > 1$ through

$$\mathfrak{B}_l^i = 2\lambda u_{3-l}^{i-1} - \mathfrak{B}_{3-l}^{i-1}. \quad (6.12)$$

Analogously as above for the entire domain, we denote here by $\langle \cdot, \cdot \rangle_{\Omega_l}$ the dual pairing between \mathcal{W}_l' and \mathcal{W}_l , by $(\cdot, \cdot)_{\Omega_l}$ and $(\cdot, \cdot)_{\Gamma}$ the inner product on $L^2(\Omega_l)$ respectively $L^2(\Gamma)$. The L^2 -norm is labeled $\|\cdot\|$. It will always be clear from the context whether it refers to either Ω_1 , Ω_2 , or the entire domain Ω . Furthermore, $\|\cdot\|_{\Gamma}$ denotes the $L^2(\Gamma)$ -norm. Note again that for $u \in \mathcal{H}_l$, we have $u \in C([0, T]; L^2(\Omega_l))$ by [\[103, Ch. 5.9, Thm. 3\]](#), such that $u|_{t=0} = u_0$ is well defined in $L^2(\Omega_l)$.

6.3. Existence of solutions and well-posedness of the SWR algorithm

In this section, we provide the existence and uniqueness results for the previously presented problems. For the original problem [\(6.1\)–\(6.3\)](#) existence and uniqueness of weak solutions in accordance with [Definition 6.1](#) has been proved by Alt and Luckhaus in [\[18\]](#).

Lemma 6.1 (Existence and uniqueness of a weak solution to (6.1)–(6.3)). *Let Assumption 6.1 hold, then there exists a unique weak solution $u \in \mathcal{H}$ to problem (6.1)–(6.3), which satisfies additionally $\partial_t u \in L^2(0, T; L^2(\Omega))$.*

Proof. Let $P(z) := \int_0^z p(y)dy$, so we have $P, P^{-1} \in C^{1,1}(\mathbb{R})$ by Assumption 6.1. We define the Kirchhoff transformed solution $w := P(u)$. The function u is a weak solution to (6.1)–(6.3), if and only if w satisfies $w|_{t=0} = w_0 := P(u_0)$ almost everywhere in Ω and

$$\int_0^T \langle \partial_t P^{-1}(w), \xi \rangle_\Omega + (\nabla w - \mathbf{f}(P^{-1}(w)), \nabla \xi)_\Omega dt = 0$$

for all $\xi \in L^2(0, T; H_0^1(\Omega))$. The existence of a unique weak solution $w \in \mathcal{H}$ follows by [18, Thms. 1.7, 2.4], while $\partial_t u = \partial_t P^{-1}(w) \in L^2(0, T; L^2(\Omega))$ follows by [18, Thm. 2.3]. Hence, we obtain the unique weak solution u by the inverse Kirchhoff transform. \square

In the next step we provide a well-posedness result for the SWR algorithm (6.5)–(6.8). The proof relies on compactness arguments as in [18] but requires iteration-independent a-priori estimates and a generalization to account for the transmission conditions in the weak form (6.11). We start with the construction of approximate solutions in time. Taking the limit, we will verify the existence of a weak solution in the sense of Definition 6.2.

Definition 6.3 (Time-discrete problem). Let $\Delta t = T/K$ for $K \in \mathbb{N}$, and $\mathfrak{D}_l \in L^2(0, T; L^2(\Gamma))$ for $l \in \{1, 2\}$ be given. For $0 \leq k \leq K$ and $l \in \{1, 2\}$ the functions $u_{k,l} \in \mathcal{W}_l$ are called a solution to the time-discrete problem iff $u_{0,l} = u_0$ in \mathcal{W}_l and

$$\left(\frac{u_{k,l} - u_{k-1,l}}{\Delta t}, \xi \right)_{\Omega_l} + (p(u_{k,l}) \nabla u_{k,l} - \mathbf{f}(u_{k,l}), \nabla \xi)_{\Omega_l} = (\mathfrak{D}_{k,l} - \lambda u_{k,l}, \xi)_\Gamma \quad (6.13)$$

for all $\xi \in \mathcal{W}_l$ and $1 \leq k \leq K$, where $\mathfrak{D}_{k,l} = \frac{1}{\Delta t} \int_{(k-1)\Delta t}^{k\Delta t} \mathfrak{D}_l(s) ds$.

Lemma 6.2. *Let Assumption 6.1 hold. For Δt small enough, $0 \leq k \leq K$ and $l \in \{1, 2\}$, there exist unique $u_{k,l} \in \mathcal{W}_l$ solving the time-discrete problem from Definition 6.3.*

Proof. The $u_{k,l}$ can be determined inductively for k as solutions of nonlinear elliptic problems. Again, let $P(z) := \int_0^z p(y)dy$, so we have $P, P^{-1} \in C^{1,1}(\mathbb{R})$ by Assumption 6.1. We define the Kirchhoff transformed solution $w_{k,l} := P(u_{k,l}) \in \mathcal{W}_l$. The function $u_{k,l}$ is a solution to (6.13), if and only if $w_{k,l}$ satisfies

$$\begin{aligned} \left(\frac{P^{-1}(w_{k,l}) - P^{-1}(w_{k-1,l})}{\Delta t}, \xi \right)_{\Omega_l} + (\nabla w_{k,l} - \mathbf{f}(P^{-1}(w_{k,l})), \nabla \xi)_{\Omega_l} \\ = (\mathfrak{D}_{k,l} - \lambda P^{-1}(w_{k,l}), \xi)_\Gamma \end{aligned} \quad (6.14)$$

for all $\xi \in \mathcal{W}_l$. One can write (6.14) in the functional form $a(w_{k,l}, \xi) = b(\xi)$ using the bounded linear operator $b : \mathcal{W}_l \rightarrow \mathbb{R}$ defined by

$$b(\xi) := \frac{1}{\Delta t} (P^{-1}(w_{k-1,l}), \xi)_{\Omega_l} + (\mathfrak{D}_{k,l}, \xi)_{\Gamma},$$

and the nonlinear operator $a : \mathcal{W}_l \times \mathcal{W}_l \rightarrow \mathbb{R}$ given by

$$a(w, \xi) := \frac{1}{\Delta t} (P^{-1}(w), \xi)_{\Omega_l} + (\nabla w - \mathbf{f}(P^{-1}(w)), \nabla \xi)_{\Omega_l} + \lambda (P^{-1}(w), \xi)_{\Gamma}.$$

Clearly, $a_w := a(w, \cdot)$ is a bounded linear operator for each $w \in \mathcal{W}_l$. Furthermore, since $\frac{1}{\|p\|_{C_b^0}} \leq (P^{-1})' \leq \frac{1}{\bar{p}}$, we have with the Cauchy–Schwarz and the Young inequality

$$\begin{aligned} a(u, u-v) - a(v, u-v) &\geq \frac{1}{\Delta t \|p\|_{C_b^0}} \|u-v\|^2 + \|\nabla(u-v)\|^2 \\ &\quad - \frac{L_f}{\bar{p}} \|u-v\| \|\nabla(u-v)\| + \frac{\lambda}{\|p\|_{C_b^0}} \|u-v\|_{\Gamma}^2 \\ &\geq \min \left\{ \frac{1}{\Delta t \|p\|_{C_b^0}} - \frac{L_f}{2\bar{p}}, \frac{1}{2} \right\} \|u-v\|_{\mathcal{W}_l}^2, \\ |a(u, \xi) - a(w, \xi)| &\leq \frac{1}{\Delta t \bar{p}} \|u-w\| \|\xi\| + \|\nabla(u-w)\| \|\nabla \xi\| \\ &\quad + \frac{L_f}{\bar{p}} \|u-w\| \|\nabla \xi\| + \frac{\lambda}{\bar{p}} \|u-w\|_{\Gamma} \|\xi\|_{\Gamma} \\ &\leq C \|u-w\|_{\mathcal{W}_l} \|\xi\|_{\mathcal{W}_l}. \end{aligned}$$

For $\Delta t < \frac{2\bar{p}}{L_f \|p\|_{C_b^0}}$, the nonlinear Lax–Milgram theorem [328, Thm. 2.H, p. 174–175] provides the existence and uniqueness of the solutions $w_{k,l} \in \mathcal{W}_l$ for all k , and thus the existence and uniqueness of the solutions $u_{k,l} \in \mathcal{W}_l$ of (6.13). \square

Having established the existence for the time-discrete problems, we proceed with investigating the SWR algorithm. To this end, we start with some a-priori estimates.

Lemma 6.3. *Let Assumption 6.1 hold. The solutions $u_{k,l}$ of the time-discrete problem from Definition 6.3 satisfy*

$$\begin{aligned} \max_{1 \leq k \leq K} \|u_{k,l}\|^2 + \sum_{k=1}^K \Delta t \|\nabla u_{k,l}\|^2 + \sum_{k=1}^K \Delta t \|u_{k,l}\|_{\Gamma}^2 &\leq C \left(1 + \|\mathfrak{D}_l\|_{L^2(0,T;L^2(\Gamma))}^2 \right), \\ \sum_{k=1}^K \Delta t \left\| \frac{u_{k,l} - u_{k-1,l}}{\Delta t} \right\|_{\mathcal{W}_l'}^2 &\leq C \left(1 + \|\mathfrak{D}_l\|_{L^2(0,T;L^2(\Gamma))}^2 \right), \end{aligned}$$

with some constant $C > 0$ independent of Δt and \mathfrak{D}_l .

Proof. Let $\xi = u_{k,l}$ in (6.13). Then, we obtain

$$\begin{aligned} \frac{1}{\Delta t} \|u_{k,l}\|^2 + \bar{p} \|\nabla u_{k,l}\|^2 + \lambda \|u_{k,l}\|_\Gamma^2 \\ \leq \frac{1}{\Delta t} (u_{k-1,l}, u_{k,l}) + (\mathbf{f}(u_{k,l}), \nabla u_{k,l}) + (\mathfrak{D}_{k,l}, u_{k,l})_\Gamma, \end{aligned}$$

and we have by the Cauchy–Schwarz and the Young inequality

$$\frac{1}{\Delta t} \|u_{k,l}\|^2 + \bar{p} \|\nabla u_{k,l}\|^2 + \lambda \|u_{k,l}\|_\Gamma^2 \leq \frac{1}{\Delta t} \|u_{k-1,l}\|^2 + \frac{|\Omega_l|}{\bar{p}} \|\mathbf{f}\|_{C_b^0}^2 + \frac{1}{\lambda} \|\mathfrak{D}_{k,l}\|_\Gamma^2.$$

Multiplication by Δt and summation over k from 1 to some $K_0 \leq K$ finally yields

$$\begin{aligned} \|u_{K_0,l}\|^2 + \bar{p} \sum_{k=1}^{K_0} \Delta t \|\nabla u_{k,l}\|^2 + \lambda \sum_{k=1}^{K_0} \Delta t \|u_{k,l}\|_\Gamma^2 \\ \leq \|u_{0,l}\|^2 + \frac{T|\Omega_l|}{\bar{p}} \|\mathbf{f}\|_{C_b^0}^2 + \frac{1}{\lambda} \|\mathfrak{D}_l\|_{L^2(0,T;L^2(\Gamma))}^2. \end{aligned}$$

This implies the first a-priori estimate. Now consider an arbitrary $\xi \in \mathcal{W}_l$ in (6.13), then we obtain with the Cauchy–Schwarz inequality and the trace theorem

$$\begin{aligned} \left| \left(\frac{u_{k,l} - u_{k-1,l}}{\Delta t}, \xi \right)_{\Omega_l} \right| \\ \leq (\bar{p} \|\nabla u_{k,l}\| + \|\mathbf{f}(u_{k,l})\|) \|\nabla \xi\| + (\|\mathfrak{D}_{k,l}\|_\Gamma + \lambda \|u_{k,l}\|_\Gamma) \|\xi\|_\Gamma \\ \leq C_1 (\|\nabla u_{k,l}\| + \|\mathbf{f}(u_{k,l})\| + \|\mathfrak{D}_{k,l}\|_\Gamma + \|u_{k,l}\|_\Gamma) \|\xi\|_{\mathcal{W}_l}. \end{aligned}$$

Dividing by $\|\xi\|_{\mathcal{W}_l}$ for $\xi \neq 0$ and taking the square, we obtain

$$\left\| \frac{u_{k,l} - u_{k-1,l}}{\Delta t} \right\|_{\mathcal{W}_l'}^2 \leq C_2 \left(\|\nabla u_{k,l}\|^2 + \|\mathbf{f}\|_{C_b^0}^2 |\Omega_l| + \|\mathfrak{D}_{k,l}\|_\Gamma^2 + \|u_{k,l}\|_\Gamma^2 \right).$$

Multiplication by Δt and summation with respect to $k = 1, \dots, K$ leads to

$$\sum_{k=1}^K \Delta t \left\| \frac{u_{k,l} - u_{k-1,l}}{\Delta t} \right\|_{\mathcal{W}_l'}^2 \leq C_2 \sum_{k=1}^K \Delta t \left(\|\nabla u_{k,l}\|^2 + \|\mathbf{f}\|_{C_b^0}^2 |\Omega_l| + \|\mathfrak{D}_{k,l}\|_\Gamma^2 + \|u_{k,l}\|_\Gamma^2 \right).$$

Using the first a-priori estimate concludes the proof. \square

Based on the a-priori estimates for the approximate solutions, we take the limit $\Delta t \rightarrow 0$ in (6.13) to conclude the existence of a weak solution of single SWR iterates in the sense of Definition 6.2. The arguments are similar to the uniqueness proof of [18, Thm. 1.7].

Theorem 6.1 (Existence of weak solutions to (6.5)–(6.8)). *Let Assumption 6.1 hold. Then, for $l \in \{1, 2\}$ and all $i \in \mathbb{N}$ there exists a weak solution $u_l^i \in \mathcal{H}_l$ to the*

SWR algorithm (6.5)–(6.8) that satisfies the estimate

$$\begin{aligned} \|u_l^i\|_{L^\infty(0,T;L^2(\Omega_l))}^2 + \|u_l^i\|_{L^2(0,T;\mathcal{W}_l)}^2 + \|\partial_t u_l^i\|_{L^2(0,T;\mathcal{W}_l')}^2 + \|u_l^i\|_{L^2(0,T;L^2(\Gamma))}^2 \\ \leq C \left(1 + \|\mathfrak{B}_l^i\|_{L^2(0,T;L^2(\Gamma))}^2\right), \end{aligned} \quad (6.15)$$

where $C \geq 0$ depends on $|\Omega_l|$, T , λ , \bar{p} , $\|p\|_{C_b^0}$, $\|f\|_{C_b^0}$ and $\|u_0\|_{H^1(\Omega_l)}$.

Proof. The time-discrete problem from Definition 6.3 with $\mathfrak{D}_l := \mathfrak{B}_l^i$ given by (6.12) has unique solutions $u_{k,l}^i \in \mathcal{W}_l$ by Lemma 6.2, which satisfy the a-priori estimates in Lemma 6.3. Let $u_{\Delta t,l}^i : \Omega_l \times [0, T] \rightarrow \mathbb{R}$ be the piece-wise linear interpolation in time of the functions $u_{0,l}^i, \dots, u_{K,l}^i$. Then we have

$$\begin{aligned} \int_0^T \|u_{\Delta t,l}^i\|^2 dt &= \sum_{k=1}^K \int_{(k-1)\Delta t}^{k\Delta t} \left\| u_{k-1,l}^i + \frac{t-(k-1)\Delta t}{\Delta t} (u_{k,l}^i - u_{k-1,l}^i) \right\|^2 dt \\ &\leq 2 \sum_{k=1}^K \int_{(k-1)\Delta t}^{k\Delta t} \|u_{k-1,l}^i\|^2 + \|u_{k,l}^i\|^2 dt \leq 2C \left(1 + \|\mathfrak{B}_l^i\|_{L^2(0,T;L^2(\Gamma))}^2\right), \end{aligned}$$

and similarly

$$\begin{aligned} \int_0^T \|\nabla u_{\Delta t,l}^i\|^2 dt &\leq 2C \left(1 + \|\mathfrak{B}_l^i\|_{L^2(0,T;L^2(\Gamma))}^2\right), \\ \int_0^T \|\partial_t u_{\Delta t,l}^i\|_{\mathcal{W}_l'}^2 dt &= \sum_{k=1}^K \int_{(k-1)\Delta t}^{k\Delta t} \left\| \frac{u_{k,l}^i - u_{k-1,l}^i}{\Delta t} \right\|_{\mathcal{W}_l'}^2 dt \leq C \left(1 + \|\mathfrak{B}_l^i\|_{L^2(0,T;L^2(\Gamma))}^2\right). \end{aligned}$$

Therefore, the family $(u_{\Delta t,l}^i)_{\Delta t > 0}$ is uniformly bounded in \mathcal{H}_l , so it has a weakly converging subsequence with limit $u_l^i \in \mathcal{H}_l$. Using the compact embedding of \mathcal{H}_l into $L^2(0, T; L^2(\Omega_l))$ (Aubin–Lions lemma), we have that $u_{\Delta t,l}^i$ converges strongly to u_l^i in $L^2(0, T; L^2(\Omega_l))$. We use now the general principle that the strong convergence of the piece-wise linear time-interpolation in $L^2(0, T; L^2(\Omega))$ implies the same convergence and limit for the piece-wise constant interpolation in time, see e.g. [205, Lemma 3.2]. Thus, we conclude that the piece-wise constant interpolation in time, defined by $\overline{u_{\Delta t,l}^i}(t) := u_{k,l}^i$ for $t \in ((k-1)\Delta t, k\Delta t]$, also converges strongly in $L^2(0, T; L^2(\Omega))$.

Further, observe that $p(\overline{u_{\Delta t,l}^i}) \nabla \overline{u_{\Delta t,l}^i}$ is bounded in $[L^2(0, T; L^2(\Omega_l))]^d$, therefore it has a weak limit ζ in this space. To identify this limit, we take arbitrary $\xi \in L^2(0, T; \mathcal{W}_l \cap C^1(\overline{\Omega_l}))$ as test functions. Then, we obtain

$$\begin{aligned} \int_0^T \left(p(\overline{u_{\Delta t,l}^i}) \nabla \overline{u_{\Delta t,l}^i} - p(u_l^i) \nabla u_l^i, \nabla \xi \right)_{\Omega_l} dt \\ = \int_0^T \left((p(\overline{u_{\Delta t,l}^i}) - p(u_l^i)) \nabla \overline{u_{\Delta t,l}^i}, \nabla \xi \right)_{\Omega_l} + \left(p(u_l^i) (\nabla \overline{u_{\Delta t,l}^i} - \nabla u_l^i), \nabla \xi \right)_{\Omega_l} dt \end{aligned}$$

$$= \int_0^T \left(\nabla \overline{u_{\Delta t,l}^i}, (p(\overline{u_{\Delta t,l}^i}) - p(u_l^i)) \nabla \xi \right)_{\Omega_l} + \left(\nabla \overline{u_{\Delta t,l}^i} - \nabla u_l^i, p(u_l^i) \nabla \xi \right)_{\Omega_l} dt.$$

Since $p(\overline{u_{\Delta t,l}^i})$ converges strongly, and $\nabla \overline{u_{\Delta t,l}^i}$ converges weakly in $L^2(0, T; L^2(\Omega_l))$ (analogously to $u_{\Delta t,l}^i$), and $\nabla \xi$ is bounded, the terms on the right hand side converge to zero. By the uniqueness of the limit, we have then $\zeta = p(u_l^i) \nabla u_l^i$.

From (6.13), we know

$$\begin{aligned} \int_0^T \langle \partial_t u_{\Delta t,l}^i, \xi \rangle_{\Omega_l} + \left(p(\overline{u_{\Delta t,l}^i}) \nabla \overline{u_{\Delta t,l}^i} - f(\overline{u_{\Delta t,l}^i}), \nabla \xi \right)_{\Omega_l} dt \\ = \int_0^T \left(\overline{\mathfrak{B}_l^i} - \lambda \overline{u_{\Delta t,l}^i}, \xi \right)_{\Gamma} dt \end{aligned}$$

for all $\xi \in L^2(0, T; \mathcal{W}_l)$. The function $\overline{\mathfrak{B}_l^i}$ is iteratively defined by $\overline{\mathfrak{B}_l^i} = 2\lambda \overline{u_{\Delta t,3-l}^{i-1}} - \overline{\mathfrak{B}_{3-l}^{i-1}}$. Due to the strong and weak convergence of $u_{\Delta t,l}^i$ and $\overline{u_{\Delta t,l}^i}$, we can consider a sequence $\Delta t \rightarrow 0$ and pass to the limit, which shows that u_l^i is a weak solution to the SWR algorithm (6.5)–(6.8). Thus, we can iteratively obtain weak solutions $u_l^i \in \mathcal{H}_l$ for $l \in \{1, 2\}$ and $i \in \mathbb{N}$, such that the estimate (6.15) is satisfied. \square

The existence of a solution to the SWR algorithm is used in the next theorem to prove the uniqueness of the solutions for the SWR iterations under an additional regularity assumption.

Theorem 6.2 (Uniqueness of the SWR iteration). *Let Assumption 6.1 hold. If a sequence of weak solutions $(u_1^i, u_2^i)_{i \in \mathbb{N}} \in \mathcal{H}_1 \times \mathcal{H}_2$ to the SWR algorithm (6.5)–(6.9) satisfies $\partial_t u_l^i \in L^2(0, T; L^2(\Omega_l))$ for $l \in \{1, 2\}$ and all $i \in \mathbb{N}$, it is unique.*

Remark 6.1. The regularity assumption $\partial_t u_l^i \in L^2(0, T; L^2(\Omega_l))$ amounts to the maximal-regularity property for parabolic equations, i.e., the required regularity when dealing with strong solutions. In [295] maximal regularity is proven for a wide class of quasi-linear parabolic equations including equations of type (6.3). The results apply if f and the diffusion coefficient p satisfy Assumption 6.1 and if the domain boundary is $C^{1,1}$ -regular. Thus, Theorem 6.3 holds under these general conditions, which are satisfied if e.g. $d = 1$ holds, or if $\partial\Omega_1$ and $\partial\Omega_2$ can be chosen to be smooth. The $C^{1,1}$ -regularity of the boundaries can be guaranteed if one of the sub-domains is immersed into the other one such that $\Gamma = \partial\Omega_1 \cap \partial\Omega_2$ does not intersect with $\partial\Omega$. For the case $\Gamma \cap \partial\Omega \neq \emptyset$ which excludes $C^{1,1}$ -regularity for Ω_1 and Ω_2 , there are to our knowledge only few general results, none of them covering (6.3) completely. The recent contribution [20] for linear evolution equations with variable coefficients establishes maximal regularity for transversal intersections of Γ with the boundary $\partial\Omega$.

Proof (of Theorem 6.2). Assume that there is another sequence of weak solutions $(\tilde{u}_1^i, \tilde{u}_2^i)_{i \in \mathbb{N}}$. Then there exists an $l \in \{1, 2\}$ and a $i \in \mathbb{N}$ minimal, such that $u_l^i \neq \tilde{u}_l^i$

and $\mathfrak{B}_l^i = \tilde{\mathfrak{B}}_l^i$. Let $\psi_\delta(z) := \max(0, \min(1, z/\delta))$. We follow the proof of Theorem 2.2 in [18] and consider the difference of the equations (6.11) for both solutions with the choice $\xi = \psi_\delta(u_l^i - \tilde{u}_l^i)\chi_{(0,\tau)}$ for $\tau \in (0, T]$. This yields

$$\begin{aligned} \int_0^\tau \int_{\Omega_l} \partial_t(u_l^i - \tilde{u}_l^i) \psi_\delta(u_l^i - \tilde{u}_l^i) dx + (p(u_l^i) \nabla u_l^i - p(\tilde{u}_l^i) \nabla \tilde{u}_l^i, \nabla \psi_\delta(u_l^i - \tilde{u}_l^i))_{\Omega_l} dt \\ + \int_0^\tau (u_l^i - \tilde{u}_l^i, \psi_\delta(u_l^i - \tilde{u}_l^i))_\Gamma dt = \int_0^\tau (\mathbf{f}(u_l^i) - \mathbf{f}(\tilde{u}_l^i), \nabla \psi_\delta(u_l^i - \tilde{u}_l^i))_{\Omega_l} dt. \end{aligned}$$

By the identity $p(u_l^i) \nabla u_l^i - p(\tilde{u}_l^i) \nabla \tilde{u}_l^i = p(\tilde{u}_l^i) \nabla(u_l^i - \tilde{u}_l^i) + (p(u_l^i) - p(\tilde{u}_l^i)) \nabla u_l^i$, the Cauchy–Schwarz inequality and the Young inequality, we get

$$\begin{aligned} \int_0^\tau \int_{\Omega_l} \partial_t(u_l^i - \tilde{u}_l^i) \psi_\delta(u_l^i - \tilde{u}_l^i) dx + \frac{\delta \bar{p}}{2} \|\nabla \psi_\delta(u_l^i - \tilde{u}_l^i)\|^2 dt \\ \leq \int_0^\tau \frac{L_p^2}{\delta \bar{p}} \|\chi_{\{0 \leq u_l^i - \tilde{u}_l^i \leq \delta\}} \|u_l^i - \tilde{u}_l^i\| \|\nabla u_l^i\|\|^2 + \frac{L_f^2}{\delta \bar{p}} \|\chi_{\{0 \leq u_l^i - \tilde{u}_l^i \leq \delta\}} (u_l^i - \tilde{u}_l^i)\|^2 dt \\ \leq \int_0^\tau \frac{\delta L_p^2}{\bar{p}} \|\nabla u_l^i\|^2 + \frac{\delta L_f^2 |\Omega_l|}{\bar{p}} dt. \end{aligned}$$

For $\delta \rightarrow 0$, the righthand side tends to zero and the first term on the left-hand side converges for almost all $\tau \in (0, T)$ to

$$\begin{aligned} \int_0^\tau \int_{\Omega_l} \partial_t(u_l^i - \tilde{u}_l^i) \chi_{\{u_l^i \geq \tilde{u}_l^i\}} dx dt = \int_0^\tau \int_{\Omega_l} \partial_t \max(u_l^i - \tilde{u}_l^i, 0) dx dt \\ = \int_{\Omega_l} \max(u_l^i(\tau) - \tilde{u}_l^i(\tau), 0) dx \geq 0. \end{aligned}$$

Interchanging the roles of u_l^i and \tilde{u}_l^i , we obtain

$$0 = \int_{\Omega_l} |u_l^i(\tau) - \tilde{u}_l^i(\tau)| dx$$

for almost all τ and hence $u_l^i = \tilde{u}_l^i$ almost everywhere. \square

6.4. Convergence of the non-overlapping SWR algorithm

We now prove that the weak solutions of the non-overlapping SWR algorithm (6.5)–(6.9) converge to the weak solution of the entire domain (mono-domain) formulation (6.1)–(6.3), and hence this method is applicable to nonlinear advection–diffusion equations. We use the conceptual idea of Caetano et al. in [63] for a semi-linear reaction diffusion equation $\partial_t u - \nu \Delta u = r(u)$ with some source function $r(u)$, but with substantial differences: the proof in [63] requires a-priori estimates in higher-order Sobolev spaces and leads in a first step only to a result locally in time. Here we exploit the low-order ansatz for weak solutions from [18] which en-

ables us to deduce directly a global error bound, which extends the similar result for stationary linear advection-diffusion equations in [239, Thm. 4.5] to nonlinear advection-diffusion equations.

Theorem 6.3 (Convergence of the SWR iteration). *Let [Assumption 6.1](#) be satisfied. By [Theorem 6.1](#), the SWR algorithm defined by (6.5)–(6.9), initialized with the guesses $g_1, g_2 \in L^2(0, T; L^2(\Gamma))$, defines a sequence of weak solutions $(u_1^i, u_2^i) \in \mathcal{H}_1 \times \mathcal{H}_2$, which is unique if $\partial_t u_l^i \in L^2(0, T; L^2(\Omega_l))$ for $l \in \{1, 2\}$ and all $i \in \mathbb{N}$ by [Theorem 6.2](#). If the unique weak solution u of the original problem (6.1)–(6.3) satisfies*

$$\nabla u \in L^2(0, T; L^\infty(\Omega)) \quad \text{and} \quad p(u) \nabla u \cdot \mathbf{n}_l \in L^2(0, T; L^2(\Gamma)),$$

then $(u_1^i, u_2^i)_{i \in \mathbb{N}}$ converges to $(u|_{\Omega_1}, u|_{\Omega_2})$ in $(L^\infty(0, T; L^2(\Omega_l)) \cap L^2(0, T; \mathcal{W}_l))_{l=1,2}$ as $i \rightarrow \infty$.

Note, that the regularity assumptions $p(u) \nabla u \cdot \mathbf{n}_l \in L^2(0, T; L^2(\Gamma))$ and $\nabla u \in L^2(0, T; L^\infty(\Omega))$ can be shown e.g. by the following regularity results in case of more regularity of the domain and of the parameter functions.

Lemma 6.4 (Improved regularity of the solution to (6.1)–(6.3)). *Let [Assumption 6.1](#) hold. If we additionally have $\partial\Omega \in C^{1,1}$ or Ω convex and $\mathbf{f}' \in C_b^0(\mathbb{R}, \mathbb{R}^d)$, then the solution u to problem (6.1)–(6.3) is in $L^2(0, T; H^2(\Omega)) \cap C([0, T]; H^1(\Omega))$.*

Proof. Since \mathbf{f}' is continuous and bounded, $\mathbf{f}'(u) \cdot \nabla u$ is Lebesgue measurable and in $L^2(0, T; L^2(\Omega))$. Thus, integration by parts in (6.4) yields

$$\begin{aligned} \int_0^T (\nabla w, \nabla \xi)_{\Omega_l} dt &:= \int_0^T (p(u) \nabla u, \nabla \xi)_{\Omega_l} dt \\ &= \int_0^T (\partial_t u + \mathbf{f}'(u) \cdot \nabla u, \xi)_{\Omega_l} dt =: \int_0^T (g, \xi)_{\Omega_l} dt \end{aligned}$$

for all $\xi \in L^2(0, T; H_0^1(\Omega))$, where $g \in L^2(0, T; L^2(\Omega))$. Since time is only a parameter, we obtain by the regularity theory in [143], that $w = P(u) \in L^2(0, T; H^2(\Omega))$. As $p = P'$ is bounded from below by $\bar{p} > 0$, this yields $\nabla u \in L^2(0, T; H^1(\Omega))$. Together with $\partial_t u \in L^2(0, T; L^2(\Omega))$, we obtain $u \in C([0, T]; H^1(\Omega))$ by [103, Ch. 5.9, Thm. 4]. \square

Lemma 6.5 (Classical solution to (6.1)–(6.3)). *Let [Assumption 6.1](#) hold, and additionally assume $\partial\Omega \in C^2$, $p \in C_b^{1,\alpha}(\mathbb{R})$ and $\mathbf{f} \in C_b^{1,\alpha}(\mathbb{R}, \mathbb{R}^d)$ for some $\alpha > 0$. If the initial data u_0 is in $C^{0,1}(\Omega)$, then there exists a unique solution $u \in C^{0,\alpha/2}([0, T] \times \bar{\Omega}) \cap C^1((0, T); C^0(\Omega)) \cap C^0((0, T); C^2(\Omega))$ to problem (6.1)–(6.3).*

Proof. By direct application of [199, Thm. 6.2]. \square

Proof of Theorem 6.3. For each $i \in \mathbb{N}$ and $l \in \{1, 2\}$, we define the errors $e_l^i := u_l^i - u|_{\Omega_l} \in \mathcal{H}_l$. Note that $\partial_t u \in L^2(0, T; L^2(\Omega))$ by regularity, such that $\langle \partial_t u, \cdot \rangle$ on Ω equals the sum of the corresponding dual pairings on Ω_1 and Ω_2 . Thus, the errors satisfy on the sub-domains the initial boundary value problems

$$\begin{aligned} \int_0^T \langle \partial_t e_l^i, \xi \rangle_{\Omega_l} + (p(u_l^i) \nabla e_l^i + (p(u_l^i) - p(u)) \nabla u - \mathbf{f}(u_l^i) + \mathbf{f}(u), \nabla \xi)_{\Omega_l} dt \\ = \int_0^T \left(\mathfrak{B}_l^{i, \text{err}} - \lambda e_l^i, \xi \right)_{\Gamma} dt, \end{aligned} \quad (6.16)$$

for all $\xi \in L^2(0, T; \mathcal{W}_l)$, together with the initial data $e_l^i|_{t=0} = 0$ in $L^2(\Omega_l)$ and the error transmission operator defined due to the assumptions and (6.9) by

$$\mathfrak{B}_l^{i, \text{err}} := \mathfrak{B}_l^i - (p(u) \nabla u - \mathbf{f}(u)) \cdot \mathbf{n}_l - \lambda u \quad \text{on } \Gamma \times (0, T). \quad (6.17)$$

Choosing $\xi = e_l^i \chi_{(0, \tau)}$ for $\tau \in (0, T]$ in (6.16) and applying the Cauchy-Schwarz inequality yields

$$\begin{aligned} \frac{1}{2} \|e_l^i(\tau)\|^2 + \int_0^\tau \bar{p} \|\nabla e_l^i\|^2 - \left(\|(p(u_l^i) - p(u)) \nabla u\| + \|\mathbf{f}(u_l^i) + \mathbf{f}(u)\| \right) \|\nabla e_l^i\| dt \\ \leq \int_0^\tau \left(\mathfrak{B}_l^{i, \text{err}} - \lambda e_l^i, e_l^i \right)_{\Gamma} dt. \end{aligned}$$

Using $p, \mathbf{f} \in C_b^{0,1}$ and the Young inequality, we obtain

$$\begin{aligned} \frac{1}{2} \|e_l^i(\tau)\|^2 + \frac{\bar{p}}{2} \int_0^\tau \|\nabla e_l^i\|^2 dt \\ \leq \int_0^\tau \left(\mathfrak{B}_l^{i, \text{err}} - \lambda e_l^i, e_l^i \right)_{\Gamma} dt + \int_0^\tau \left(\frac{L_p^2}{\bar{p}} \|\nabla u\|_{L^\infty(\Omega_l)}^2 + \frac{L_f^2}{\bar{p}} \right) \|e_l^i\|^2 dt. \end{aligned}$$

Next, we replace the transmission term using the identity $\mathfrak{B}_l^{i, \text{err}} = 2\lambda e_{3-l}^{i-1} - \mathfrak{B}_{3-l}^{i-1, \text{err}}$ (see (6.10) and (6.12)) yielding

$$\|\mathfrak{B}_l^{i, \text{err}}\|_{\Gamma}^2 = \|\mathfrak{B}_{3-l}^{i-1, \text{err}}\|_{\Gamma}^2 - 4\lambda \left(\mathfrak{B}_{3-l}^{i-1, \text{err}}, e_l^i \right)_{\Gamma} + 4\lambda^2 \|e_{3-l}^{i-1}\|_{\Gamma}^2,$$

such that we have by shifting l and i

$$\left(\mathfrak{B}_l^{i, \text{err}} - \lambda e_l^i, e_l^i \right)_{\Gamma} = \frac{1}{4\lambda} \left(\|\mathfrak{B}_l^{i, \text{err}}\|_{\Gamma}^2 - \|\mathfrak{B}_{3-l}^{i+1, \text{err}}\|_{\Gamma}^2 \right).$$

Hence, we get

$$\begin{aligned} \|e_l^i(\tau)\|^2 + \bar{p} \int_0^\tau \|\nabla e_l^i\|^2 dt \\ \leq \frac{1}{2\lambda} \int_0^\tau \|\mathfrak{B}_l^{i, \text{err}}\|_{\Gamma}^2 - \|\mathfrak{B}_{3-l}^{i+1, \text{err}}\|_{\Gamma}^2 dt + \int_0^\tau C_E(t) \|e_l^i\|^2 dt, \end{aligned} \quad (6.18)$$

where

$$C_E(t) = \frac{2L_p^2}{\bar{p}} \|\nabla u(t)\|_{L^\infty(\Omega_l)}^2 + \frac{2L_f^2}{\bar{p}} > 0.$$

Adding terms up to step $I \in \mathbb{N}$ for both sub-domains, we define

$$\begin{aligned} \mathfrak{E}^I(\tau) &:= \sum_{i=1}^I \sum_{l=1}^2 \|e_l^i(\tau)\|^2, & \mathfrak{F}^I(\tau) &:= \bar{p} \sum_{i=1}^I \sum_{l=1}^2 \int_0^\tau \|\nabla e_l^i\|^2 dt, \\ \mathfrak{G}^I(\tau) &:= \frac{1}{2\lambda} \sum_{l=1}^2 \int_0^\tau \|\mathfrak{B}_l^{I,\text{err}}\|_{\Gamma}^2 dt. \end{aligned}$$

Summing (6.18) over $i = 1, \dots, I$ and $l = 1, 2$, we obtain the inequality

$$\mathfrak{E}^I(\tau) + \mathfrak{F}^I(\tau) + \mathfrak{G}^{I+1}(\tau) \leq \mathfrak{G}^1(\tau) + \int_0^\tau C_E(t) \mathfrak{E}^I(t) dt.$$

Note that $C_E \in L^1(0, T)$ by assumption, $\mathfrak{E}^I \in C([0, T])$, so that we conclude by Gronwall's lemma

$$\mathfrak{E}^I(\tau) \leq \mathfrak{G}^1(\tau) + \int_0^\tau \mathfrak{G}^1(t) C_E(t) \exp\left(\int_t^\tau C_E(s) ds\right) dt =: C(\tau) < \infty, \quad (6.19)$$

$$\mathfrak{F}^I(\tau) \leq \mathfrak{G}^1(\tau) + \int_0^\tau C_E(t) C(t) dt < \infty. \quad (6.20)$$

Since the righthand side of the estimates (6.19) and (6.20) are independent of I , the sequences $(\mathfrak{E}^i)_{i \in \mathbb{N}}$ and $(\mathfrak{F}^i)_{i \in \mathbb{N}}$ are uniformly bounded in $L^\infty(0, T)$. Therefore, u_l^i converges to $u|_{\Omega_l}$ in $L^\infty(0, T; L^2(\Omega_l)) \cap L^2(0, T; \mathcal{W}_l)$. \square

6.5. Numerical discretization for two-dimensional domains

To implement the SWR algorithm we suggest to discretize the equations by a finite volume method. This allows us in particular to enforce the transmission conditions quite naturally via numerical fluxes across the interface.

6.5.1. The general finite volume method

We consider for $d = 2$ the bounded domain $\Omega = (-1, 1)^2$. For the SWR algorithm, the (mono-)domain Ω is divided at $\Gamma = \{0\} \times [-1, 1]$ into the two (sub-)domains $\Omega_1 = (-1, 0) \times (-1, 1)$ and $\Omega_2 = (0, 1) \times (-1, 1)$. For all domains $\omega \in \{\Omega, \Omega_1, \Omega_2\}$ we use as discretization a first-order finite volume method on a conforming structured mesh $\mathcal{T}_{\omega, \Delta x}$ of equilateral triangles; the mesh parameter $\Delta x > 0$ denotes the length of the edges. For some $\mathcal{T} \in \mathcal{T}_{\omega, \Delta x}$ we denote by $\mathcal{S}(\mathcal{T})$ the set of edges of \mathcal{T} . To discretize advection-diffusion problems on these triangular meshes, we suggest a combination of the approach of Kurganov and Petrova in [198] for the hyperbolic

part and the discretization of parabolic fluxes as by Eymard et al. in [105]. The use of equilateral triangles ensures the consistent discretization of the parabolic fluxes by evaluation in the centers of gravity.

This method-of-lines approach is completed by the forward Euler scheme in time. To this end let $t^0 := 0 < t^1 < \dots < t^K := T$ for $K \in \mathbb{N}$ be a partition of $(0, T)$ with time step $\Delta t^k = t^{k+1} - t^k$ for $k \in \{0, \dots, K-1\}$. All in all, one gets a scheme, which is first-order accurate in space and time.

Definition 6.4 (Finite volume method on a domain ω). For $k \in \{0, \dots, K-1\}$ and each triangle \mathcal{T} of the triangulation $\mathcal{T}_{\omega, \Delta x}$, the approximate cell average $u_{\mathcal{T}}^{k+1}$ at time t^{k+1} is computed by

$$u_{\mathcal{T}}^{k+1} = u_{\mathcal{T}}^k - \frac{\Delta t^k \Delta x}{|\mathcal{T}|} \sum_{\sigma \in \mathcal{S}(\mathcal{T})} F_{\sigma}^k. \quad (6.21)$$

If σ is the edge of another triangle $\mathcal{T}' \in \mathcal{T}_{\omega, \Delta x}$ the numerical flux F_{σ}^k is given by

$$F_{\sigma}^k := -\frac{P(u_{\mathcal{T}'}^k) - P(u_{\mathcal{T}}^k)}{\Delta x / \sqrt{3}} + \left(\frac{a_{\sigma}^{\text{in}} f(u_{\mathcal{T}'}^k) + a_{\sigma}^{\text{out}} f(u_{\mathcal{T}}^k)}{a_{\sigma}^{\text{in}} + a_{\sigma}^{\text{out}}} \right) \cdot \mathbf{n}_{\mathcal{T}} + \frac{a_{\sigma}^{\text{in}} a_{\sigma}^{\text{out}}}{a_{\sigma}^{\text{in}} + a_{\sigma}^{\text{out}}} (u_{\mathcal{T}'}^k - u_{\mathcal{T}}^k). \quad (6.22)$$

Here, $P = P(u)$ is a primitive of $p(u)$, and the numbers $a_{\sigma}^{\text{in}}, a_{\sigma}^{\text{out}} \geq 0$ are estimated local inward and outward directional wave speeds at the edge σ of \mathcal{T} , which has the outer normal $\mathbf{n}_{\mathcal{T}}$. For $\sigma \in \partial\omega \cap \partial\Omega$ the flux F_{σ}^k is determined from the boundary conditions (depending on specific settings in Section 6.6), whereas for $\sigma \in \partial\omega \cap \Gamma$ the flux F_{σ}^k is defined from the discrete transmission conditions (see (6.27) below). The initial approximation $u_{\mathcal{T}}^0$ is set as approximation of the cell average. For our first-order method, we use simply $u_{\mathcal{T}}^0 = u_0(\mathbf{x}_{\mathcal{T}})$, with $\mathbf{x}_{\mathcal{T}}$ denoting the barycenter of \mathcal{T} .

Note that these choices of a_{σ}^{in} and a_{σ}^{out} imply that the numerical algorithm from Definition 6.4 can be applied for any directional flux $\mathbf{f} \cdot \mathbf{n}_{\mathcal{T}}$ regardless of its derivative sign, see [198]. However, it recovers the upwind flux depending on the sign.

Due to the time-explicit approach, the size of the time-step Δt^k is limited by the Courant-Friedrichs-Lewy condition and the Péclet condition

$$\max \left\{ \left(\max_u |f_1'(u)| + \max_u |f_2'(u)| \right) \frac{\Delta t^k}{\Delta x}, \max_u p(u) \frac{2\Delta t^k}{\Delta x^2} \right\} \leq C_{\max}. \quad (6.23)$$

The constant $C_{\max} \leq 1$ depends on the mesh topology.

Having computed the cell-average values $u_{\mathcal{T}}^k$ on the mono-domain the discrete solution $u_{\Omega, \Delta x} \in L^2(\Omega \times (0, T))$ is defined as a piece-wise constant function by

$$u_{\Omega, \Delta x}(\mathbf{x}, t) = u_{\mathcal{T}}^k \quad \mathbf{x} \in \mathcal{T} \subset \mathcal{T}_{\Omega, \Delta x}, \quad t \in [t^k, t^{k+1}). \quad (6.24)$$

The finite-volume computations on the sub-domains Ω_1, Ω_2 have to be redone in

each iteration within the SWR algorithm. We denote for $i \in \mathbb{N}$ the corresponding cell-average values therefore by $u_{\mathcal{T}}^{i,k}$, the numerical fluxes by $F_{\sigma}^{i,k}$ and the discrete solution by $u_{\omega,\Delta x}^i \in L^2(\omega \times (0, T))$ with ω being one of the sub-domains Ω_1, Ω_2 . It is again computed from the cell averages, i.e.,

$$u_{\omega,\Delta x}^i(\mathbf{x}, t) = u_{\mathcal{T}}^{i,k} \quad \mathbf{x} \in \mathcal{T} \subset \mathcal{T}_{\omega,\Delta x}, t \in [t^k, t^{k+1}). \quad (6.25)$$

6.5.2. Discretization of the transmission condition

To complete the discrete SWR algorithm we need besides initial iterates a discrete version of the transmission condition (6.9) that provides the numerical flux in Definition 6.4 across some edge on Γ .

We assume that the meshes for $\Omega, \Omega_1, \Omega_2$ are designed such that the interface $\Gamma = \{0\} \times (-1, 1)$ between the sub-domains coincides with the edges of the triangles. To compute a numerical flux on Ω_1 (the case for the right sub-domain is completely analogous) consider a pair $(\mathcal{T}, \mathcal{T}') \subset \Omega_1 \times \Omega_2$ such that these two triangles share an edge σ which lies on Γ . Following Section 5.3, we search a ghost value $u_{\sigma,1}^{i,k}$ as approximation of the discrete solution in the triangle \mathcal{T}' on the other side of the edge σ . This value is used to compute the flux $F_{\sigma}^{i,k} = F_{\sigma,1}^{i,k}$.

Due to the transmission condition (6.9), in the i -th SWR iteration and at discrete time t^k , the discrete normal flux $F_{\sigma,1}^{i,k}$ associated to the triangle \mathcal{T} on this edge is then given by (6.22) as

$$\begin{aligned} F_{\sigma,1}^{i,k} := & -\frac{P(u_{\sigma,1}^{i,k}) - P(u_{\mathcal{T}}^{i,k})}{\Delta x / \sqrt{3}} + \left(\frac{a_{\sigma}^{\text{in}} f(u_{\sigma,1}^{i,k}) + a_{\sigma}^{\text{out}} f(u_{\mathcal{T}}^{i,k})}{a_{\sigma}^{\text{in}} + a_{\sigma}^{\text{out}}} \right) \cdot \mathbf{n}_{\mathcal{T}} \\ & + \frac{a_{\sigma}^{\text{in}} a_{\sigma}^{\text{out}}}{a_{\sigma}^{\text{in}} + a_{\sigma}^{\text{out}}} (u_{\sigma,1}^{i,k} - u_{\mathcal{T}}^{i,k}), \end{aligned} \quad (6.26)$$

such that $u_{\sigma,1}^{i,k}$ satisfies (see (6.9))

$$F_{\sigma,1}^{i,k} = \lambda(\beta_1 u_{\mathcal{T}}^{i,k} + (1 - \beta_1) u_{\sigma,1}^{i,k}) - \mathfrak{B}_{\sigma,1}^{i,k}. \quad (6.27)$$

Analogously, we compute $F_{\sigma,2}^{i,k}$ for Ω_2 , which leads us to determine $u_{\sigma,2}^{i,k}$ from

$$F_{\sigma,2}^{i,k} = \lambda(\beta_2 u_{\mathcal{T}'}^{i,k} + (1 - \beta_2) u_{\sigma,2}^{i,k}) - \mathfrak{B}_{\sigma,2}^{i,k}. \quad (6.28)$$

The weighting parameters β_1, β_2 in (6.27) and (6.28) are taken from the interval $[0, 1]$. They allow us to interpolate between the cell average and the ghost value at the interface, and they have no counterpart at the continuous level. In Chapter 5, we analyzed a simple linear model problem and showed that introducing the weighting parameters can be used to construct discrete SWR algorithms that are convergent for $\Delta x \rightarrow 0$ and $i \rightarrow \infty$, consistent for fixed Δx and $i \rightarrow \infty$, and asymptotic-preserving for vanishing viscosity (see Section 6.6.1 for precise defini-

tions). We cannot transfer the proofs to the nonlinear case here, but we will show in [Section 6.6](#) that the preferred choice from [Section 5.3](#) remains to be effective in our case.

We will use two choices for β_1, β_2 . The first one accounts for the local transport direction at the edge σ . It is considered to be a novel contribution for the treatment of advection-diffusion equations. Motivated by the analysis for a linear one-dimensional model problem in [Section 5.3](#) it is defined by

$$\beta_1 = \begin{cases} \frac{1}{2} & \mathbf{f}'(u_{\mathcal{T}}^{i,k}) \cdot \mathbf{n}_{\mathcal{T}} \geq 0, \\ 0 & \text{otherwise,} \end{cases} \quad \text{and} \quad \beta_2 = \begin{cases} \frac{1}{2} & \mathbf{f}'(u_{\mathcal{T}'}^{i,k}) \cdot \mathbf{n}_{\mathcal{T}'} \geq 0, \\ 0 & \text{otherwise.} \end{cases} \quad (\text{A})$$

Note that this first choice (A) realizes a switch between a centered approximation and a pure upwind one. In [Section 6.6.3](#) we will show that (A) behaves much better in the hyperbolic limit regime than the second choice, which is a pure centered approximation, typically used for diffusion equations (realizing a second-order discretization in space). It is given by

$$\beta_1 = \beta_2 = \frac{1}{2}. \quad (\text{B})$$

It remains to define $\mathfrak{B}_{\sigma,1}^{i,k}$ and $\mathfrak{B}_{\sigma,2}^{i,k}$ in (6.27) and (6.28). The value $\mathfrak{B}_{\sigma,1}^{i,k}$ is computed based on (6.9) from the previous SWR iteration using (6.26) and (6.27) with $u_{\mathcal{T}'}^{i-1,k}$ and $u_{\sigma,2}^{i-1,k}$ replacing $u_{\sigma,1}^{i,k}$ and $u_{\mathcal{T}}^{i,k}$. The analogous procedure provides $\mathfrak{B}_{\sigma,2}^{i,k}$. An alternative definition not used here exploits (6.12) leading for Ω_1 to $\mathfrak{B}_{\sigma,1}^{i,k} := \lambda((1 + \beta_1 - \beta_2)u_{\sigma,2}^{i-1,k} + (1 - \beta_1 + \beta_2)u_{\mathcal{T}'}^{i-1,k}) - \mathfrak{B}_{\sigma,2}^{i-1,k}$. Finally, the initial guesses g_l for $l \in \{1, 2\}$ in all considered cases are chosen as discrete approximations of $\mathfrak{B}_l(u_0)$ using (6.9).

Even though the time stepping in the scheme from [Definition 6.4](#) is explicit, the unknowns $u_{\sigma,l}^{i,k}$ for $l \in \{1, 2\}$ at the interface have to be determined from the generally nonlinear equations (6.26) and (6.27). We use a damped Newton method, and emphasize that only a local Newton iteration for each triangle at the interface has to be performed.

6.6. Numerical results

First, we consider a simple problem with known closed-form solution to study both the convergence properties of the discretization and the iterative solver. We then study the performance of the solver on the two-phase flow equation for the saturated flow of two immiscible and incompressible fluids. In particular, we are interested in the behavior of the SWR algorithm for advection-dominated flow and in the role of the transmission parameter λ and the weighting parameters β_1, β_2 in the transmission conditions.

Before we start with some preliminaries on error measurement and associated notations let us note that various non-overlapping domain decomposition approaches have been developed in the context of two-phase flow. Ahmed et al. have studied a-posteriori error estimates and stopping criteria based on space-time domain decomposition for two-phase flow between different rock types in [6, 7]. Seus et al. proposed robust linear domain decomposition methods of the time-discrete equations for partially saturated flow as well as for two-phase flow in porous media in [285, 286]. This was extended in [219] by Lunowa et al. for two-phase flow in porous media involving dynamic capillarity and hysteresis, see Chapter 4. For domain decomposition strategies used as preconditioners for solving multi-phase flow problems we refer to [292].

6.6.1. Error functionals and notations

We introduce some notations for measuring different kinds of errors. Precisely, we use two functionals: for studying the convergence of the iterative algorithm, we fix the mesh parameter Δx and use the mono-domain finite volume solution $u_{\Omega, \Delta x}$ from (6.24). We define the *iteration space-time L^2 -error* $\mathcal{E}_{\Delta x}^i$ given by

$$\mathcal{E}_{\Delta x}^i := \sqrt{\sum_{l=1}^2 \left\| u_{\Omega_l, \Delta x}^i - u_{\Omega, \Delta x} \right\|_{L^2(\Omega_l \times (0, T))}^2}. \quad (6.29)$$

It controls the distance between the discrete SWR iterates on the sub-domains Ω_1 , Ω_2 and the discrete mono-domain solution on Ω . The SWR algorithm is *consistent* with respect to iterations if $\mathcal{E}_{\Delta x}^i \rightarrow 0$ holds for $i \rightarrow \infty$. The SWR algorithm is *asymptotic-preserving* in the limit of vanishing viscosity, if it converges then in a finite number of iterations, i.e., there holds $\mathcal{E}_{\Delta x}^i = 0$ for all $i > i_0 \in \mathbb{N}$ when $p \equiv 0$. This means, that the limit SWR algorithm behaves as expected of domain decomposition methods for hyperbolic PDEs, for details on this issue see Chapter 5.

If the exact solution u is available we also consider the difference between the SWR iterates $u_{\Omega_l, \Delta x}^i$ (see (6.25)) and the exact solution u leading to the combined *iteration and discretization space-time L^2 -error* $\tilde{\mathcal{E}}_{\Delta x}^i$ defined by

$$\tilde{\mathcal{E}}_{\Delta x}^i := \sqrt{\sum_{l=1}^2 \left\| u_{\Omega_l, \Delta x}^i - u \right\|_{L^2(\Omega_l \times (0, T))}^2}. \quad (6.30)$$

If $\tilde{\mathcal{E}}_{\Delta x}^i \rightarrow 0$ for $\Delta x \rightarrow 0$, $i \rightarrow \infty$ the SWR algorithm *converges* to u .

Besides the behavior of $\mathcal{E}_{\Delta x}^i$ and $\tilde{\mathcal{E}}_{\Delta x}^i$ for $\Delta x \rightarrow 0$ and $i \rightarrow \infty$ we will also investigate how the limit behavior of the SWR algorithm depends on the transmission parameter λ .

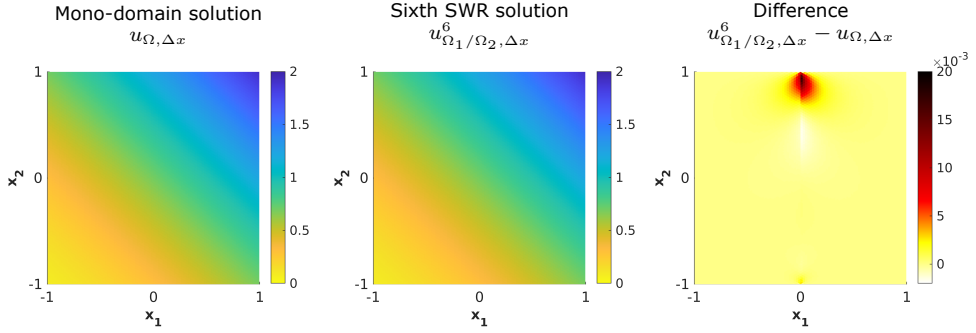


Figure 6.1.: The numerical mono-domain solution (*left*) and the SWR solution at the sixth iteration (*middle*) are hardly distinguishable from each other for the smooth example at $t = 2$ using $\Delta x = 0.025$ and $\lambda = 1.5$. In fact, the errors are concentrated almost entirely at the interface (*right*).

6.6.2. A problem with known solution

The function

$$u(\mathbf{x}, t) = \frac{(3 + x_1 + x_2)^2}{25 - 6t}$$

solves the nonlinear advection-diffusion equation

$$\partial_t u + \nabla \cdot (\mathbf{v} u^2) - \nabla \cdot (u \nabla u) = 0 \quad \text{in } \Omega \times (0, T) := (-1, 1)^2 \times (0, 2),$$

where the velocity $\mathbf{v} = \mathbf{v}(\mathbf{x})$ is given by $\mathbf{v}(\mathbf{x}) = \frac{1}{3+x_1+x_2}(1, 1)^T$. The problem is completed by Dirichlet boundary conditions and an initial condition given by evaluating u on $\partial\Omega$ and at $t = 0$. Note that [Assumption 6.1](#) is satisfied, as discussed there, because the solution satisfies $0 < u_{\min} \leq u \leq u_{\max} < \infty$ almost everywhere.

We choose the temporal step-size $\Delta t = (\Delta x)^2/25$, which suffices in this case to satisfy (6.23), and the SWR transmission parameter $\lambda = 1.5$. The plots in [Fig. 6.1](#) show the results of the finite volume method on the mono-domain Ω and of the SWR algorithm with parameter choice (A), where we have chosen the sixth iteration with $\Delta x = 0.025$ at time $t = 2$. Clearly, the error is concentrated at the interface Γ , especially where the flux across the interface is large.

In [Fig. 6.2](#) we see on the left that the iteration L^2 -error $\mathcal{E}_{\Delta x}^i$ from (6.29) decreases monotonically for versions (A) and (B), suggesting that the SWR algorithm is consistent for both choices of the weighting parameters. Note that our convergence analysis does not predict a monotonic behavior. The fact that the convergence does not seem to depend on the spatial step-size is because we start the iteration by extending the initial condition constant in time, and the solution and thus the iterations do not really have any high frequency content. Using a random initial guess would lead to different behavior, see [119] for linear problems with con-

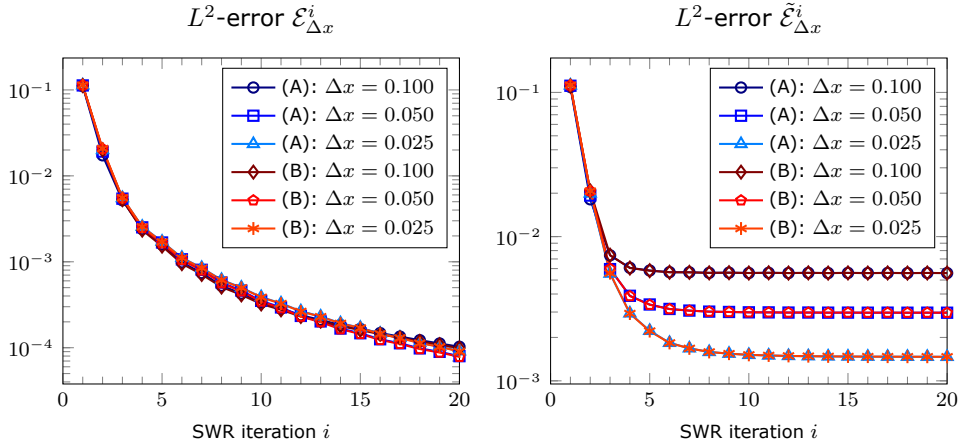


Figure 6.2.: Error decay for the different spatial resolutions in the example with known solution using $\lambda = 1.5$ and both choices (A) and (B). *Left*: the iteration L^2 -error $\mathcal{E}_{\Delta x}^i$ decreases monotonically. *Right*: the combined iteration and discretization L^2 -error $\tilde{\mathcal{E}}_{\Delta x}^i$ also decreases monotonically until the discretization error level is reached after a few iterations.

stant coefficients, where mesh dependence is observed, and [114, Sec. 5.1] for a detailed explanation.

Since we know the exact solution in this case, we can also compute the combined discretization and iteration L^2 -error $\tilde{\mathcal{E}}_{\Delta x}^i$ from (6.30). As shown in Fig. 6.2 on the right, we observe that $\tilde{\mathcal{E}}_{\Delta x}^i \rightarrow 0$ for $\Delta x \rightarrow 0$ and $i \rightarrow \infty$ supporting the convergence statement of Theorem 6.3. We observe for fixed mesh parameter again a monotone decay of $\tilde{\mathcal{E}}_{\Delta x}^i$ over the SWR iterations. After about 3–5 iterations, the discretization error clearly dominates and we observe stagnation of the combined discretization and iteration error. The discretization error is approximately reduced by a factor of two when halving the spatial step-size Δx , as expected for a first order scheme. Again versions (A) and (B) do not differ substantially.

Let us fix the spatial step-size to $\Delta x = 0.05$ and use the choice (A) only. To study the effect of the transmission parameter, we apply the SWR iteration for different choices of the transmission parameter λ . The impact on the convergence rate is clearly visible from the results shown in Fig. 6.3. On the left, we see that an optimal choice of λ exists which leads to fastest convergence of the SWR iteration for the specific frequency content in the solution. We also see that after a certain number of iterations the slopes of the convergence curves become similar, and in that regime typically very high or very low frequency error components dominate. On the right we see that the truncation error accuracy is however reached much earlier, so a good choice is indeed $\lambda = 1.5$ for this problem.

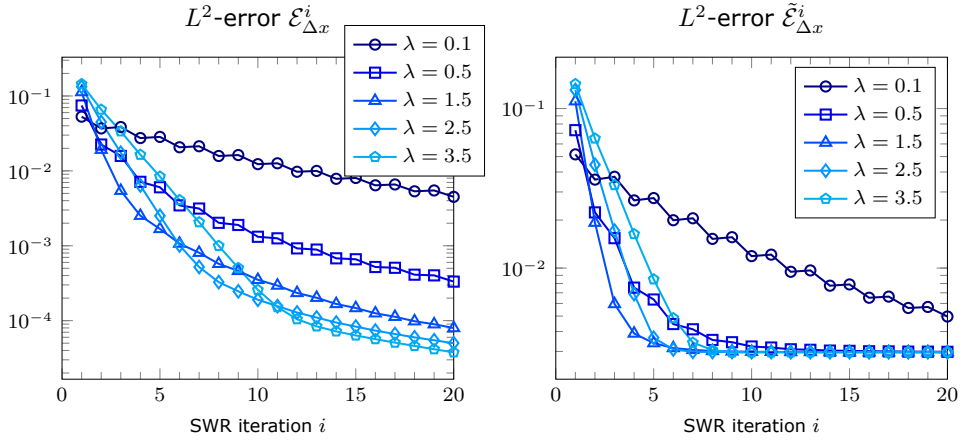


Figure 6.3.: Error decay over the number of SWR iterations for different transmission parameters λ in the example with exact solution using $\Delta x = 0.05$ and the choice (A). *Left:* iteration L^2 -error $\mathcal{E}_{\Delta x}^i$. *Right:* combined discretization and iteration L^2 -error $\tilde{\mathcal{E}}_{\Delta x}^i$.

6.6.3. Simplified two-phase flow with capillary pressure

We consider a nonlinear advection-diffusion equation that is used to model the incompressible flow of two immiscible fluids in a porous medium, such as the displacement of oil by water in a reservoir. This model is discussed in [Section 1.3.2](#). We assume the total velocity $\mathbf{v} : \Omega \rightarrow \mathbb{R}^d$ to be given. Neglecting gravitational effects, (1.13) then reads

$$\phi \partial_t u + \nabla \cdot (f_{BL}(u) \mathbf{v}) + \nabla \cdot (\kappa(u) \mathbf{K} \nabla p_c(u)) = 0 \quad \text{in } \Omega \times (0, T). \quad (6.31)$$

The saturation $u = u(\mathbf{x}, t) \in [0, 1]$ is the unknown, whereas the porosity $\phi \in (0, 1]$, the fractional flux function $f_{BL} : [0, 1] \rightarrow \mathbb{R}$, the total mobility $\kappa : [0, 1] \rightarrow (0, \infty)$, the homogeneous intrinsic permeability $\mathbf{K} \in \mathbb{R}^{d \times d}$ and the capillary pressure $p_c : [0, 1] \rightarrow \mathbb{R}$ are given functions. For our numerical studies, we simply choose the domain $\Omega := (-1, 1)^2$, the final time $T = 1$, as well as a constant porosity $\phi = 1$ and a constant flow velocity $\mathbf{v} = (v_1, v_2)^T \in \mathbb{R}^2$. The constant intrinsic permeability \mathbf{K} is set to be the identity matrix, and a standard parameterization of the fractional flux function is

$$f_{BL}(u) = \frac{u^2}{u^2 + (1 - u)^2}.$$

For $\kappa \equiv 0$, (6.31) becomes the so-called Buckley–Leverett equation which is a purely hyperbolic conservation law exhibiting weak discontinuous solutions.

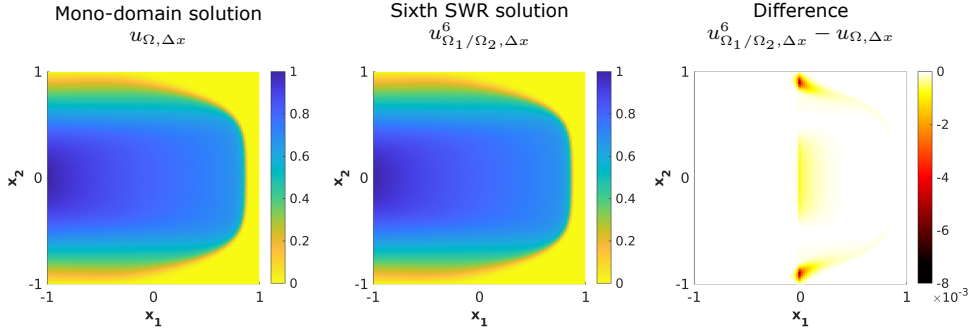


Figure 6.4.: Discrete mono-domain solution (*left*) and SWR solutions at the sixth iteration (*middle*) for the simplified two-phase flow equation for $\kappa = 10^{-2}$, $\mathbf{v} = (1.5, 0)^T$ at time $t = 1$ using $\Delta x = 0.025$, $\lambda = 2$ and weighting parameters from (A). The errors are concentrated almost entirely at the interface Γ and along the infiltration front (*right*).

Diffusion-dominated regimes

We consider a simplified setting with linear capillary pressure, $p_c(u) = 1 - u$. The problem is completed with the initial condition $u_0 \equiv 0$ and the Dirichlet boundary condition given for $\mathbf{x} \in \partial\Omega$ and $t \in [0, 1]$ by

$$u(\mathbf{x}, t) = \begin{cases} 1 - x_2^2 & \text{if } x_1 = -1, \\ 0 & \text{if } x_1 = 1 \text{ or } x_2 = \pm 1. \end{cases}$$

Thus, the solution of (6.31) will display a right-moving infiltration front as long as the velocity components satisfy $v_1 > v_2 \equiv 0$. In fact, this will be our choice in all subsequent experiments. As an internal layer the front will scale according to the size of the mobility parameter κ , which is taken constant. For the sake of illustration we show in Fig. 6.4 the results of a mono-domain computation and the sixth iteration of the SWR algorithm at the final time $t = 1$. Clearly, the difference of these discrete solutions prevails at the interface Γ and the infiltration front. Since the flow direction is from left to right, the errors occur almost entirely in the second sub-domain.

Turning to quantitative tests of the SWR algorithm we consider in this section examples which can include advection but are still diffusion-dominated. Since explicit solutions for (6.31) are not available we study the iteration L^2 -error $\mathcal{E}_{\Delta x}^i$ only. In the first example, condition (6.23) is satisfied by choosing the time step-size $\Delta t^k = \Delta x^2/20$. The SWR transmission parameter is fixed to be $\lambda = 2$. In Fig. 6.5 we show the results for a fixed mobility $\kappa = 1$ varying the velocity v_1 in x_1 -direction for different mesh resolutions. As a purely diffusive reference case we consider $v_1 = 0$ such that (6.31) becomes the heat equation (see also the results in Section 6.6.3 for the opposite limit case: the Buckley–Leverett equation). For all mesh

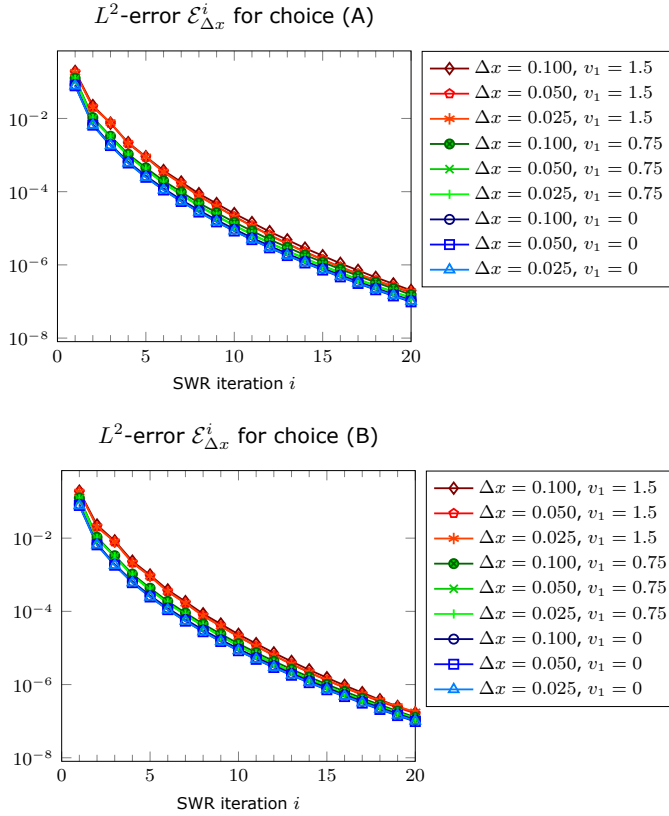


Figure 6.5.: The iteration L^2 -error versus the number of SWR iterations for different spatial resolutions and different velocities $\mathbf{v} = (v_1, 0)^T$. The mobility is always $\kappa = 1$.

parameters we observe that the iteration error $\mathcal{E}_{\Delta x}^i$ decreases monotonically in i . Moreover, the differences between the weighting parameter choices (A) and (B) is negligible.

Next, we study again the impact of the transmission parameter. We set $\Delta x = 0.05$ or $\Delta x = 0.025$ and $\Delta t^k = \Delta x/20$, and apply the SWR iteration with different choices of the transmission parameter λ , with $\mathbf{v} = (1.5, 0)^T$ and $\kappa = 10^{-2}$, i.e., a more advection-dominated regime which triggers a step-like behavior for the evolution of $\mathcal{E}_{\Delta x}^i$. This results from the parallel formulation (6.8) of the SWR algorithm for two subdomains yielding iterates that differ significantly only every second iteration due to the main information transfer from the left to the right subdomain in the advection-dominated regime. The effect of the transmission parameter on the convergence rate is clearly visible from the results shown in Fig. 6.6, the best choice here being around $\lambda = 1.5$. We also observe that the weighting choice (B) is not equivalent in the present discretization when advection becomes dominant

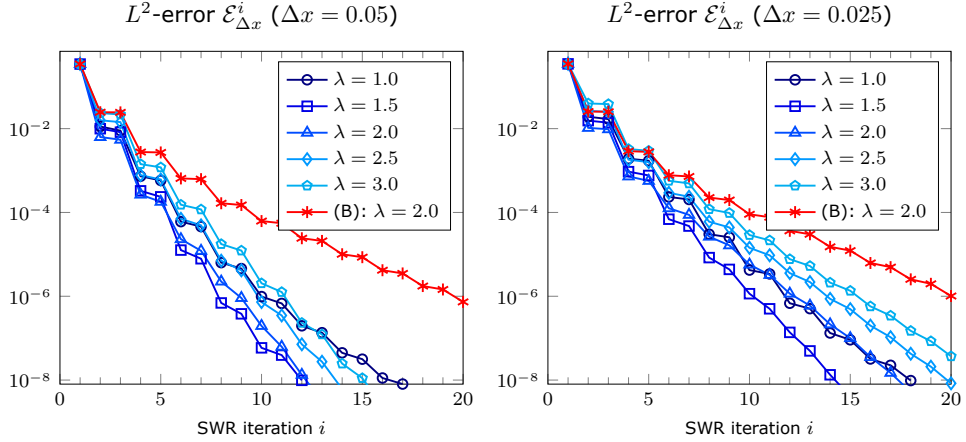


Figure 6.6.: The decay of the L^2 -error over the number of SWR iterations varies for different transmission parameters λ for the simplified two-phase flow equation with $\Delta x = 0.05$ and $\Delta x = 0.025$ using the choice (A). The optimum $\lambda \approx 1.5$ seems to be independent of the step-size for this initial guess.

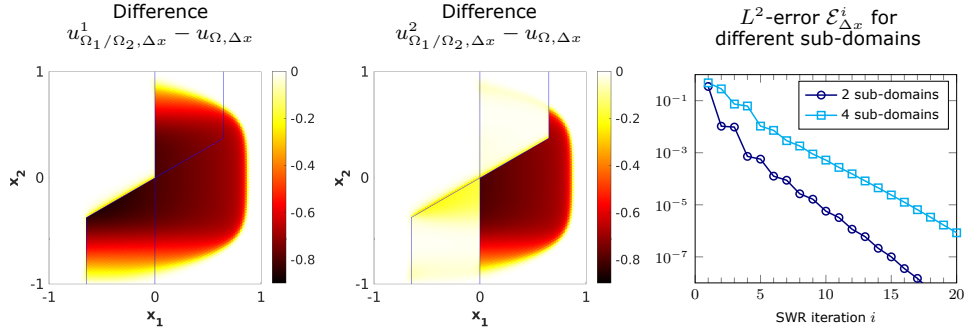


Figure 6.7.: The discrete difference at the first (*left*) and second (*middle*) iteration for four sub-domains in the case of the simplified two-phase flow equation ($\kappa = 10^{-2}$, $\mathbf{v} = (1.5, 0)^T$, $t = 1$, $\Delta x = 0.025$, $\lambda = 2$, weighting (A)). The interfaces are shown in blue. The L^2 -error decays linearly, but slightly slower compared to the case of only two sub-domains (*right*).

(see e.g. (B): $\lambda = 2$ in Fig. 6.6), because it remains a Robin transmission condition, while choice (A) effectively leads to a Dirichlet update in the hyperbolic limit $\kappa \rightarrow 0$, cf. Chapter 5.

Furthermore, we study the numerical scheme for a decomposition into multiple sub-domains, see Fig. 6.7. As in the case of two sub-domains, the discrete difference, and hence the iteration L^2 -error $\mathcal{E}_{\Delta x}^i$ is reduced in a step-like manner in the first few iterations, and shows linear convergence, but at a slightly lower rate compared to the case of only two sub-domains.

From advection-dominated regimes to the hyperbolic limit

We investigate the SWR algorithm for the same infiltration setting as presented in [Section 6.6.3](#) but fixing $\mathbf{v} = (1.5, 0)^T$ and focusing on decreasing values of the total mobility κ . If the mesh parameter Δx is kept constant for advection-dominated regimes one enters under-resolved situations. Note that the finite-volume scheme from [Definition 6.4](#) remains even then stable due to the upwind flux choice [\[198\]](#). However, it is not able to resolve (internal and boundary) layers scaling like $\mathcal{O}(\kappa)$. In the limit $\kappa \rightarrow 0$, equation [\(6.31\)](#) becomes a purely hyperbolic evolution law with discontinuous weak solutions. Notably, the sub-domain problems of the SWR algorithm given by [Definition 6.2](#) are not well-defined in the hyperbolic limit, i.e., the Robin boundary condition [\(6.8\)](#) and [\(6.9\)](#) involve Neumann traces that might not exist. Nevertheless, the discrete formulation by [Definition 6.4](#) together with [\(6.26\)](#) and [\(6.27\)](#) can still be executed.

Remark 6.2 (SWR algorithm for the hyperbolic limit, choice of λ , β_1 and β_2). For the case $\kappa = 0$ the SWR algorithm using Dirichlet transmission conditions gives the mono-domain solution on Ω in finitely many steps, for the unidirectional flux in [\(6.31\)](#) in fact in two steps only. Using Robin transmission conditions as in [\(6.27\)](#) requires further conditions for this property to hold, see [Chapter 5](#): in the linear case, the algorithm is asymptotic-preserving iff the parameters β_1, β_2 are chosen to satisfy $\kappa/\beta_1(\kappa) = o(1)$ and $\beta_2(\kappa) = \mathcal{O}(\kappa)$ as $\kappa \rightarrow 0$. Since this condition is independent of λ , we expect similar behavior here, and illustrate this below. Note that choice [\(A\)](#) satisfies the conditions but not [\(B\)](#).

We consider the advection-dominated regime for $\kappa \in (0, 10^{-2}]$ and set $\Delta x = 0.025$ and $\Delta t^k = \Delta x/20$. All other settings are as in [Section 6.6.3](#). In [Fig. 6.8](#) we show the L^2 -errors $\mathcal{E}_{\Delta x}^i$ for weighting parameters from [\(A\)](#). As in [Section 6.6.3](#) we observe linear convergence, which gets faster as κ becomes smaller, until we get two-step convergence for $\kappa = 0$ ($\mathcal{E}_{\Delta x}^2 < 10^{-12}$) independently of the value of the transmission parameter. This is also in agreement with the analysis for linear problems, see [Remark 6.2](#). We note in passing that using the alternative determination of $\mathfrak{B}_{\sigma, 1/2}^{i,k}$ using [\(6.12\)](#) shows also decaying behavior but requires four iterations in the limit.

On the right in [Fig. 6.8](#) we show the results for the transmission condition update [\(B\)](#), which clearly is not equivalent to [\(A\)](#) in the present discretization, see the discussion in the previous subsection: the choice [\(B\)](#) is not asymptotic-preserving.

6.6.4. Two-phase flow with strongly nonlinear capillary pressure

As a concluding example we consider the two-phase flow equation [\(6.31\)](#), together with the Brooks–Corey model [\[156\]](#),

$$\kappa(u) = \frac{u^2(1-u)^2}{u^2 + (1-u)^2}, \quad p_c(u) = p_d u^{-\frac{1}{\lambda_{BC}}}.$$

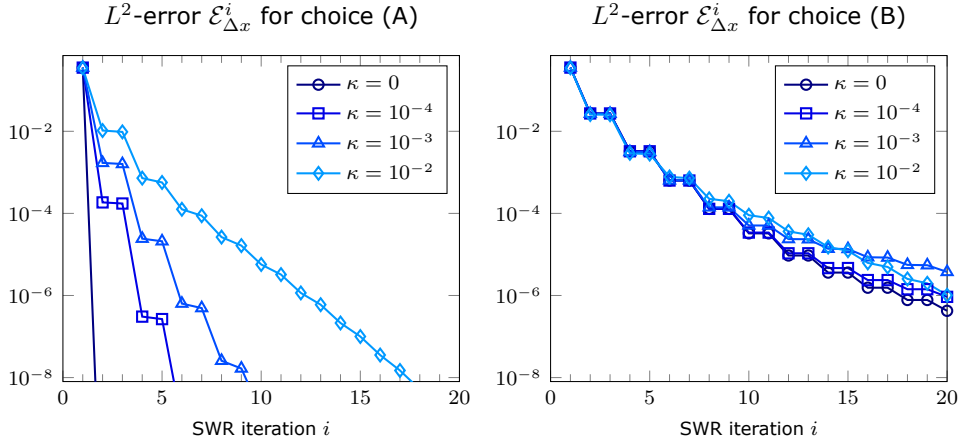


Figure 6.8.: The L^2 -errors $\mathcal{E}_{\Delta x}^i$ for $\lambda = 2$ and step-size $\Delta x = 0.025$. *Left:* For the choice (A), the rate of decay of $\mathcal{E}_{\Delta x}^i$ over the number of SWR iterations depends on total mobility κ strongly improving when κ decreases. *Right:* For the choice (B), the rate of decay does not improve to finite-step convergence in the hyperbolic limit when $\kappa \rightarrow 0$.

Here $p_d > 0$ is the so-called entry pressure, i.e., the minimal pressure necessary for the non-wetting phase to displace the wetting phase, and $\lambda_{BC} > 0$ describes the uniformity of the porous medium. We choose the parameters $p_d = 1$ and $\lambda_{BC} = 3$ and the initial condition $u_0 = 0.1$ together with homogeneous Neumann boundary conditions at $x_2 = \pm 1$, and Dirichlet boundary conditions at $x_1 = \pm 1$ given by

$$u(x, t) = \begin{cases} 0.1 + 0.8(1 - x_2^2)^2 & \text{if } x_1 = -1, \\ 0.1 & \text{if } x_1 = 1. \end{cases}$$

For the numerical computations of this completely nonlinear infiltration problem, we select the temporal step-size $\Delta t = (\Delta x)^2/4$ and the SWR transmission parameter $\lambda = 2$. According to the results from Section 6.6.3 we use choice (A) only. The plots in Fig. 6.9 show the results with and without the SWR algorithm for the sixth SWR iteration and $\Delta x = 0.025$ at time $t = 1$. Also for this strongly nonlinear problem, the error is concentrated at the interface Γ and in Ω_2 , since the flow direction is from left to right. The error decreases monotonically over the SWR iterations, as shown in Fig. 6.10.

6.7. Conclusion

We designed and analyzed a new non-overlapping Schwarz waveform-relaxation algorithm for nonlinear advection-diffusion equations using nonlinear Robin transmission conditions. We proved existence of a unique sequence of weak solutions

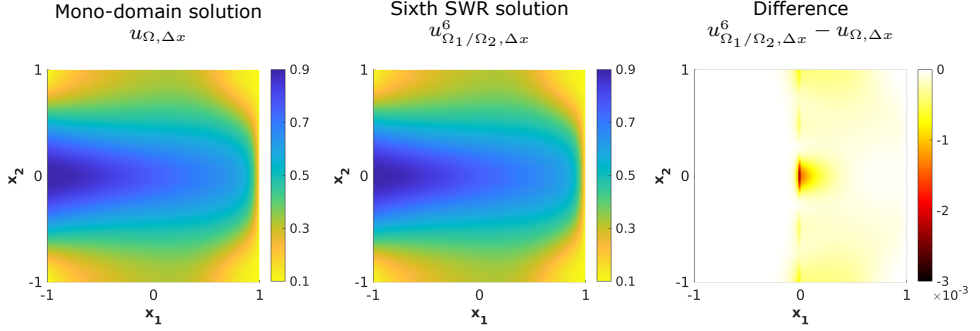


Figure 6.9.: The numerical mono-domain solution (*left*) and the SWR solution at the sixth iteration (*middle*) are hardly distinguishable from each other for the two-phase flow equation with Brooks-Corey parameterization at $t = 1$ using $\Delta x = 0.025$. Differences can be observed mostly at the interface Γ but less for the wave-front position (*right*).

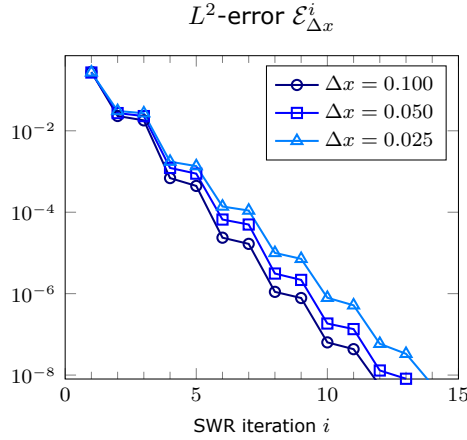


Figure 6.10.: The L^2 -error $\mathcal{E}_{\Delta x}^i$ decreases monotonically over the number of SWR iterations for the different spatial resolutions for the two-phase flow equation with Brooks-Corey parameterization with $\lambda = 2.5$.

that converges under the assumption of bounded gradients, extending the area of application of Schwarz waveform-relaxation to a whole new class of nonlinear problems. We also presented a fully-discrete finite volume scheme which is asymptotic-preserving for the Robin transmission conditions and hence robust in the hyperbolic limit leading to two-step convergence of the iterative solver. We tested our new solver on several examples ranging from validation models to strongly nonlinear porous media flow problems. We observed linear convergence towards the discrete solution, and robust two-step convergence in the hyperbolic limit. We also made preliminary numerical tests for the impact of the transmission parameter λ on the convergence rate, for which we do not yet have a theoretical basis.

Conclusion and outlook

In this work, we considered dynamic capillarity and hysteresis in two-phase flow in porous media. The work is divided in two parts according to the studied scales and effects. In the first part, we discussed the modeling at the pore scale incorporating a moving contact line, and the subsequent upscaling. In particular, the resulting up-scaled models for single pores include a dynamic and hysteretic capillary pressure, which plays an important role at the Darcy scale. Such non-equilibrium effects were discussed in the second part of this work, where we focused on robust numerical discretization techniques at the Darcy scale. In detail, we considered linearization and domain decomposition methods for nonlinear parabolic partial differential equations which may degenerate. In the following, we summarize the main results of the respective parts and give an outlook to future work and remaining open challenges.

7.1. Two-Phase Flow in Single Pores

In the first part, we considered a mathematical model for the flow of two immiscible fluids in a single pore, which is idealized to a thin strip or tube. The fluids are separated by a moving interface, which is in contact with the pore wall. Its evolution is driven by the fluid flow, the surface tension and a dynamic and possibly hysteretic contact-angle law at the moving contact line. Assuming a scale separation between the typical width and the length of the thin pore, we formally derived the transversally averaged model. The resulting effective relations are a Darcy-type equation for the local flow, and a capillary pressure - saturation relationship involving dynamic and hysteretic effects. Together, the model forms a system of differential algebraic equations for the interface position and the total flux.

We provided numerical experiments and discussed the effects of a varying pore width, of the viscosity ratio, of the slip length, as well as of having a dynamic and a hysteretic contact-angle law. In particular, the results for a varying pore width

illustrate that the geometry has a large influence on the effective quantities and their behavior. While dynamic effects occur even for a static contact-angle model, hysteresis in the capillary pressure is only present when a hysteretic contact-angle model is used.

To validate the effective model, we compared it to experiments of the capillary rise of different fluids in cylindrical tubes. In this application, the effective model extends the classical Lucas–Washburn model by incorporating a dynamic contact angle and slippage. Furthermore, we extended the model to account for inertial effects, which can be relevant at early times. In contrast to the classical Lucas–Washburn model, the numerical results of the models with dynamic contact angle match well with the experimental data. In summary, we showed that the presented models predict the capillary-driven flow in tubular systems and that the dynamic contact-angle relation must be explicitly included.

The discussed upscaling in thin pores may be generalized in various directions. First of all, more complicated geometries may be considered. Pores in realistic situations are often asymmetric and tortuous. Then, the flow is not unidirectional any more, but follows the curve of the pore. Additionally, the cross-section can have arbitrary shape, which results in a non-spherical fluid-fluid interface. These aspects could be incorporated by an appropriate formulation of the geometrical features. In this context, also wall roughness should be mentioned. The upscaling in this work relies essentially on the fact that the pore walls are smooth and slowly varying. However, when kinks are present, the contact line is pinned at the kink while the interface adapts to the change in the contact angle. Furthermore, the fluid flow at such points is perturbed. In case of fast variations of the pore wall, the dynamics of the contact line, as well as the topology may change. This occurs in particular when the movement of the fluid-fluid interface leads to attachment at several positions of the wall, and thus small drops of the wetting phase remain trapped between the non-wetting fluid and the oscillatory wall. Moreover, accounting for multiple pores, which might even bifurcate, requires the detailed modeling of topological changes when the fluid-fluid interface separates at the junction, or reversely, when several interfaces from different pores unite at the junction. For such local perturbation effects, and topological changes, an diffuse interface approach, e.g. a phase-field model [1, 257], might be successfully applied. In a preceding step, the effect of multiple, separated interfaces may be studied as a rather straightforward extension, as outlined in [Section 7.3](#) for a pore-network model.

Furthermore, the modeling of the contact angle provides various opportunities for future work. As discussed in the introduction, several descriptions of the moving contact line and of the contact angle exist in literature. Due to the technically difficult measurements and the minor differences when compared to the models, there is no consensus about which one is preferable. Nevertheless, the presented upscaling results are valid as long as there is a unique velocity to contact-angle

relation. Additionally, the surface tension of many materials is inhomogeneous, e.g. for minerals with heterogeneous chemical composition, and may be altered over time due to reactions, such as precipitation and dissolution, or because of surfactants. Then, these additional processes must be modeled and coupled to the flow of the fluid phases. All these aspects require an extension of the presented analysis and might lead to upscaled equations that give further insight for pore-scale two-phase flow in natural porous media.

Moreover, the derivation of upscaled models in this work was done formally. Rigorous estimates of the convergence, and ideally even error estimates for the upscaling are still necessary to prove the correctness of the approach. However, this requires a detailed mathematical analysis of the coupling of the Navier–Stokes equations for two fluids with a free boundary, which is in contact with the pore wall. Another approach is the comparison of the solutions of the upscaled one-dimensional model to numerical solutions of the full two- or three-dimensional model with moving interface. Eventually, comparison to further, more general experiments in tubular structures is necessary to assess the correspondence between the modeling, including its assumptions, and the empirically observable reality.

Finally, there is a scale gap between the modeling of single pores and the desired description of two-phase flow at the Darcy scale. Therefore, modeling and upscaling at an intermediate scale is necessary. For this, simple bundle-of-tubes models, or more intricate dynamic pore-network models can be used. In the end of this chapter, we elaborate on this topic, which is ongoing work. In particular, we propose a dynamic pore-network model, in which the effective models derived in [Chapter 2](#) are used in the pore throats. The effective Darcy-scale quantities can then be found by averaging the solutions over representative volumes of the network.

7.2. Numerical Methods at the Darcy Scale

The second part of this work is dedicated to numerical methods for partial differential equations at the Darcy scale. The main focus was on linearization and domain decomposition methods for non-equilibrium two-phase flow models in porous media and for nonlinear, possibly degenerate advection-diffusion equations.

First, we considered the two-phase flow equations in a porous medium, which consists of adjacent regions with possibly different parametrizations. The model accounts for non-equilibrium effects like dynamic capillarity and hysteresis. After temporal discretization, we proposed two linearized domain decomposition schemes, which combine a stabilizing fixed-point iteration, the L-scheme, and a non-overlapping domain decomposition into one iteration. We proved that the linear iterative problems of the two schemes have unique solutions, which converge towards the solution of the time-discrete, nonlinear equations on the whole domain.

This convergence is global, i.e., independent of the initial guess, and requires only a mild restriction on the time step, independently of the spatial discretization. Due to the L-scheme, the use of derivatives as in Newton or Picard iterations is avoided. The presented numerical examples confirm stability and robustness of both developed schemes. In particular, the inverted formulation for the capillary pressure used for the second scheme considerably improves the performance for models including hysteresis.

Both schemes can be easily implemented for realistic applications. For appropriately chosen parameters, the convergence rate is improved significantly. The presented analysis leads to good estimates for the linearization parameters, while an estimate for the domain decomposition parameter is still an open problem. Furthermore, an optimized choice of these parameters could depend on the position and the current solution, leading to similar methods as in [12, 236]. Alternatively, these schemes can be combined with Anderson acceleration [174, 211], or might be used as preconditioners for the Newton method. Moreover, an a-posteriori error analysis similar to [6] would lead to efficient and adaptive stopping criteria, which increase the performance and allow for adaptivity.

For more general applications, the schemes should be adapted and analyzed when porosity or dynamic capillarity and hysteresis are spatially varying. Furthermore, the involved coefficients in general also depend on the saturation. Typically used parametrizations, such as the Brooks–Corey model, are only Hölder-continuous, which could be incorporated similar to the analysis in [48, 262]. Moreover, the case of vanishing phase-mobility typically occurs when a fluid saturation tends to zero. The resulting degeneration of the equations must be taken into account by e.g. using a global pressure formulation. Additionally, nonlinear interface conditions for entry-pressure models between different porous media should include the effect of dynamic and hysteretic capillarity [157, 158, 310]. Subsequently, such conditions can be incorporated into numerical schemes.

Since the equations may degenerate in realistic applications, we also considered singularly perturbed advection-diffusion problems. We analyzed in detail a non-overlapping domain decomposition method with Robin transmission conditions for the linear stationary advection-diffusion equation in one dimension. We found a significant difference between the domain decomposition method on the continuous level and on the discrete level using cell-centered finite volumes. In the limit of vanishing diffusion, the continuous method converges in finite iterations only if the transmission parameter tends to the advection speed. The discrete method can inherit this property. However, using a proper, but asymmetric choice of centered and upwind discretizations in the Robin transmission conditions, we obtained an asymptotic-preserving discrete method without constraint on the transmission parameter. We illustrated the theoretical results by numerical examples in one and two spatial dimensions.

Based on these results, we proposed a non-overlapping domain decomposition algorithm of Schwarz waveform-relaxation type for nonlinear advection-diffusion equations. It relies on nonlinear Robin transmission conditions that ensure the continuity of the converged solution and of its normal flux across the interface. We proved the existence of weak solutions to the iterative problems, which are unique under additional assumptions on the data. Furthermore, we showed that the iterative solutions converge under the assumption of bounded gradients. Thereby, we extended the area of application of Schwarz waveform-relaxation to a whole class of nonlinear problems.

Moreover, we presented a simple numerical discretization for the iterative problems using a forward Euler discretization in time and a finite volume method in space. Therefore, only the transmission conditions require a local nonlinear solver. This discrete algorithm uses the asymptotic-preserving Robin transmission conditions, and thus is robust in the hyperbolic limit leading to two-step convergence of the iterative solver. Finally, we presented several numerical examples ranging from validation models to strongly nonlinear two-phase flow problems in porous media. In particular, we observed linear convergence towards the discrete solution, and robust two-step convergence in the hyperbolic limit.

We also made preliminary numerical tests for the impact of the transmission parameter on the convergence rate, for which there is no theoretical basis yet. The analysis of the parameter optimization, as well as the asymptotic-preserving property for nonlinear, time-dependent problems, possibly also incorporating reaction terms, remains an open challenge. This would lay a solid foundation for the application to degenerate multi-phase and multi-component flow in porous media. Combined with a-posteriori error analysis and adaptivity, the simulation results could be improved while keeping the computational costs low. For this purpose, also multilevel domain decomposition methods, moving meshes and optimized preconditioners are relevant, and should be considered.

7.3. Ongoing work on dynamic pore-network models

To overcome the scale gap between the modeling of single pores and the desired description of two-phase flow at the Darcy scale, we discuss dynamic pore-network models and show how the effective models derived in [Chapter 2](#) can be incorporated to model the flow in the pore throats. For a general introduction to pore-network modeling, we refer to the reviews [\[2, 44, 178, 267\]](#).

The fundamental idea of pore-network models is to represent the complicated geometry at the pore scale by a set of pore bodies $\mathcal{P} \subset \mathbb{N}$ at the positions $\mathbf{x}_i \in \mathbb{R}^3$ [m], $i \in \mathcal{P}$, which are connected by a set of pore throats $\mathcal{T} \subset \mathcal{P} \times \mathcal{P}$ (denoted ij instead of (i, j) for simplicity). This network can be extracted from experimental data, see [Fig. 7.1](#) for an illustration, or artificially created based on material-specific

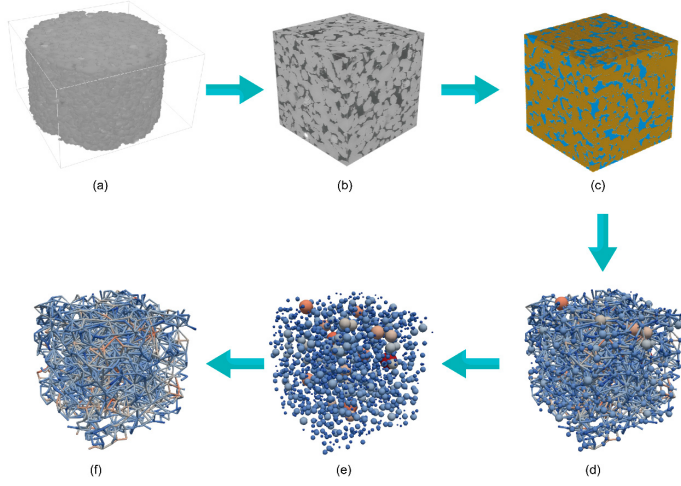


Figure 7.1.: Extraction of a pore-network geometry. From the CT images (a), a sub-volume (b) is segmented into pore space and solid (c). From this, the pore-network geometry is extracted (d), which consists of pore bodies (e) and pore throats (f). Figure taken from [138, Fig. 3] (CC-BY 4.0).

properties. The pore-space volumes can be distributed in various ways, depending on where one chooses the transition from pore body to pore throat [267]. Often, all volume is concentrated in the pore bodies, such that the pore throats only have resistances (typically assuming short throats). On the opposite, all volume can be concentrated in the (then long) pore throats, resulting in pore bodies being just junction points. Alternatively, one can divide the volumes and resistances between the pore bodies and the connecting pore throats to improve the representation of the local geometry. In either case, the shape of pore bodies and throats is simplified into regular structures. Here, we consider either spherical pore bodies, or use volume-less pore bodies as simplification. Furthermore, we assume cylindrical pore throats of varying radius to directly apply the results from Chapter 2. However, note that this neglects the existence of corner flow along the edges of pore throats with angular cross sections, which can be relevant in imbibition.

The model for two-phase flow in the pore network consists of the mass balance at the pore bodies, typically written in terms of the saturation $S_{\alpha,i}$ [-] of phase $\alpha \in \{n, w\}$ in the pore body $i \in \mathcal{P}$ as

$$V_i \frac{dS_{\alpha,i}}{dt} + \sum_{j \in \mathcal{N}(i)} q_{\alpha,ij} = 0. \quad (7.1)$$

Here, $V_i \geq 0$ [m³] denotes the volume of the pore body i , and $q_{\alpha,ij}$ [m³/s] is the flux of phase α through the pore throat ij towards the neighboring pore body $j \in \mathcal{N}(i) = \{j \in \mathcal{P} \mid ij \in \mathcal{T}\}$. In the pore throats, we extend the upscaled model

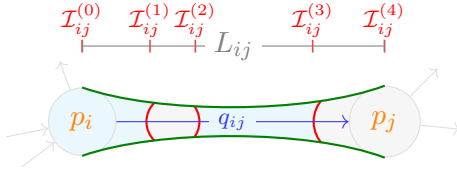


Figure 7.2: Flux q_{ij} in the pore throat ij with three interfaces.

from Section 2.5 for multiple interfaces. In each pore throat $ij \in \mathcal{T}$, there are $N_{ij} \in \mathbb{N}_0$ interfaces at (dimensionless) positions $\mathcal{I}_{ij}^{(m)} \in [0, 1]$ $[-]$, $1 \leq m \leq N_{ij}$, see Fig. 7.2. Furthermore, we let $\mathcal{I}_{ij}^{(0)} = 0$, $\mathcal{I}_{ij}^{(N_{ij}+1)} = 1$, and use the vector $\mathcal{I}_{ij} = (\mathcal{I}_{ij}^{(0)}, \dots, \mathcal{I}_{ij}^{(N_{ij}+1)})^T$ for all interface positions in the pore throat. Using (2.116), the total flux q_{ij} [m³/s] in pore throat $ij \in \mathcal{T}$ is then given by

$$q_{ij} = g_{ij}(\mathcal{I}_{ij}) \left(p_i - p_j - p_{ij}^g(\mathcal{I}_{ij}) - p_{ij}^c(\mathcal{I}_{ij}) \right). \quad (7.2)$$

Here, g_{ij} [m³/(Pa s)] denotes the conductance of the throat, p_i and p_j [Pa] are the pressures of the phase present at the entrance of pore body i and j , respectively, while p_{ij}^g and p_{ij}^c [Pa] denote the hydrostatic and capillary pressures in pore throat ij . Note that the flux $q_{\alpha,ij}$ is given by q_{ij} , if phase α is present at the entrance from pore body i into pore throat ij , and $q_{\alpha,ij} = 0$ otherwise. The interface-dependent parameters are given by

$$\begin{aligned} g_{ij}(\mathcal{I}_{ij}) &= \left(\sum_{m=0}^{N_{ij}} \int_{\mathcal{I}_{ij}^{(m)}}^{\mathcal{I}_{ij}^{(m+1)}} \frac{8|\mathbf{L}_{ij}|\mu_m}{\pi(R_{ij}(z))^3(R_{ij}(z) + 4\lambda_{ij})} dz \right)^{-1}, \\ p_{ij}^g(\mathcal{I}_{ij}) &= \mathbf{g} \cdot \mathbf{L}_{ij} \sum_{m=0}^{N_{ij}} \rho_m \left(\mathcal{I}_{ij}^{(m+1)} - \mathcal{I}_{ij}^{(m)} \right), \\ p_{ij}^c(\mathcal{I}_{ij}) &= \sum_{m=1}^{N_{ij}} \frac{2\sigma_{ij} \cos \theta_{ij}^m \left(\frac{q_{ij}}{\pi(R_{ij}(\mathcal{I}_{ij}^{(m)}))^2} \right)}{R_{ij}(\mathcal{I}_{ij}^{(m)})}, \end{aligned}$$

where $\mathbf{L}_{ij} = \mathbf{x}_j - \mathbf{x}_i$ [m] denotes the (oriented) length of pore throat ij , R_{ij} [m] is the (varying) throat radius, and λ_{ij} [m] is the slip length. Furthermore, μ_m [Pa s], ρ_m [kg/m³] are the viscosity and the density of the phase between the interfaces $m-1$ and m , while σ_{ij} [Pa m] is the surface tension between the phases, and $\mathbf{g} = (0, 0, 9.81)^T$ [m/s²] denotes the gravitational acceleration. We assume a linearized contact-angle model (cf. Sections 1.2.2 and 3.2)

$$\cos \theta_{ij}^{(m)}(v) = (-1)^m \cos \theta_{ij}^s + \eta_{ij} v, \quad 1 \leq m \leq N_{ij}$$

where θ_{ij}^s [deg] denotes the static contact angle and η_{ij} [m/s] is the dynamic contact-angle parameter. Note that the alternating sign is due to the alternating orientation from wetting to non-wetting phase and vice versa. Then, (7.2) can be

reformulated as

$$q_{ij} = \tilde{g}_{ij}(\mathcal{I}_{ij})(p_i - p_j - \tilde{p}_{ij}^c(\mathcal{I}_{ij}) - p_{ij}^g(\mathcal{I}_{ij})), \quad (7.3)$$

where

$$\tilde{g}_{ij}(\mathcal{I}_{ij}) := \frac{g_{ij}(\mathcal{I}_{ij})}{1 + \sum_{m=1}^{N_{ij}} \frac{2\sigma_{ij}\eta_{ij}g_{ij}(\mathcal{I}_{ij})}{\pi(R_{ij}(\mathcal{I}_{ij}^{(m)}))^3}}, \quad \tilde{p}_{ij}^c = \sum_{m=1}^{N_{ij}} \frac{2\sigma_{ij}(-1)^m \cos \theta_{ij}^s}{R_{ij}(\mathcal{I}_{ij}^{(m)})}.$$

By (2.109), the interfaces in each pore throat $ij \in \mathcal{T}$ move according to

$$\frac{d\mathcal{I}_{ij}^{(m)}}{dt} = \frac{q_{ij}}{\pi(R_{ij}(\mathcal{I}_{ij}^{(m)}))^2 L_{ij}}, \quad 1 \leq m \leq N_{ij}, \quad (7.4)$$

as long as $\mathcal{I}_{ij}^{(m)} \in (0, 1)$.

To close the problem, there are two typical approaches: either the pore bodies have a positive volume, and both phases can coexist in the pore bodies, or the pore bodies are volume-less, and only one phase can occupy it. In the former case, one uses (7.1) to solve for the pore-body saturations in combination with a capillary pressure relation $p_i^c(S_{w,i}) = p_{n,i} - p_{w,i}$ depending on the geometry of the pore body. Furthermore, discrete rules are necessary to decide when a new interface forms at the entrance of a pore throat. Hence, one solves for both pressures $p_{n,i}$ and $p_{w,i}$ in all pore bodies and the interface positions \mathcal{I}_{ij} in all pore throats. This is similar to classical two-pressure pore-network models without resolved interface positions [21, 177, 179, 253, 289, 299, 304]. On the other hand, the volume-less approach neglects the storage term in (7.1), such that it becomes a simple flux continuity equation. Then, each pore body is either filled by the wetting or the non-wetting phase, the latter being the case when the non-wetting phase is at an adjacent pore-throat entry. Therefore, each pore body has only one pressure p_i of the occupying phase. When an interface leaves a pore throat, the occupying phase in the adjacent pore body might change, and new interfaces might be formed in the connected pore throats, which must also be prescribed by discrete rules. Then, one solves for the phases in the pore bodies, their pressures p_i and the interface positions \mathcal{I}_{ij} in the pore throats. This is similar to classical one-pressure pore-network models, either without fully resolved interface motion [11, 45, 180, 195, 242, 248], and the ones taking continuous interface movement into account [9, 10, 85, 136, 291].

In the following, we shortly discuss the discretization and preliminary results for the simpler, one-pressure approach with volume-less pore bodies. Note that (7.1), (7.3), and (7.4) form a nonlinear system of differential-algebraic equations that requires initial conditions for the interface positions and boundary conditions for the pressure and/or the flux, which are not discussed for brevity and can be found e.g. in [10, 136, 291]. For $T > 0$ [s], let $0 = t^0 < t^1 < \dots < t^K = T$

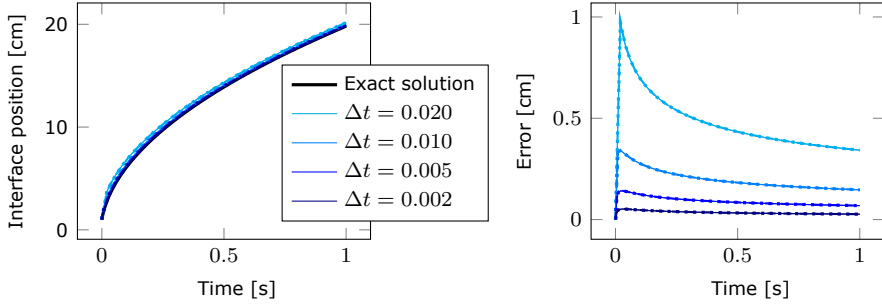


Figure 7.3.: Horizontal flow driven by one water-air interface for several time-step sizes Δt . (solid / dotted / dashed: 1 / 5 / 10 pore throats).

be a discretization of the time interval $[0, T]$ using $K \in \mathbb{N}$ time steps with sizes $\Delta t_k = t^k - t^{k-1}$, $1 \leq k \leq K$. In the following, we denote by f^k the approximation of $f(t^k)$ for a quantity f . At time t^k , the pressures p_i^k are determined using (7.1) and (7.3) (note $V_i = 0$) by

$$\sum_{j \in \mathcal{N}(i)} \tilde{g}_{ij}(\mathcal{I}_{ij}^k)(p_i^k - p_j^k) = \sum_{j \in \mathcal{N}(i)} \tilde{g}_{ij}(\mathcal{I}_{ij}^k)(\tilde{p}_{ij}^c(\mathcal{I}_{ij}^k) + p_{ij}^g(\mathcal{I}_{ij}^k)). \quad (7.5)$$

Using the explicit Euler method, we obtain for (7.4) using (7.2)

$$\mathcal{I}_{ij}^{(m),k} = \mathcal{I}_{ij}^{(m),k-1} + \Delta t_k \frac{\tilde{g}_{ij}(\mathcal{I}_{ij}^{k-1}) \left(p_i^{k-1} - p_j^{k-1} - \tilde{p}_{ij}^c(\mathcal{I}_{ij}^{k-1}) - p_{ij}^g(\mathcal{I}_{ij}^{k-1}) \right)}{\pi(R_{ij}(\mathcal{I}_{ij}^{(m),k-1}))^2 L_{ij}}. \quad (7.6)$$

When the interface leaves the pore throat ($\mathcal{I}_{ij}^{(m)} \notin (0, 1)$), the respective volume must be transferred via the pores bodies with no volume to adjacent pore throats and this exchange may create new interfaces. This is done heuristically, similar to the meniscus algorithm in [136, 291].

We implement a preliminary version of the discretization in Python 3.8 using the package openPNM 2.8.2 [139]. As simple examples, we consider the capillary-driven imbibition of water (against air) in a tube with constant radius $R = 1.0$ mm. For simplicity, contact-angle dynamics are neglected. The results are depicted in Fig. 7.3 for a horizontal tube, and in Fig. 7.4 for a vertical tube. In both cases, the error decreases with decreasing time-step size as expected. The results are consistent when splitting the tube into several pore throats, since the discretization is locally mass conservative.

The presented dynamic pore-network model aims at bridging the scale-gap between single-pore models and Darcy-scale models by averaging over representative volumes with many pores. However, many open challenges must be overcome to achieve this goal. First of all, the model itself is currently rather simplistic. Adding further effects, such as simultaneous flow and snap-off due to corners, including

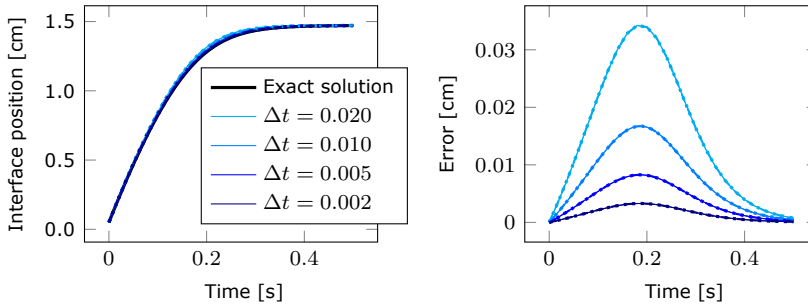


Figure 7.4.: Vertical flow driven by one water-air interface for several time-step sizes Δt . (solid / dotted / dashed: 1 / 5 / 10 pore throats).

more realistic pore geometries and heterogeneity of the medium, and extending it to the two-pressure formulation are required to represent realistic processes. Additionally, the discrete rules for the formation of new interfaces must be studied carefully, and its choice might depend on the considered process (capillary-driven vs. viscosity-driven). Furthermore, the discretization must take these events into account, which requires small time steps. Implicit, possibly higher order numerical methods and multi-rate schemes might improve the solutions significantly. A prerequisite is, however, that the resulting nonlinear problem can be solved in an efficient and robust way. Hence, a suitable linearization strategy should be developed and analyzed. Eventually, the simulations of the dynamic pore-network model can be averaged over representative elementary volumes to obtain effective Darcy-scale quantities and their relationships.

Combined effects for the averaged two-phase flow in a thin strip

In [Chapter 2](#), we discussed the upscaling of two-phase flow in single pores. In particular, we discussed the effect of the slip length, of the viscosity ratio, as well as the effect of a dynamic and hysteretic contact-angle model. For this, we depicted several numerical examples in [Section 2.7](#). Here, we illustrate further numerical examples in which the different effects are combined. We consider two thin-strip geometries with a constriction of different length.

Thin strip with short constriction

We consider the thin strip from [Section 2.7.2](#) with varying width

$$w(x_1) = \frac{2}{3} + \frac{1}{3} \cos(2\pi x_1),$$

describing a pore throat with short constriction, see [Fig. A.1](#) (left). First, we solve the upscaled model [\(2.74\)](#) and [\(2.75\)](#) with fixed contact angle $\theta \equiv \pi/3$ (cf. [Table 2.3](#)). All the other parameters are varied simultaneously. The solutions for imposed pressure boundary condition are depicted in [Fig. A.2](#). The movement is faster for higher slip length λ (left to right), and slows down or speeds up over

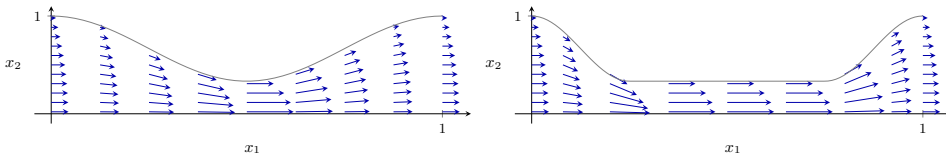


Figure A.1.: Geometry and velocity solution for the thin strip with short (*left*) and long (*right*) constriction.

time according to the viscosity ratio M (top to bottom). These effects interact with the slowdown as the fluid-fluid interface passes through the constriction, which is more pronounced for low capillary number \overline{Ca} .

When imposing a fixed flux boundary condition, the interface movement is the same for all parameter choices, see the solutions shown in Fig. A.3. However, the inlet pressure decreases for increasing slip length (left to right). It is higher while the majority of the thin strip is filled with the higher viscous fluid, i.e., in the end for $M < 1$ and in beginning for $M > 1$ (top to bottom). Additionally, the local capillary pressure is significant for low capillary number \overline{Ca} , especially when the fluid-fluid interface passes through the constriction.

Furthermore, we solve the upscaled model (2.74) and (2.75) using the dynamic contact angle model (2.133), i.e.,

$$\theta(u) = \arccos \left(\max \left(\min(\cos(\theta_s) + \eta \overline{Ca} u, 1), -1 \right) \right).$$

The solutions using an pressure boundary condition are depicted in Fig. A.4 for varying parameters. Qualitatively similar results to the constant contact angle case are obtained. However the dynamic effect significantly decelerates the interface movement, especially when passing through the constriction. For a fixed flux boundary condition, the dynamic effect similarly increases the inlet pressure due to a higher local capillary pressure, see the solutions in Fig. A.5.

Thin strip with long constriction

We consider a thin strip with varying width

$$w(x_1) := \begin{cases} \frac{1}{3} & \text{for } \frac{1}{4} < x_1 < \frac{3}{4}, \\ \frac{2}{3} + \frac{1}{3} \cos(4\pi x_1) & \text{otherwise.} \end{cases}$$

describing a pore throat with long constriction, see Fig. A.1 (right). First, we solve the upscaled model (2.74) and (2.75) with fixed contact angle $\theta \equiv \pi/3$ (cf. Table 2.3). All the other parameters are varied simultaneously. The solutions are depicted in Fig. A.6 imposing a pressure boundary condition, and in Fig. A.7 imposing a flux boundary condition. The results are very similar to those for the short constriction. However, the effects of the local capillary pressure and of the slip length are amplified due to the higher length of the constriction.

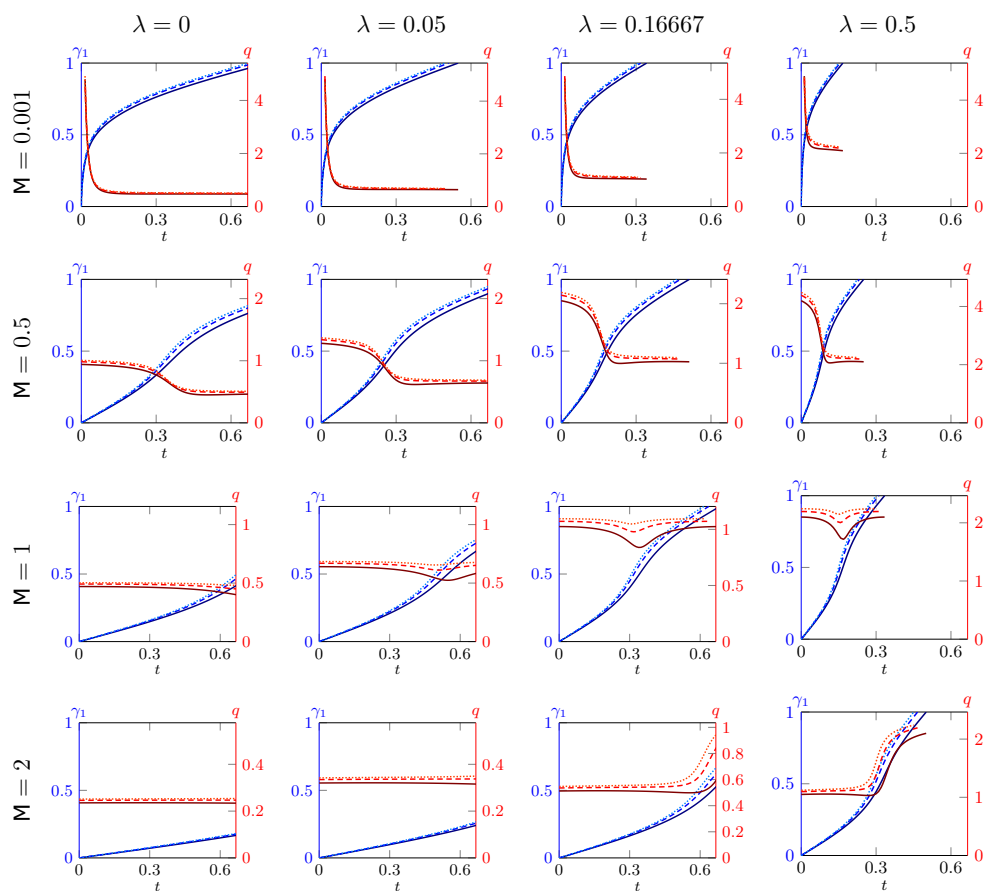


Figure A.2.: Solution of the upscaled model for the short constriction with pressure boundary condition $p_{\text{in}} = 12$, when varying the viscosity ratio M , the slip length λ and the capillary number $\overline{\text{Ca}}$ (solid: $\overline{\text{Ca}} = \frac{1}{2}$, dashed: $\overline{\text{Ca}} = 1$, dotted: $\overline{\text{Ca}} = 2$).

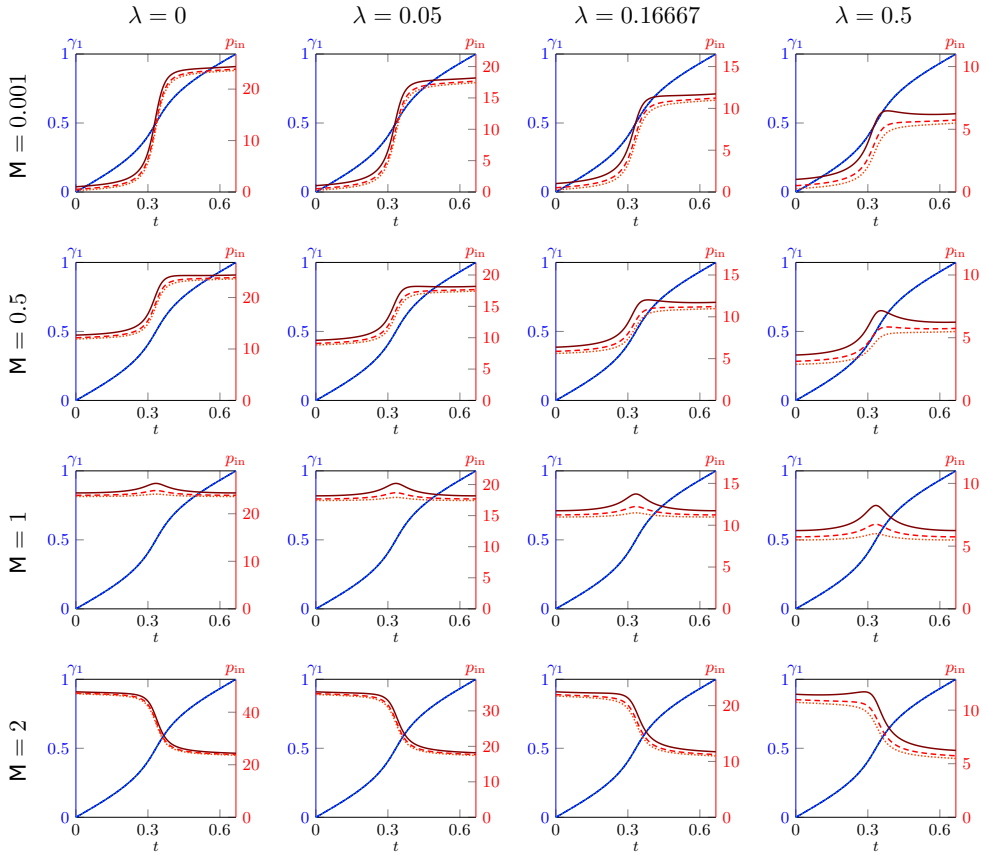


Figure A.3.: Solution of the upscaled model for the short constriction with flux boundary condition $q = 1$, when varying the viscosity ratio M , the slip length λ and the capillary number Ca (solid: $\text{Ca} = \frac{1}{2}$, dashed: $\text{Ca} = 1$, dotted: $\text{Ca} = 2$).

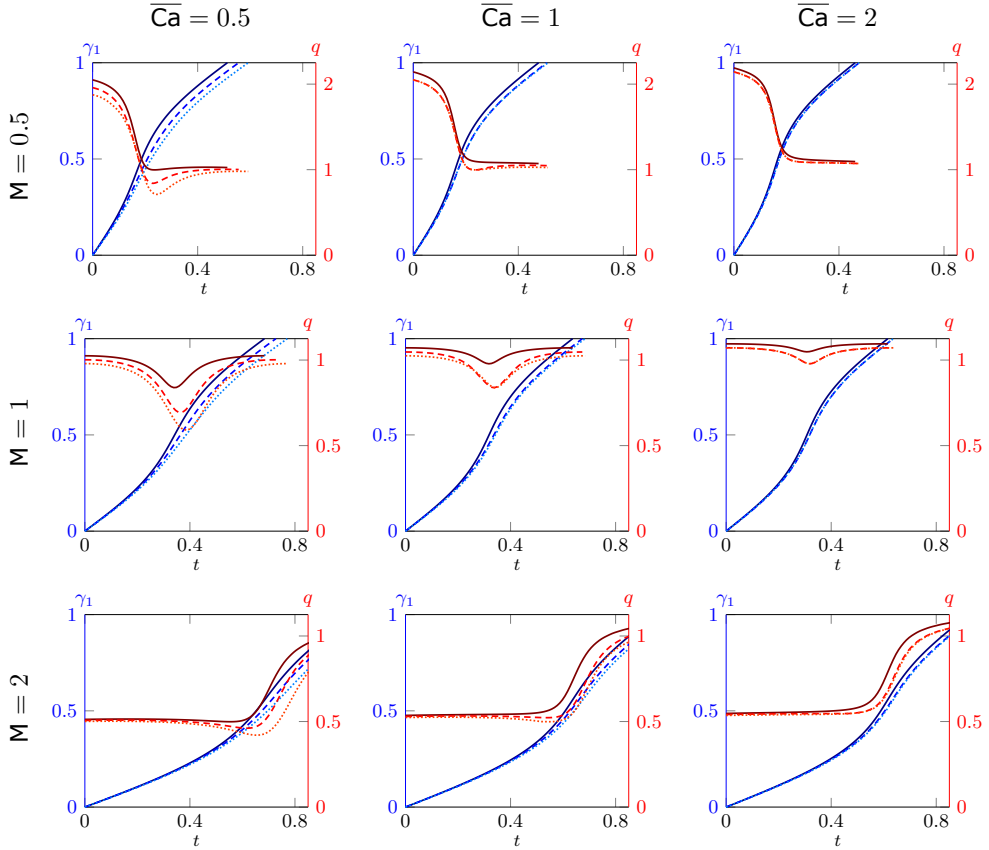


Figure A.4.: Solution of the upscaled model for the short constriction with pressure boundary condition $p_{\text{in}} = 12$, when varying the viscosity ratio M , the capillary number Ca and the dynamic coefficient η (solid: $\eta = 0$, dashed: $\eta = \frac{1}{4}$, dotted: $\eta = \frac{1}{2}$) for fixed $\lambda = \frac{1}{6}$.

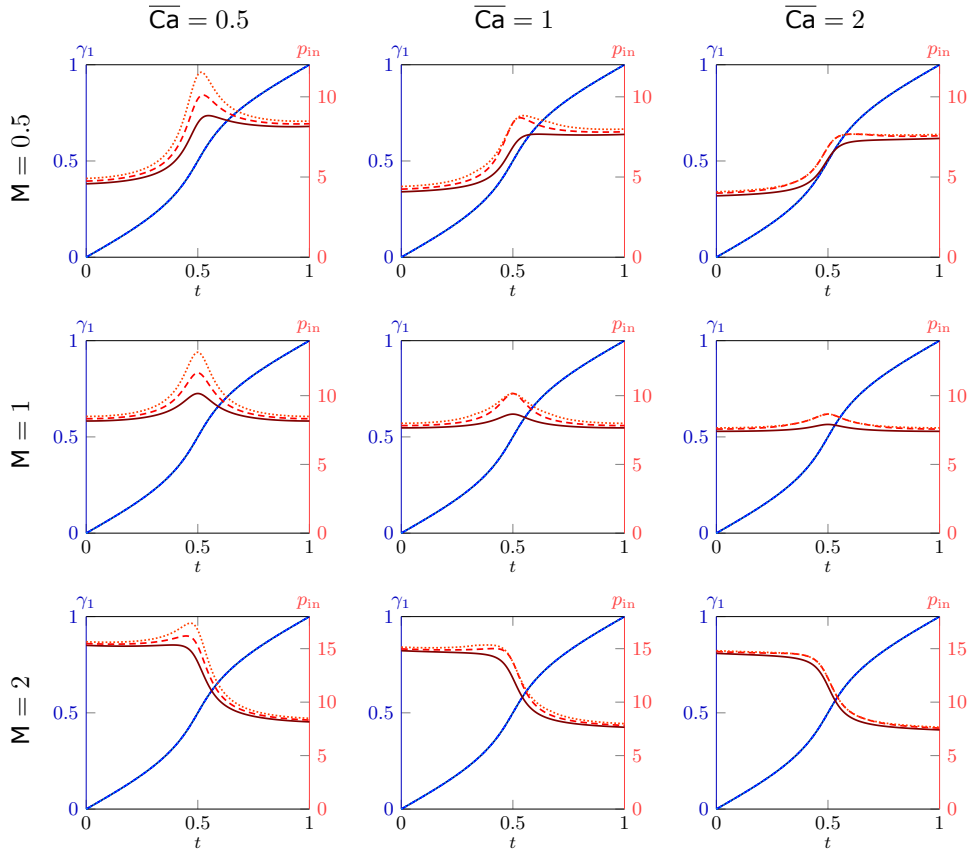


Figure A.5.: Solution of the upscaled model for the short constriction with flux boundary condition $q = 1$, when varying the viscosity ratio M , the capillary number Ca and the dynamic coefficient η (solid: $\eta = 0$, dashed: $\eta = \frac{1}{4}$, dotted: $\eta = \frac{1}{2}$) for fixed $\lambda = \frac{1}{6}$.

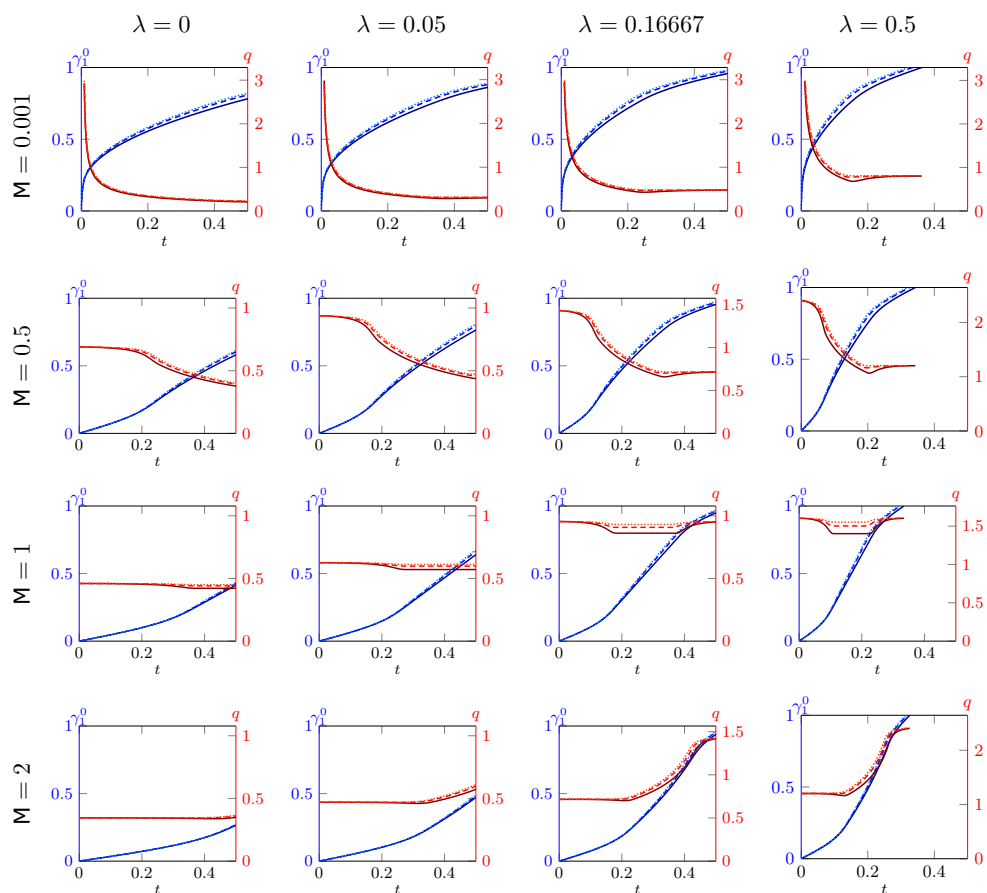


Figure A.6.: Solution of the upscaled model for the long constriction with pressure boundary condition $p_{\text{in}} = 12$, when varying the viscosity ratio M , the slip length λ and the capillary number \overline{Ca} (solid: $\overline{Ca} = \frac{1}{2}$, dashed: $\overline{Ca} = 1$, dotted: $\overline{Ca} = 2$).

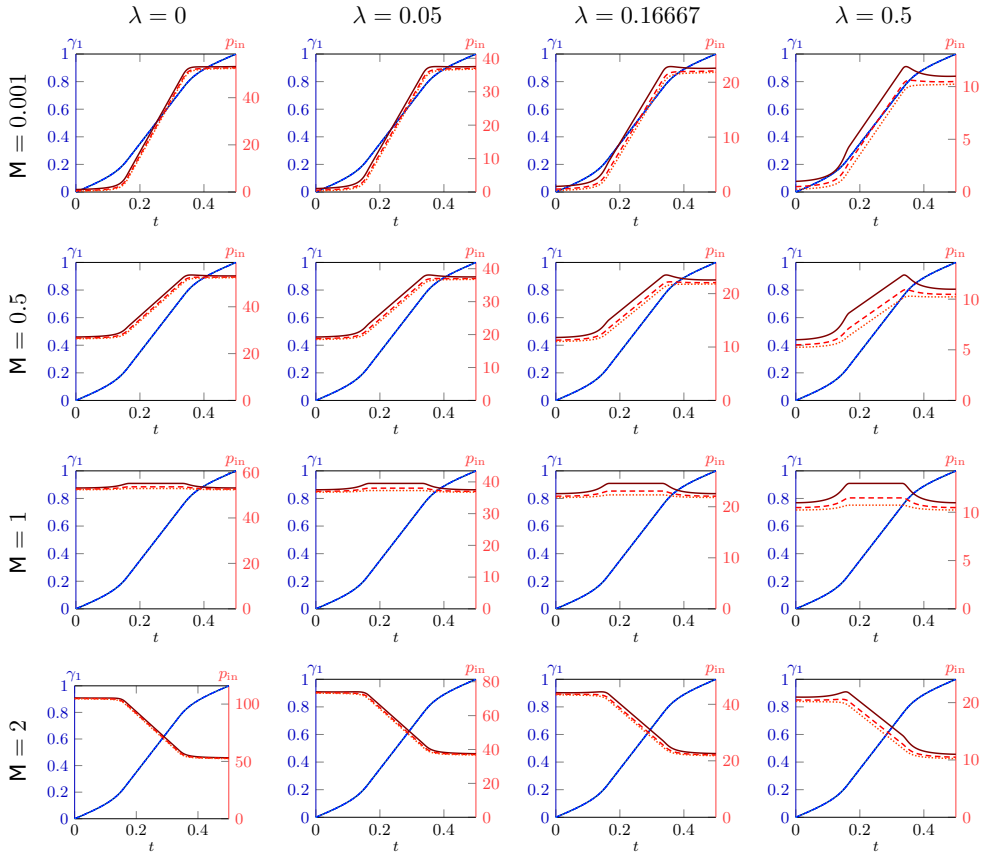


Figure A.7.: Solution of the upscaled model for the long constriction with flux boundary condition $q = 1$, when varying the viscosity ratio M , the slip length λ and the capillary number Ca (solid: $\text{Ca} = \frac{1}{2}$, dashed: $\text{Ca} = 1$, dotted: $\text{Ca} = 2$).

Appendix **B**

Detailed results of the fitting for the capillary rise experiments

In [Chapter 3](#), we discussed the comparison between the upscaled and extended models for capillary rise dynamics and the experimental data. In this appendix, detailed results of the fitting are presented in detail. First, in [Fig. B.1](#) we illustrate the different fits of the upscaled model obtained for glycerol. The fits of the upscaled and the extended model for Soltrol 170 are presented in [Figs. B.2 to B.4](#). Finally, the fits of the two models for water are presented in [Table B.1](#) and [Figs. B.5 to B.7](#), including the results for the simultaneous fit of the dynamic parameter η and the slip length λ .

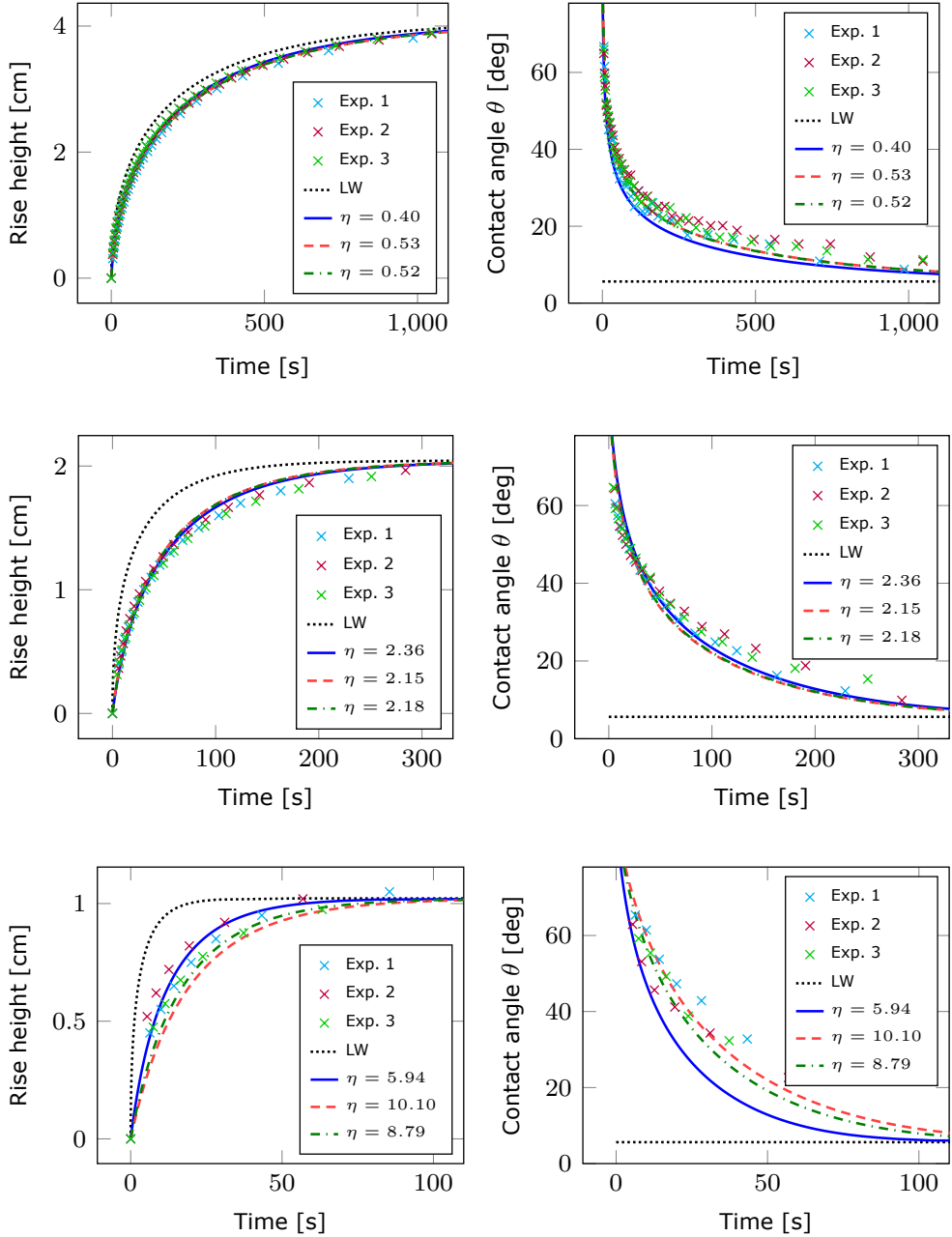


Figure B.1.: Simulation results of the Lucas-Washburn model (LW) and of the fitted upscaled model for the glycerol experiments. *Top row:* radius $R = 0.25$ mm. *Center row:* radius $R = 0.5$ mm. *Bottom row:* radius $R = 1.0$ mm. Solid blue: h -fit; Dashed red: θ -fit; Dash-dotted green: both-fit.

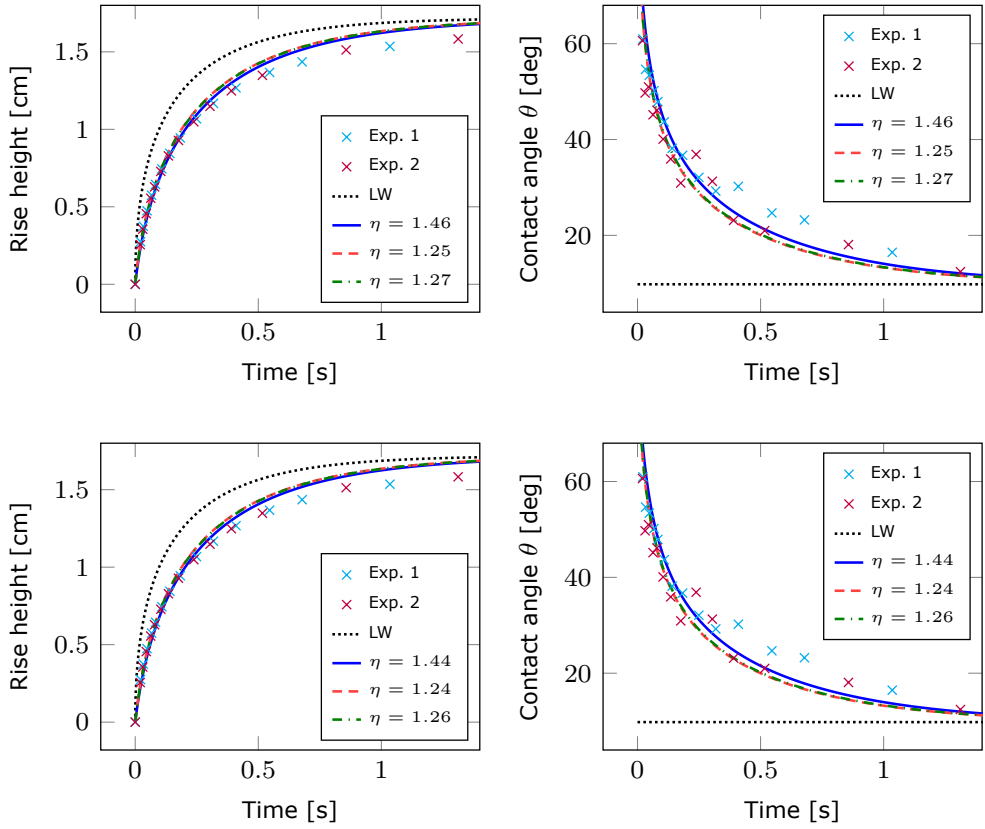


Figure B.2.: Simulation results of the Lucas-Washburn model (LW) and of the fitted upscaled (*top row*) and extended (*bottom row*) models for the Soltrol 170 experiments at radius $R = 0.375$ mm. Solid blue: h -fit; Dashed red: θ -fit; Dash-dotted green: both-fit.

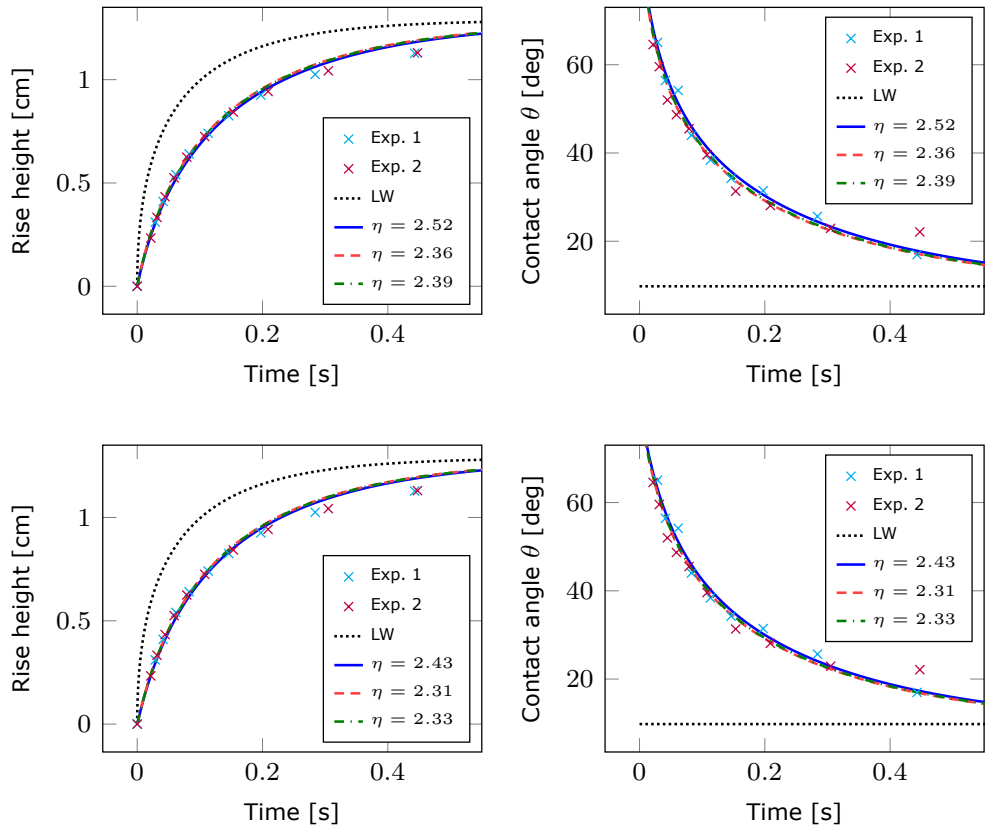


Figure B.3.: Simulation results of the Lucas-Washburn model (LW) and of the fitted upscaled (*top row*) and extended (*bottom row*) models for the Soltrol 170 experiments at radius $R = 0.5$ mm. Solid blue: h -fit; Dashed red: θ -fit; Dash-dotted green: both-fit.

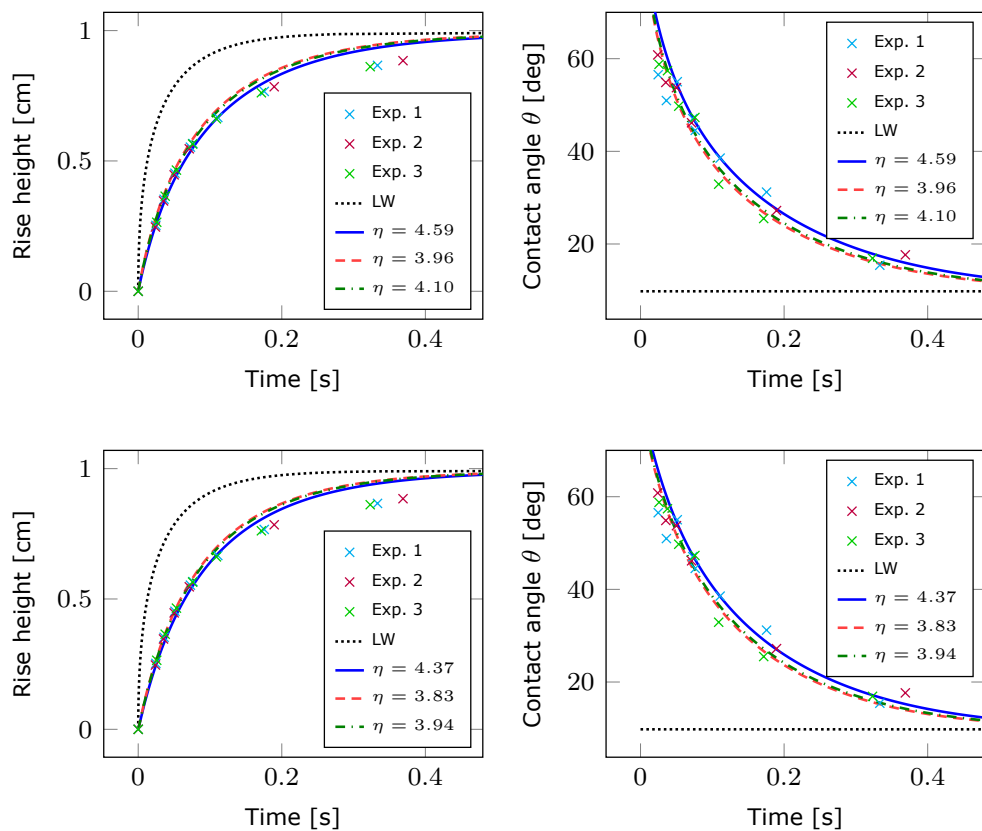


Figure B.4.: Simulation results of the Lucas-Washburn model (LW) and of the fitted upscaled (*top row*) and extended (*bottom row*) models for the Soltrol 170 experiments at radius $R = 0.65$ mm. Solid blue: h -fit; Dashed red: θ -fit; Dash-dotted green: both-fit.

Radius [mm]	(fit)	Upscaled					Extended				
		η	χ_ν^2	η	λ	χ_ν^2	η	χ_ν^2	η	λ	χ_ν^2
0.375	(h)	0.451	0.558	1.017	0.288	0.051	0.162	0.058	0.329	0.043	0.023
0.375	(θ)	0.414	1.981	0.414	5e-11	2.013	0.377	2.054	0.377	1e-11	2.088
0.375	(b)	0.416	1.252	0.413	0.016	1.244	0.367	1.143	0.357	0.045	1.041
0.500	(h)	0.924	2.433	2.081	5*	0.222	0.111	0.153	0.548	0.123	2.7e-3
0.500	(θ)	0.605	2.599	0.516	0.683	1.349	0.498	0.037	0.498	7e-11	0.039
0.500	(b)	0.637	2.738	0.637	4e-3	2.767	0.476	2.249	0.463	0.070	2.039
0.650	(h)	4.036	1.147	5.228	5*	0.436	2.849	0.234	3.334	0.149	0.197
0.650	(θ)	1.488	3.524	1.461	0.248	3.232	1.052	4.595	1.052	6e-12	4.683
0.650	(b)	1.907	6.552	1.907	7e-10	6.612	1.248	4.203	1.248	7e-10	4.242

*) Maximal allowed value in the fitting procedure, to avoid unphysically large slip lengths.

Table B.1.: Dynamic coefficient η , slip length λ and reduced residuals χ_ν^2 for the different fits (h: height, θ : contact angle, b: both) of the upscaled and extended models, for the water experiments.

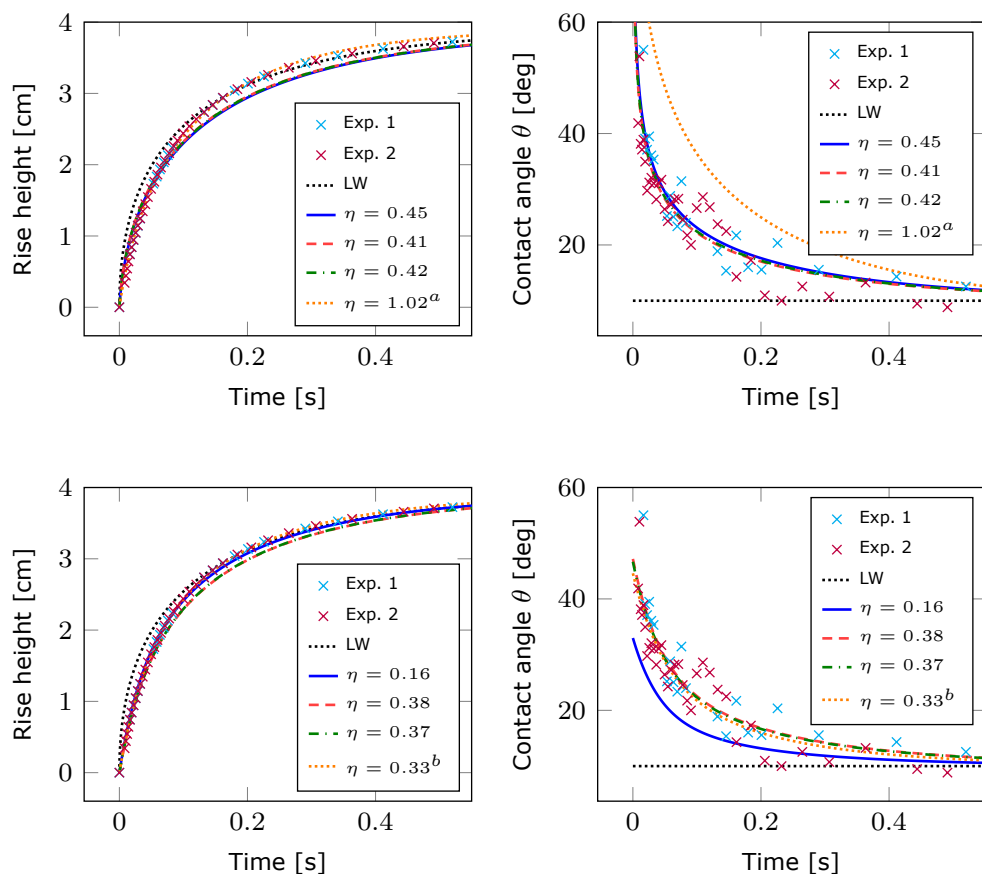


Figure B.5.: Simulation results of the Lucas-Washburn model (LW) and of the fitted upscaled (*top row*) and extended (*bottom row*) models for the water experiments at radius $R = 0.375$ mm. Solid blue: h -fit; Dashed red: θ -fit; Dash-dotted green: both-fit. Dotted orange: h -fit including slip (a: $\lambda = 0.29$, b: $\lambda = 0.04$).

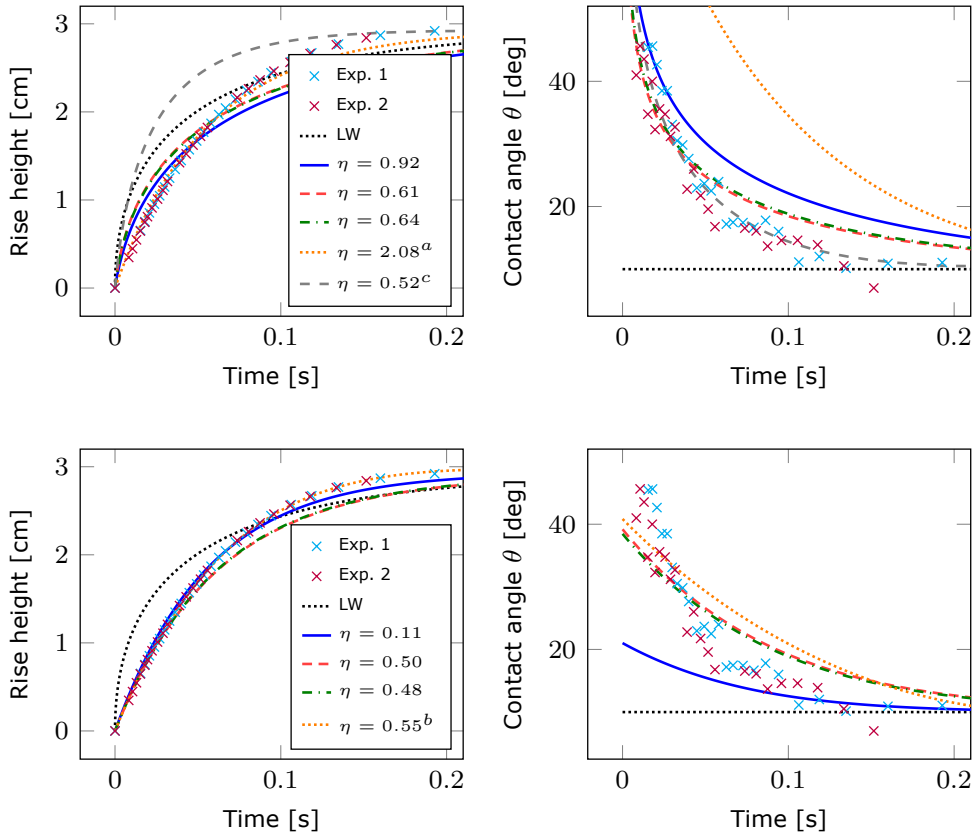


Figure B.6.: Simulation results of the Lucas-Washburn model (LW) and of the fitted upscaled (*top row*) and extended (*bottom row*) models for the water experiments at radius $R = 0.5$ mm. Solid blue: h -fit; Dashed red: θ -fit; Dash-dotted green: both-fit. Dotted orange: h -fit including slip (a: $\lambda = 5$, b: $\lambda = 0.12$). Wide-dashed gray: θ -fit including slip (c: $\lambda = 0.68$).

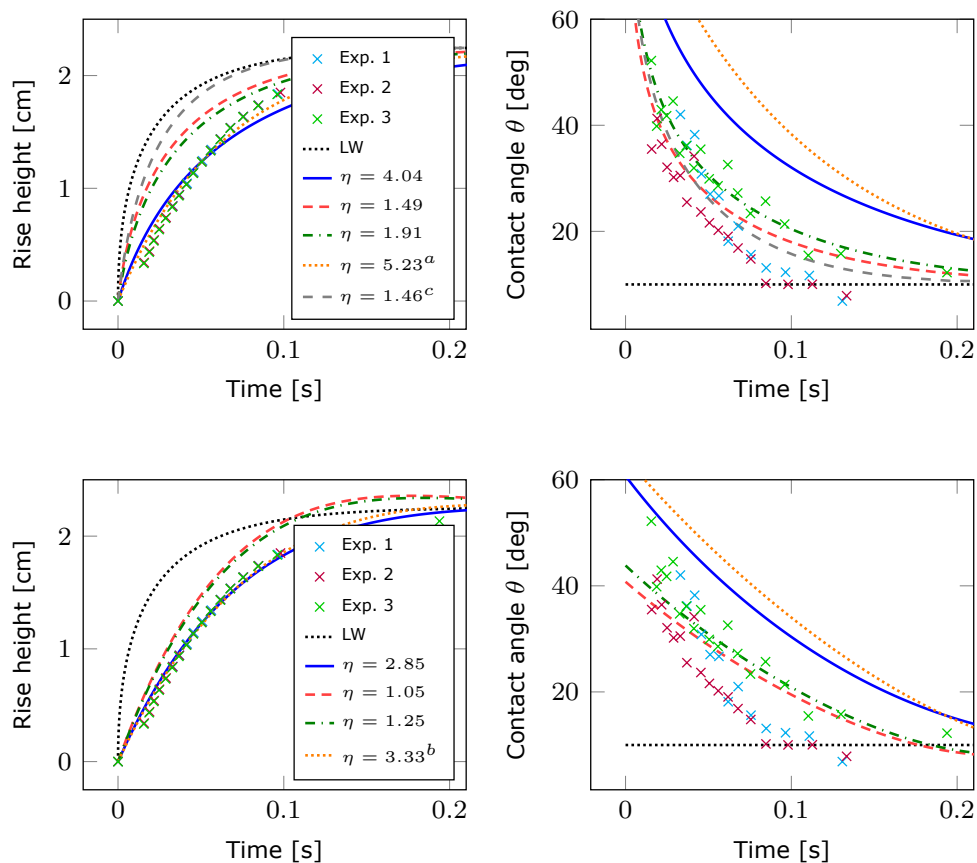


Figure B.7.: Simulation results of the Lucas-Washburn model (LW) and of the fitted upscaled (*top row*) and extended (*bottom row*) models for the water experiments at radius $R = 0.65$ mm. Solid blue: h -fit; Dashed red: θ -fit; Dash-dotted green: both-fit. Dotted orange: h -fit including slip (a: $\lambda = 5$, b: $\lambda = 0.15$). Wide-dashed gray: θ -fit including slip (c: $\lambda = 0.25$).

Bibliography

- [1] H. ABELS, H. GARCKE, AND G. GRÜN, *Thermodynamically consistent, frame indifferent diffuse interface models for incompressible two-phase flows with different densities*, Mathematical Models and Methods in Applied Sciences, 22 (2012), p. 1150013, <https://doi.org/10.1142/S0218202511500138>.
- [2] A. AGHAEI AND M. PIRI, *Direct pore-to-core up-scaling of displacement processes: Dynamic pore network modeling and experimentation*, Journal of Hydrology, 522 (2015), pp. 488–509, <https://doi.org/10.1016/j.jhydrol.2015.01.004>.
- [3] L. AGÉLAS, M. SCHNEIDER, G. ENCHÉRY, AND B. FLEMISCH, *Convergence of nonlinear finite volume schemes for two-phase porous media flow on general meshes*, IMA Journal of Numerical Analysis, 42 (2020), pp. 515–568, <https://doi.org/10.1093/imanum/draa064>.
- [4] E. AHMED, *Splitting-based domain decomposition methods for two-phase flow with different rock types*, Advances in Water Resources, 134 (2019), p. 103431, <https://doi.org/10.1016/j.advwatres.2019.103431>.
- [5] E. AHMED, A. FUMAGALLI, A. BUDIŠA, E. KEILEGAVLEN, J. M. NORDBOTTEN, AND F. A. RADU, *Robust linear domain decomposition schemes for reduced nonlinear fracture flow models*, SIAM Journal of Numerical Analysis, 59 (2021), pp. 583–612, <https://doi.org/10.1137/19M1268392>.
- [6] E. AHMED, S. A. HASSAN, C. JAPHET, M. KERN, AND M. VOHRALÍK, *A posteriori error estimates and stopping criteria for space-time domain decomposition for two-phase flow between different rock types*, The SMAI Journal of Computational Mathematics, 5 (2019), pp. 195–227, <https://doi.org/doi.org/10.5802/smai-jcm.47>.
- [7] E. AHMED, C. JAPHET, AND M. KERN, *Space-time domain decomposition for two-phase flow between different rock types*, Computer Methods in Applied Mechanics and Engineering, 371 (2020), p. 113294, <https://doi.org/10.1016/j.cma.2020.113294>.

- [8] V. AIZINGER, A. RUPP, J. SCHÜTZ, AND P. KNABNER, *Analysis of a mixed discontinuous Galerkin method for instationary Darcy flow*, Computational Geosciences, 22 (2018), pp. 179–194, <https://doi.org/10.1007/s10596-017-9682-8>.
- [9] E. AKER, K. J. MÅLØY, AND A. HANSEN, *Simulating temporal evolution of pressure in two-phase flow in porous media*, Physical Review E, 58 (1998), pp. 2217–2226, <https://doi.org/10.1103/PhysRevE.58.2217>.
- [10] E. AKER, K. J. MÅLØY, A. HANSEN, AND G. G. BATROUNI, *A two-dimensional network simulator for two-phase flow in porous media*, Transport in Porous Media, 32 (1998), pp. 163–186, <https://doi.org/10.1023/A:1006510106194>.
- [11] M. S. AL-GHARBI AND M. J. BLUNT, *Dynamic network modeling of two-phase drainage in porous media*, Physical Review E, 71 (2005), p. 016308, <https://doi.org/10.1103/PhysRevE.71.016308>.
- [12] G. ALBUJA AND A. I. ÁVILA, *A family of new globally convergent linearization schemes for solving Richards' equation*, Applied Numerical Mathematics, 159 (2021), pp. 281–296, <https://doi.org/10.1016/j.apnum.2020.09.012>.
- [13] G. ALLAIRE, *Homogenization of the Stokes flow in a connected porous medium*, Asymptotic Analysis, 2 (1989), pp. 203–222, <https://doi.org/10.3233/ASY-1989-2302>.
- [14] G. ALLAIRE, *Homogenization of the Navier-Stokes equations in open sets perforated with tiny holes I: Abstract framework, a volume distribution of holes*, Archive for Rational Mechanics and Analysis, 113 (1991), pp. 209–259, <https://doi.org/10.1007/BF00375065>.
- [15] G. ALLAIRE, *Homogenization of the Navier-Stokes equations in open sets perforated with tiny holes II: Non-critical sizes of the holes for a volume distribution and a surface distribution of holes*, Archive for Rational Mechanics and Analysis, 113 (1991), pp. 261–298, <https://doi.org/10.1007/BF00375066>.
- [16] G. ALLAIRE, *Homogenization of the Navier-Stokes equations with a slip boundary condition*, Communications on Pure and Applied Mathematics, 44 (1991), pp. 605–641, <https://doi.org/10.1002/cpa.3160440602>.
- [17] G. ALLAIRE, *Homogenization and two-scale convergence*, SIAM Journal on Mathematical Analysis, 23 (1992), pp. 1482–1518, <https://doi.org/10.1137/0523084>.

- [18] H. W. ALT AND S. LUCKHAUS, *Quasilinear elliptic-parabolic differential equations*, Mathematische Zeitschrift, 183 (1983), pp. 311–341, <https://doi.org/10.1007/BF01176474>.
- [19] G. ALZETTA, D. ARNDT, W. BANGERTH, V. BODDU, B. BRANDS, D. DAVYDOV, R. GASSMÖLLER, T. HEISTER, L. HELTAI, K. KORMANN, M. KRONBICHLER, M. MAIER, J.-P. PELTERET, B. TURCKIN, AND D. WELLS, *The deal.II library, version 9.0*, Journal of Numerical Mathematics, 26 (2018), pp. 173–183, <https://doi.org/10.1515/jnma-2018-0054>.
- [20] H. AMANN, *Maximal regularity of parabolic transmission problems*, Journal of Evolution Equations, 21 (2021), pp. 3375–3420, <https://doi.org/10.1007/s00028-020-00612-y>.
- [21] S. AN, H. ERFANI, O. E. GODINEZ-BRIZUELA, AND V. NIASAR, *Transition from viscous fingering to capillary fingering: Application of GPU-based fully implicit dynamic pore network modeling*, Water Resources Research, 56 (2020), p. e2020WR028149, <https://doi.org/10.1029/2020WR028149>.
- [22] T. ARBOGAST AND M. F. WHEELER, *A nonlinear mixed finite element method for a degenerate parabolic equation arising in flow in porous media*, SIAM Journal of Numerical Analysis, 33 (1996), pp. 1669–1687, <https://doi.org/10.1137/S0036142994266728>.
- [23] D. N. ARNOLD, F. BREZZI, B. COCKBURN, AND L. D. MARINI, *Unified analysis of discontinuous Galerkin methods for elliptic problems*, SIAM Journal of Numerical Analysis, 39 (2002), pp. 1749–1779, <https://doi.org/10.1137/S0036142901384162>.
- [24] J. AURIAULT, *Nonsaturated deformable porous media: Quasistatics*, Transport in Porous Media, 2 (1987), pp. 45–64, <https://doi.org/10.1007/BF00208536>.
- [25] J.-L. AURIAULT, O. LEBAGUE, AND G. BONNET, *Dynamics of two immiscible fluids flowing through deformable porous media*, Transport in Porous Media, 4 (1989), pp. 105–128, <https://doi.org/10.1007/BF00134993>.
- [26] T. A. BAER, R. A. CAIRNCROSS, R. SCHUNK, R. R. RAO, AND P. A. SACKINGER, *A finite element method for free surface flows of incompressible fluids in three dimensions. Part II. Dynamic wetting lines*, International Journal for Numerical Methods in Fluids, 33 (2000), pp. 405–427, [https://doi.org/10.1002/1097-0363\(20000615\)33:3<405::AID-FLD14>3.0.CO;2-4](https://doi.org/10.1002/1097-0363(20000615)33:3<405::AID-FLD14>3.0.CO;2-4).
- [27] G. J. BARCLAY, D. F. GRIFFITHS, AND D. J. HIGHAM, *Theta method dynamics*, LMS Journal of Computation and Mathematics, 3 (2000), pp. 27–43, <https://doi.org/10.1112/S146115700000019X>.

- [28] A. BASSON AND D. GÉRARD-VARET, *Wall laws for fluid flows at a boundary with random roughness*, Communications on Pure and Applied Mathematics, 61 (2008), pp. 941–987, <https://doi.org/10.1002/cpa.20237>.
- [29] M. BAUSE AND P. KNABNER, *Computation of variably saturated subsurface flow by adaptive mixed hybrid finite element methods*, Advances in Water Resources, 27 (2004), pp. 565–581, <https://doi.org/10.1016/j.advwatres.2004.03.005>.
- [30] J. BEAR, *Dynamics of Fluids in Porous Media*, American Elsevier Publishing Company, Inc., New York, NY, 1972.
- [31] J. BEAR, *Modeling Phenomena of Flow and Transport in Porous Media*, vol. 31 of Theory and Applications of Transport in Porous Media, Springer, Cham, 2018, <https://doi.org/10.1007/978-3-319-72826-1>.
- [32] A. Y. BELIAEV AND S. M. HASSANIZADEH, *A theoretical model of hysteresis and dynamic effects in the capillary relation for two-phase flow in porous media*, Transport in Porous Media, 43 (2001), pp. 487–510, <https://doi.org/10.1023/A:1010736108256>.
- [33] A. Y. BELIAEV AND R. J. SCHOTTING, *Analysis of a new model for unsaturated flow in porous media including hysteresis and dynamic effects*, Computational Geosciences, 5 (2001), pp. 345–368, <https://doi.org/10.1023/A:1014547019782>.
- [34] A. BELJADID, L. CUETO-FELGUEROSO, AND R. JUANES, *A continuum model of unstable infiltration in porous media endowed with an entropy function*, Advances in Water Resources, 144 (2020), p. 103684, <https://doi.org/10.1016/j.advwatres.2020.103684>.
- [35] D. BENNEQUIN, M. J. GANDER, L. GOUARIN, AND L. HALPERN, *Optimized Schwarz waveform relaxation for advection reaction diffusion equations in two dimensions*, Numerische Mathematik, 134 (2016), pp. 513–567, <https://doi.org/10.1007/s00211-015-0784-8>.
- [36] D. BENNEQUIN, M. J. GANDER, AND L. HALPERN, *A homographic best approximation problem with application to optimized Schwarz waveform relaxation*, Mathematics of Computation, 78 (2009), pp. 185–223, <https://doi.org/10.1090/S0025-5718-08-02145-5>.
- [37] H. BERNINGER, R. KORNHUBER, AND O. SANDER, *Convergence behaviour of Dirichlet–Neumann and Robin methods for a nonlinear transmission problem*, in Domain Decomposition Methods in Science and Engineering XIX, Y. Huang, R. Kornhuber, O. Widlund, and J. Xu, eds.,

- Berlin, Heidelberg, 2011, Springer, pp. 87–98, https://doi.org/10.1007/978-3-642-11304-8_8.
- [38] H. BERNINGER, S. LOISEL, AND O. SANDER, *The 2-Lagrange multiplier method applied to nonlinear transmission problems for the Richards equation in heterogeneous soil with cross points*, SIAM Journal of Scientific Computing, 36 (2014), pp. A2166–A2198, <https://doi.org/10.1137/120901064>.
- [39] M. BERTSCH, R. D. PASSO, AND C. J. VAN DUIN, *Analysis of oil trapping in porous media flow*, SIAM Journal on Mathematical Analysis, 35 (2003), pp. 245–267, <https://doi.org/10.1137/S0036141002407375>.
- [40] M. BJØRHHUS, *On Domain Decomposition, Subdomain Iteration and Waveform Relaxation*, PhD thesis, University of Trondheim, Norway, 1995.
- [41] T. D. BLAKE, *Dynamic contact angles and wetting kinetics*, in Wettability, J. C. Berg, ed., Marcel Dekker, New York, NY, 1993, pp. 251–309.
- [42] T. D. BLAKE, *The physics of moving wetting lines*, Journal of Colloid and Interface Science, 299 (2006), pp. 1–13, <https://doi.org/10.1016/j.jcis.2006.03.051>.
- [43] T. D. BLAKE AND J. M. HAYNES, *Kinetics of liquid/liquid displacement*, Journal of Colloid and Interface Science, 30 (1969), pp. 421–423, [https://doi.org/10.1016/0021-9797\(69\)90411-1](https://doi.org/10.1016/0021-9797(69)90411-1).
- [44] M. J. BLUNT, B. BIJELJIC, H. DONG, O. GHARBI, S. IGLAUER, P. MOSTAGHIMI, A. PALUSZNY, AND C. PENTLAND, *Pore-scale imaging and modelling*, Advances in Water Resources, 51 (2013), pp. 197–216, <https://doi.org/10.1016/j.advwatres.2012.03.003>.
- [45] M. J. BLUNT AND P. KING, *Relative permeabilities from two- and three-dimensional pore-scale network modelling*, Transport in Porous Media, 6 (1991), pp. 407–433, <https://doi.org/10.1007/BF00136349>.
- [46] D. BONN, J. EGGERS, J. INDEKEU, J. MEUNIER, AND E. ROLLEY, *Wetting and spreading*, Reviews of Modern Physics, 81 (2009), pp. 739–805, <https://doi.org/10.1103/RevModPhys.81.739>.
- [47] C. H. BOSANQUET, *On the flow of liquids into capillary tubes*, The London, Edinburgh, and Dublin Philosophical Magazine and Journal of Science, 45 (1923), pp. 525–531, <https://doi.org/10.1080/14786442308634144>.
- [48] J. W. BOTH, K. KUMAR, J. M. NORDBOTTEN, I. S. POP, AND F. A. RADU, *Iterative linearization schemes for doubly degenerate parabolic equations*, in Numerical

- Mathematics and Advanced Applications ENUMATH 2017, F. A. Radu, K. Kumar, I. Berre, J. M. Nordbotten, and I. S. Pop, eds., Cham, 2019, Springer, pp. 49–63, https://doi.org/10.1007/978-3-319-96415-7_3.
- [49] J. W. BOTH, K. KUMAR, J. M. NORDBOTEN, AND F. A. RADU, *Anderson accelerated fixed-stress splitting schemes for consolidation of unsaturated porous media*, Computers & Mathematics with Applications, 77 (2019), pp. 1479–1502, <https://doi.org/https://doi.org/10.1016/j.camwa.2018.07.033>.
- [50] S. BOTTERO, S. M. HASSANIZADEH, P. J. KLEINGELD, AND T. J. HEIMOVAARA, *Nonequilibrium capillarity effects in two-phase flow through porous media at different scales*, Water Resources Research, 47 (2011), p. W10505, <https://doi.org/10.1029/2011WR010887>.
- [51] K. BOUADJILA, A. MOKRANE, S. A. SAAD, AND M. SAAD, *Numerical analysis of a finite volume scheme for two incompressible phase flow with dynamic capillary pressure*, Computers & Mathematics with Applications, 75 (2018), pp. 3614–3631, <https://doi.org/10.1016/j.camwa.2018.02.021>.
- [52] A. BOURGEAT AND M. PANFILOV, *Effective two-phase flow through highly heterogeneous porous media: Capillary nonequilibrium effects*, Computational Geosciences, 2 (1998), pp. 191–215, <https://doi.org/10.1023/A:1011502303588>.
- [53] K. BRENNER, C. CANCÈS, AND D. HILHORST, *Finite volume approximation for an immiscible two-phase flow in porous media with discontinuous capillary pressure*, Computational Geosciences, 17 (2013), pp. 573–597, <https://doi.org/10.1007/s10596-013-9345-3>.
- [54] K. BRENNER, R. MASSON, E. H. QUENJEL, AND J. DRONIOU, *Total velocity-based finite volume discretization of two-phase Darcy flow in highly heterogeneous media with discontinuous capillary pressure*, IMA Journal of Numerical Analysis, 42 (2021), pp. 1231–1272, <https://doi.org/10.1093/imanum/drab018>.
- [55] F. BREZZI AND M. FORTIN, *Mixed and Hybrid Finite Element Methods*, vol. 15 of Springer Series In Computational Mathematics, Springer, New York, NY, 1991, <https://doi.org/10.1007/978-1-4612-3172-1>.
- [56] F. BREZZI, T. J. R. HUGHES, L. D. MARINI, AND A. MASUD, *Mixed discontinuous Galerkin methods for Darcy flow*, Journal of Scientific Computing, 22 (2005), pp. 119–145, <https://doi.org/10.1007/s10915-004-4150-8>.
- [57] F. BREZZI, K. LIPNIKOV, AND V. SIMONCINI, *A family of mimetic finite difference methods on polygonal and polyhedral meshes*, Mathematical Models and

- Methods in Applied Sciences, 15 (2005), pp. 1533–1551, <https://doi.org/10.1142/S0218202505000832>.
- [58] C. BRINGEDAL, I. BERRE, I. S. POP, AND F. A. RADU, *A model for non-isothermal flow and mineral precipitation and dissolution in a thin strip*, Journal of Computational and Applied Mathematics, 289 (2015), pp. 346–355, <https://doi.org/10.1016/j.cam.2014.12.009>.
- [59] R. H. BROOKS AND A. T. COREY, *Properties of porous media affecting fluid flow*, Journal of the Irrigation and Drainage Division, 92 (1966), pp. 61–88, <https://doi.org/10.1061/JRCEA4.0000425>.
- [60] C.-H. BRUNEAU AND P. FABRIE, *New efficient boundary conditions for incompressible Navier-Stokes equations: A well-posedness result*, ESAIM: Mathematical Modelling and Numerical Analysis, 30 (1996), pp. 815–840, http://www.numdam.org/item/M2AN_1996__30_7_815_0/.
- [61] J. C. BUTCHER, *Numerical Methods for Ordinary Differential Equations*, John Wiley & Sons, 3 ed., 2016, <https://doi.org/10.1002/9781119121534>.
- [62] F. BUZZI, M. LENZINGER, AND B. SCHWEIZER, *Interface conditions for degenerate two-phase flow equations in one space dimension*, Analysis, 29 (2009), pp. 299–316, <https://doi.org/10.1524/anly.2009.1036>.
- [63] F. CAETANO, M. J. GANDER, L. HALPERN, AND J. SZEFTTEL, *Schwarz waveform relaxation algorithms for semilinear reaction-diffusion equations*, Networks and Heterogeneous Media, 5 (2010), pp. 487–505, <https://doi.org/10.3934/nhm.2010.5.487>.
- [64] J. CAI, T. JIN, J. KOU, S. ZOU, J. XIAO, AND Q. MENG, *Lucas–Washburn equation-based modeling of capillary-driven flow in porous systems*, Langmuir, 37 (2021), pp. 1623–1636, <https://doi.org/10.1021/acs.langmuir.0c03134>.
- [65] D.-G. CALUGARU AND D. TROMEUR-DERVOUT, *Non-overlapping DDMs to solve flow in heterogeneous porous media*, in Domain Decomposition Methods in Science and Engineering, T. J. Barth et al., eds., Springer, Berlin, Heidelberg, 2005, pp. 529–536, https://doi.org/10.1007/3-540-26825-1_55.
- [66] C. CANCÈS, *Finite volume scheme for two-phase flows in heterogeneous porous media involving capillary pressure discontinuities*, ESAIM: Mathematical Modelling and Numerical Analysis, 43 (2009), pp. 973–1001, <https://doi.org/10.1051/m2an/2009032>.
- [67] C. CANCÈS, *Asymptotic behavior of two-phase flows in heterogeneous porous media for capillarity depending only on space. II. Nonclassical shocks to*

- model oil-trapping*, SIAM Journal on Mathematical Analysis, 42 (2010), pp. 972–995, <https://doi.org/10.1137/090747993>.
- [68] C. CANCÈS AND M. PIERRE, *An existence result for multidimensional immiscible two-phase flows with discontinuous capillary pressure field*, SIAM Journal on Mathematical Analysis, 44 (2012), pp. 966–992, <https://doi.org/10.1137/11082943X>.
- [69] C. CANCÈS, I. S. POP, AND M. VOHRÁLIK, *An a posteriori error estimate for vertex-centered finite volume discretizations of immiscible incompressible two-phase flow*, Mathematics of Computation, 83 (2014), pp. 153–188, <https://doi.org/10.1090/S0025-5718-2013-02723-8>.
- [70] X. CAO AND K. MITRA, *Error estimates for a mixed finite element discretization of a two-phase porous media flow model with dynamic capillarity*, Journal of Computational and Applied Mathematics, 353 (2019), pp. 164–178, <https://doi.org/10.1016/j.cam.2018.12.022>.
- [71] X. CAO, S. F. NEMADJIEU, AND I. S. POP, *Convergence of an MPFA finite volume scheme for a two-phase porous media flow model with dynamic capillarity*, IMA Journal of Numerical Analysis, 39 (2018), pp. 512–544, <https://doi.org/10.1093/imanum/drx078>.
- [72] X. CAO AND I. S. POP, *Two-phase porous media flows with dynamic capillary effects and hysteresis: uniqueness of weak solutions*, Computers & Mathematics with Applications, 69 (2015), pp. 688–695, <https://doi.org/10.1016/j.camwa.2015.02.009>.
- [73] X. CAO AND I. S. POP, *Uniqueness of weak solutions for a pseudo-parabolic equation modeling two phase flow in porous media*, Applied Mathematics Letters, 46 (2015), pp. 25–30, <https://doi.org/10.1016/j.aml.2015.01.022>.
- [74] X. CAO AND I. S. POP, *Degenerate two-phase porous media flow model with dynamic capillarity*, Journal of Differential Equations, 260 (2016), pp. 2418–2456, <https://doi.org/10.1016/j.jde.2015.10.008>.
- [75] C. CARLENZOLI AND A. QUARTERONI, *Adaptive domain decomposition methods for advection-diffusion problems*, in Modeling, Mesh Generation, and Adaptive Numerical Methods for Partial Differential Equations, I. Babuska, W. D. Henshaw, J. E. Oliger, J. E. Flaherty, J. E. Hopcroft, and T. Tezduyar, eds., Springer, New York, 1995, pp. 165–186, https://doi.org/10.1007/978-1-4612-4248-2_9.

- [76] M. A. CELIA, E. T. BOULOUTAS, AND R. L. ZARBA, *A general mass-conservative numerical solution for the unsaturated flow equation*, Water Resources Research, 26 (1990), pp. 1483–1496, <https://doi.org/10.1029/WR026i007p01483>.
- [77] R. CHEBBI, *Dynamics of liquid penetration into capillary tubes*, Journal of Colloid and Interface Science, 315 (2007), pp. 255–260, <https://doi.org/10.1016/j.jcis.2007.06.073>.
- [78] J.-D. CHEN, *Experiments on a spreading drop and its contact angle on a solid*, Journal of Colloid and Interface Science, 122 (1988), pp. 60–72, [https://doi.org/10.1016/0021-9797\(88\)90287-1](https://doi.org/10.1016/0021-9797(88)90287-1).
- [79] B. W. CHERRY AND C. M. HOLMES, *Kinetics of wetting of surfaces by polymers*, Journal of Colloid and Interface Science, 29 (1969), pp. 174–176, [https://doi.org/10.1016/0021-9797\(69\)90367-1](https://doi.org/10.1016/0021-9797(69)90367-1).
- [80] N. CHRISTOFI AND I. B. IVSHINA, *Microbial surfactants and their use in field studies of soil remediation*, Journal of Applied Microbiology, 93 (2002), pp. 915–929, <https://doi.org/10.1046/j.1365-2672.2002.01774.x>.
- [81] O. CIOBANU, L. HALPERN, X. JUVIGNY, AND J. RYAN, *Overlapping domain decomposition applied to the Navier-Stokes equations*, in Domain Decomposition Methods in Science and Engineering XXII, T. Dickopf, M. J. Gander, L. Halpern, R. Krause, and L. Pavarino, eds., Cham, 2016, Springer, pp. 461–470, https://doi.org/10.1007/978-3-319-18827-0_47.
- [82] P. COLLI FRANZONE, L. F. PAVARINO, AND S. SCACCHI, *A numerical study of scalable cardiac electro-mechanical solvers on HPC architectures*, Frontiers in Physiology, 9 (2018), <https://doi.org/10.3389/fphys.2018.00268>.
- [83] R. G. COX, *The dynamics of the spreading of liquids on a solid surface. Part 1. Viscous flow*, Journal of Fluid Mechanics, 168 (1986), pp. 169–194, <https://doi.org/10.1017/S0022112086000332>.
- [84] J. H. CUSHMAN, L. S. BENNETHUM, AND B. X. HU, *A primer on upscaling tools for porous media*, Advances in Water Resources, 25 (2002), pp. 1043–1067, [https://doi.org/10.1016/S0309-1708\(02\)00047-7](https://doi.org/10.1016/S0309-1708(02)00047-7).
- [85] H. K. DAHLE AND M. A. CELIA, *A dynamic network model for two-phase immiscible flow*, Computational Geosciences, 3 (1999), pp. 1–22, <https://doi.org/10.1023/A:1011522808132>.
- [86] H. P. G. DARCY, *Les Fontaines publiques de la ville de Dijon. Exposition et application des principes à suivre et des formules à employer dans les questions de distribution d'eau, etc*, V. Dalamont, 1856.

- [87] P. G. DE GENNES, *Wetting: Statics and dynamics*, Reviews of Modern Physics, 57 (1985), pp. 827–863, <https://doi.org/10.1103/RevModPhys.57.827>.
- [88] Q. DENG, *Timely communication: An analysis for a nonoverlapping domain decomposition iterative procedure*, SIAM Journal of Scientific Computing, 18 (1997), pp. 1517–1525, <https://doi.org/10.1137/S1064827595286797>.
- [89] P. DEUFLHARD, *Newton Methods For Nonlinear Problems: Affine Invariance and Adaptive Algorithms*, vol. 35 of Springer Series in Computational Mathematics, Springer Berlin Heidelberg, 2005, <https://doi.org/10.1007/978-3-642-23899-4>.
- [90] D. A. DI PIETRO AND A. ERN, *Mathematical Aspects of Discontinuous Galerkin Methods*, vol. 69 of Mathématiques et Applications, Springer, Berlin, Heidelberg, 2012, <https://doi.org/10.1007/978-3-642-22980-0>.
- [91] D. A. DICARLO, *Experimental measurements of saturation overshoot on infiltration*, Water Resources Research, 40 (2004), p. W04215, <https://doi.org/10.1029/2003WR002670>.
- [92] H.-J. G. DIERSCH, V. CLAUSNITZER, V. MYRNYI, R. ROSATI, M. SCHMIDT, H. BERUDA, B. J. EHRSPEGER, AND R. VIRGILIO, *Modeling unsaturated flow in absorbent swelling porous media: Part 1. Theory*, Transport in Porous Media, 83 (2010), pp. 437–464, <https://doi.org/10.1007/s11242-009-9454-6>.
- [93] V. DOLEAN, P. JOLIVET, AND F. NATAF, *An Introduction to Domain Decomposition Methods: Algorithms, Theory, and Parallel Implementation*, vol. 144 of Other Titles in Applied Mathematics, Society for Industrial and Applied Mathematics, 2015, <https://doi.org/10.1137/1.9781611974065>.
- [94] V. DOLEJŠÍ AND M. FEISTAUER, *Discontinuous Galerkin Method: Analysis and Applications to Compressible Flow*, vol. 48 of Springer Series in Computational Mathematics, Springer, Cham, 2015, <https://doi.org/10.1007/978-3-319-19267-3>.
- [95] F. DOSTER, P. A. ZEGELING, AND R. HILFER, *Numerical solutions of a generalized theory for macroscopic capillarity*, Physical Review E, 81 (2010), p. 036307, <https://doi.org/10.1103/PhysRevE.81.036307>.
- [96] J. DRONIOU AND R. EYMARD, *High-order mass-lumped schemes for nonlinear degenerate elliptic equations*, SIAM Journal of Numerical Analysis, 58 (2020), pp. 153–188, <https://doi.org/10.1137/19M1244500>.
- [97] E. B. DUSSAN V., *On the spreading of liquids on solid surfaces: Static and dynamic contact lines*, Annual Review of Fluid Mechanics, 11 (1979), pp. 371–400, <https://doi.org/10.1146/annurev.fl.11.010179.002103>.

- [98] E. B. DUSSAN V. AND S. H. DAVIS, *On the motion of a fluid-fluid interface along a solid surface*, Journal of Fluid Mechanics, 65 (1974), pp. 71–95, <https://doi.org/10.1017/S0022112074001261>.
- [99] G. ENCHÉRY, R. EYMARD, AND A. MICHEL, *Numerical approximation of a two-phase flow problem in a porous medium with discontinuous capillary forces*, SIAM Journal of Numerical Analysis, 43 (2006), pp. 2402–2422, <https://doi.org/10.1137/040602936>.
- [100] Y. EPSHTEYN AND B. M. RIVIÈRE, *Fully implicit discontinuous finite element methods for two-phase flow*, Applied Numerical Mathematics, 57 (2007), pp. 383–401, <https://doi.org/10.1016/j.apnum.2006.04.004>.
- [101] Y. EPSHTEYN AND B. M. RIVIÈRE, *Analysis of hp discontinuous Galerkin methods for incompressible two-phase flow*, Journal of Computational and Applied Mathematics, 225 (2009), pp. 487–509, <https://doi.org/10.1016/j.cam.2008.08.026>.
- [102] A. ERN, I. MOZOLEVSKI, AND L. SCHUH, *Discontinuous Galerkin approximation of two-phase flows in heterogeneous porous media with discontinuous capillary pressures*, Computer Methods in Applied Mechanics and Engineering, 199 (2010), pp. 1491–1501, <https://doi.org/10.1016/j.cma.2009.12.014>.
- [103] L. C. EVANS, *Partial Differential Equations*, vol. 19 of Graduate Studies in Mathematics, American Mathematical Society, Providence, RI, second ed., 2010.
- [104] R. E. EWING AND M. F. WHEELER, *Galerkin methods for miscible displacement problems in porous media*, SIAM Journal of Numerical Analysis, 17 (1980), pp. 351–365, <https://doi.org/10.1137/0717029>.
- [105] R. EYMARD, T. GALLOUËT, AND R. HERBIN, *Finite volume methods*, in Solution of Equation in \mathbb{R}^n (Part 3), Techniques of Scientific Computing (Part 3), P. G. Ciarlet and J. L. Lions, eds., vol. 7 of Handbook of Numerical Analysis, Elsevier, North Holland, 2000, pp. 713–1020, [https://doi.org/10.1016/S1570-8659\(00\)07005-8](https://doi.org/10.1016/S1570-8659(00)07005-8).
- [106] R. EYMARD, C. GUICHARD, R. HERBIN, AND R. MASSON, *Gradient schemes for two-phase flow in heterogeneous porous media and Richards equation*, Zeitschrift für Angewandte Mathematik und Mechanik, 94 (2014), pp. 560–585, <https://doi.org/10.1002/zamm.201200206>.
- [107] M. S. FABIEN, M. G. KNEPLEY, AND B. M. RIVIÈRE, *A hybridizable discontinuous Galerkin method for two-phase flow in heterogeneous porous media*, Inter-

- national Journal for Numerical Methods in Engineering, 116 (2018), pp. 161–177, <https://doi.org/10.1002/nme.5919>.
- [108] M. FERMIGIER AND P. JENFFER, *An experimental investigation of the dynamic contact angle in liquid-liquid systems*, Journal of Colloid and Interface Science, 146 (1991), pp. 226–241, [https://doi.org/10.1016/0021-9797\(91\)90020-9](https://doi.org/10.1016/0021-9797(91)90020-9).
- [109] N. FRIES AND M. DREYER, *An analytic solution of capillary rise restrained by gravity*, Journal of Colloid and Interface Science, 320 (2008), pp. 259–263, <https://doi.org/10.1016/j.jcis.2008.01.009>.
- [110] N. FRIES AND M. DREYER, *The transition from inertial to viscous flow in capillary rise*, Journal of Colloid and Interface Science, 327 (2008), pp. 125–128, <https://doi.org/10.1016/j.jcis.2008.08.018>.
- [111] M. J. GANDER, *Overlapping Schwarz for parabolic problems*, in Ninth International Conference on Domain Decomposition, P. E. Bjørstad, M. S. Espedal, and D. E. Keyes, eds., DDM.org, 1996, pp. 97–104, <http://www.ddm.org/DD9/Gander.pdf>.
- [112] M. J. GANDER, *A waveform relaxation algorithm with overlapping splitting for reaction diffusion equations*, Numerical Linear Algebra with Applications, 6 (1999), pp. 125–145, [https://doi.org/10.1016/S0021-9797\(99\)00074-4](https://doi.org/10.1016/S0021-9797(99)00074-4).
- [113] M. J. GANDER, *Optimized Schwarz methods*, SIAM Journal of Numerical Analysis, 44 (2006), pp. 699–731, <https://doi.org/10.1137/S0036142903425409>.
- [114] M. J. GANDER, *Schwarz methods over the course of time*, Electronic Transactions on Numerical Analysis, 31 (2008), pp. 228–255, <https://etna.math.kent.edu/volumes/2001-2010/vol31/abstract.php?vol=31&pages=228-255>.
- [115] M. J. GANDER, *50 years of time parallel time integration*, in Multiple Shooting and Time Domain Decomposition Methods, T. Carraro, M. Geiger, K. S., and R. Rannacher, eds., vol. 9 of Contributions in Mathematical and Computational Sciences, Springer, Cham, 2015, pp. 69–113, https://doi.org/10.1007/978-3-319-23321-5_3.
- [116] M. J. GANDER AND O. DUBOIS, *Optimized Schwarz methods for a diffusion problem with discontinuous coefficient*, Numerical Algorithms, 69 (2015), pp. 109–144, <https://doi.org/10.1007/s11075-014-9884-2>.
- [117] M. J. GANDER, L. GOUARIN, AND L. HALPERN, *Optimized Schwarz waveform relaxation methods: A large scale numerical study*, in Domain Decomposition

- Methods in Science and Engineering XIX, Y. Huang, R. Kornhuber, O. Widlund, and J. Xu, eds., Berlin, Heidelberg, 2011, Springer, pp. 261–268, https://doi.org/10.1007/978-3-642-11304-8_29.
- [118] M. J. GANDER AND L. HALPERN, *Absorbing boundary conditions for the wave equation and parallel computing*, Mathematics of Computation, 74 (2004), pp. 153–176, <https://doi.org/10.1090/S0025-5718-04-01635-7>.
- [119] M. J. GANDER AND L. HALPERN, *Optimized Schwarz waveform relaxation methods for advection reaction diffusion problems*, SIAM Journal of Numerical Analysis, 45 (2007), pp. 666–697, <https://doi.org/10.1137/050642137>.
- [120] M. J. GANDER, L. HALPERN, AND V. MARTIN, *A new algorithm based on factorization for heterogeneous domain decomposition*, Numerical Algorithms, 73 (2016), pp. 167–195, <https://doi.org/10.1007/s11075-015-0091-6>.
- [121] M. J. GANDER, L. HALPERN, AND V. MARTIN, *Multiscale analysis of heterogeneous domain decomposition methods for time-dependent advection reaction diffusion problems*, Journal of Computational and Applied Mathematics, 344 (2018), pp. 904–924, <https://doi.org/10.1016/j.cam.2018.05.058>.
- [122] M. J. GANDER, L. HALPERN, AND F. NATAF, *Optimal convergence for overlapping and non-overlapping Schwarz waveform relaxation*, in Eleventh International Conference of Domain Decomposition Methods, C.-H. Lai, P. E. Bjørstad, M. Cross, and O. B. Widlund, eds., DDM.org, 1999, <http://www.ddm.org/DD11/Gander.pdf>.
- [123] M. J. GANDER, L. HALPERN, AND F. NATAF, *Optimal Schwarz waveform relaxation for the one dimensional wave equation*, SIAM Journal of Numerical Analysis, 41 (2003), pp. 1643–1681, <https://doi.org/10.1137/S003614290139559X>.
- [124] M. J. GANDER, S. B. LUNOWA, AND C. ROHDE, *Non-overlapping Schwarz waveform-relaxation for nonlinear advection-diffusion equations*. UHasselt CMAT Preprint available at www.uhasselt.be/media/mufgoyse/up2103.pdf, 2021.
- [125] M. J. GANDER, S. B. LUNOWA, AND C. ROHDE, *Consistent and asymptotic-preserving finite-volume Robin transmission conditions for singularly perturbed elliptic equations*, in Domain Decomposition Methods in Science and Engineering XXVI, S. C. Brenner, E. T. S. Chung, A. Klawonn, F. Kwok, J. Xu, and J. Zou, eds., Lecture Notes in Computational Science and Engineering, Cham, 2022, Springer, pp. 419–426. In Press. link.springer.com/book/9783030950248.

- [126] M. J. GANDER, F. MAGOULÈS, AND F. NATAF, *Optimized Schwarz methods without overlap for the Helmholtz equation*, SIAM Journal of Scientific Computing, 24 (2002), pp. 38–23, <https://doi.org/10.1137/S1064827501387012>.
- [127] M. J. GANDER AND C. ROHDE, *Overlapping Schwarz waveform relaxation for convection-dominated nonlinear conservation laws*, SIAM Journal of Scientific Computing, 27 (2005), pp. 415–439, <https://doi.org/10.1137/030601090>.
- [128] M. J. GANDER AND A. M. STUART, *Space-time continuous analysis of waveform relaxation for the heat equation*, SIAM Journal of Scientific Computing, 19 (1998), pp. 2014–2031, <https://doi.org/10.1137/S1064827596305337>.
- [129] M. J. GANDER AND H. ZHANG, *A class of iterative solvers for the Helmholtz equation: Factorizations, sweeping preconditioners, source transfer, single layer potentials, polarized traces, and optimized Schwarz methods*, SIAM Review, 61 (2019), pp. 3–76, <https://doi.org/10.1137/16M109781X>.
- [130] F. GASTALDI, L. GASTALDI, AND A. QUARTERONI, *ADN and ARN domain decomposition methods for advection-diffusion equations*, in Ninth International Conference On Domain Decomposition Methods, P. E. Bjørstad, M. S. Espedal, and D. E. Keyes, eds., DDM.org, 1998, pp. 334–341, <http://www.ddm.org/DD9/Gastaldi.pdf>.
- [131] D. GÉRARD-VARET AND N. MASMOUDI, *Relevance of the slip condition for fluid flows near an irregular boundary*, Communications in Mathematical Physics, 295 (2010), pp. 99–137, <https://doi.org/10.1007/s00220-009-0976-0>.
- [132] T. GHOSH, C. BRINGEDAL, R. HELMIG, AND G. P. RAJA SEKHAR, *Upscaled equations for two-phase flow in highly heterogeneous porous media: Varying permeability and porosity*, Advances in Water Resources, 145 (2020), p. 103716, <https://doi.org/10.1016/j.advwatres.2020.103716>.
- [133] E. GILADI AND H. B. KELLER, *Space-time domain decomposition for parabolic problems*, Numerische Mathematik, 93 (2002), pp. 279–313, <https://doi.org/10.1007/s002110100345>.
- [134] V. GIRAULT, B. M. RIVIÈRE, AND L. CAPPANERA, *A finite element method for degenerate two-phase flow in porous media. Part I: Well-posedness*, Journal of Numerical Mathematics, 29 (2021), pp. 81–101, <https://doi.org/10.1515/jnma-2020-0004>.
- [135] V. GIRAULT, B. M. RIVIÈRE, AND L. CAPPANERA, *A finite element method for degenerate two-phase flow in porous media. Part II: Convergence*, Journal of Numerical Mathematics, 29 (2021), pp. 187–219, <https://doi.org/doi:10.1515/jnma-2020-0005>.

- [136] M. A. GJENNESTAD, M. VASSVIK, S. KJELSTRUP, AND A. HANSEN, *Stable and efficient time integration of a dynamic pore network model for two-phase flow in porous media*, *Frontiers in Physics*, 6 (2018), <https://doi.org/10.3389/fphy.2018.00056>.
- [137] R. J. GLASS, T. S. STEENHUIS, AND J.-Y. PARLANGE, *Mechanism for finger persistence in homogeneous, unsaturated, porous media: Theory and verification*, *Soil Science*, 148 (1989), pp. 60–70, <https://doi.org/10.1097/00010694-198907000-00007>.
- [138] L. GONG, L. NIE, AND Y. XU, *Geometrical and topological analysis of pore space in sandstones based on X-ray computed tomography*, *Energies*, 13 (2020), p. 3774, <https://doi.org/10.3390/en13153774>.
- [139] J. GOSTICK, M. AGHIGHI, J. HINEBAUGH, T. TRANTER, M. A. HOEH, H. DAY, B. SPELLACY, M. SHARQAWY, A. BAZYLAK, A. BURNS, AND W. LEHNERT, *OpenPNM: A pore network modeling package*, *Computing in Science & Engineering*, 18 (2016), pp. 60–74, <https://doi.org/10.1109/MCSE.2016.49>.
- [140] T. GOUDON, S. KRELL, AND G. LISSONI, *DDFV method for Navier-Stokes problem with outflow boundary conditions*, *Numerische Mathematik*, 142 (2019), pp. 55–102, <https://doi.org/10.1007/s00211-018-1014-y>.
- [141] T. GOUDON, S. KRELL, AND G. LISSONI, *Non-overlapping Schwarz algorithms for the incompressible Navier-Stokes equations with DDFV discretizations*, *EMMNA*, 55 (2021), pp. 1271–1321, <https://doi.org/10.1051/m2an/2021024>.
- [142] H. P. GREENSPAN, *On the motion of a small viscous droplet that wets a surface*, *Journal of Fluid Mechanics*, 84 (1978), pp. 125–143, <https://doi.org/10.1017/S0022112078000075>.
- [143] P. GRISVARD, *Elliptic Problems in Nonsmooth Domains*, vol. 69 of *Classics in Applied Mathematics*, Society for Industrial and Applied Mathematics, Philadelphia, PA, 1985, <https://doi.org/10.1137/1.9781611972030>.
- [144] F. HÄBERLEIN AND L. HALPERN, *Optimized Schwarz waveform relaxation for nonlinear systems of parabolic type*, in *Domain Decomposition Methods in Science and Engineering XXI*, J. Erhel, M. J. Gander, L. Halpern, G. Pichot, T. Sassi, and O. Widlund, eds., Cham, 2014, Springer, pp. 29–42, https://doi.org/10.1007/978-3-319-05789-7_3.
- [145] F. HÄBERLEIN, L. HALPERN, AND A. MICHEL, *Newton-Schwarz optimised waveform relaxation Krylov accelerators for nonlinear reactive transport*, in *Domain Decomposition Methods in Science and Engineering XX*, R. Bank, M. Holst,

- O. Widlund, and J. Xu, eds., Berlin, Heidelberg, 2013, Springer, pp. 387–394, https://doi.org/10.1007/978-3-642-35275-1_45.
- [146] E. HAIRER AND G. WANNER, *Solving Ordinary Differential Equations II: Stiff and Differential-Algebraic Problems*, vol. 14 of Springer Series in Computational Mathematics, Springer-Verlag Berlin Heidelberg, 2 ed., 1996, <https://doi.org/10.1007/978-3-642-05221-7>.
- [147] E. HAIRER, G. WANNER, AND S. P. NØRSETT, *Solving Ordinary Differential Equations I: Nonstiff Problems*, vol. 8 of Springer Series in Computational Mathematics, Springer-Verlag Berlin Heidelberg, 2 ed., 1993, <https://doi.org/10.1007/978-3-540-78862-1>.
- [148] P. J. HALEY AND M. J. MIKSI, *The effect of the contact line on droplet spreading*, Journal of Fluid Mechanics, 223 (1991), pp. 57–81, <https://doi.org/10.1017/S0022112091001337>.
- [149] L. HALPERN AND J. SZEFTTEL, *Nonlinear nonoverlapping Schwarz waveform relaxation for semilinear wave propagation*, Mathematics of Computation, 78 (2009), pp. 865–889, <https://doi.org/10.1090/S0025-5718-08-02164-9>.
- [150] A. HAMRAOUI AND T. NYLANDER, *Analytical approach for the Lucas–Washburn equation*, Journal of Colloid and Interface Science, 250 (2002), pp. 415–421, <https://doi.org/10.1006/jcis.2002.8288>.
- [151] A. HAMRAOUI, K. THURESSON, T. NYLANDER, AND V. YAMINSKY, *Can a dynamic contact angle be understood in terms of a friction coefficient?*, Journal of Colloid and Interface Science, 226 (2000), pp. 199–204, <https://doi.org/10.1006/jcis.2000.6830>.
- [152] C. R. HARRIS, K. J. MILLMAN, S. J. VAN DER WALT, R. GOMMERS, P. VIRTANEN, D. COUNAPEAU, E. WIESER, J. TAYLOR, S. BERG, N. J. SMITH, R. KERN, M. PICUS, S. HOYER, M. H. VAN KERKWIJK, M. BRETT, A. HALDANE, J. F. DEL RÍO, M. WIEBE, P. PETERSON, P. GÉRARD-MARCHANT, K. SHEPPARD, T. REDDY, W. WECKESSER, H. ABBASI, C. GOHLKE, AND T. E. OLIPHANT, *Array programming with NumPy*, Nature, 585 (2020), pp. 357–362, <https://doi.org/10.1038/s41586-020-2649-2>.
- [153] S. M. HASSANIZADEH AND W. G. GRAY, *General conservation equations for multiphase systems: 1. Averaging procedure*, Advances in Water Resources, 2 (1979), pp. 131–144, [https://doi.org/10.1016/0309-1708\(79\)90025-3](https://doi.org/10.1016/0309-1708(79)90025-3).
- [154] S. M. HASSANIZADEH AND W. G. GRAY, *Thermodynamic basis of capillary pressure in porous media*, Water Resources Research, 29 (1993), pp. 3389–3405, <https://doi.org/10.1029/93WR01495>.

- [155] S. M. HASSANIZADEH AND W. G. GRAY, *Toward an improved description of the physics of two-phase flow*, *Advances in Water Resources*, 16 (1993), pp. 53–67, [https://doi.org/10.1016/0309-1708\(93\)90029-F](https://doi.org/10.1016/0309-1708(93)90029-F).
- [156] R. HELMIG, *Multiphase Flow and Transport Processes in the Subsurface: A Contribution to the Modeling of Hydrosystems*, *Environmental Science and Engineering*, Springer, Berlin, Heidelberg, 1997.
- [157] R. HELMIG, A. WEISS, AND B. I. WOHLMUTH, *Dynamic capillary effects in heterogeneous porous media*, *Computational Geosciences*, 11 (2007), pp. 261–274, <https://doi.org/10.1007/s10596-007-9050-1>.
- [158] R. HELMIG, A. WEISS, AND B. I. WOHLMUTH, *Variational inequalities for modeling flow in heterogeneous porous media with entry pressure*, *Computational Geosciences*, 13 (2009), pp. 373–389, <https://doi.org/10.1007/s10596-008-9125-7>.
- [159] P. HENNING, M. OHLBERGER, AND B. SCHWEIZER, *Homogenization of the degenerate two-phase flow equations*, *Mathematical Models and Methods in Applied Sciences*, 23 (2013), pp. 2323–2352, <https://doi.org/10.1142/S0218202513500334>.
- [160] M. HESHMATI AND M. PIRI, *Experimental investigation of dynamic contact angle and capillary rise in tubes with circular and noncircular cross sections*, *Langmuir*, 30 (2014), pp. 14151–14162, <https://doi.org/10.1021/la501724y>.
- [161] J. S. HESTHAVEN AND T. WARBURTON, *Nodal Discontinuous Galerkin Methods: Algorithms, Analysis, and Applications*, vol. 54 of *Texts in Applied Mathematics*, Springer, New York, NY, 2008, <https://doi.org/10.1007/978-0-387-72067-8>.
- [162] R. HILFER, *Capillary pressure, hysteresis and residual saturation in porous media*, *Physica A: Statistical Mechanics and its Applications*, 359 (2006), pp. 119–128, <https://doi.org/10.1016/j.physa.2005.05.086>.
- [163] R. HILFER, *Macroscopic capillarity and hysteresis for flow in porous media*, *Physical Review E*, 73 (2006), p. 016307, <https://doi.org/10.1103/PhysRevE.73.016307>.
- [164] R. HILFER, *Macroscopic capillarity without a constitutive capillary pressure function*, *Physica A: Statistical Mechanics and its Applications*, 371 (2006), pp. 209–225, <https://doi.org/10.1016/j.physa.2006.04.051>.
- [165] R. HILFER, F. DOSTER, AND P. A. ZEGELING, *Nonmonotone saturation profiles for hydrostatic equilibrium in homogeneous porous media*, *Vadose Zone Journal*, 11 (2012), pp. vzj2012–0021, <https://doi.org/10.2136/vzj2012.0021>.

- [166] R. HILFER AND R. STEINLE, *Saturation overshoot and hysteresis for twophase flow in porous media*, The European Physical Journal Special Topics, 223 (2014), pp. 2323–2338, <https://doi.org/10.1140/epjst/e2014-02267-x>.
- [167] L. M. HOCKING, *A moving fluid interface on a rough surface*, Journal of Fluid Mechanics, 76 (1976), pp. 801–817, <https://doi.org/10.1017/S0022112076000906>.
- [168] R. L. HOFFMAN, *A study of the advancing interface. I. Interface shape in liquid–gas systems*, Journal of Colloid and Interface Science, 50 (1975), pp. 228–241, [https://doi.org/10.1016/0021-9797\(75\)90225-8](https://doi.org/10.1016/0021-9797(75)90225-8).
- [169] U. HORNUNG, ed., *Homogenization and Porous Media*, vol. 6 of Interdisciplinary Applied Mathematics, Springer, New York, NY, 1997, <https://doi.org/10.1007/978-1-4612-1920-0>.
- [170] C. HUH AND S. G. MASON, *Effects of surface roughness on wetting (theoretical)*, Journal of Colloid and Interface Science, 60 (1977), pp. 11–38, [https://doi.org/10.1016/0021-9797\(77\)90251-X](https://doi.org/10.1016/0021-9797(77)90251-X).
- [171] C. HUH AND S. G. MASON, *The steady movement of a liquid meniscus in a capillary tube*, Journal of Fluid Mechanics, 81 (1977), pp. 401–419, <https://doi.org/10.1017/S0022112077002134>.
- [172] C. HUH AND L. E. SCRIVEN, *Hydrodynamic model of steady movement of a solid/liquid/fluid contact line*, Journal of Colloid and Interface Science, 35 (1971), pp. 85–101, [https://doi.org/10.1016/0021-9797\(71\)90188-3](https://doi.org/10.1016/0021-9797(71)90188-3).
- [173] O. ILIEV, A. MIKELIĆ, T. PRILL, AND A. SHERLY, *Homogenization approach to the upscaling of a reactive flow through particulate filters with wall integrated catalyst*, Advances in Water Resources, 146 (2020), p. 103779, <https://doi.org/10.1016/j.advwatres.2020.103779>.
- [174] D. ILLIANO, J. W. BOTH, I. S. POP, AND F. A. RADU, *Efficient solvers for nonstandard models for flow and transport in unsaturated porous media*. ArXiv preprint 2012.14773, 2020, <https://arxiv.org/abs/2012.14773>.
- [175] W. JÄGER AND J. KAČUR, *Solution of doubly nonlinear and degenerate parabolic problems by relaxation schemes*, ESAIM: Mathematical Modelling and Numerical Analysis, 29 (1995), pp. 605–627, http://www.numdam.org/item/M2AN_1995__29_5_605_0/.
- [176] S. JIN, *Asymptotic preserving (AP) schemes for multiscale kinetic and hyperbolic equations: a review*, Rivista di Matematica della Università di Parma. New Series. A Journal of Pure and Applied Mathematics, 3 (2012), pp. 177–216, <http://www.rivmat.unipr.it/vols/2012-3-2/01.html>.

- [177] V. JOEKAR-NIASAR AND S. M. HASSANIZADEH, *Effect of fluids properties on non-equilibrium capillarity effects: Dynamic pore-network modeling*, International Journal of Multiphase Flow, 37 (2011), pp. 198–214, <https://doi.org/10.1016/j.ijmultiphaseflow.2010.09.007>.
- [178] V. JOEKAR-NIASAR AND S. M. HASSANIZADEH, *Analysis of fundamentals of two-phase flow in porous media using dynamic pore-network models: A review*, Critical Reviews in Environmental Science and Technology, 42 (2012), pp. 1895–1976, <https://doi.org/10.1080/10643389.2011.574101>.
- [179] V. JOEKAR-NIASAR, S. M. HASSANIZADEH, AND H. K. DAHLE, *Non-equilibrium effects in capillarity and interfacial area in two-phase flow: dynamic pore-network modelling*, Journal of Fluid Mechanics, 655 (2010), pp. 38–71, <https://doi.org/10.1017/S00222112010000704>.
- [180] V. JOEKAR-NIASAR, S. M. HASSANIZADEH, AND A. LEIJNSE, *Insights into the relationships among capillary pressure, saturation, interfacial area and relative permeability using pore-network modeling*, Transport in Porous Media, 74 (2008), pp. 201–219, <https://doi.org/10.1007/s11242-007-9191-7>.
- [181] P. JOLIVET, F. HECHT, F. NATAF, AND C. PRUD'HOMME, *Scalable domain decomposition preconditioners for heterogeneous elliptic problems*, in Proceedings of the International Conference on High Performance Computing, Networking, Storage and Analysis (SC '13), New York, NY, 2013, Association for Computing Machinery, <https://doi.org/10.1145/2503210.2503212>.
- [182] M. S. JOSHAGHANI, V. GIRAULT, AND B. M. RIVIÈRE, *A vertex scheme for two-phase flow in heterogeneous media*, Journal of Computational Physics, 449 (2022), p. 110778, <https://doi.org/10.1016/j.jcp.2021.110778>.
- [183] M. S. JOSHAGHANI, B. M. RIVIÈRE, AND M. SEKACHEV, *Maximum-principle-satisfying discontinuous Galerkin methods for incompressible two-phase immiscible flow*, Computer Methods in Applied Mechanics and Engineering, 391 (2022), p. 114550, <https://doi.org/10.1016/j.cma.2021.114550>.
- [184] W. JÄGER AND J. KAČUR, *Solution of porous medium type systems by linear approximation schemes*, Numerische Mathematik, 60 (1991), pp. 407–427, <https://doi.org/10.1007/BF01385729>.
- [185] W. JÄGER AND A. MIKELIĆ, *On the roughness-induced effective boundary conditions for an incompressible viscous flow*, Journal of Differential Equations, 170 (2001), pp. 96–122, <https://doi.org/10.1006/jdeq.2000.3814>.
- [186] S. KARPINSKI AND I. S. POP, *Analysis of an interior penalty discontinuous Galerkin scheme for two phase flow in porous media with dynamic cap-*

- illary effects*, Numerische Mathematik, 136 (2017), pp. 249–286, <https://doi.org/10.1007/s00211-016-0839-5>.
- [187] S. KARPINSKI, I. S. POP, AND F. A. RADU, *Analysis of a linearization scheme for an interior penalty discontinuous Galerkin method for two-phase flow in porous media with dynamic capillarity effects*, International Journal for Numerical Methods in Engineering, 112 (2017), pp. 553–577, <https://doi.org/https://doi.org/10.1002/nme.5526>.
- [188] H. P. KAVEHPOUR, B. OVRYN, AND G. H. MCKINLEY, *Microscopic and macroscopic structure of the precursor layer in spreading viscous drops*, Physical Review Letters, 91 (2003), p. 196104, <https://doi.org/10.1103/PhysRevLett.91.196104>.
- [189] S. F. KISTLER, *Hydrodynamics of wetting*, in Wettability, J. C. Berg, ed., Marcel Dekker, New York, NY, 1993, pp. 311–430.
- [190] A. KLAWONN, S. KÖHLER, M. LANSER, AND O. RHEINBACH, *Computational homogenization with million-way parallelism using domain decomposition methods*, Computational Mechanics, 65 (2020), pp. 1–22, <https://doi.org/10.1007/s00466-019-01749-5>.
- [191] J. KOCH, A. RÄTZ, AND B. SCHWEIZER, *Two-phase flow equations with a dynamic capillary pressure*, European Journal of Applied Mathematics, 24 (2013), pp. 49–75, <https://doi.org/10.1017/S0956792512000307>.
- [192] J. KOPLIK AND J. R. BANAVAR, *Continuum deductions from molecular hydrodynamics*, Annual Review of Fluid Mechanics, 27 (1995), pp. 257–292, <https://doi.org/10.1146/annurev.fl.27.010195.001353>.
- [193] J. KOPLIK, J. R. BANAVAR, AND J. F. WILLEMSSEN, *Molecular dynamics of Poiseuille flow and moving contact lines*, Physical Review Letters, 60 (1988), pp. 1282–1285, <https://doi.org/10.1103/PhysRevLett.60.1282>.
- [194] J. KOPLIK, J. R. BANAVAR, AND J. F. WILLEMSSEN, *Molecular dynamics of fluid flow at solid surfaces*, Physics of Fluids A: Fluid Dynamics, 1 (1989), pp. 781–794, <https://doi.org/10.1063/1.857376>.
- [195] J. KOPLIK AND T. J. LASSETER, *Two-phase flow in random network models of porous media*, Society of Petroleum Engineers Journal, 25 (1985), pp. 89–100, <https://doi.org/10.2118/11014-PA>.
- [196] S. KRÄUTLE, *The semismooth newton method for multicomponent reactive transport with minerals*, Advances in Water Resources, 34 (2011), pp. 137–151, <https://doi.org/10.1016/j.advwatres.2010.10.004>.

- [197] K. KUMAR, T. L. VAN NOORDEN, AND I. S. POP, *Effective dispersion equations for reactive flows involving free boundaries at the microscale*, Multiscale Modeling and Simulation, 9 (2011), pp. 29–58, <https://doi.org/10.1137/100804553>.
- [198] A. KURGANOV AND G. PETROVA, *Central-upwind schemes on triangular grids for hyperbolic systems of conservation laws*, Numerical Methods for Partial Differential Equations, 21 (2005), pp. 536–552, <https://doi.org/10.1002/num.20049>.
- [199] O. A. LADYŽENSKAJA, V. A. SOLONNIKOV, AND N. N. URAL'CEVA, *Linear and Quasilinear Equations of Parabolic Type*, vol. 23 of Translations of Mathematical Monographs, American Mathematical Society, Providence, RI, 1968.
- [200] L. W. LAKE, *Enhanced oil recovery*, Prentice Hall Inc., Old Tappan, NJ, 1989.
- [201] A. LAMACZ, A. RÄTZ, AND B. SCHWEIZER, *A well-posed hysteresis model for flows in porous media and applications to fingering effects*, Advances in Mathematical Sciences and Applications, 21 (2011), pp. 33–64.
- [202] D. LANDA-MARBÁN, N. LIU, I. S. POP, K. KUMAR, P. PETTERSSON, G. BØDTKER, T. SKAUGE, AND F. A. RADU, *A pore-scale model for permeable biofilm: Numerical simulations and laboratory experiments*, Transport in Porous Media, 127 (2019), pp. 643–660, <https://doi.org/10.1007/s11242-018-1218-8>.
- [203] N. LE GRAND, A. DAERR, AND L. LIMAT, *Shape and motion of drops sliding down an inclined plane*, Journal of Fluid Mechanics, 541 (2005), pp. 293–315, <https://doi.org/10.1017/S0022112005006105>.
- [204] E. LELARASMEE, A. E. RUEHLI, AND A. L. SANGIOVANNI-VINCENTELLI, *The waveform relaxation method for time-domain analysis of large scale integrated circuits*, IEEE Transactions on Computer-Aided Design of Integrated Circuits and Systems, 1 (1982), pp. 131–145, <https://doi.org/10.1109/TCAD.1982.1270004>.
- [205] M. LENZINGER AND B. SCHWEIZER, *Two-phase flow equations with outflow boundary conditions in the hydrophobic–hydrophilic case*, Nonlinear Analysis: Theory, Methods & Applications, 73 (2010), pp. 840–853, <https://doi.org/10.1016/j.na.2010.03.040>.
- [206] S. LEVINE, J. LOWNDES, E. J. WATSON, AND G. NEALE, *A theory of capillary rise of a liquid in a vertical cylindrical tube and in a parallel-plate channel: Washburn equation modified to account for the meniscus with slippage at the contact line*, Journal of Colloid and Interface Science, 73 (1980), pp. 136–151, [https://doi.org/10.1016/0021-9797\(80\)90131-9](https://doi.org/10.1016/0021-9797(80)90131-9).

- [207] X. LI, X. FAN, AND S. BRANDANI, *Difference in pore contact angle and the contact angle measured on a flat surface and in an open space*, Chemical Engineering Science, 117 (2014), pp. 137–145, <https://doi.org/10.1016/j.ces.2014.06.024>.
- [208] D. LIANG AND Z. ZHOU, *The conservative splitting domain decomposition method for multicomponent contamination flows in porous media*, Journal of Computational Physics, 400 (2020), pp. 1–27, <https://doi.org/10.1016/j.jcp.2019.108974>.
- [209] P.-L. LIONS, *On the Schwarz alternating method III: A variant for nonoverlapping subdomains*, in Third International Symposium on Domain Decomposition Methods for Partial Differential Equations, T. Chan, R. Glowinski, J. Périaux, and O. Widlund, eds., Philadelphia, PA, 1990, Society for Industrial and Applied Mathematics, pp. 202–223, [http://www.ddm.org/DD03/On_the_Schwarz_Alternating_Method_III_A_Variant_for_Nonoverlapping_Subdomains_\(Lions\).pdf](http://www.ddm.org/DD03/On_the_Schwarz_Alternating_Method_III_A_Variant_for_Nonoverlapping_Subdomains_(Lions).pdf).
- [210] F. LIST AND F. A. RADU, *A study on iterative methods for solving Richards' equation*, Computational Geosciences, 20 (2016), pp. 341–353, <https://doi.org/10.1007/s10596-016-9566-3>.
- [211] P. A. LOTT, H. F. WALKER, C. S. WOODWARD, AND U. M. YANG, *An accelerated picard method for nonlinear systems related to variably saturated flow*, Advances in Water Resources, 38 (2012), pp. 92–101, <https://doi.org/10.1016/j.advwatres.2011.12.013>.
- [212] G. LUBE, L. MÜLLER, AND F.-C. OTTO, *A non-overlapping domain decomposition method for the advection-diffusion problem*, Computing, 64 (2000), pp. 49–68, <https://doi.org/10.1007/s006070050003>.
- [213] R. LUCAS, *Über das Zeitgesetz des kapillaren Aufstiegs von Flüssigkeiten*, Kolloid-Zeitschrift, 23 (1918), pp. 15–22, <https://doi.org/10.1007/BF01461107>.
- [214] S. B. LUNOWA, *Linearization and domain decomposition methods for two-phase flow in porous media*, master's thesis, Eindhoven University of Technology, The Netherlands, 2018, <https://research.tue.nl/en/studentTheses/linearization-and-domain-decomposition-methods>.
- [215] S. B. LUNOWA, *s-lunowa/AsymptoticThinStripMCLSolver: Solver for the asymptotic model of immiscible two-phase flow with moving contact line in a thin strip*, 2020, <https://github.com/s-lunowa/AsymptoticThinStripMCLSolver>.

- [216] S. B. LUNOWA, *s-lunowa/dynamic-capillary-rise: Software for fitting the up-scaled and extended model of capillary rise to experimental data*, 2021, <https://github.com/s-lunowa/dynamic-capillary-rise>.
- [217] S. B. LUNOWA, C. BRINGEDAL, AND I. S. POP, *On an averaged model for immiscible two-phase flow with surface tension and dynamic contact angle in a thin strip*, *Studies in Applied Mathematics*, 147 (2021), pp. 84–126, <https://doi.org/10.1111/sapm.12376>.
- [218] S. B. LUNOWA, A. MASCINI, C. BRINGEDAL, T. BULTREYS, V. CNUDDÉ, AND I. S. POP, *Dynamic effects during the capillary rise of fluids in cylindrical tubes*, *Langmuir*, 38 (2022), pp. 1680–1688, <https://doi.org/10.1021/acs.langmuir.1c02680>.
- [219] S. B. LUNOWA, I. S. POP, AND B. KOREN, *Linearized domain decomposition methods for two-phase porous media flow models involving dynamic capillarity and hysteresis*, *Computer Methods in Applied Mechanics and Engineering*, 372 (2020), p. 113364, <https://doi.org/10.1016/j.cma.2020.113364>.
- [220] S. B. LUNOWA, I. S. POP, AND B. KOREN, *A linear domain decomposition method for non-equilibrium two-phase flow models*, in *Numerical Mathematics and Advanced Applications ENUMATH 2019*, V. F. J. and V. C., eds., Cham, 2021, Springer, pp. 145–153, https://doi.org/10.1007/978-3-030-55874-1_13.
- [221] U. LĀCIS, P. JOHANSSON, T. FULLANA, B. HESS, G. AMBERG, S. BAGHERI, AND S. ZALESKI, *Steady moving contact line of water over a no-slip substrate*, *The European Physical Journal Special Topics*, 229 (2020), pp. 1897–1921, <https://doi.org/10.1140/epjst/e2020-900280-9>.
- [222] K.-A. MARDAL, M. E. ROGNES, T. B. THOMPSON, AND L. M. VALNES, *Mathematical Modeling of the Human Brain: From Magnetic Resonance Images to Finite Element Simulation*, vol. 10 of *Simula SpringerBriefs on Computing*, Springer, Cham, 2022, <https://doi.org/10.1007/978-3-030-95136-8>.
- [223] G. MARTIC, J. DE CONINCK, AND T. D. BLAKE, *Influence of the dynamic contact angle on the characterization of porous media*, *Journal of Colloid and Interface Science*, 263 (2003), pp. 213–216, [https://doi.org/10.1016/S0021-9797\(03\)00283-2](https://doi.org/10.1016/S0021-9797(03)00283-2).
- [224] G. MARTIC, F. GENTNER, D. SEVENO, D. COULON, J. DE CONINCK, AND T. D. BLAKE, *A molecular dynamics simulation of capillary imbibition*, *Langmuir*, 18 (2002), pp. 7971–7976, <https://doi.org/10.1021/la020068n>.

- [225] V. MARTIN, *An optimized Schwarz waveform relaxation method for the unsteady convection diffusion equation in two dimensions*, Applied Numerical Mathematics, 52 (2005), pp. 401–428, <https://doi.org/10.1016/j.apnum.2004.08.022>.
- [226] E. MARUŠIĆ-PALOKA, *Average of the Navier’s law on the rapidly oscillating boundary*, Journal of Mathematical Analysis and Applications, 259 (2001), pp. 685–701, <https://doi.org/10.1006/jmaa.2001.7505>.
- [227] E. MARUŠIĆ-PALOKA AND A. MIKELIĆ, *The derivation of a nonlinear filtration law including the inertia effects via homogenization*, Nonlinear Analysis: Theory, Methods & Applications, 42 (2000), pp. 97–137, [https://doi.org/10.1016/S0362-546X\(98\)00346-0](https://doi.org/10.1016/S0362-546X(98)00346-0).
- [228] A. MIKELIĆ, *Homogenization of nonstationary Navier-Stokes equations in a domain with a grained boundary*, Annali di Matematica Pura ed Applicata, 158 (1991), pp. 167–179, <https://doi.org/10.1007/BF01759303>.
- [229] A. MIKELIĆ, *Homogenization theory and applications to filtration through porous media*, in Filtration in Porous Media and Industrial Application, A. Fasano, ed., vol. 1734 of Lecture Notes in Mathematics, Springer, Berlin, Heidelberg, 2000, pp. 127–214, <https://doi.org/10.1007/BFb0103977>.
- [230] A. MIKELIĆ, C. J. VAN DUIN, AND I. S. POP, *Effective equations for two-phase flow with trapping on the micro scale*, SIAM Journal on Applied Mathematics, 62 (2002), pp. 1531–1568, <https://doi.org/10.1137/S0036139901385564>.
- [231] A. MIKELIĆ, *On an averaged model for the 2-fluid immiscible flow with surface tension in a thin cylindrical tube*, Computational Geosciences, 7 (2003), pp. 183–196, <https://doi.org/10.1023/A:1025527716078>.
- [232] A. MIKELIĆ, *A global existence result for the equations describing unsaturated flow in porous media with dynamic capillary pressure*, Journal of Differential Equations, 248 (2010), pp. 1561–1577, <https://doi.org/10.1016/j.jde.2009.11.022>.
- [233] A. MIKELIĆ AND L. PAOLI, *On the derivation of the Buckley-Leverett model from the two fluid Navier–Stokes equations in a thin domain*, Computational Geosciences, 1 (1997), pp. 59–83, <https://doi.org/10.1023/A:1011509010432>.
- [234] J.-P. MILIŠIĆ, *The unsaturated flow in porous media with dynamic capillary pressure*, Journal of Differential Equations, 264 (2018), pp. 5629–5658, <https://doi.org/10.1016/j.jde.2018.01.014>.

- [235] K. MITRA, T. KÖPPL, I. S. POP, C. J. VAN DUIJN, AND R. HELMIG, *Fronts in two-phase porous media flow problems: The effects of hysteresis and dynamic capillarity*, *Studies in Applied Mathematics*, 144 (2020), pp. 449–492, <https://doi.org/10.1111/sapm.12304>.
- [236] K. MITRA AND I. S. POP, *A modified L-scheme to solve nonlinear diffusion problems*, *Computers & Mathematics with Applications*, 77 (2019), pp. 1722–1738, <https://doi.org/10.1016/j.camwa.2018.09.042>.
- [237] K. MITRA AND C. J. VAN DUIJN, *Wetting fronts in unsaturated porous media: The combined case of hysteresis and dynamic capillary pressure*, *Nonlinear Analysis: Real World Applications*, 50 (2019), pp. 316–341, <https://doi.org/10.1016/j.nonrwa.2019.05.005>.
- [238] N. R. MORROW AND C. C. HARRIS, *Capillary equilibrium in porous materials*, *Society of Petroleum Engineers Journal*, 5 (1965), pp. 15–24, <https://doi.org/10.2118/1011-PA>.
- [239] F. NATAF AND F. ROGIER, *Factorization of the convection-diffusion operator and the Schwarz algorithm*, *Mathematical Models and Methods in Applied Sciences*, 5 (1995), pp. 67–93, <https://doi.org/10.1142/S021820259500005X>.
- [240] M. NEWVILLE, R. OTTEN, A. NELSON, A. INGARGIOLA, T. STENSITZKI, D. ALLAN, A. FOX, F. CARTER, MICHAŁ, D. PUSTAKHOD, LNEUHAUS, S. WEIGAND, R. OSBORN, GLENN, C. DEIL, MARK, A. L. R. HANSEN, G. PASQUEVICH, L. FOKS, N. ZOBRIST, O. FROST, A. BEELEN, STUERMER, KWERTYOPS, A. POLLORENO, S. CALDWELL, A. ALMARZA, A. PERSAUD, B. GAMARI, AND B. F. MAIER, *Imfit/Imfit-py 1.0.2*, Feb. 2021, <https://doi.org/10.5281/zenodo.4516651>.
- [241] G. NGUETSENG, *A general convergence result for a functional related to the theory of homogenization*, *SIAM Journal on Mathematical Analysis*, 20 (1989), pp. 608–623, <https://doi.org/10.1137/0520043>.
- [242] V. H. NGUYEN, A. P. SHEPPARD, M. A. KNACKSTEDT, AND W. VAL PINCZEWSKI, *The effect of displacement rate on imbibition relative permeability and residual saturation*, *Journal of Petroleum Science and Engineering*, 52 (2006), pp. 54–70, <https://doi.org/10.1016/j.petrol.2006.03.020>.
- [243] J. NIESSNER AND S. M. HASSANIZADEH, *A model for two-phase flow in porous media including fluid-fluid interfacial area*, *Water Resources Research*, 44 (2008), p. W08439, <https://doi.org/10.1029/2007WR006721>.
- [244] R. H. NOCHETTO AND C. VERDI, *Approximation of degenerate parabolic problems using numerical integration*, *SIAM Journal of Numerical Analysis*, 25 (1988), pp. 784–814, <https://doi.org/10.1137/0725046>.

- [245] J. M. NORDBOTTEN AND M. A. CELIA, *Geological Storage of CO₂: Modeling Approaches for Large-Scale Simulation*, John Wiley & Sons, Hoboken, NJ, 2011, <https://doi.org/10.1002/9781118137086>.
- [246] J. M. NORDBOTTEN, M. A. CELIA, H. K. DAHLE, AND S. M. HASSANIZADEH, *Interpretation of macroscale variables in Darcy's law*, *Water Resources Research*, 43 (2007), p. W08430, <https://doi.org/10.1029/2006WR005018>.
- [247] J. M. NORDBOTTEN, M. A. CELIA, H. K. DAHLE, AND S. M. HASSANIZADEH, *On the definition of macroscale pressure for multi-phase flow in porous media*, *Water Resources Research*, 44 (2008), p. W06S02, <https://doi.org/10.1029/2006WR005715>.
- [248] H. F. NORDHAUG, M. A. CELIA, AND H. K. DAHLE, *A pore network model for calculation of interfacial velocities*, *Advances in Water Resources*, 26 (2003), pp. 1061–1074, [https://doi.org/10.1016/S0309-1708\(03\)00100-3](https://doi.org/10.1016/S0309-1708(03)00100-3).
- [249] A. PAPAFOIOU, H. SHETA, AND R. HELMIG, *Numerical modeling of two-phase hysteresis combined with an interface condition for heterogeneous porous media*, *Computational Geosciences*, 14 (2009), pp. 273–287, <https://doi.org/10.1007/s10596-009-9151-0>.
- [250] J. C. PARKER AND R. J. LENHARD, *A model for hysteretic constitutive relations governing multiphase flow: 1. saturation-pressure relations*, *Water Resources Research*, 23 (1987), pp. 2187–2196, <https://doi.org/10.1029/WR023i012p02187>.
- [251] M. PESZYNSKA AND S.-Y. YI, *Numerical methods for unsaturated flow with dynamic capillary pressure in heterogeneous porous media*, *International Journal of Numerical Analysis and Modeling*, 5 (2008), pp. 126–149, <https://www.math.ualberta.ca/ijnam/Volume-5-2008/Special-08/09.pdf>.
- [252] D. PICCHI AND I. BATTIATO, *The impact of pore-scale flow regimes on upscaling of immiscible two-phase flow in porous media*, *Water Resources Research*, 54 (2018), pp. 6683–6707, <https://doi.org/10.1029/2018WR023172>.
- [253] M. PIRI AND M. J. BLUNT, *Three-dimensional mixed-wet random pore-scale network modeling of two- and three-phase flow in porous media. I. Model description*, *Physical Review E*, 71 (2005), p. 026301, <https://doi.org/10.1103/PhysRevE.71.026301>.
- [254] I. S. POP, F. A. RADU, AND P. KNABNER, *Mixed finite elements for the richards' equation: linearization procedure*, *Journal of Computational and Applied Mathematics*, 168 (2004), pp. 365–373, <https://doi.org/10.1016/j.cam.2003.04.008>.

- [255] I. S. POP, C. J. VAN DUIN, J. NIESSNER, AND S. M. HASSANIZADEH, *Horizontal redistribution of fluids in a porous medium: The role of interfacial area in modeling hysteresis*, *Advances in Water Resources*, 32 (2009), pp. 383–390, <https://doi.org/10.1016/j.advwatres.2008.12.006>.
- [256] M. N. POPESCU, J. RALSTON, AND R. SEDEV, *Capillary rise with velocity-dependent dynamic contact angle*, *Langmuir*, 24 (2008), pp. 12710–12716, <https://doi.org/10.1021/la801753t>.
- [257] T. QIAN, X.-P. WANG, AND P. SHENG, *A variational approach to moving contact line hydrodynamics*, *Journal of Fluid Mechanics*, 564 (2006), p. 333–360, <https://doi.org/10.1017/S0022112006001935>.
- [258] C. QIN AND S. HASSANIZADEH, *Multiphase flow through multilayers of thin porous media: General balance equations and constitutive relationships for a solid–gas–liquid three-phase system*, *International Journal of Heat and Mass Transfer*, 70 (2014), pp. 693–708, <https://doi.org/10.1016/j.ijheatmasstransfer.2013.11.059>.
- [259] A. QUARTERONI AND A. VALLI, *Domain Decomposition Methods for Partial Differential Equations*, Oxford Science Publications, Oxford, UK, 1999.
- [260] D. QUÉRÉ, *Inertial capillarity*, *Europhysics Letters*, 39 (1997), pp. 533–538, <https://doi.org/10.1209/epl/i1997-00389-2>.
- [261] M. QUINTARD AND S. WHITAKER, *Two-phase flow in heterogeneous porous media: The method of large-scale averaging*, *Transport in Porous Media*, 3 (1988), pp. 357–413, <https://doi.org/10.1007/BF00233177>.
- [262] F. A. RADU, K. KUMAR, J. M. NORDBOTTEN, AND I. S. POP, *A robust, mass conservative scheme for two-phase flow in porous media including Hölder continuous nonlinearities*, *IMA Journal of Numerical Analysis*, 38 (2017), pp. 884–920, <https://doi.org/10.1093/imanum/drx032>.
- [263] F. A. RADU, J. M. NORDBOTTEN, I. S. POP, AND K. KUMAR, *A robust linearization scheme for finite volume based discretizations for simulation of two-phase flow in porous media*, *Journal of Computational and Applied Mathematics*, 289 (2015), pp. 134–141, <https://doi.org/10.1016/j.cam.2015.02.051>.
- [264] F. A. RADU, I. S. POP, AND P. KNABNER, *Newton-type methods for the mixed finite element discretization of some degenerate parabolic equations*, in *Numerical Mathematics and Advanced Applications ENUMATH 2005*, A. B. de Castro, D. Gómez, P. Quintela, and P. Salgado, eds., Berlin, Heidelberg, 2006, Springer, pp. 1192–1200, https://doi.org/10.1007/978-3-540-34288-5_120.

- [265] J. RALSTON, M. POPESCU, AND R. SEDEV, *Dynamics of wetting from an experimental point of view*, Annual Review of Materials Research, 38 (2008), pp. 23–43, <https://doi.org/10.1146/annurev.matsci.38.060407.130231>.
- [266] T. RAMAKRISHNAN, P. WU, H. ZHANG, AND D. T. WASAN, *Dynamics in closed and open capillaries*, Journal of Fluid Mechanics, 872 (2019), pp. 5–38, <https://doi.org/10.1017/jfm.2019.328>.
- [267] T. RAMSTAD, C. F. BERG, AND K. THOMPSON, *Pore-scale simulations of single- and two-phase flow in porous media: Approaches and applications*, Transport in Porous Media, 130 (2019), pp. 77–104, <https://doi.org/10.1007/s11242-019-01289-9>.
- [268] J. REBACK, J. BROCKMENDL, W. MCKINNEY, J. VAN DEN BOSSCHE, T. AUGSPURGER, P. CLOUD, S. HAWKINS, G. F. YOUNG, S. INHRKS, M. ROESCHKE, A. KLEIN, T. PETERSEN, J. TRATNER, C. SHE, W. AYD, P. HOEFLE, S. NAVEH, M. GARCIA, J. SCHENDEL, A. HAYDEN, D. SAXTON, M. E. GORELLI, R. SHADRACH, V. JANCAUSKAS, A. MCMASTER, F. LI, P. BATTISTON, S. SEABOLD, ATTACK68, AND K. DONG, *pandas-dev/pandas: Pandas 1.3.0*, July 2021, <https://doi.org/10.5281/zenodo.5060318>.
- [269] W. REN AND W. E, *Boundary conditions for the moving contact line problem*, Physics of Fluids, 19 (2007), p. 022101, <https://doi.org/10.1063/1.2646754>.
- [270] W. REN, D. HU, AND W. E, *Continuum models for the contact line problem*, Physics of Fluids, 22 (2010), p. 102103, <https://doi.org/10.1063/1.3501317>.
- [271] L. A. RICHARDS, *Capillary conduction of liquids through porous mediums*, Physics, 1 (1931), pp. 318–333, <https://doi.org/10.1063/1.1745010>.
- [272] E. K. RIDEAL, *On the flow of liquids under capillary pressure*, The London, Edinburgh, and Dublin Philosophical Magazine and Journal of Science, 44 (1922), pp. 1152–1159, <https://doi.org/10.1080/14786441008634082>.
- [273] B. M. RIVIÈRE, *Discontinuous Galerkin methods for solving elliptic and parabolic equations: Theory and implementation*, Frontiers in Applied Mathematics, Society for Industrial and Applied Mathematics, Philadelphia, PA, 2008, <https://doi.org/10.1137/1.9780898717440>.
- [274] T. F. RUSSELL AND M. F. WHEELER, *Finite element and finite difference methods for continuous flows in porous media*, in The Mathematics of Reservoir Simulation, R. E. Ewing, ed., Frontiers in Applied Mathematics, Society for Industrial and Applied Mathematics, Philadelphia, PA, 1983, ch. 2, pp. 35–106, <https://doi.org/10.1137/1.9781611971071.ch2>.

- [275] A. RÄTZ AND B. SCHWEIZER, *Hysteresis models and gravity fingering in porous media*, Zeitschrift für Angewandte Mathematik und Mechanik, 94 (2014), pp. 645–654, <https://doi.org/10.1002/zamm.201200052>.
- [276] E. SANCHEZ-PALENCIA, *Non-Homogeneous Media and Vibration Theory*, vol. 127 of Lecture Notes in Physics, Springer, Berlin, Heidelberg, 1980, <https://doi.org/10.1007/3-540-10000-8>.
- [277] M. SCHNEIDER, T. KÖPPL, R. HELMIG, R. STEINLE, AND R. HILFER, *Stable propagation of saturation overshoots for two-phase flow in porous media*, Transport in Porous Media, 121 (2018), pp. 621–641, <https://doi.org/10.1007/s11242-017-0977-y>.
- [278] H. A. SCHWARZ, *Über einen Grenzübergang durch alternirendes Verfahren*, Vierteljahrsschrift der Naturforschenden Gesellschaft in Zürich, 15 (1870), pp. 272–286, https://www.ngzh.ch/archiv/1870_15/15_3/15_19.pdf.
- [279] B. SCHWEIZER, *Homogenization of a fluid problem with a free boundary*, Communications on Pure and Applied Mathematics, 53 (2000), pp. 1118–1152, [https://doi.org/10.1002/1097-0312\(200009\)53:9<1118::AID-CPA3>3.0.CO;2-J](https://doi.org/10.1002/1097-0312(200009)53:9<1118::AID-CPA3>3.0.CO;2-J).
- [280] B. SCHWEIZER, *Regularization of outflow problems in unsaturated porous media with dry regions*, Journal of Differential Equations, 237 (2007), pp. 278–306, <https://doi.org/10.1016/j.jde.2007.03.011>.
- [281] B. SCHWEIZER, *Homogenization of degenerate two-phase flow equations with oil trapping*, SIAM Journal on Mathematical Analysis, 39 (2008), pp. 1740–1763, <https://doi.org/10.1137/060675472>.
- [282] B. SCHWEIZER, *Instability of gravity wetting fronts for Richards equations with hysteresis*, Interfaces and Free Boundaries, 14 (2012), pp. 37–64, <https://doi.org/10.4171/IFB/273>.
- [283] B. SCHWEIZER, *The Richards equation with hysteresis and degenerate capillary pressure*, Journal of Differential Equations, 252 (2012), pp. 5594–5612, <https://doi.org/10.1016/j.jde.2012.01.026>.
- [284] B. SCHWEIZER, *Hysteresis in porous media: Modelling and analysis*, Interfaces and Free Boundaries, 19 (2017), pp. 417–447, <https://doi.org/10.4171/IFB/388>.
- [285] D. SEUS, K. MITRA, I. S. POP, F. A. RADU, AND C. ROHDE, *A linear domain decomposition method for partially saturated flow in porous media*, Computer Methods in Applied Mechanics and Engineering, 333 (2018), pp. 331–355, <https://doi.org/10.1016/j.cma.2018.01.029>.

- [286] D. SEUS, F. A. RADU, AND C. ROHDE, *A linear domain decomposition method for two-phase flow in porous media*, in Numerical Mathematics and Advanced Applications ENUMATH 2017, F. A. Radu, K. Kumar, I. Berre, J. M. Nordbotten, and I. S. Pop, eds., Cham, 2019, Springer, pp. 603–614, https://doi.org/10.1007/978-3-319-96415-7_55.
- [287] S. SHARMIN, C. BRINGEDAL, AND I. S. POP, *On upscaling pore-scale models for two-phase flow with evolving interfaces*, Advances in Water Resources, 142 (2020), p. 103646, <https://doi.org/10.1016/j.advwatres.2020.103646>.
- [288] P. SHENG AND M. ZHOU, *Immiscible-fluid displacement: Contact-line dynamics and the velocity-dependent capillary pressure*, Physical Review A, 45 (1992), pp. 5694–5708, <https://doi.org/10.1103/PhysRevA.45.5694>.
- [289] Q. SHENG AND K. THOMPSON, *A unified pore-network algorithm for dynamic two-phase flow*, Advances in Water Resources, 95 (2016), pp. 92–108, <https://doi.org/10.1016/j.advwatres.2015.12.010>.
- [290] S. SHIOZAWA AND H. FUJIMAKI, *Unexpected water content profiles under flux-limited one-dimensional downward infiltration in initially dry granular media*, Water Resources Research, 40 (2004), p. W07404, <https://doi.org/10.1029/2003WR002197>.
- [291] S. SINHA, M. A. GJENNESTAD, M. VASSVIK, AND A. HANSEN, *Fluid meniscus algorithms for dynamic pore-network modeling of immiscible two-phase flow in porous media*, Frontiers in Physics, 8 (2021), <https://doi.org/10.3389/fphy.2020.548497>.
- [292] J. O. SKOGESTAD, E. KEILEGAVLEN, AND J. M. NORDBOTTEN, *Domain decomposition strategies for nonlinear flow problems in porous media*, Journal of Computational Physics, 234 (2013), pp. 439–451, <https://doi.org/10.1016/j.jcp.2012.10.001>.
- [293] M. SLODICKA, *A robust and efficient linearization scheme for doubly nonlinear and degenerate parabolic problems arising in flow in porous media*, SIAM Journal of Scientific Computing, 23 (2002), pp. 1593–1614, <https://doi.org/10.1137/S1064827500381860>.
- [294] B. SMITH, P. E. BJØRSTAD, AND W. D. GROPP, *Domain Decomposition - Parallel Multilevel Methods for Elliptic Partial Differential Equations*, Cambridge University Press, 1996.
- [295] L. G. SOFTOVA AND P. WEIDEMAIER, *Quasilinear parabolic problem in spaces of maximal regularity*, Journal of Nonlinear and Convex Analysis, 7 (2006), pp. 529–540.

- [296] K. SPAYD AND M. SHEARER, *The Buckley–Leverett equation with dynamic capillary pressure*, SIAM Journal on Applied Mathematics, 71 (2011), pp. 1088–1108, <https://doi.org/10.1137/100807016>.
- [297] M. STANGE, M. E. DREYER, AND H. J. RATH, *Capillary driven flow in circular cylindrical tubes*, Physics of Fluids, 15 (2003), pp. 2587–2601, <https://doi.org/10.1063/1.1596913>.
- [298] Y. SUI, H. DING, AND P. D. SPELT, *Numerical simulations of flows with moving contact lines*, Annual Review of Fluid Mechanics, 46 (2014), pp. 97–119, <https://doi.org/10.1146/annurev-fluid-010313-141338>.
- [299] T. SWEIJEN, S. M. HASSANIZADEH, B. CHAREYRE, AND L. ZHUANG, *Dynamic pore-scale model of drainage in granular porous media: The pore-unit assembly method*, Water Resources Research, 54 (2018), pp. 4193–4213, <https://doi.org/10.1029/2017WR021769>.
- [300] A. TAHER, X. CAO, I. S. POP, A. J. J. VAN DER ZANDEN, AND H. J. H. BROUWERS, *Moisture transport in concrete during wetting/drying cycles*, Chemistry and Materials Research, 5 (2013), pp. 86–90, <https://iiste.org/Journals/index.php/CMR/article/view/11348>.
- [301] L. H. TANNER, *The spreading of silicone oil drops on horizontal surfaces*, Journal of Physics D: Applied Physics, 12 (1979), pp. 1473–1484, <https://doi.org/10.1088/0022-3727/12/9/009>.
- [302] L. TARTAR, *Incompressible fluid flow in a porous medium - convergence of the homogenization process*, in Non-Homogeneous Media and Vibration Theory, vol. 127 of Lecture Notes in Physics, Springer, Berlin, Heidelberg, 1980. Appendix of [276].
- [303] THE MATHWORKS INC., *MATLAB® version 9.8.0.1417392 (R2020a)*, 2020, <http://www.mathworks.com/products/matlab.html>.
- [304] K. E. THOMPSON, *Pore-scale modeling of fluid transport in disordered fibrous materials*, AIChE Journal, 48 (2002), pp. 1369–1389, <https://doi.org/10.1002/aic.690480703>.
- [305] P. A. THOMPSON, W. B. BRINCKERHOFF, AND M. O. ROBBINS, *Microscopic studies of static and dynamic contact angles*, Journal of Adhesion Science and Technology, 7 (1993), pp. 535–554, <https://doi.org/10.1163/156856193X00844>.
- [306] P. A. THOMPSON AND M. O. ROBBINS, *Simulations of contact-line motion: Slip and the dynamic contact angle*, Physical Review Letters, 63 (1989), pp. 766–769, <https://doi.org/10.1103/PhysRevLett.63.766>.

- [307] A. TOSELLI AND O. WIDLUND, *Domain Decomposition Methods - Algorithms and Theory*, vol. 34 of Springer Series in Computational Mathematics, Springer, Berlin, Heidelberg, 2005, <https://doi.org/10.1007/b137868>.
- [308] G. TRYGGVASON, R. SCARDOVELLI, AND S. ZALESKI, *Direct numerical simulations of gas-liquid multiphase flows*, Cambridge University Press, 2011.
- [309] K. VAFAI, ed., *Porous Media: Applications in Biological Systems and Biotechnology*, CRC Press, 2010, <https://doi.org/10.1201/9781420065428>.
- [310] C. J. VAN DUIJN, X. CAO, AND I. S. POP, *Two-phase flow in porous media: Dynamic capillarity and heterogeneous media*, *Transport in Porous Media*, 114 (2016), pp. 283–308, <https://doi.org/10.1007/s11242-015-0547-0>.
- [311] C. J. VAN DUIJN AND M. J. DE NEEF, *Similarity solution for capillary redistribution of two phases in a porous medium with a single discontinuity*, *Advances in Water Resources*, 21 (1998), pp. 451–461, [https://doi.org/10.1016/S0309-1708\(97\)00012-2](https://doi.org/10.1016/S0309-1708(97)00012-2).
- [312] C. J. VAN DUIJN, Y. FAN, L. A. PELETIER, AND I. S. POP, *Travelling wave solutions for degenerate pseudo-parabolic equations modelling two-phase flow in porous media*, *Nonlinear Analysis: Real World Applications*, 14 (2013), pp. 1361–1383, <https://doi.org/10.1016/j.nonrwa.2012.10.002>.
- [313] C. J. VAN DUIJN AND K. MITRA, *Hysteresis and horizontal redistribution in porous media*, *Transport in Porous Media*, 122 (2018), pp. 375–399, <https://doi.org/10.1007/s11242-018-1009-2>.
- [314] C. J. VAN DUIJN, J. MOLENAAR, AND M. J. DE NEEF, *The effect of capillary forces on immiscible two-phase flow in heterogeneous porous media*, *Transport in Porous Media*, 21 (1995), pp. 71–93, <https://doi.org/10.1007/BF00615335>.
- [315] C. J. VAN DUIJN, L. A. PELETIER, AND I. S. POP, *A new class of entropy solutions of the Buckley–Leverett equation*, *SIAM Journal on Mathematical Analysis*, 39 (2007), pp. 507–536, <https://doi.org/10.1137/05064518X>.
- [316] J. C. VAN DUIJN, H. EICHEL, R. HELMIG, AND I. S. POP, *Effective equations for two-phase flow in porous media: the effect of trapping on the microscale*, *Transport in Porous Media*, 69 (2007), pp. 411–428, <https://doi.org/10.1007/s11242-006-9089-9>.
- [317] M. VAN DYKE, *Perturbation Methods in Fluid Mechanics*, The Parabolic Press, Stanford, CA, 1975. Annotated Edition.

- [318] M. T. VAN GENUCHTEN, *A closed-form equation for predicting the hydraulic conductivity of unsaturated soils*, Soil Science Society of America Journal, 44 (1980), pp. 892–898, <https://doi.org/10.2136/sssaj1980.03615995004400050002x>.
- [319] T. L. VAN NOORDEN, *Crystal precipitation and dissolution in a thin strip*, European Journal of Applied Mathematics, 20 (2009), pp. 69–91, <https://doi.org/10.1017/S0956792508007651>.
- [320] P. VIRTANEN, R. GOMMERS, T. E. OLIPHANT, M. HABERLAND, T. REDDY, D. COURNAPEAU, E. BUROVSKI, P. PETERSON, W. WECKESSER, J. BRIGHT, S. J. VAN DER WALT, M. BRETT, J. WILSON, K. J. MILLMAN, N. MAYOROV, A. R. J. NELSON, E. JONES, R. KERN, E. LARSON, C. J. CAREY, İ. POLAT, Y. FENG, E. W. MOORE, J. VANDERPLAS, D. LAXALDE, J. PERKTOLD, R. CIRMANN, I. HENRIKSEN, E. A. QUINTERO, C. R. HARRIS, A. M. ARCHIBALD, A. H. RIBEIRO, F. PEDREGOSA, P. VAN MULBREGT, A. VIJAYKUMAR, A. P. BARDELLI, A. ROTHBERG, A. HILBOLL, A. KLOECKNER, A. SCOPATZ, A. LEE, A. ROKEM, C. N. WOODS, C. FULTON, C. MASSON, C. HÄGGSTRÖM, C. FITZGERALD, D. A. NICHOLSON, D. R. HAGEN, D. V. PASECHNIK, E. OLIVETTI, E. MARTIN, E. WIESER, F. SILVA, F. LENDERS, F. WILHELM, G. YOUNG, G. A. PRICE, G.-L. INGOLD, G. E. ALLEN, G. R. LEE, H. AUDREN, I. PROBST, J. P. DIETRICH, J. SILTERRA, J. T. WEBBER, J. SLAVIČ, J. NOTHMAN, J. BUCHNER, J. KULICK, J. L. SCHÖNBERGER, J. V. DE MIRANDA CARDOSO, J. REIMER, J. HARRINGTON, J. L. C. RODRÍGUEZ, J. NÚÑEZ-IGLESIAS, J. KUCZYNSKI, K. TRITZ, M. THOMA, M. NEWVILLE, M. KÜMMERER, M. BOLINGBROKE, M. TARTRE, M. PAK, N. J. SMITH, N. NOWACZYK, N. SHEBANOV, O. PAVLYK, P. A. BRODTKORB, P. LEE, R. T. MCGIBBON, R. FELDBAUER, S. LEWIS, S. TYGIER, S. SIEVERT, S. VIGNA, S. PETERSON, S. MORE, T. PUDLIK, T. OSHIMA, T. J. PINGEL, T. P. ROBITAILLE, T. SPURA, T. R. JONES, T. CERA, T. LESLIE, T. ZITO, T. KRAUSS, U. UPADHYAY, Y. O. HALCHENKO, Y. VÁZQUEZ-BAEZA, AND SCI-PY 1.0 CONTRIBUTORS, *SciPy 1.0: Fundamental Algorithms for Scientific Computing in Python*, Nature Methods, 17 (2020), pp. 261–272, <https://doi.org/10.1038/s41592-019-0686-2>.
- [321] O. V. VOINOV, *Hydrodynamics of wetting*, Fluid Dynamics, 11 (1976), pp. 714–721, <https://doi.org/10.1007/BF01012963>.
- [322] E. W. WASHBURN, *The dynamics of capillary flow*, Physical Review, 17 (1921), pp. 273–283, <https://doi.org/10.1103/PhysRev.17.273>.
- [323] S. WHITAKER, *Flow in porous media II: The governing equations for immiscible, two-phase flow*, Transport in Porous Media, 1 (1986), pp. 105–125, <https://doi.org/10.1007/BF01036523>.
- [324] B. I. WOHLMUTH, *Discretization Methods and Iterative Solvers Based on Domain Decomposition*, vol. 17 of Lecture Notes in Computational Science and Engineering, Springer-Verlag, Berlin, Heidelberg, 2001, <https://doi.org/10.1007/978-3-642-56767-4>.

- [325] Y. XIAO, F. YANG, AND R. PITCHUMANI, *A generalized analysis of capillary flows in channels*, Journal of Colloid and Interface Science, 298 (2006), pp. 880–888, <https://doi.org/10.1016/j.jcis.2006.01.005>.
- [326] H. T. XUE, Z. N. FANG, Y. YANG, J. P. HUANG, AND L. W. ZHOU, *Contact angle determined by spontaneous dynamic capillary rises with hydrostatic effects: Experiment and theory*, Chemical Physics Letters, 432 (2006), pp. 326–330, <https://doi.org/10.1016/j.cplett.2006.10.017>.
- [327] I. YOTOV, *A mixed finite element discretization on non-matching multiblock grids for a degenerate parabolic equation arising in porous media flow*, East-West Journal of Numerical Mathematics, 5 (1997), pp. 211–230.
- [328] E. ZEIDLER, *Applied Functional Analysis: Applications to Mathematical Physics*, vol. 108 of Applied Mathematical Sciences, Springer, New York, NY, 1995, <https://doi.org/10.1007/978-1-4612-0815-0>.
- [329] F. ZENG, Q. ZHANG, J. GUO, Y. MENG, X. SHAO, AND Y. ZHENG, *Capillary imbibition of confined water in nanopores*, Capillarity, 3 (2020), pp. 8–15, <https://doi.org/10.26804/capi.2020.01.02>.
- [330] B. V. ZHMUD, F. TIBERG, AND K. HALLSTENSSON, *Dynamics of capillary rise*, Journal of Colloid and Interface Science, 228 (2000), pp. 263–269, <https://doi.org/10.1006/jcis.2000.6951>.
- [331] Z. ZHOU AND D. LIANG, *The mass-preserving and modified-upwind splitting DDM scheme for time-dependent convection-diffusion equations*, Journal of Computational and Applied Mathematics, 317 (2017), pp. 247–273, <https://doi.org/10.1016/j.cam.2016.10.031>.
- [332] L. ZHUANG, S. M. HASSANIZADEH, C.-Z. QIN, AND A. DE WAAL, *Experimental investigation of hysteretic dynamic capillarity effect in unsaturated flow*, Water Resources Research, 53 (2017), pp. 9078–9088, <https://doi.org/10.1002/2017WR020895>.
- [333] L. ZHUANG, S. M. HASSANIZADEH, C. VAN DUIJN, S. ZIMMERMANN, I. ZIZINA, AND R. HELMIG, *Experimental and numerical studies of saturation overshoot during infiltration into a dry soil*, Vadose Zone Journal, 18 (2019), p. 180167, <https://doi.org/10.2136/vzj2018.09.0167>.

Curriculum vitae

Stephan Benjamin Lunowa was born on January 22, 1995 in Nürtingen, Germany. In 2016, he obtained a Bachelor of Science in *Simulation Technology* at the University of Stuttgart, Germany. Subsequently, Stephan pursued a joint Master of Science in *Simulation Technology* and *Industrial and Applied Mathematics* at the University of Stuttgart and Eindhoven University of Technology, The Netherlands. In 2018, he graduated with honors with the thesis "Linearization and domain decomposition methods for two-phase flow in porous media" supervised by Prof. Dr. Iuliu Sorin Pop (Hasselt University), Prof. Dr. Barry Koren (Eindhoven University of Technology) and Prof. Dr. Christian Rohde (University of Stuttgart).

Stephan was awarded the Deutschlandstipendium (scholarship for the studies) by the University of Stuttgart and Werner & Balci GmbH in Esslingen, Germany, between October 2013 and March 2014, followed by a scholarship by the German Academic Scholarship Foundation (Studienstiftung des deutschen Volkes e.V.) for the five years of studies. For the studies abroad in The Netherlands in 2017/18, he was granted scholarships by the Baden-Württemberg Stiftung and by the ALSP scholarship foundation of the University of Eindhoven.

In September 2018, Stephan began a doctoral program in mathematics at Hasselt University, Belgium, under the supervision of Prof. Dr. Iuliu Sorin Pop. During the studies, he was awarded an Oberwolfach Leibniz Graduate Students grant. In the course of his doctorate, he attended 18 summer schools and international conferences. The main results obtained during his PhD studies are presented in this dissertation. The PhD position was funded by the Special Research Fund (BOF) at Hasselt University (project BOF17NI01) and the Research Foundation Flanders (FWO, project G051418N).